Order Number 9230480

Radiative temperature measurements of the Puu o'o-Kupaianaha eruption with implications for satellite remote sensing

Flynn, Luke Paul, Ph.D.

University of Hawaii, 1992

U·M·I

300 N. Zeeb Rd.
Ann Arbor, MI 48106

RADIATIVE TEMPERATURE MEASUREMENTS OF THE PUU O'O - KUPAIANAHA ERUPTION WITH IMPLICATIONS FOR SATELLITE REMOTE SENSING

A DISSERTATION SUBMITTED TO THE GRADUATE DIVISION OF THE UNIVERSITY OF HAWAII IN PARTIAL FULFILLMENT OF THE REQUIREMENTS FOR THE DEGREE OF

DOCTOR OF PHILOSOPHY

IN

GEOLOGY AND GEOPHYSICS

MAY 1992

By

Luke Paul Flynn

Dissertation Committee:

Peter Mouginis-Mark, Chairman
Jonathan Gradie
Paul Lucey
Bernard Ray Hawke
Matthew McGranaghan

Acknowledgements

There are many people who helped with the final product of 5 1/2 years of research which appears in the following pages. I would first like to thank the members of my dissertation committee for all of their hard work and valuable comments in making the final polished copy: B. Ray Hawke for all of his abundant support from my comprehensive exams to the dissertation submission, Paul Lucey for the useful discussions about calibration spectra and spectroradiometers, and Matthew McGranaghan for saving the day and serving on my committee at the last minute (or last month)!

I have saved the two advisors who did the most for last. I thank the both of them for participating in many of the journeys in all types of inclement weather across miles of basalt and rain forest with "field-portable" equipment. To Jonathan Gradie, who I have known for 10 years, thank you for bringing me out to Hawaii. I sincerely appreciate all of the whirlwind, but highly enlightening, technical discussions on spectra and spectroradiometers. To Peter Mouginis-Mark, my dissertation committee chairman, I am sincerely indebted to you for all of your hard work and help throughout my graduate career. Thank you for all of the color photos of volcanic activity which appear in this dissertation. I will always remain deeply impressed with the abundant commitment and constant positive support for me and this project, especially during the long years of instrument calibration when it seemed that only he and I believed in its successful conclusion. Pete, thank you for being a teacher, an advisor, and most importantly, a friend.

I also extend many thanks to my colleagues who helped with numerous trips to Kilauea and discussions about this work; among these are Duncan Munro, Harold Garbeil,

Scott Rowland, Henning Haack, Marc Norman, Keith Horton, and Scott Moncrief. I also would like to thank the folks at SETS Technology, Inc. for providing the spectroradiometer and calibration equipment to make much of this work possible.

Most importantly, I would like to thank the members of my family for their support. To Mom, for of her love, for always believing, and for her help with Algebra word problems (which goes a long way in computer programming!), I thank you. To Dad, thank you for your gems of wisdom which acquire more luster with time. To my brothers, you are all as great friends as anyone could wish for. (Thanks Dave for the "life-preserver" letter you threw at a critical time in February!) And especially to little Victoria, thank you for showing me the wonders of the world through new eyes. To Pastor Bruce and Kay Craft, thank you for all of the love and support that you have shown to Mele and I. You made our world a much more enjoyable place!

Lastly, I dedicate this dissertation to two people who have been my greatest friends. To my Pepere, my first best friend, thank you for always having had endless hours to spend with a little boy and make him feel important. Your spirit is with me always. To my new best friend, my wife Mele, I have never met anyone with so much love to give. Thank you for all of your hard work and support during the long years of pursuing this goal. Thank you for being a wonderful Mama, and wife during a seemingly endless and most difficult time. This dissertation is partly yours, since the final product would have been impossible without your buoyant spirit, and constant support and enthusiasm. I will love you always.

Abstract

This dissertation presents the results of three research projects that use visible to near-infrared multi-spectral data to investigate the radiative signatures of active volcanic regions. Chapter 2 introduces a new tool, the use of hyperspectral data from a spectroradiometer, to study multiple thermal components of small (< 1 m^2) areas on active volcanic surfaces. The number of channels (~200) available for radiative temperature and area calculations represents a very significant improvement over the use of radiometers (1 channel) and Landsat TM data (2 channels for temperature/area calculations).

In Chapter 3, numerical models are developed to take advantage of the large number of available data and to identify multiple radiative components of the lava lake surface. Three stages of activity, based on video observations, are identified for the lava lake. Over 90% of the time, greater than 90% of the lava lake surface was covered by large plates of crust which had radiative temperatures as low as 150°C, but averaging ~280°C. Identification of these "cool" crust temperatures is important because it shows that these radiative temperatures can be an indicator of an active eruption and that the current generation of satellites may not be adequate to identify degrees of severity of volcanic activity.

One of the problems with acquiring spectral measurements during daylight hours is that the flux emitted by small hot radiators may not be significant compared to the flux from reflected sunlight. To eliminate this problem, the data presented in Chapter 4 were acquired at night. A turbulent lava channel and a cooling lava flow provided important end member temperature information for lava flow emplacement. Without

solar contamination, the spectral response in the acquired data was solely due to radiation from thermal sources.

Chapter 5 uses Landsat TM data to compare the differences between temperature, hot fractional area, and energy budget calculations using A-format (uncorrected) and P-format (geometrically corrected) data for a wide variety of volcanic activity. Although the energy budget estimates using both formats were consistent, the P-format correction process tended to smear pixels. Thus, A-format data is more useful for radiative temperature studies of active volcanoes

Table of Contents

page

page

page

List of Tables

List of Figures

Chapter 1: Introduction

1.1 Volcanic Hazards and Monitoring

Throughout recorded history, active volcanoes have been a source of hazard to human life. The incredible destruction wrought by Vesuvius (79 A.D.) on the tiny Roman city of Pompeii has only recently been recognized as exhumed skeletons and artifacts reveal the abruptness of the cataclysm. More recent eruptions such as El Chichon (1982), Nevado del Ruiz (1985), and Mt. Pinatubo (1991) have shown that in our era of high technology, long dormant volcanoes can still be very unpredictable and give little warning before coming back to life in a devastating fashion.

Seismic networks and tilt stations on potentially active volcanoes represent methods currently available to monitor the underground movement of magma and the dilation of the magma reservoir, respectively. However, these systems are very expensive both in terms of money and manpower. In addition, economic resources frequently do not exist in many second and third world countries to support elaborate efforts to study volcanic hazards. In many countries, such as Chile and Peru, so many volcanoes have been historically active that a prohibitively expensive effort would be necessary to continuously measure the seismicity and tilt of individual volcanoes. Even if the necessary funds could be gathered to support such efforts, the inaccessibility (mainly due to geographic location, but in some cases, such as Erta'Ale, Ethiopia, due to political turmoil) of many volcanoes would multiply the costs of setting up and maintaining monitoring networks.

Fortunately, another promising means of overseeing potentially active volcanoes lies in the field of remote sensing. Advances in satellite technology have made it possible to monitor many volcanoes in many different locations with a single space-borne platform. Orbiting satellites (such as the Landsat satellites) can target potentially active volcanoes over a large part of the globe. Satellites operating in geostationary orbits would be able to continuously record the activity of even the most remote volcanoes (with the exceptions of polar volcanoes, such as Mt. Erebus, Antarctica, which would lie over the horizon with respect to the satellite) provided that cloud cover did not obscure the scene.

Two characteristics of volcanic eruptions which can be detected from space are ash and sulfur dioxide plumes (Kreuger, 1983) in the vicinity of the volcano and hot (anomalously high radiant single or groups of pixels) spots within the surface extent of the volcano. It is very important to be able to recognize both signals of an eruption in progress since many volcanoes can exhibit either of these characteristics. Eruptions such as those that took place at Mt. St. Helens (1980) and Mt. Pinatubo (1991) are associated with massive outbursts of ash which can easily be spotted with the help of a satellite (i.e., Matson et al., 1991). Historically, eruptions taking place on Kilauea Volcano, Hawaii have lacked the ash clouds associated with some of the more silicic volcanoes, but sulfur dioxide and steam plumes may be discernible with satellite imagery, especially if the magma is erupting into seawater.

The other characteristic of a volcanic eruption that can be detected by satellites is an existence or an increase of hot radiant pixels on the edifice (for example, Rothery et al., 1988). Satellite sensors measuring radiant fluxes in wavelength bands in the visible to infrared part of the electromagnetic spectrum may be used to identify recently

erupted lava flows (for example, Pieri et al., 1990), active lava lakes (for example, Rothery et al., 1988), and increased fumarolic activity. The crux of quantitatively describing radiant temperatures occupying subpixel areas is the accurate identification of the sources of radiant flux entering the sensor at the satellite. Once the amount of radiant energy produced by volcanic activity can be identified, then the temperatures and sizes of different radiative areas of the surface may be identified. The goals of this dissertation are to develop new techniques using a narrow band spectroradiometer to identify sources of radiant flux from an active volcanic surface, to calculate radiant flux temperatures of volcanic activity and view the results in a temporal and spatial context, and to use both corrected (P-format) and uncorrected (A-format) Landsat Thematic Mapper (Landsat TM, henceforth) data to investigate the "artificial" radiant flux produced by "smearing" when raw data is resampled to produce square pixels.

1.2 Measurements of Lava Temperature by Conduction

Traditionally, the measurement of lava temperature has been carried out primarily using instruments which measure thermal energy either by conduction or radiation (Macdonald, 1972, p. 54 - 61), although petrologic efforts, such as measuring the abundance of crystal fragments in pumice samples (Peck and Kinoshita, 1976) have been carried out. Measuring lava temperature by conduction requires that the instrument be in contact with the test surface. Early attempts at estimating lava temperature at Kilauea used ceramic temperature indicators or Seger cones (Jaggar, 1917). These were not very accurate estimates since the deformation of the cones occurred at fairly widely spaced temperature intervals (20 - 40°C).

Currently, the thermocouple is the most commonly used instrument when measuring lava temperature by conductive means. It would be inappropriate here to list all of the studies using thermocouples which were carried out on active volcanic areas; however, as useful examples to be used as comparisons of magma temperature, I will cite some efforts which measured the temperature of molten basalt in lava lakes. In 1963, Peck et al. (1964) estimated the temperature of magma in Alae lava lake to be 1140°C, based on thermocouple readings of 1136°C in the base of a drill hole in the lake surface. Thermocouple measurements by Le Guern et al. (1979) at Erta'Ale showed that lava covered 7% of the lake at 1100°C, with the remainder of the surface exhibiting a glowing crust at 577°C. Le Guern (1987) also measured a lava fountain temperature of 1260°C at Niragongo. While thermocouples may give a fairly accurate molten magma temperature measurement, they will not yield, based on the observations of this study, accurate radiative skin temperature measurements, because the crust of the lake is a poor thermal conductor; hence, the temperature of the surface of a crusted-over lava lake is very much lower than that of the molten magma moving below the solid layer.

1.3 Measurements of Lava Temperature by Emitted Radiation

Certainly, the oldest method for estimating lava temperature is a radiative approach. Standing by an active flow, one can feel the increase in emitted energy as a new breakout occurs. After a few hours of standing next to active flows, an observer can obtain a good qualitative feel for the relative amounts of radiated energy produced by a wide variety of circumstances. Thus, measuring the radiative energy of volcanic activity can be accomplished remotely. Instruments measuring radiative temperatures

may be up to hundreds of kilometers distant since quanta of light or photons emitted by the source are detected by sensors calibrated to certain wavelength bands.

Previous field measurements of lava radiative temperatures have used primarily optical pyrometers (Macdonald, 1972, p. 55 - 57). The optical pyrometer is basically a telescope with a glowing filament. When the filament blends in color with the observed lava, the temperature of the lava may then be calculated. Thus, the pyrometer's lower effective limit is the lowest visible red detected by the human eye, which in this case serves as the sensor that is calibrated to the visible portion of the electromagnetic spectrum. Macdonald (1972, p. 56) gives the lowest temperature limit of the optical pyrometer as 475°C, which corresponds to the dullest red visible at night. Optical pyrometer measurements of the 1963 fire fountains at Alae lava lake, Hawaii gave maximum radiative temperatures of 1090 - 1100°C for freshly erupted magma measured at night. Pyrometers are more easily employed in the study of temperatures of very recently erupted magma. In order to study surfaces at cooler temperatures (150 - 450°C) measurements are more easily made in the near infrared (1 - 5 μm) (Rothery et al., 1988).

Recent advances in the remote thermal investigation of active volcanoes have demonstrated the ability of near-infrared and infrared sensors to estimate the radiative temperature of lava lakes, lava flows, and fumaroles. The instruments used to measure the radiative flux in such studies can be separated generally into two categories: satellite-borne sensors, primarily the Landsat TM (e.g. Rothery et al., 1988; Glaze et al., 1989; Pieri et al., 1990; Andres and Rose, 1991; and Oppenheimer, 1991) and the Advanced Very High Resolution Radiometer (AVHRR, Wiesnet and D'Aguanno, 1982), and field portable single-channel radiometers, such as the Minolta/Land Cyclops infrared

thermometers (Oppenheimer and Rothery, 1991). An exception falling out of both of these categories is a study in which a helicopter with a thermal infrared sensor that was flown over a Mauna Loa fire fountain obtained a radiative temperature of 1150°C (Pieri et al., 1985).

Both types of instruments have proved to be very important in the evolution of remote methods for studying volcanoes. For example, satellite sensors have been particularly useful in advancing the understanding of regional characteristics of active volcanoes. Rothery et al. (1988) pioneered the adaption of the "dual-band" method of separating two sub-pixel thermal radiators developed by Matson and Dozier (1981) and Dozier (1981) to Landsat TM data collected over a number of volcanic areas. An example of this temperature determination for a basaltic lava lake is a January 1986 TM image of Erta'Ale in Ethiopia which gave a dual-band solution of 800°C – 1000°C occupying 0.2 - 0.04% of a pixel for the northern 60 m diameter lake. Using the same dual-band technique, Glaze et al. (1989) attempted to quantify the energy budget of Lascar volcano using Landsat TM images. They recognized that the radiation emitting from the cooler background contributes much more to the overall flux of a radiant pixel than the fractionally small hot, magmatic area. Since the total energy flux increases as T^4, it is thus very important to choose a background temperature as carefully as possible.

To date, ground truth measurements necessary to confirm many of the observations reached using satellite data are surprisingly sparse. The analysis of Oppenheimer and Rothery (1991) is a notable exception, in that they calculate the radiative energy budget of a fumarole at Vulcano, Italy, using the Stephan-Boltzmann relationship and brightness temperatures generated by a Minolta/Land Cyclops thermometer. It was

determined that radiant energy of the fumarole would have been insufficient to produce a noticeable effect in a Landsat TM pixel.

While instantaneous regional views of hot volcanic surfaces have been obtained by satellite observations, and some ground truth brightness temperatures for small area volcanic surfaces have been obtained using single-channel radiometers, critical questions remain to be explored: what are the radiative components of an active lava lake as a function of temperature, and how do these components fluctuate with time? TM observations provide estimates of lava temperatures and the percentage of the image pixel that is filled by material at this temperature, but lack the temporal context or the spatial variability of dynamic lava lakes. Under optimum conditions, an image of any particular volcano can only be obtained from Landsat once every 16 days, so that only approximations to the thermal characteristics of any volcano can be derived (Glaze et al., 1989). In addition, all Landsat studies of active volcanoes are severely limited because only two bands are usable for temperature calculations. Only TM band 5 (1.55 - 1.72 μm) and band 7 (2.08 - 2.35 μm) may be used to calculate the radiative response of most volcanic areas (Rothery et al., 1988), so that even a simple solution to single pixel unmixing problems (Dozier, 1981) cannot be derived without assuming at least one of the three independent variables (the temperatures of the hot and cool radiators, and the fraction of the pixel occupied by either the hot or cool radiator). In addition, band widths for the TM are very wide (0.17 μm for band 5 and 0.27 μm for band 7), which limits the accuracy of the temperature determination due to the uncertainty in the distribution of flux over the particular band width.

1.4 Summary of Chapters

The purpose of this dissertation is to answer many of the questions advanced above and thus provide greater understanding about the radiative behavior of active and potentially dangerous volcanic hazards. Chapter 2 describes the experimental details of a ground truth survey in which a 1000-channel, narrow-band spectroradiometer was used to collect data at the then active Kupaianaha lava lake, Kilauea Volcano, Hawaii on the afternoons of October 12, 1987 and January 23, 1988. Chapter 3 includes the development of two- and three-component models to fit the collected spectral data and gives the results of the spectral study. The discussion in Chapter 3 answers questions about the importance the flux contribution of reflected sunlight on variable surface activity.

Using the knowledge gained from Chapters 2 and 3, Chapter 4 presents the results of spectral observations of active flows at night. The advantage of nighttime data is that there is no reflected sunlight component; hence, all of the flux measured by the spectroradiometer is radiation emitted by the surface in the field of view. In Chapter 4, the two-component model is used to calculate radiative temperatures and areas of sections of an active lava flow channel and cooling lava flow.

Numerous previous studies (e.g. Rothery et al.,1988; and Glaze et al., 1989) have hinted that A-format (uncorrected, raw data) Landsat TM data may eliminate the effects of pixel "smearing" found in P-format (corrected) data. In Chapter 5, I calculate radiative temperatures and areas using the dual-band method (Dozier, 1981) with both A- and P-format data collected over the East Rift Zone of Kilauea on July 23, 1991. I use the Rothery et al. (1988) method of using the midpoint of the wavelength band for calculations and I explore the possibilities of a new method which takes into account the

distribution thermal energy across the wavelength band. I compare temperature and area results of a number of different active centers including the Puu O'o cone (which reportedly contained a 5 m diameter lava lake); small (subpixel), hot skylights; and extensive (~100 pixels in total area) active lava flow fields. I calculate and compare the total energy budget, Q, for the entire area using both sets of data. Next, I compare average flux densities of a number of areas for both data sets.

Chapter 6 contains a summary of the major discoveries of the dissertation and ideas for data reduction of current and future satellite data sets. I also advance a number of suggestions to make future ground-truth efforts more useful for satellite studies.

References

Andres, R. J. and W. I. Rose, Detection of Thermal Anomalies Associated with the Santiaguito Dome, Guatemala With Landsat Thematic Mapper Imagery Abstracts of the Fall 1991 American Geophysical Union Conference, *EOS supplement*, 523, 1991.

Dozier, J., A method for satellite identification of surface temperature fields of subpixel resolution, *Remote Sens. Environ., 11,* 221 - 229, 1981.

Glaze, L., P. W. Francis, and D. A. Rothery, Measuring thermal budgets of active volcanoes by satellite remote sensing, *Nature, 338,* 144 - 146, 1989.

Jaggar, T. A., Thermal Gradient of Kilauea Lava Lake, *Journal of the Washington Academy of Sciences, v. 7*, p. 397-405, 1917.

Kreuger, A. J., Sighting of the El Chichon sulfur dioxide clouds with Nimbus-7 Total Ozone Mapping Spectrometer, *Science, 220,* 1377 - 1379, 1983.

Le Guern, F., J. Carbonelle, H. Tazieff, Erta ' Ale lava lake: Heat and gas transfer to the atmosphere, *J. Volcanol. Geotherm. Res., 6,* 27 - 48, 1979.

Le Guern, F., Mechanism of energy transfer in the lava lake of Niragongo (Zaire), 1959 - 1977, *J. Volcanol. Geotherm. Res., 31,* 17 - 31, 1987.

Macdonald, G. A., *Volcanoes* , Prentice-Hall, Englewood Cliffs, N.J., 1972.

Matson, M. and J. Dozier, Identification of subresolution high temperature sources using a thermal IR sensor, *Photogramm. Eng. Remote Sens., 47,* 1311 - 1318, 1981.

Matson, M., G. Stephens, and J. S. Lynch, A Satellite View of the Mount Pinatubo Eruptions, Abstracts of the Fall 1991 American Geophysical Union Conference, *EOS supplement*, 63, 1991.

Oppenheimer, C., Lava flow cooling estimated from Landsat Thematic Mapper infrared data: the Lonquimay eruption (Chile, 1989), *J. Geophys. Res., 96,* 21,865 - 21,878, 1991.

Oppenheimer, C. M. M., and D. A. Rothery, Infrared monitoring of volcanoes by satellite, *Journal of the Geological Society, London, 148,* 563 - 569, 1991.

Peck, D. L. and W. T. Kinoshita, The eruption of August 1963 and the formation of Alae lava lake, Hawaii, *U. S. Geol. Survey Prof. Paper 935 - A,* A1 - A23, 1976.

Peck, D. L., J. G. Moore, and G. Kojima, Temperatures in the crust and melt of Alae lava lake, Hawaii, after the August 1963 eruption of Kilauea Volcano - A preliminary report, *U. S. Geol. Survey Prof. Paper 501-D,* D1 - D7, 1964.

Pieri, D. C., A. R. Gillespie, A. B. Kahle, and S. M. Baloga, Thermal infrared observations of lava flows during the 1984 Mauna Loa eruption (abstract), Rep. Plan. Geol. Geophys. program, 1984, *NASA TM-87563,* 251, 1985.

Pieri, D. C., L. S. Glaze, and M. J. Abrams, Thermal radiance obseravtions of an active lava flow during the June 1984 eruption of Mount Etna, *Geology, 18,* 1018 - 1022, 1990.

Rothery, D. A., P. W. Francis, and C. A. Wood, Volcano monitoring using short wavelength infrared data from satellites, *Journal of Geophysical Research, 93,* 7993 - 8008, 1988.

Wiesnet, D. R., and J. D'Aguanno, Thermal imagery of Mt. Erebus from the NOAA-6 satellite, *Antarct. J. U.S., 17,* 32 - 34, 1982.

Chapter 2: Field Instrument, Measurement Technique and Calibration

2.1 Introduction

Chapter 2 introduces a powerful new tool for field studies of the radiative temperature of volcanic anomalies, namely, the calculation of radiative temperatures and areas of multi-component hot surfaces using multi-spectral data from field spectroradiometers. The Geophysical Environmental Research (GER) Mark IV spectroradiometer provides 1000 narrow wavelength band (2 - 4 nm) data per measurement in the wavelength range of 0.35 - 3.0 μm. Spectra collected with the GER spectroradiometer (or any similar narrow band multi-channel spectroradiometer) of hot volcanic sources can be used to compute temperatures by matching the measured spectral curve to Planck blackbody curves of different temperatures. The discussion below indicates the advantages of the GER spectroradiometer over previous instruments used to study radiative temperatures of volcanic sources.

Chapter 2 is devoted to the description of the features of the GER spectroradiometer, the target area where the instrument acquired data of an active lava lake, and the problems associated with both the calibration of the instrument and the correction of the collected spectra for the effects of reflected sunlight. The goal of Chapter 2 is to show the steps which were taken to reduce the spectroradiometer data from the raw (newly acquired with no corrections) form to that which could be used in numerical models presented in Chapter 3.

A second purpose of this chapter is to describe the field area where the spectroradiometer was used and describe the field set-up. Part of the description of the Kupaianaha lava lake field area includes a summary of important discoveries obtained by reviewing a video record which was collected concurrently with the spectral data. This record proved to be essential to this investigation, not only as a reminder of the prevailing conditions at the lava lake on 10/12/87 and 1/23/88 when spectra were acquired, but also for two other important purposes. The first was that the video record allowed us to study the activity of the surface of the lava lake to look for details which would otherwise have been lost in the excitement and hustle to acquire spectra. The realization that the activity of the lava lake can be categorized as one of three stages of activity is a result of observations of the video data. The second advantage of the video record was that it allowed me to measure the movement of plates of crust across the surface of the lava lake both in terms of the approximate velocity of individual plates and the total time required for plates to traverse the surface of the lava lake from one end to the other.

Before getting into the details of the GER spectroradiometer, it is important to review previous efforts to measure the radiative energy of volcanic sources and indicate where this work represents a significant advance over those efforts. As the use of satellites to monitor volcanic activity grows, it becomes increasingly more important to thoroughly investigate the radiative behavior of active volcanic areas. Field studies are necessary to quantify the radiative output of a wide variety of volcanic activity and thus provide a catalog of characteristics for satellite monitoring of volcanoes. Unfortunately, field studies attempting to quantify the radiative output of various volcanic surfaces are

few and far between (Le Guern et al.,1979; Le Guern, 1987; Jones et al., 1990; Oppenheimer and Rothery, 1991; and Oppenheimer, 1991).

Previous radiative field studies of active volcanic areas have been conducted using radiometers which measure emitted energy in only one broad wavelength band (Le Guern et al.,1979; Le Guern, 1987; Jones et al., 1990; Oppenheimer and Rothery, 1991; and Oppenheimer, 1991). While the portability of these radiometers in the field setting is a plus (they are generally very compact and light-weight) the usefulness of the data from instruments such as the Minolta/Land Cyclops radiometer system is questionable even by those investigators that use them (Oppenheimer and Rothery, 1991). The main problem with using these devices for studying active lava flows and lava lakes is that each measurement yields only one datum in a specified wavelength range. Thus, what the instrument actually reports is a "brightness" temperature. This is the temperature calculated from the total flux collected within the wavelength range of the radiometer's detector for the entire field of view. The radiometer can not discriminate between the following two examples of anomalies having the same total radiant flux: large areas occupying the entire field of view radiating at a uniform temperature and small hot subareas within the field of view radiating the majority of the measured flux with the remainder of the field of view radiating a fraction of the total flux. In both of these instances, the reported brightness temperature may be the same although the activity in the field of view may be dramatically different.

There are two problems with making the assumption that even small areas, such as those viewed by the radiometer (for Cyclops, 5.2 cm diameter from 1.5 m at 45°, Oppenheimer and Rothery, 1991), can be represented by a single radiative temperature. The first is that even for a small field of view, recently erupted magma

does not cool uniformly. Webs, strands, and small patches of crust on the millimeter and sub-millimeter scale form almost instantaneously on the newly erupted lava (Horton, 1991, personal communication and unpublished data). From video and visual observations of erupting flows on Kilauea, Hawaii, it would be impossible to locate a small patch of newly erupted material that is radiatively emitting energy at a uniform temperature. This means that soon after emplacement, the lava flow being measured by the single band radiometer would exhibit a brightness temperature which would be cooler than the magmatic surface and warmer than the new crust in the field of view.

The second problem with using single-band radiometers as radiative thermometers of lava flows (e.g., Jones et al., 1990; Oppenheimer, 1991) and lakes (Le Guern et al.,1979; Le Guern, 1987) is that in many cases the field of view may be deforming or moving between successive measurements. An erupting lava toe, for instance would be difficult to measure with a radiometer having a limited field of view, because the movement of the flow surface as it expands and forms would make studies of the cooling history of the toe impossible. It would be very difficult to pinpoint the exact area viewed in the previous measurement. This problem would increase with distance from the source of activity as small movements of the operator or tripod (if mounted) would change the field of view. A good example of this problem would be trying to study the cooling history of the surface of a lava lake, such as Kupaianaha, Kilauea, Hawaii. The main difficulty that the operator would face is that the lava lake surface in the field of view would be constantly moving, meaning that each measurement would have to be followed by a repositioning of the radiometer. Obtaining the same field of view for each measurement would not be assured.

To alleviate the problems of single channel radiometer measurements of active flows and lakes, multi-channel radiometers capable of acquiring spectral information in a number of wavelength bands must be used. The addition of more spectral channels allows one to solve for multiple areas radiating at multiple temperatures in the field of view (Flynn et al., 1990; Oppenheimer and Rothery, 1991). The problems and solutions for field instruments with point detectors (one measurement per field of view per spectral channel) are very similar to those discussed for sub-pixel radiators in Advanced Very High Resolution Radiometer (AVHRR) data in Dozier (1981) and Matson and Dozier (1981).

In order to address the temporal and spatial distribution of temperatures on an active lava lake, observations were made in 1987 and 1988 of the Kupaianaha lava lake, Hawaii, using a commercial GER (Geophysical and Environmental Research) visible/infrared dual-beam spectroradiometer made available for this study by SETS Technology, Inc. This instrument collects 1,000 data in the 0.35 - 3.00 μm spectral range with a spectral resolution of about 2 - 4 nm ($\lambda/d\lambda$ = 300 - 600). Use of this instrument represents a significant improvement over previous radiometer and remote sensing techniques for several reasons:

(1) The very large number of data points (the GER spectroradiometer collects ~200 usable data within atmospheric windows vs. only 2 for the Landsat TM and 1 for single-channel radiometers);

(2) The increased dynamic range of the instrument (GER ~40,000 vs. 256 for Landsat TM. The Minolta/Land Cyclops infrared radiometers give temperature readouts. The temperature ranges for the Cyclops 33 and 52 are 1050°C (-50

- 1000°C) and 2400°C (600 - 3000°C), respectively (Oppenheimer and Rothery, 1991);

(3) The greater spectral resolution (~56 times that of Landsat TM, ~150 times that of Cyclops 33, and ~225 times that of Cyclops 52).

These three characteristics of the GER spectroradiometer allow the flux distribution of the lava lake to be much more precisely determined than is possible with single channel field radiometers or spaceborne sensors. In addition, the ability to make high spatial resolution measurements (< 0.6 m^2) at frequent resampling (~1 minute) intervals enabled us to correlate the measured thermal characteristics with visual observations of the dynamics of the lake surface. Observations made over a time period of several hours also provide insights into the temporal variability of the volcano at a time scale unobtainable by spaceborne sensors that have overflight repeat frequencies of 16 days for Landsat TM or several hours for AVHRR.

2.2 The Geophysical and Environmental Research Mark IV Spectroradiometer

The GER IRIS Mark IV Spectroradiometer (Figure 2.1) is a dual-beam system so that two targets (with 3.0° angular separation) may be viewed simultaneously. The instrument is equipped with a viewing window and superimposed grid which allows the operator to center the spectroradiometer on a target using the same optics which are then used to take a measurement. The spectral window from 0.35 - 3.0 μm is covered in one continuous scan, during which time two spectra are acquired, one for each field-of-view. During the acquisition of a spectrum, gain is automatically adjusted by a microprocessor to accommodate for especially strong or weak signals. Scan rate (30 - 120 seconds for a single pair of spectra) can be varied by the operator.

The GER field spectroradiometer has four thumbwheel switches which set the speed factor, integration factor, gain setting and scan mode of the instrument. The speed factor allows the operator to choose between quick spectrum collection and increased dynamic range. For this study, almost all of the data were taken at speed factor 1 which gave 12-bit resolution in each gain used. Each measurement was completed in ~30 seconds. Seven of spectra were collected using speed factor 4 which gave 15-bit resolution in each gain used but with a 90-second measurement time. One pair of spectra were collected using speed factor 3 which gave 14-bit resolution in each gain used with a 70-second measurement time.

The other three thumbwheel settings were constant for all of the measurements completed at the Kupaianaha lava lake. For our observations, the integration factor was set at 1, meaning that one measurement was taken for each datum (i.e. multiple data values were not taken to yield an average value for a particular datum). The gain factor was set at 2, meaning that the 0 dB and 20 dB gains were used allowing for greater resolution in the measurements (12-bit resolution in each gain for most spectra). The fourth thumbwheel setting, which is the scan mode, allows for greater spectral resolution at certain wavelengths depending on the gratings which are assigned to cover wavelength regions. For our purposes, scan mode 2 was chosen because this is the normal laboratory scan mode covering the 0.35- 3.0 μm range. As a note to those who wish to use this instrument for further field studies, scan modes 1 or 3, which cover the 0.35- 2.5 μm range would be adequate for radiative measurements since a large water and carbon dioxide absorption band occupies the 2.5-3.0 μm range.

2.3 Description of Field Area

Most active lava lakes (e.g. Erta Ale, Erebus, Nyiragongo) are almost inaccessible, either due to political reasons or geographic location. An exception was the Kupaianaha lava lake, Hawaii (Figure 2.2), which was continuously active from July 1986 until August 1990. For more than four years, the Kupaianaha lava lake experienced constant semi-periodic overturning, followed by thick, stable, immobile crust formation, making it an excellent field site for our radiative temperature measurements. Periods when the lake surface was covered by a slow-moving crust and periods of vigorous magma fountaining provide important end-members for this thermal study.

Field spectra were collected of the active Kupaianaha lava lake on October 12, 1987 and on January 23, 1988. On 10/12/87, Jonathan Gradie and I set up the spectroradiometer and collected spectral measurements while Peter Mouginis-Mark and Joan Hayashi recorded the activity of the lake with a video camera and 35 mm photography, and helped to point out targets of interest for spectral measurements. I was not present when data were collected on 1/23/88 by Jonathan Gradie, Peter Mouginis-Mark, Duncan Munro, and Gerard Fryer.

The Kupaianaha lava lake was roughly the same size on both occasions when spectra were collected, but the distance between the surface of the lake and the rim of the crater varied. On October 12, 1987, the lava lake was ~50 m in diameter with a small, roughly rectangular, 30 m x 10 m channel. The lake surface was 1 – 2 m below the crater rim. On January 23, 1988, the lava lake was ~50 m in diameter but the channel had partially crusted over in the interim period. The surface of the lake was now ~10 m below the crater rim. On October 12, 1987, the field spectroradiometer was mounted on a 1.5 m high tripod which was situated on the edge of a ~6 m-high ledge (Figure 2.3),

with the instrument aimed so that the field of view (~1.5° x 3.0°) of the two beams encompassed relatively small (~0.23 m^2 each) areas of the lake surface. On January 23, 1988, the instrument was placed within 2 m of the crater rim ~10 m above the lake surface (Figure 2.4), and the field of view of each of the two beams was ~0.55 m^2. The viewing angle of the lake surface was 55° from the vertical on both occasions. Because the field of view was completely filled by the lake, the values of distance from the spectroradiometer to the lake surface and the area of the lake surface do not enter into the analysis of the blackbody temperatures. In addition to collecting 20 spectra over a time period of 1.5 hours on October 12, 1987, and 100 spectra on January 23, 1988, we also obtained 3.5 hours of video film on both days and made visual observations of the dynamics of the lake surface. These spectral observations covered a wide range of activity stages of the lake surface: some spectra were obtained when the lake was in a quiescent state, others when small (~2 m high) fountaining was taking place, and others when the lake surface was vigorously overturning.

An example of the raw data of the quiescent lake surface collected with the spectroradiometer is given in Figure 2.5. The spectrum provides an example of how the spectroradiometer automatically adjusts for strong signals. The abrupt decrease in counts at channel 770 is due to a gain change where the microprocessor switched from the 0dB to the 20dB gain. The abrupt increase in counts at channel 880 is due to a gain change from 20dB back to 0dB. The same spectra corrected for the effects of automatic gain change and plotted with respect to wavelength is given in Figure 2.6. The spectral range is 0.4 - 2.5 μm which corresponds to channels 30 - 860 in Figure 2.5.

2.4 Video Observations

While the spectra were being acquired, a video camera recorded the dynamics of the lake surface. The video camera was located within 3 meters of the spectroradiometer on both occasions so that the areas where spectral measurements were being made could be recorded on video tape. The surface of the Kupaianaha lava lake exhibited a wide range of activity from solid immobile crust to vigorous fountaining episodes. The video record proved to be an invaluable source of information which was referred to during the preparation of this dissertation. By reviewing it a number of times, I was able to identify different types of surface activity, to estimate the temporal and spatial extent of these types of activity over the whole lake surface, thus allowing the spatially limited spectral measurements to be extrapolated to the scale of the entire lake surface, and to make crude velocity measurements of portions of the lake surface.

Analysis of the video tape of the lake surface showed that Kupaianaha exhibited three stages of activity. The stages of activity identified in the video were used to categorize the collected spectra by matching the general characteristics of the physical appearance of the three stages on the surface of the lava lake with the conditions seen in the field of view of the spectroradiometer. As will be seen in Chapter 3, each stage of activity had unique thermal characteristics. Stage 1, which lasted only a few seconds to minutes at a time, was dominated by active and rapid rifting and fountaining. Large rifts (Figure 2.7) which formed between plates of the lake crust were up to 5 m wide and about 5 - 10 cm deep from visual estimation. Frequently large rifting events were also accompanied by the "subduction" of one plate of crust beneath another overriding plate. When subduction events occurred, large (many square meters) fans of magma erupted out of the rifts and engulfed the subducted plate. While the fresh magma rapidly formed

a thin skin and solidified, the effervescence of small (on the order of 10 - 50 cm in diameter) gas bubbles could be seen. Other Stage 1 activity included small (up to 5 m high) fountaining events which mainly occurred at the perimeter of the lake, with larger, less frequent events occurring in the center of the lake (Figure 2.8). The length of time between Stage 1 events was extremely variable and could reoccur as frequently as once every 10 minutes, or as long as a repose period of 30 minutes. At most, Stage 1 could have occupied 15% of the total surface area of the pond during an extremely brief but spatially large fountaining and subduction event; however, typically, Stage 1 occupied < 1% of the lava lake surface.

The second type of activity (Stage 2), identified with the video record, occurred on the surface of Kupaianaha lava lake when the surface began to form long (many meters), but narrow (0.5 - 2 m) fissures as the crust slowly pulled apart (Figure 2.9). During Stage 2, the surface was cut by several opening rifts which exposed hotter material that quickly solidified. Stage 2 fissures were present where new plates were being formed and where two plates of crust were moving past one another across the lake surface. Stage 2 rifts were present in all of the video record over limited (spatially) areas of the lake surface. For the duration of the video record, Stage 2 rifts occupied surface areas ranging from 0 - 25% of the lake surface. Typically, Stage 2 occupied <10% of the total surface area of the lava lake. Stage 2 rifts could be found at any time during our visits to Kupaianaha both at the perimeter of the lake and across the lake surface.

Stage 3, the third type of surface activity identified with the video record collected of Kupaianaha, is defined to be a quiescent stage which lasted up to thirty minutes at a time and was characterized by a thick, glassy crust moving slowly across the surface (Figure 2.10). By looking at events during which the surface crust buckled and cracked

(Figure 2.11), Stage 3 plates of crust exhibited thicknesses of up to 10 cm. Stage 3 activity occupied large portions (>90% of the total area) of the lake surface for the duration of the video record.

With the aid of the video film, I was able to study the surface of the lava lake and estimate levels of activity in terms of the three stages identified above. More than 90% of the time, Kupaianaha exhibited a state which could be most accurately described as being <1% Stage 1, <10% Stage 2, and >90% Stage 3. During these periods, Stage 1 fountaining or overturning episodes would frequently occur in very limited areas along the perimeter of the lava lake, with narrow rifts (Stage 2) developing between large (up to few hundred square meters) and rigid plates (Stage 3) dominating the rest of the lake surface. During periods of very sporadic (tens of minutes between episodes) increased activity, one plate would subduct beneath another, exposing fresh magma, or two plates would collide and deform one another until one cracked (Figure 2.11), again exposing fresh magma. On rare occasions, a magma fountain would erupt onto the surface from a rift between two plates.

The activity described above matches observations of other basaltic lava lakes. Tazieff (1979) provides a detailed description (supported by vivid color photographs) of Niragongo lava lake, Zaire for six field expeditions between 1953 and 1972. The photographs plainly show the three stages of activity (Tazieff (1979), pages 130 - 131 are good full-color examples) described here for Kupaianaha. In another study involving another African basaltic lava lake, Le Guern et al. (1979) describe the northernmost of the two basalt lava lakes at Erta'Ale as a 70 m diameter lake with 80 - 95% of the surface covered by a crust about 2 cm thick, floating on magma.

Approximate velocity measurements of the surface of Kupaianaha lava lake were derived from the video data (Figures 2.12 and 2.13). The motion of the lava lake surface on both days was roughly west to east. Distances were estimated from side-view pictures of the lake by scaling the size of people operating the spectroradiometer. Velocity values were checked by timing the movement of objects (apple cores) on the lake surface. Data collected on 10/12/87 (Figure 2.12) illustrate the stochastic nature of the motion. The highest "crustal" velocity observed was ~18 cm/sec for a fresh magma flowing across older crust, although more typical velocities would fall in the range of 0 - 4 cm/s. Large plates of crust would frequently impede the forward movement of the lake surface. Comparable data were also collected on 1/23/88 (Figure 2.13); however, the surface of the lava lake seems to have been in constant motion (average velocities of between 4 and 8 m/s) most of the time on this date as opposed to that of 10/12/87. The limited video coverage over both days suggests that the ~50 m wide lake was completely resurfaced every 20 - 30 minutes. This estimation is derived from measuring the time required for plates of crust to traverse the length of the lava lake. These observations of pond activity and crustal recycling rates are important in the context of satellite observations of active lava lakes because they highlight the temporal brevity of events when compared to the lengths of time between satellite acquisitions (a few hours at best for AVHRR). The video record shows that the level of activity (and, thus, the total emitted radiative energy) can change drastically on a minute to tens of minutes time scale. Thus, the satellites (Landsat and AVHRR) most commonly used presently for the study of active volcanoes, can only provide snapshots of volcanic activity. These satellite snapshots can be very misleading depending on whether

or not the volcanic anomaly is experiencing an extreme (a lull or an intense burst) in activity at the time of data acquisition.

2.5 Spectroradiometer Calibration

The raw uncorrected GER spectroradiometer data require correcting for instrument response across the spectral region, and for the amount of reflected sunlight. Instrument response is affected by the amount of electrical signal that is present when the spectroradiometer is operating with the aperture closed, and by the non-uniform registering of photons of different wavelengths. The former correction is frequently called the "dark measurement" which can easily be measured by covering the entrance optics of the spectroradiometer and taking a spectrum with no outside radiation affecting the detectors. Dark measurements were typically 60 – 62 counts in both the field and laboratory before and after the calibration spectra were collected. In all cases, dark measurements were found to be consistent with the different speed factors used. This spectroradiometer signal contribution was subtracted out of the raw data.

A common method used to correct for the spectroradiometer response to different amounts of photons of different wavelengths is to measure a spectrally-calibrated object for the wavelength range in question. In this study, two separate instruments which acted spectrally like blackbodies were used to calculate the field instrument's response. An EG&G Gamma Scientific Incorporated RS10A tungsten-halogen lamp with an RS-70-2 Diffuser (which was the property of SETS Technology, inc.) was used to calibrate the 0.4 -1.1 μm spectral region. The lamp-diffuser combination had a correlated color temperature of 2351°C ± 50°C according to laboratory supplied calibrations. The lamp and diffuser were set up so that the light exiting the diffuser

covered the aperture of the spectroradiometer. A total of twenty-two spectra were taken using the lamp/diffuser combination. The shape of the spectral curves for target and reference beams, at the same thumbwheel settings used for the collection of lava lake data, were found to be identical. An example of a calibration spectrum used to correct the lava lake data for instrument response is given in Figure 2.14. Note the bi-modal result which shows how the spectroradiometer records a 2351°C blackbody. A blackbody radiating at 2351°C should theoretically exhibit a spectrum in which flux increases with wavelength until ~1.1 μm (Wien's Law maximum), after which the flux will drop off gradually with increasing wavelength. This is not evident when viewing the spectroradiometer's response to the tunsten-halogen lamp. Order separating filters (i.e., filters that block-off specific wavelength regions), the blaze of spectroradiometer gratings (the "blaze" is the wavelength where the grating will return a maximum flux given a signal of constant flux intensity), and the sensitivity of the detector all contribute to the instrument response function. The instrument response function in this case could be explained as the product of the grating response with wavelength and the blackbody flux. The grating that the GER spectroradiometer used to collect data in this part of the spectrum is blazed at 0.66 μm (i.e., the maximum effectiveness of the grating is at 0.66 μm), resulting in a maximum in the instrument response curve at this wavelength. Longward of 0.66 μm the grating becomes less effective but the flux of the 2351°C blackbody is rapidly increasing, resulting in a second maximum at about 0.98 μm. A grating change occurs at about 1.05 μm, which is the reason for the downward spike in Figure 2.14.

A 900 ± 0.5°C blackbody source was provided for this study by using an Infrared Industries, Inc. Model IR-463 Source with a Model 101C Temperature Controller

(property of SETS Technology, Inc.). This source was capable of covering the whole wavelength range from 0.4 - 3.0 μm but I found that better signal to noise was obtained from two sources. Thus, the Model IR-463 Source was used to calibrate the wavelength region from 1.0 – 3.0 μm where the noise was insignificant. A total of 42 spectral pairs or 84 spectra were taken during four calibration sessions. (Since this was the first time that I ever calibrated a spectroradiometer, I wanted to make sure that the results would be consistent.) Blackbody spectra were taken using the GER spectroradiometer with the same various thumbwheel settings used while recording data in the field. Figure 2.15 and Figure 2.16 show the spectra used to reduce the target and reference data, respectively. Subtle differences in the shapes of the blackbody curves collected for the target and reference beams made it necessary to include examples of each here.

The resulting calibration spectra, one of a 2351°C tungsten-halogen lamp calibrated at 0.4 - 1.1 μm and the other of a 900°C blackbody source covering 1.0 - 3.0 μm for each of the target and reference beams, were compared to calculated blackbody values using Planck's Law.

In the form of an equation, the data correction reduces to the following:

$$\text{Data} = \frac{\text{BB (calc)}}{\text{BB(meas)}} * (\text{Dn} - \text{Dark}) \qquad (1)$$

where: "Data" are the channel flux values corrected for instrument response and dark measurement;

BB(calc) is the calculated value (in W cm^{-2} μm^{-1} sr^{-1}) of a blackbody at a particular wavelength (2351°C at 0.4 - 1.1 μm, 900°C at 1.0 - 3.0 μm) using Planck's function;

BB(meas), measured in counts, is the response of the spectroradiometer to a 2351°C blackbody at 0.4 - 1.1μm or to a 900°C blackbody at 1.0 - 3.0 μm;

Dn, measured in counts, is the uncorrected measurement of flux actually entering the spectroradiometer from the lava lake surface;

Dark, measured in counts, is the flux measured by the spectroradiometer when its aperture is closed to outside stimuli (dark measurement).

The calculated blackbody curve at a given wavelength divided by the GER spectroradiometer measured flux value at the same wavelength, yielded the instrument response correction for a particular wavelength (Figure 2.17). The instrument response of the tungsten filament lamp was normalized to that of the 900°C blackbody source at 1.09485 μm. The large peak in Figure 2.17 at ~ 1.1 μm marks the effectiveness limits of the two blackbody sources. The tungsten filament lamp had an effective calibration range of 0.4 - 1.1 μm, while the flux from the Infrared Industries Model IR-463 source was very low shortward of 1.0 μm. For the purposes of this investigation, data for the numerical models introduced in Chapter 3 were chosen from the wavelength range of 1.24 - 2.25 μm where the instrument response curve was fairly flat.

An example of a spectrum (Figure 2.6) corrected for the effects of instrument response is given in Figure 2.18. The data for Figure 2.18 were produced using equation 1, above. Since I did not measure the instrument response of the spectroradiometer with spectral standards that would have allowed for absolute calibration, the data are plotted in terms of relative radiance ($W/cm^2/\mu m/sr$). I am confident that the channel to channel calibrations are accurate given the performance specifications of the calibration

equipment and the identical repeatability of the calibration measurements. In Chapter 3, I will point out why relative radiance is all that is necessary to calculate blackbody temperatures from the spectral data. The major differences between Figures 2.6 and 2.18 is that the reflected solar flux is more apparent in the 0.5 - 1.24 μm range in Figure 2.18, and the rise in flux after 2.0 μm has a slightly shallower slope in Figure 2.18 than in Figure 2.6.

For the purposes of this study, the instrument response corrections were then normalized to results obtained at 1.09485 μm, which falls within the effective region (1.0 - 1.1 μm) where the signal to noise ratios are low for both instruments used for the instrument response corrections. Table 2.1 shows the instrument response correction for the target and reference beams (Some spectra were acquired while a neutral density filter covered the entrance port of the spectroradiometer. For a discussion of the effects that the filter had on spectra, see Chapter 3, section 3.5). After the instrument response correction is applied, data values in the near infrared region (around 1.24 μm) of the spectrum were enhanced relative to those in the visible (o.45 - 0.8 μm) and longer infrared region (> 1.53 μm) of the spectrum.

2.6 Reflected Sunlight Corrections

The final correction which must be made to the data is to separate the reflected sunlight flux from the lake-generated thermal flux. The sun is an approximate 5530°C (5800K) blackbody (Shu, 1982) with a peak radiative emission at about 0.554 μm. I studied the radiative response of the lava lake in the wavelength region of 0.95 - 2.25 μm, where the contribution of reflected sunlight from the newly formed lava crust decreases with increasing wavelength. Adjustment for reflected sunlight is especially

important up to 1.50 μm where the amount of flux contributed by reflected sunlight is significant compared to the amount of flux contributed by magmatic sources. In some cases, where the lake is covered by a thick crust (Stage 3), it can be above 90% of the total instrument-response corrected signal. For wavelengths <1.5 μm, the primary thermal flux contribution comes from radiators of magmatic temperature. It is therefore important to subtract out reflected sunlight as accurately as possible to make calculations of the radiative temperature and area of the magma on the lake surface as accurate as possible. Flux contributed by the relatively cool surface crust increases exponentially with increasing wavelength in the 1.5 - 2.10 μm region. Thus, spectral values measured at wavelengths longer than 1.5 μm are increasingly dominated by the lava lake thermal emissions, and reflected sunlight has a rapidly diminishing effect on the data.

Fortunately, the correction for reflected sunlight can be done readily since the effect of the solar component is easily recognized in the spectral data as a blackbody having a peak at about 0.554 μm (see Figure 2.6). The method that was used to eliminate this flux was to first collect spectra of the sun reflected off of a white pad. A total of 20 pairs of spectra were taken on two days using the same white paper which was also measured at the time that spectra were collected at the lava lake. Figures 2.19 and 2.20 are the target and reference (respectively) spectra collected of a white pad in direct sunlight. Values from Figures 2.19 and 2.20 were used to estimate the amount of reflected sunlight contributing to the total flux collected at the wavelengths used for calculations in this study. The white pad spectral data were used to calculate the ratio of the flux measured at the wavelengths used in this study to the flux measured at 0.554 μm where the reflected sunlight curve is near its maximum. The resultant ratios, when

multiplied by the instrument response corrected spectral value at a given wavelength, give the amount of reflected sunlight in the spectral data.

A number of assumptions had to be made to use this approximation; namely, the flux entering the spectroradiometer at 0.554 μm must be only reflected sunlight; the amount of sunlight reflecting off of the test surface (the white pad) and the lake surface must be constant over the time interval that the spectroradiometer was obtaining data; and the reflectance of the lava lake surface and the white pad must behave in the same manner with respect to wavelength. The first assumption is valid and can be proved numerically by calculating the amount of solar flux reflected off of the lava lake surface at 0.554 μm and comparing it with the amount of thermal energy produced for the same piece of crust at 0.554 μm. The amount of solar irradiance at 0.554 μm striking an area at sea level is 135 mW cm^{-2} μm^{-1} (Wolfe and Zissis, 1985). If the lake surface reflects only 0.5% of this radiation, then the reflected solar radiance becomes 7.16 x 10^{-2} mW cm^{-2} μm^{-1} sr^{-1}. I can compare this amount with the thermal radiance of the lava lake surface by using Planck's law which is given as

$$B_\lambda(T) = \frac{2hc^2}{\lambda^5} \frac{1}{e^{(hc/\lambda kT)}-1} \qquad (2)$$

where $B_\lambda(T)$ is the power at wavelength λ radiated per unit wavelength per unit solid angle into a small cone from a piece of the surface of an opaque body with uniform temperature T (in Kelvin), with the piece having unit area in the projection perpendicular to the axis of the cone; h is Planck's constant (6.63 x 10^{-34} J s); c is the speed of light (3.00 x 10^8 m s^{-1}); and k is Boltzmann's constant (1.38 x 10^{-23} J K^{-1}) (Shu, 1982). Using Planck's law, it is possible to calculate the amount of flux produced at 0.554 μm by blackbodies radiating at typical magmatic temperatures. Since

this study concentrated on measuring the thermal output of crusted over portions of the lava lake, we will consider a test case (shown below to be typical of Stage 3 activity) in which 0.0001% of the area on the lake surface exhibited a magmatic temperature of 1150°C, while the remainder of the surface was radiating at 200°C. The thermal radiance of the surface at 0.554 μm is 8.72×10^{-6} mW cm^{-2} μm^{-1} sr^{-1} which is four orders of magnitude below the amount of reflected solar radiation calculated above and is therefore negligible. A second test case more representative of Stage 1 activity in which 0.05% of the area on the lake surface exhibited a magmatic temperature of 1200°C, while the rest of the surface radiated at 450°C yields a thermal radiance at 0.554 μm of 2.44×10^{-3} mW cm^{-2} μm^{-1} sr^{-1}. In this case, the thermal radiance is about 3% of the total flux at 0.554 μm. However, it will be shown in Chapter 3 that for Stage 1 activity the reflected solar component is less than 3.5% of the total flux at the wavelengths used for calculations in this study; meaning that even in the upper limit test case, the error resulting from our assumption that all of the flux at 0.554 μm is reflected solar energy is extremely small. The spectral response at 0.554 μm is dominated in every case in our study by reflected sunlight.

The validity of the second assumption, which was whether or not sun illumination was constant during the times when spectral measurements were being collected, depends on the conditions which were observed when the measurements were made. The white pad reflectance spectra were collected on cloudless days when the amount of sunlight incident on the pad was fairly constant. The amount of direct sunlight present during the field measurements was also fairly constant at a 30-second time scale, allowing for periods of constant illumination to be used for data collection. As has been noted previously, the reflected sunlight component in the data has little effect (<2% in

all cases) in the resultant spectrum longward of 2.00 μm where the thermal flux from the crust of the lake dominates. Given a 30-second total measurement time, the error due to changes in reflected sunlight is the difference in lighting which occurred over the span of roughly 25 seconds (the time taken to collect data from 0.5 - 2.25 μm).

To determine differences, if any, between the reflectance of the white pad and the fresh basalt surface, the spectral response curves of the both were measured using laboratory spectrometers. The white pad used in this study, when compared to a halon standard, was found to vary in reflectance by ~40% over the 0.55 - 2.25 μm range (Figure 2.21); consequently, we determined that it was necessary to correct reflected sun estimates by the values obtained from the white pad data. Corrections for all wavelengths used in this study can easily be achieved by dividing the amount of reflected sunlight flux calculated above using Figures 2.19 and 2.20 by the white pad/ halon reflectance read from Figure 2.21. Next, the reflectance of fresh (three days old) basalt was also measured to check for changes in reflectance with wavelength. The reflectance of the basalt was extremely low (on the order of the reflectance from a black hole, which was also measured and should theoretically have a reflectance of zero) and was found to be less than 0.5% over the 0.55 - 2.25 μm wavelength region. Special attention was required to orient the basalt sample so that specular reflection was kept to a minimum.

The effects of sunlight were then subtracted from all channels used in this study by ratioing the spectral response of the reflected sun spectrum at 0.554 μm to the responses at those wavelengths used in the study. The amount of flux present in the spectra at 0.554 μm multiplied by the ratio determined from the white pad (corrected

by the white pad over halon reflectance) gave the amount of sunlight which must be subtracted from that particular spectral channel.

The resultant thermal spectrum is thus corrected for instrument response and the variable effect of reflected sunlight, which generally decreases in importance with increasing wavelength, and is in a form suitable for processing via the numerical model described in Chapter 3. It is important to note that it was unnecessary to correct any channels which were not used in the study since a limited number of data located in atmospheric windows were all that was necessary to perform the blackbody calculations. Application of this calibration technique produces the values given in Table 2.2 for the spectrum shown in Figure 2.6. Note the value given for 1.24 μm (Table 2.2) is very low because the flux from sunlight reflecting off of the thick-crusted (Stage 3) lake surface makes up ~90% of the total flux at this wavelength. Since the amount of radiation emitted by the lake surface is not comparably significant at wavelengths such as this, and calculations using these data would include potentially high errors, these data were not used in the numerical models for Stage 3 enumerated in Chapter 3.

2.8 Summary

In Chapter 2, I introduce a new instrument, the GER Mark IV spectroradiometer, for field studies of the radiative temperatures of active volcanic areas. The advantages of spectroradiometers, such as the one described in this chapter, over previous instruments used for the same purpose are the greater number of data collected per measurement, allowing for the solution of multiple subareas at multiple temperatures within a single field of view; the increased dynamic range of the instruments, which provide more precise measurements of radiance in each channel of detection; the greater

spectral resolution, which increases the probability of an even distribution of flux across the individual wavelength bands; and the simultaneous collection of two sets of data with an angular separation of 3.0°, allowing for the study of small scale variations of radiative temperature on the surface of the lava lake.

The GER spectroradiometer was used to collect spectral data at the then-active Kupaianaha lava lake, Hawaii on 10/12/87 and 1/23/88. The acquired spectra had to be corrected for the effects of instrument response and reflected sunlight. The instrument response calibrations were derived from measurements of blackbody standards of known temperature. Corrections for reflected sunlight were more involved in that they required measurements of the reflectance of a white pad in sunlight, and the spectral characteristics of a white pad and basalt glass samples.

Chapter 2 also provides a description of the field set up and observed activity at the Kupaianaha lava lake. A video record, which was acquired concurrently with the spectral measurements, provides important information about the dynamics of the lake surface. With the video record, three stages of activity have been identified which will serve as categories for the spectral measurements, depending on the conditions present within the field of view of the spectroradiometer when the spectral data were acquired. The video record also shows that the radiative output of the lava lake changes on minute to ten minute time scales meaning that snapshots of activity obtained by the current generation of satellites may not give an accurate picture of the extent of activity over an erupting volcano.

In the context of this dissertation, Chapter 2 describes an instrument which was used to collect spectral data that are presented in Chapters 3 and 4. The calibrations explained in Chapter 2 are the necessary steps required for processing the spectral data

which will then be used in the numerical models presented in Chapter 3. The video record described in Chapter 2 provides the delineations between stages of activity which are used to group spectra acquired while the lake was exhibiting roughly consistent activity. The spectra representing the three stages of activity will be studied in Chapter 3 to try to assign radiative temperature and area characteristics to complement the visual differences between stages reported in Chapter 2.

References

Dozier, J., A method for satellite identification of surface temperature fields of subpixel resolution, *Remote Sens. Environ., 11,* 221 - 229, 1981.

Flynn, L. P., P. J. Mouginis-Mark, and J. C. Gradie, Radiative Temperature Measurements of Kilauea Volcano, Hawaii, paper presented at International Volcanological Congress, *Int. Assoc. Volcanol. Chem. Earth's Interior,* Mainz, Germany, Sept. 3-8, 1990.

Jones, A. C., L. Wilson, and H. Pinkerton, Surface temperature measurements of active Hawaiian lava flows, paper presented at International Volcanological Congress, *Int. Assoc. Volcanol. Chem. Earth's Interior,* Mainz, Germany, Sept. 3-8, 1990.

Le Guern, F., Mechanism of energy transfer in the lava lake of Niragongo (Zaire), 1959 - 1977, *J. Volcanol. Geotherm. Res., 31*, 17 - 31, 1987.

Le Guern, F., J. Carbonelle, H. Tazieff, Erta'Ale lava lake: Heat and gas transfer to the atmosphere, *J. Volcanol. Geotherm. Res., 6*, 27 - 48, 1979.

Matson, M. and J. Dozier, Identification of subresolution high temperature sources using a thermal IR sensor, *Photogramm. Eng. Remote Sens., 47,* 1311 - 1318, 1981.

Oppenheimer, C. M. M., and D. A. Rothery, Infrared monitoring of volcanoes by satellite, *Journal of the Geological Society, London, 148,* 563 - 569, 1990.

Oppenheimer, C., Lava flow cooling estimated from Landsat Thematic Mapper infrared data: the Lonquimay eruption (Chile, 1989), *J. Geophys. Res., 96,* 21,865 - 21,878, 1991.

Shu, F. H., *The Physical Universe: An Introduction to Astronomy*, University Science Books, Mill Valley, California, 1982.

Wolfe, W. L., and G. J. Zissis, *The Infrared Handbook*, Infrared Information and Analysis (IRIA) Center, Environmental Research Institute of Michigan, Ann Arbor, Michigan, 1985.

Table 2.1

List of normalizations for target and reference beams of the spectroradiometer for wavelengths most frequently used as input for model calculations in Chapter 3. Normalizations derived from Figures 2.14 - 2.16.

Wavelength (μm)	Normalization target	Normalization reference
0.554	0.35915	0.34834
1.098	1.00000	1.00000
1.230	0.73229	0.69677
1.240	0.64845	0.62274
1.250	0.58545	0.55681
1.530	0.40320	0.37527
1.660	0.41878	0.38682
1.700	0.42399	0.39428
2.080	0.23929	0.23147
2.100	0.25171	0.23281
2.250	0.24111	0.26484

Table 2.2

Example of data reduction for Kupaianaha spectral data. Data from Figure 2.6, normalizations determined from Figures 2.14 and 2.15, solar component calculated from data from Figures 2.17 and 2.19.

Wavelength(μm)	Raw Data	Normalized Data	Solar Component	Thermal Component
0.554	16103.1	5783.4	5783.4	0.0
1.240	2382.6	1545.0	1281.6	263.4
1.530	4075.3	1643.2	682.8	960.4
1.660	6182.9	2589.3	591.2	1998.1
1.700	6914.3	2931.6	507.3	2424.3
2.080	55009.1	13163.1	216.9	12946.2
2.100	60485.5	14414.9	243.8	14171.1
2.250	93403.3	23510.5	317.3	23193.2

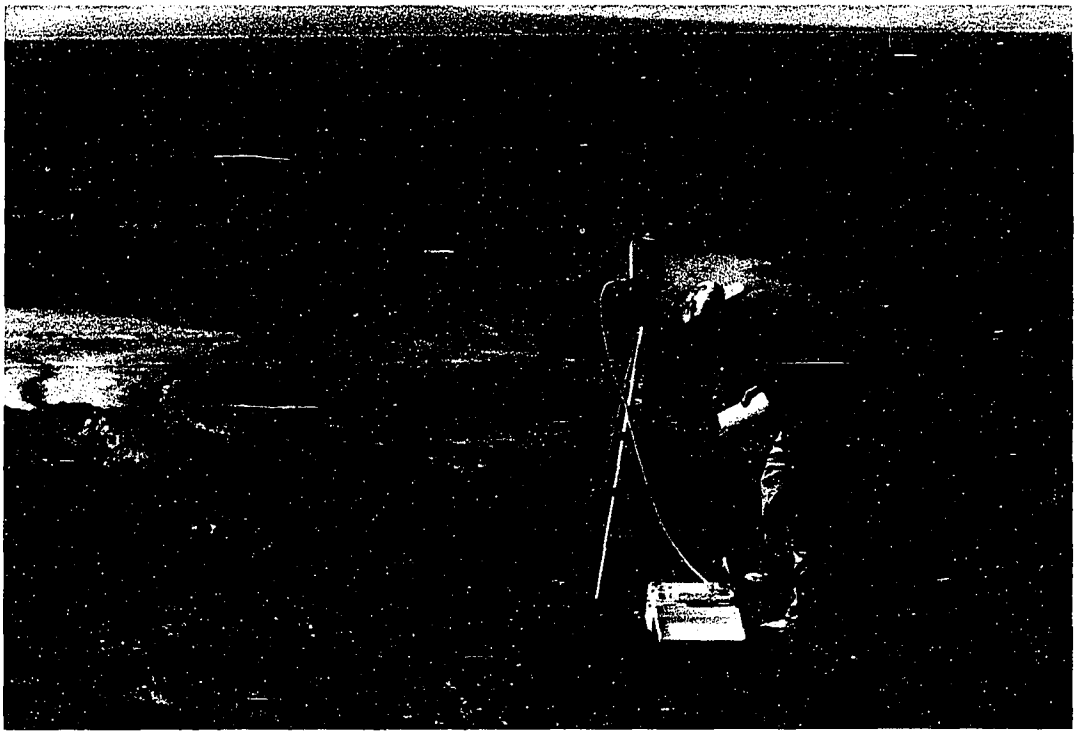

Figure 2.1. The spectroradiometer in operation on 10/12/87 at Kupaianaha lava lake.

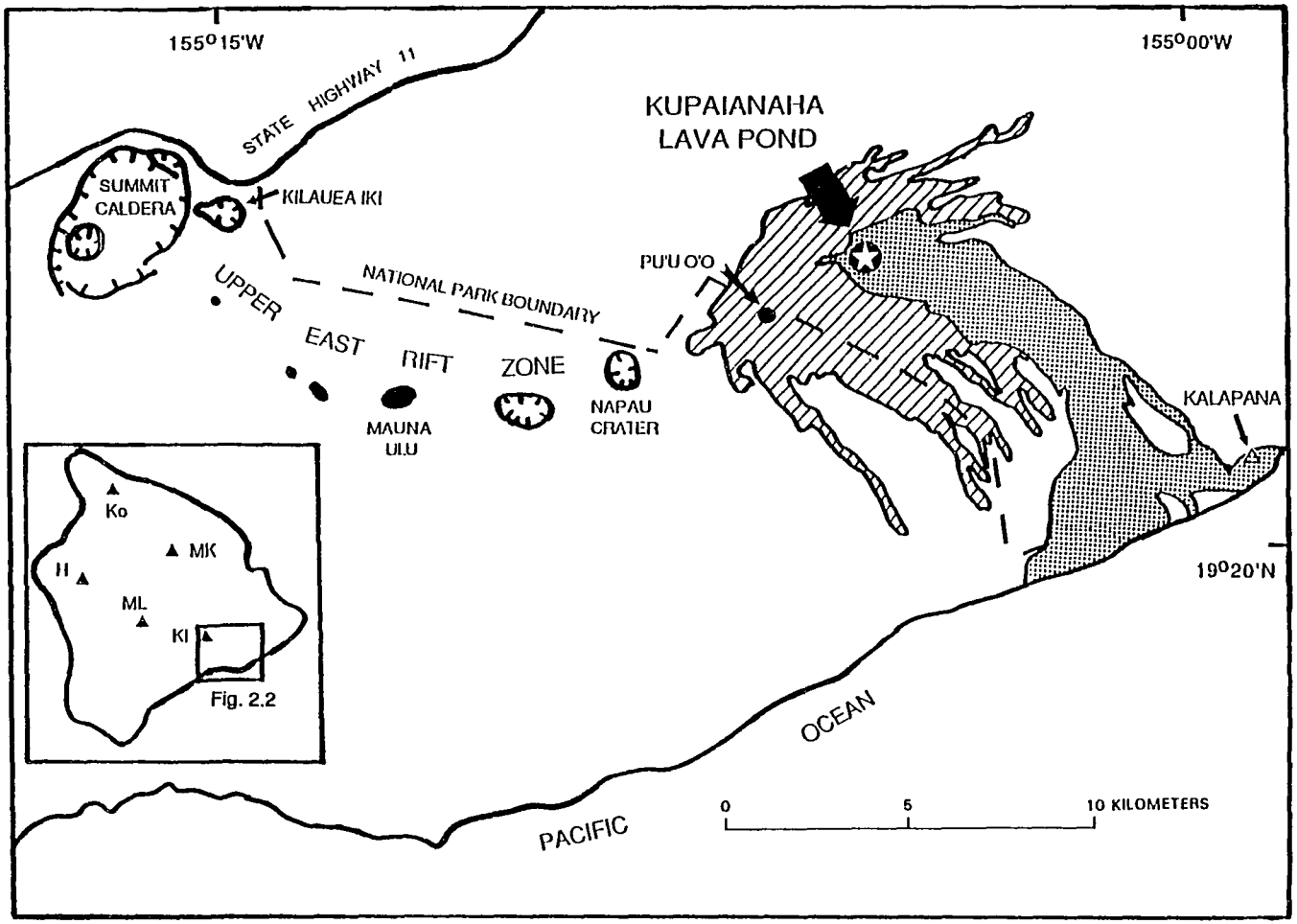

Figure 2.2. Location map for Kupaianaha lava lake (denoted by a star) on the East Rift Zone of Kilauea Volcano, Hawaii. Stippled region marks approximate boundaries of flows associated with Kupaianaha up to its cessation of activity in August, 1990. Slashed region shows the approximate extent of Pu'u O'o flows up to August, 1990.

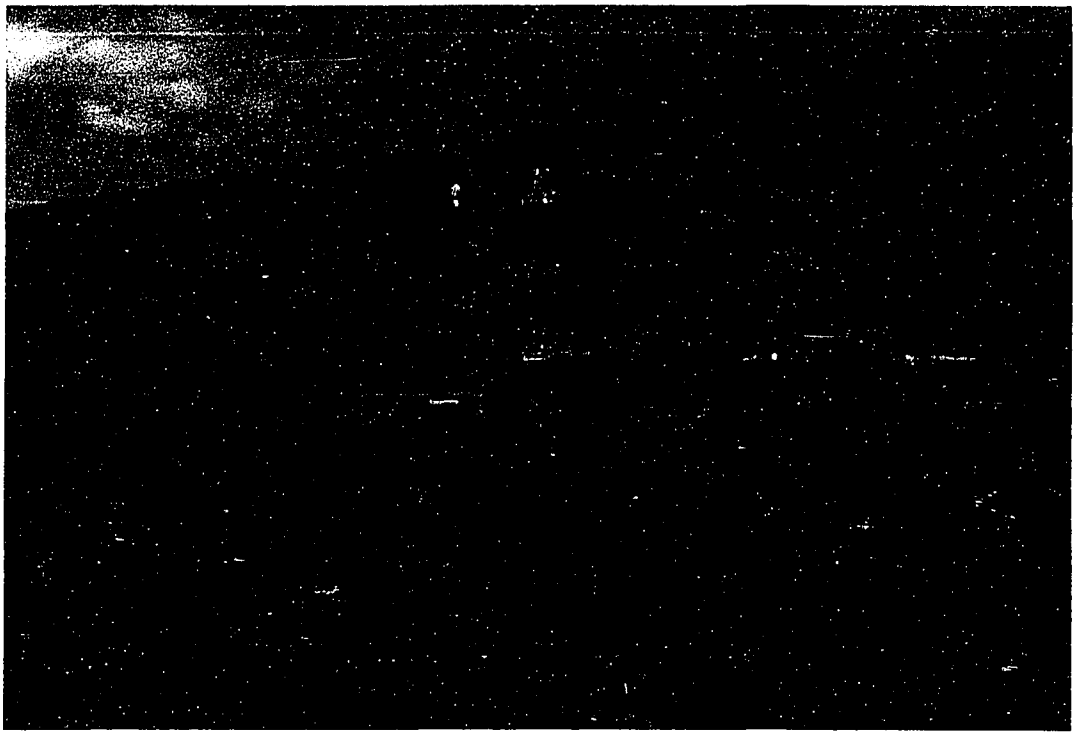

Figure 2.3. The operational deployment of the spectroradiometer as viewed from across Kupaianaha lava lake. Note that the ledge on which the spectroradiometer was located was approximately 6 m high.

Figure 2.4. The operational deployment of the spectroradiometer on 1/23/88 at Kupaianaha lava lake. Note the declination angle (~55° from vertical) of the spectroradiometer's optical head (on tripod).

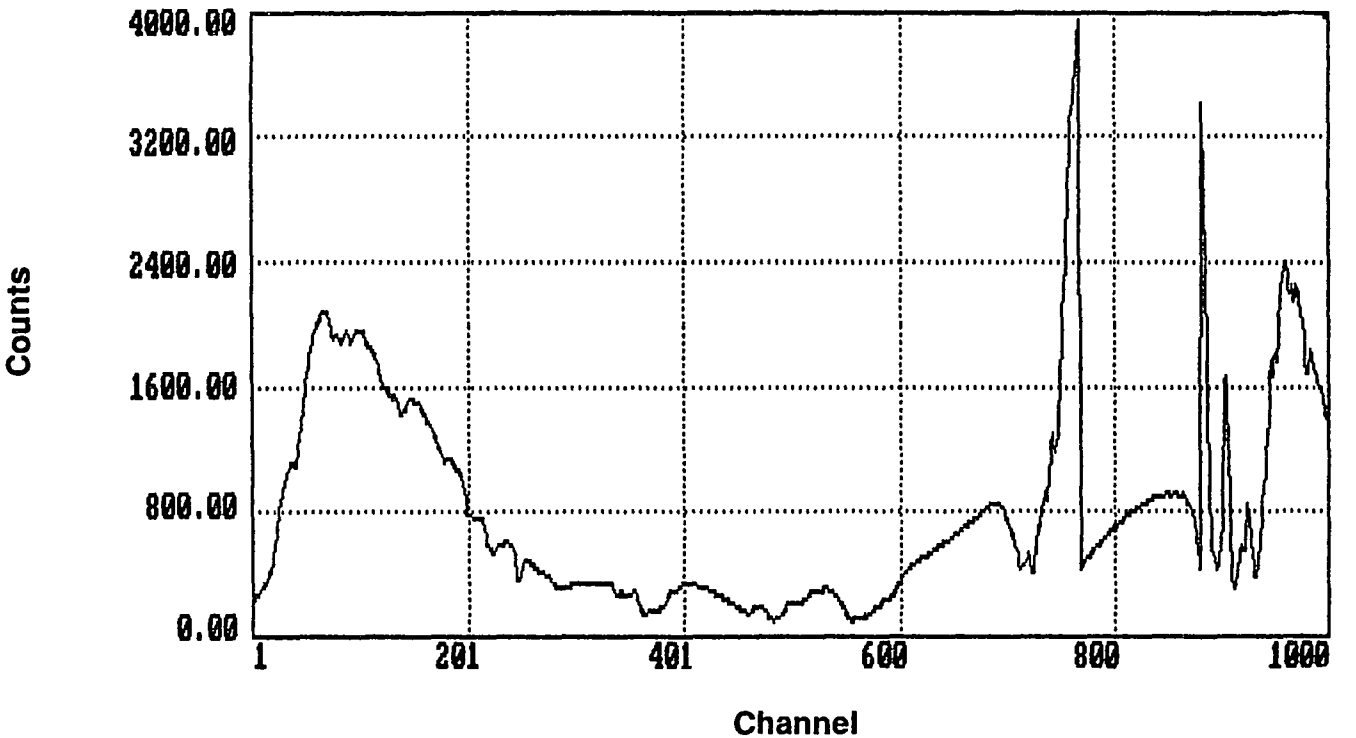

Figure 2.5. Example of raw data collected with the spectroradiometer at the Kupaianaha lava lake on October 12, 1987. The lake was in a quiescent state when these data were collected. Horizontal axis plots channels (1000 measurements from 0.35 - 3.0 μm). Vertical axis is in number of counts, which varied for each spectrum that was collected due to the automatic gain feature of the GER spectroradiometer. Sharp drops and increases in counts (at channel 780, for instance) mark places where automatic changes in gain occurred.

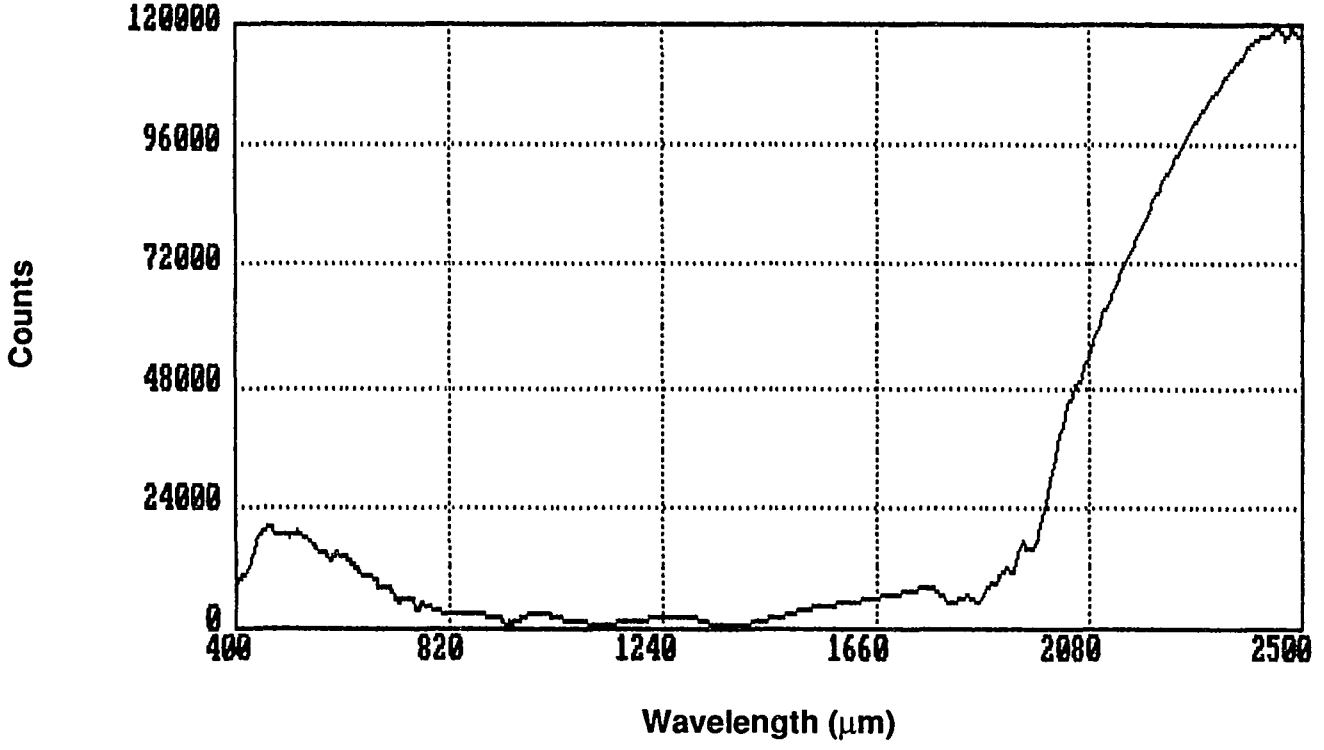

Figure 2.6. Example of raw data, corrected for automatic gain change, collected with the spectroradiometer at the Kupaianaha lava lake on October 12, 1987. The lake was in a quiescent state when these data were collected. Horizontal axis plots wavelength between 0.4 and 2.5 μm. Vertical axis is in number of counts, which varied for each spectrum that was collected due to the automatic gain feature of the GER spectroradiometer. Although data was collected to 3.0 μm, large water and carbon dioxide absorption features occupying 2.5 - 3.0 μm severely limited the usefulness of this data for this study.

Figure 2.7. Incandescent magma exposed within seconds of a large rifting event (Stage 1) on the lake surface, 10/12/87. During these events, large sections of plate crust frequently subducted beneath an overriding plate.

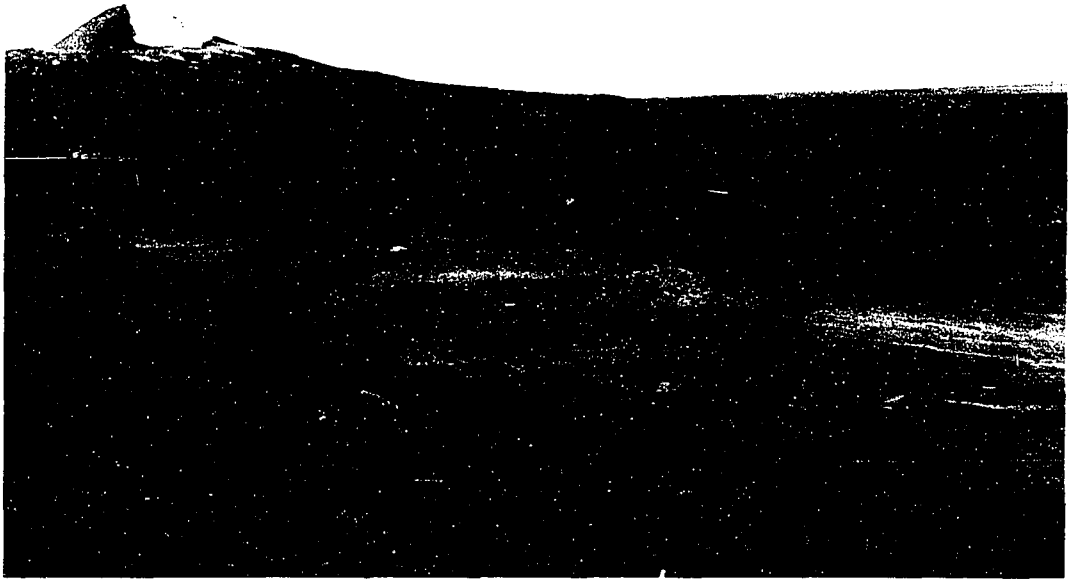

Figure 2.8. Stage 1 fountaining event occurring in the center of the Kupaianaha lava lake, 10/12/87. Fountain is approximately 1 - 2 m high.

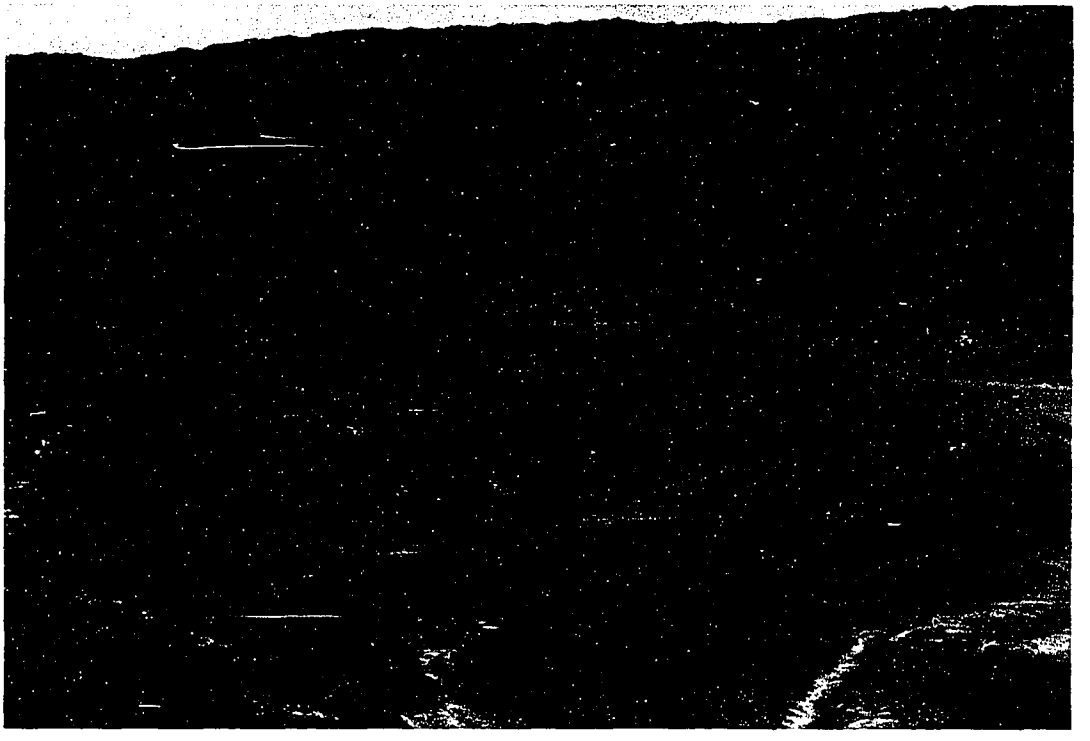

Figure 2.9. Stage 2 narrow rifts (in the foreground) on the surface of Kupaianaha lava lake, 1/23/88.

Figure 2.10. Stage 3 plates of crust covering a section of Kupaianaha lava lake on 1/23/88. Puu O'o is in the background.

Figure 2.11. Deformation and buckling of the lava lake crust. Cracked plates show thicknesses of a 2 - 6 centimeters.

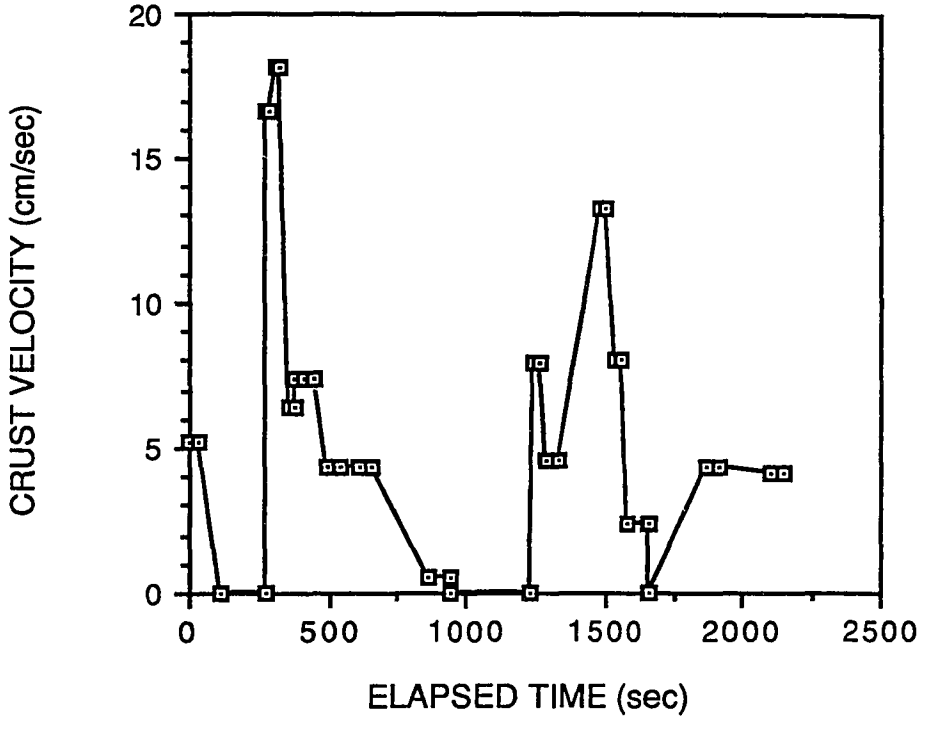

Figure 2.12. Estimated velocity measurements (in cm/sec) of the surface of the lake on 10/12/87, derived from measurements of movement of the lake surface seen in video data collected concurrent with the spectral data.

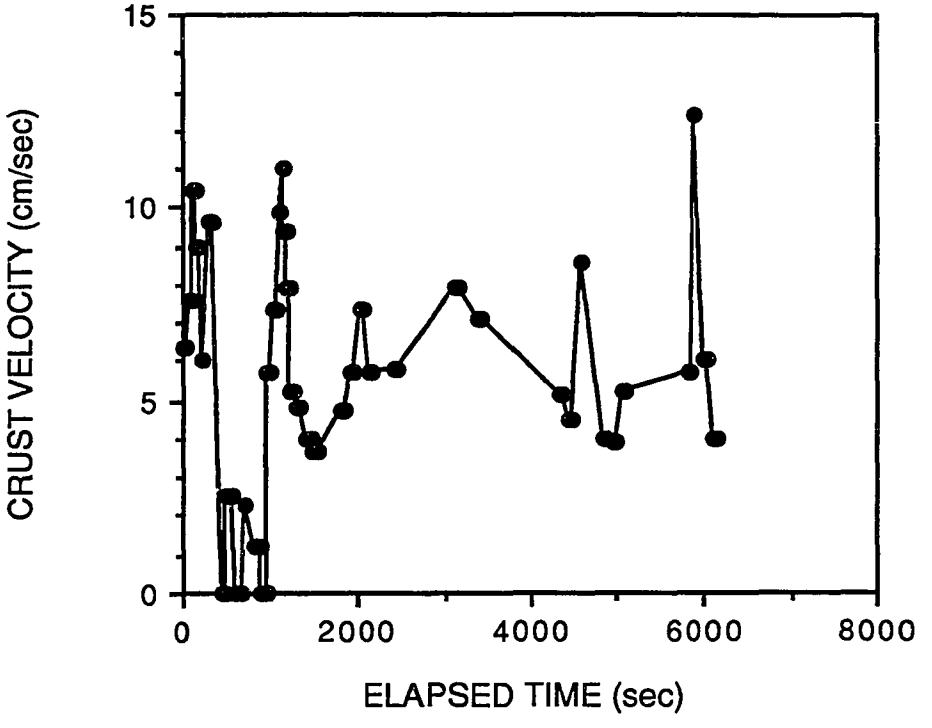

Figure 2.13. Estimated velocity measurements (in cm/sec) of the surface of the lake on 1/23/88, derived from measurements of movement of the lake surface seen in video data collected concurrent with the spectral data.

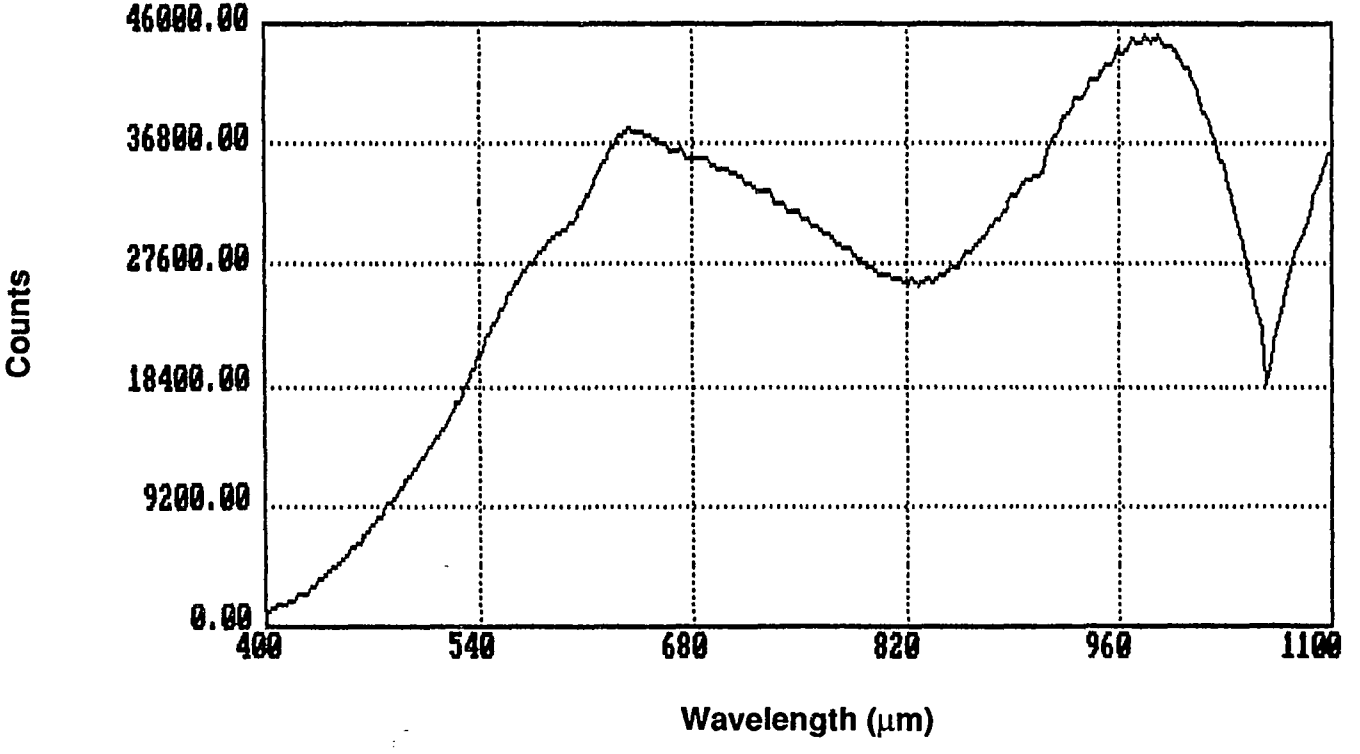

Figure 2.14. An example of a calibration spectra used to correct the lava lake data for instrument response in the 0.4 - 1.1 μm region. The lamp-diffuser combination had a correlated color temperature of 2351°C ± 50°C according to laboratory supplied calibrations. Data are presented in the same format as Figure 2.6.

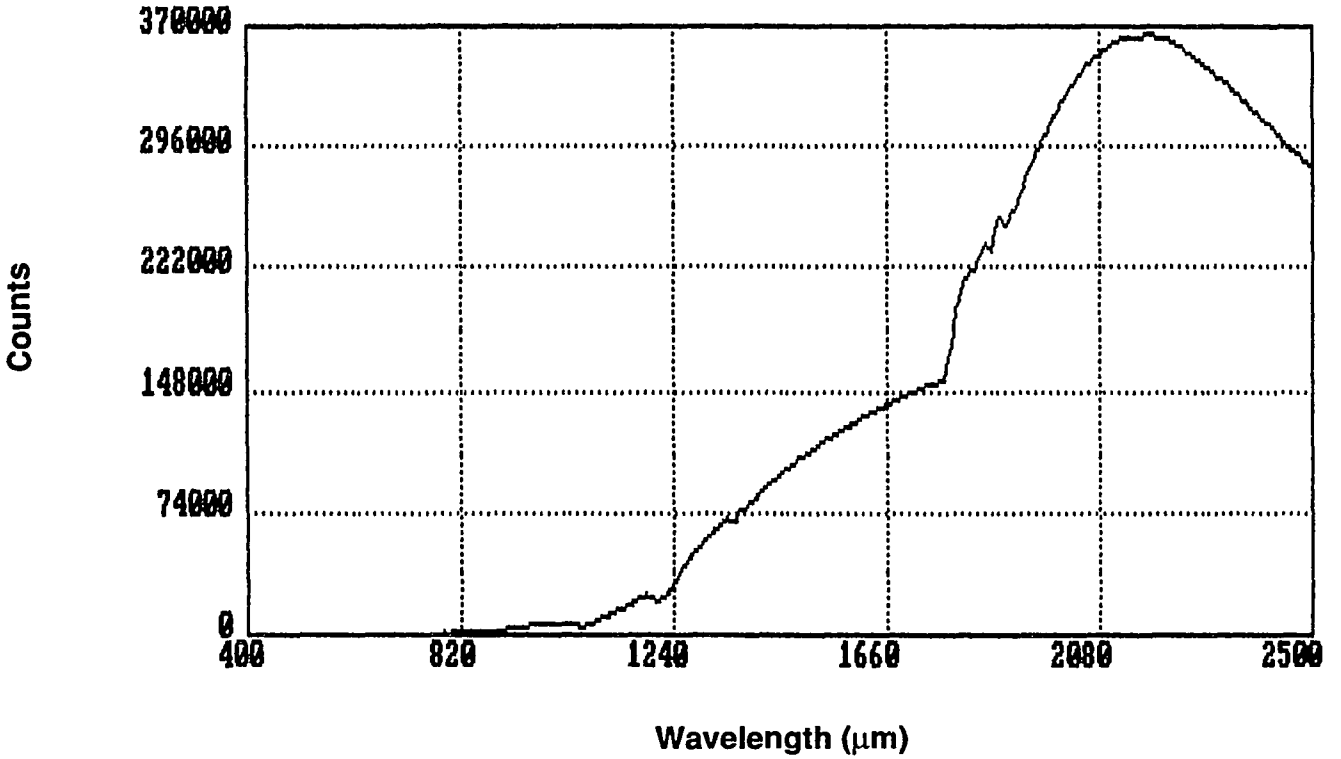

Figure 2.15. Laboratory blackbody (900°C) spectrum taken using the GER spectroradiometer with the same instrument parameters used while recording data at the Kupaianaha lava lake. This spectrum was used for the target beam calibration of the 1.0 - 3.0 μm range. Data are presented in the same format as Figure 2.6.

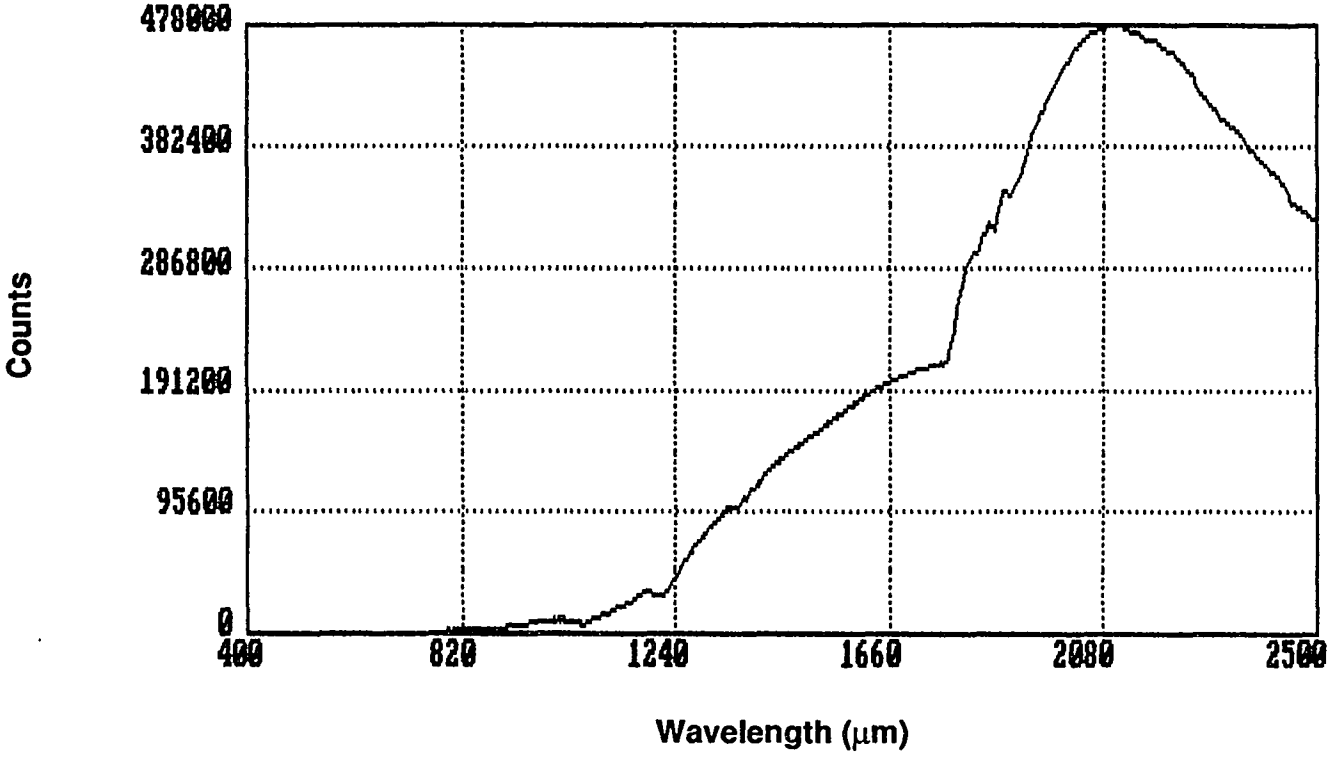

Figure 2.16. Laboratory blackbody (900°C) spectrum taken using the GER spectroradiometer with the same instrument parameters used while recording data at the Kupaianaha lava lake. This spectrum was used for the reference beam calibration of the 1.0 - 3.0 μm range. Data are presented in the same format as Figure 2.6.

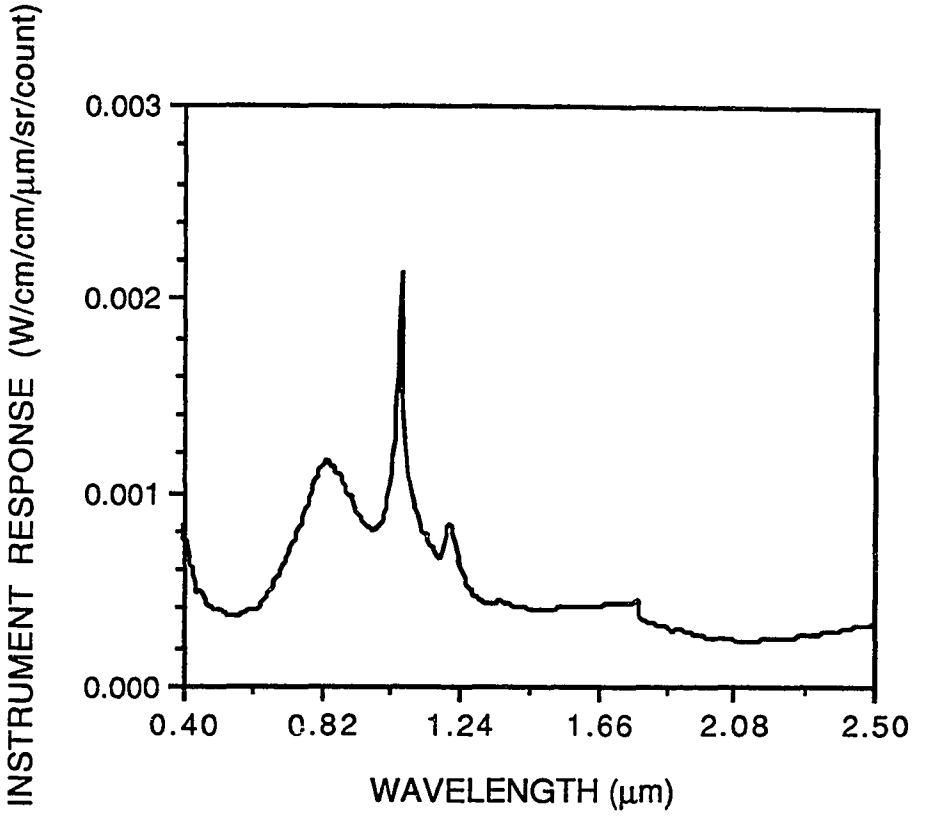

Figure 2.17. Instrument response function for GER spectroradiometer target beam. Horizontal axis is wavelength in microns. Vertical axis is the conversion from counts to radiance of each spectral channel and is given as relative radiance (W cm^{-2} μm^{-1} sr^{-1}) per count, since the channel to channel calibration of the spectroradiometer is accurate, but due to the autoscaling feature of the GER spectroradiometer, absolute radiances are unobtainable by the calibration method discussed in the text. Relative radiances were all that was required for this study because a blackbody radiating at a given temperature exhibits a characteristic spectral curve. Data for numerical models were chosen from region after 1.2 μm where the instrument response was fairly flat and featureless.

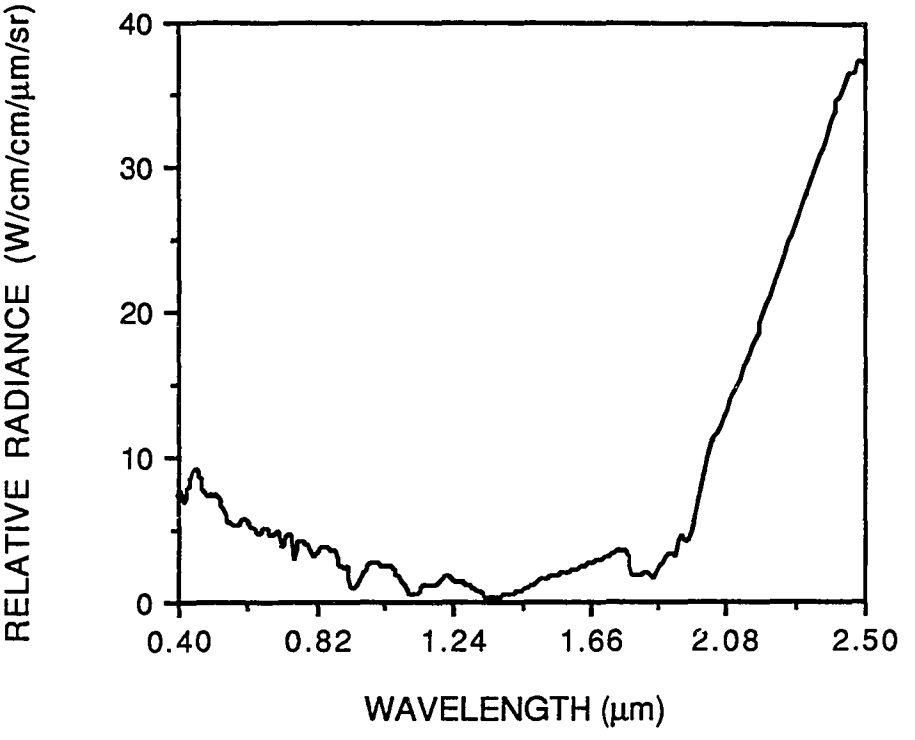

Figure 2.18. Sample spectrum (Figure 2.6) corrected for instrument response (Figure 2.17). The horizontal axis is wavelength in microns. The vertical axis is in relative radiance for reasons discussed in the text.

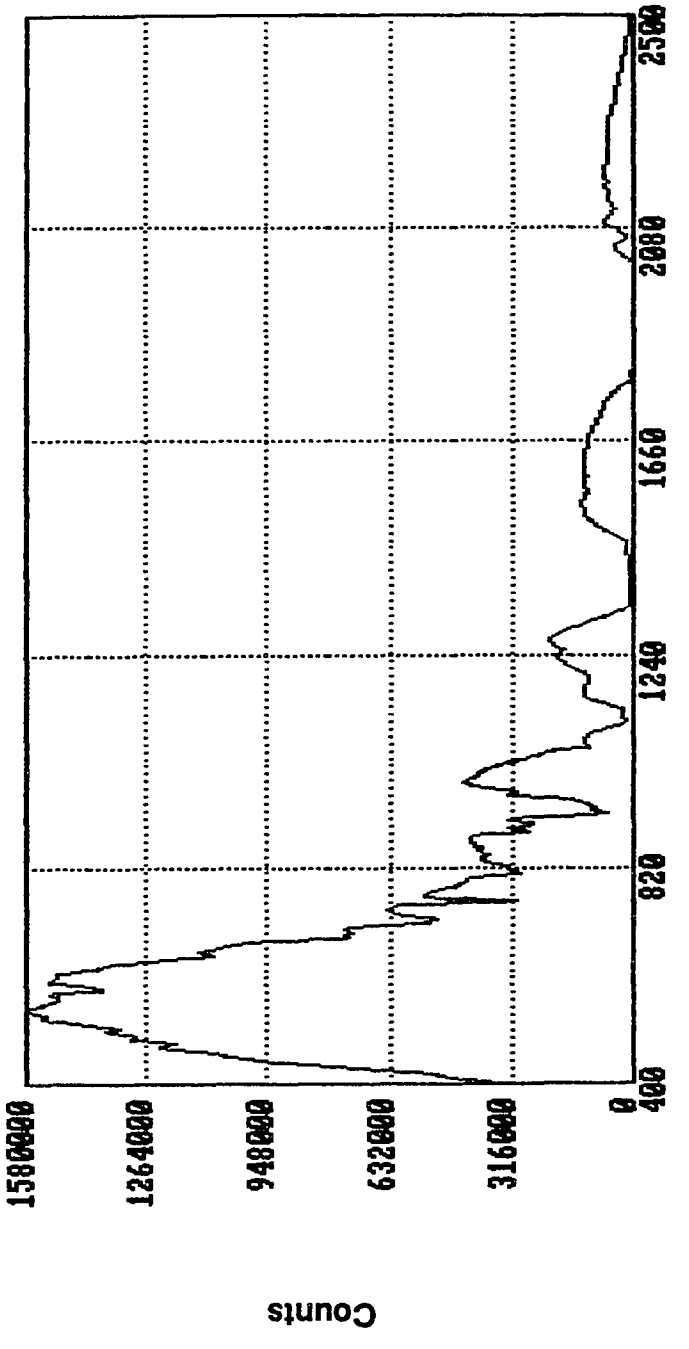

Figure 2.19. Target beam spectrum of sunlight reflected off of a white pad using the GER spectroradiometer.

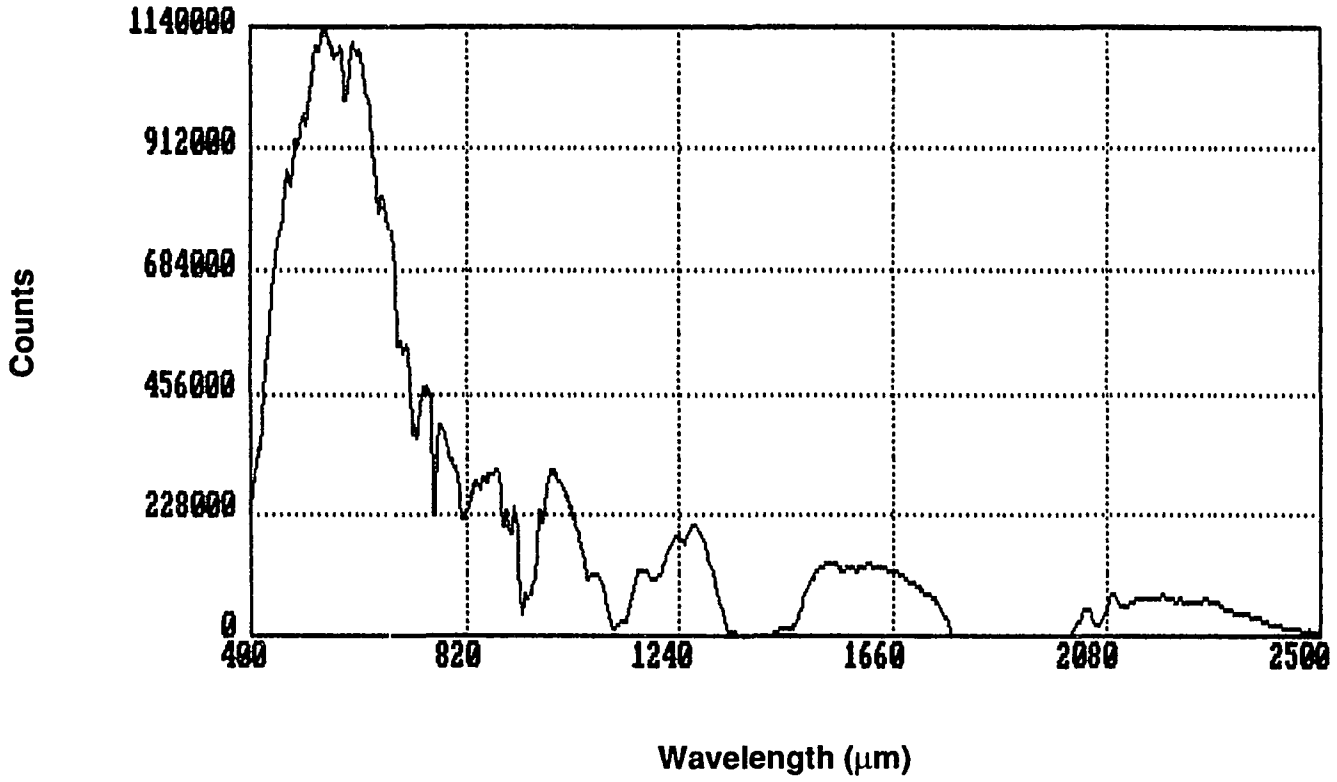

Figure 2.20. Reference beam spectrum of sunlight reflected off of a white pad using the GER spectroradiometer.

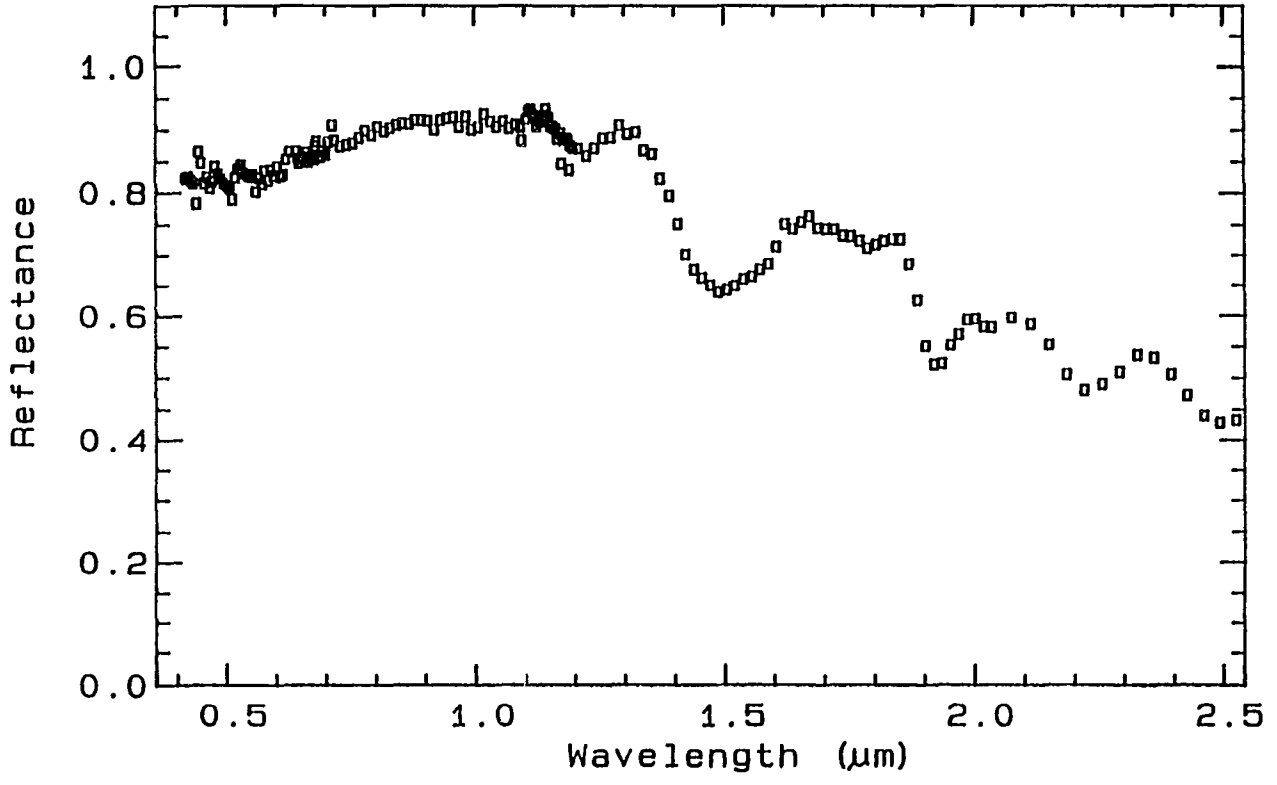

Figure 2.21. Ratio of the white pad divided by a halon standard as measured in the laboratory. Wavelength measurements are in percent reflectance. Note the marked decrease in reflectance with wavelength of the white pad.

Chapter 3: Kupaianaha Lava Lake Results

3.1 Introduction

In Chapter 2, I described the general characteristics of my field technique and the spectroradiometer, which I used to collect data in 1000 narrow spectral channels between 0.35 and 3.0 μm. Approximately 200 of these data are located in atmospheric windows where the absorption of radiation due to gaseous atmospheric constituents is minimal. Data taken in these channels may be used to calculate temperatures and proportions of radiating areas occupying the field of view of the spectroradiometer.

The goal of Chapter 3 is to try to categorize the stages of activity observed at the Kupaianaha lava lake on 10/12/87 and 1/23/88 in terms of characteristic radiative temperatures, hot fractional areas, and average flux densities (Q/A). To accomplish this, I first develop numerical models for two and three discreet radiative subareas within a single field of view. Next, I use the spectral data acquired at Kupaianaha as input for the numerical models and obtain results in terms of the radiating areas and the temperatures of the components with the hottest component representing exposed magma having a range of temperatures from 900 - 1250°C. Results of model fits to the spectra are grouped by the three stages of activity observed in the video record described in Chapter 2. The best fits of each collected spectrum are presented in Tables 3.1 - 3.3 and 3.5. Characteristics of each stage of activity are identified and used along with the video record to estimate the radiative energy budget of the entire lava lake.

Before analyzing the results of this study, it is important to set the context of the current attempts at measuring the radiative temperatures of thermally distinct volcanic anomalies. Previous methods of calculating the radiative temperature of volcanic

sources have been severely hampered by an insufficient number of spectral channels per measurement. Studies of lava temperature utilizing single channel radiometers (e.g. Jones et al., 1990, and Oppenheimer and Rothery, 1991) rely on the instrument's ability to accurately quantify the temperature occupying the field of view of the instrument. As I pointed out in Chapter 2, the brightness temperature reported by these instruments is an average of the temperatures occupying subareas of the field of view.

Landsat TM (Rothery et al., 1988; Glaze et al., 1989; Pieri et al., 1990; and Oppenheimer, 1991) and AVHRR (e.g., Matson and Dozier, 1981; Wiesnet and D'Aguanno, 1982) studies have been a bit more complex than the radiometer studies since these satellite data typically yield two usable channels for temperature/area calculations. However, the two data channels acquired by these instruments are not enough to solve the problem of a single pixel having two subareas radiating at different temperatures (Rothery et al.,1988). The dual-band method developed in Dozier (1981) and applied to volcanic sources by Rothery et al. (1988) requires the assumption of one of the three variables of the problem which are the temperatures of the two subareas and the proportion of the entire pixel occupied by one of the subareas. In cases such as Matson and Dozier (1981) in which the targets of the study were steel mills and gas flares associated with oil wells, the temperature of the background may be assumed with reasonable accuracy. The dual-band method can be a very useful and accurate tool, in such instances as solving for the temperature of the steel mill or gas flare and its proportional area of the entire pixel.

Extending this technique to lava flows presents some difficulties. A Landsat TM pixel acquired over the edge of a lava flow field can easily have at least three major radiative components - an area occupied by molten material of near magmatic

temperature, an area occupied by recently erupted flows which have developed an overlying crust radiating at about 250°C, and an area of thoroughly cooled flows warmed by the sun to a temperature of about 40°C (possible for Hawaii and other tropical volcanic areas). This scenario does not take into account the many radiative components due to recently erupted flow units of slightly different age (e.g. flow units that are minutes to a few hours old).

It is important to provide hyperspectral ground truth measurements to identify radiative temperatures and areas of active volcanic regions to constrain both the quantity and values of parameters (radiative temperatures and their emitting areas expressed as fractions of the total pixel) used in satellite studies of these areas. This study attempts to do that by quantifying the radiative output of the Kupaianaha lava lake at the scale of less than 1 square meter. However, since this is the first hyperspectral (visible to near-infrared) study, to our knowledge, carried out in a volcanic environment, a technique must be formulated to separate areas radiating at different characteristic temperatures. The number of data collected per measurement with the GER spectroradiometer allows for much more rigorous solutions to multiple radiators within a single field of view than that of the dual-band method.

The numerical models that I have developed as part of this dissertation are presented below. These models take advantage of the fact that the GER spectroradiometer provides ~200 data in atmospheric windows which can be used for the calculation of Planckian blackbody curves. As stated in Chapter 2, the amount of spectral data gained in a single measurement is a vast improvement over the two usable channels (bands 5 and 7) available from Landsat TM data. Unlike previous TM studies where the lack of data necessitated an estimation of the temperature of the cool (background) radiating

area (Rothery et al., 1988) or the temperature of the hot radiating area (Oppenheimer and Rothery, 1991; Oppenheimer, 1991) for a 2-component model, the GER spectroradiometer yields enough data that the problem of having not sufficient data for the number of variables to be solved for is not significant unless the number of radiating areas becomes very large (>100). A large number of areas and temperatures can be included in this model, although experience has shown me that 2 or 3 radiating areas are typically sufficient to describe the lake surface at the scale of less than 0.6 m^2.

3.2 The Numerical Models

I will begin by presenting the theoretical basis for the models and constructing them from first principles. I will start with the less complex 2-component model and move on to the 3-component model.

3.2.1 The two-component model

The basic flux equation for an object radiating at temperature T(K) is given by Planck's equation (2). A given area displaying multiple fractional portions, i, radiating at different temperatures, T_i, at wavelength, λ, may be expressed as:

$$F_n(\lambda)=\Sigma A_i B(I,T_i) \qquad (3)$$

where $F_n(\lambda)$ is the total flux of n contributors at wavelength λ, Σ represents the sum of separate radiating areas exhibiting different temperatures from 1 to n, A_i represents the radiating area of contributor i, and $B(\lambda,T_i)$ represents the flux of a blackbody radiating in area A_i. An area exhibiting one relatively hot subarea (A_h) and one relatively cool (A_c) subarea would result in

$$F(\lambda) = A_h B(\lambda, T_h) + A_c B(\lambda, T_c) \quad (4)$$

where $A_c = 1 - A_h$. The number of variables prevents a unique solution with fewer than 3 channels measured. Clearly, single-band radiometers can not be used to collect data for a unique solution to the 2-component model.

The major advantage of the GER spectroradiometer over Landsat TM and single-channel radiometers is the much greater number of channels (discreet wavelength-band measurements) available for numerical models, which in turn allow for a determination of the amount of radiation contributed by individual subareas to the overall flux. This can be seen in the following system of equations to determine the three variables (A_h, T_h, and T_c) for the 2-component model:

$$F(\lambda_1) = ET(A_h B(\lambda_1, T_h) + (1 - A_h) B(\lambda_1, T_c)) \quad (5)$$

$$F(\lambda_2) = ET(A_h B(\lambda_2, T_h) + (1 - A_h) B(\lambda_2, T_c)) \quad (6)$$

$$F(\lambda_3) = ET(A_h B(\lambda_3, T_h) + (1 - A_h) B(\lambda_3, T_c)) \quad (7)$$

where $F(\lambda_1)$, $F(\lambda_2)$, $F(\lambda_3)$ are measured radiance values at different wavelengths in atmospheric transmission zones, leaving A_h, T_h, and T_c as the quantities which must be solved for. E and T are the emissivity and the atmospheric transmissivity, respectively. Laboratory spectra of glassy, recently formed (within 3 days of cooling) basalt samples (measured by Paul Lucey and myself) exhibit reflectances of <0.5% over the wavelength region from 0.9 - 2.25 μm where the data for this study were acquired. Here I assume that the emissivity of the lake surface is greater than 0.995 and does not vary significantly. Hence, the emissivity has been treated as a constant which will drop out of subsequent equations ratioing $F(\lambda_1)$, $F(\lambda_2)$,

and $F(\lambda_3)$; however, it must be recognized that if the targets of the study were andesitic or rhyolitic flows, the emissivity would probably vary with wavelength and could not be dropped from flux ratios. To investigate the effects of changes in spectral emissivity for two radiative surface components at different temperatures, I allowed the emissivity to vary by 5 and 10% between the 3 atmospheric windows from which data were chosen for this study (1.2 - 1.3 μm, 1.52 - 1.79 μm, and 2.03 - 2.34 μm) and found that the best fit crust component temperature varied by < 20°C for Stage 1 activity and < 6°C for Stage 3 activity. I also allowed the emissivity of the hot component to vary by up to 20% from the emissivity of the crust component and found that the best fit results varied by <3°C for Stage 1 activity and < 2°C for Stage 3 activity. Clearly, changes in emissivity between channels in different atmospheric windows resulted in larger potential errors than the errors associated with changes in emissivity due to different radiative temperature components.

The atmospheric transmissivity is not a concern for this study since data points were chosen in only well-defined atmospheric windows between 0.9 - 2.25 μm (Figure 3.1) in which T is very nearly equal to 1. Figure 3.1 (Wolfe and Zissis, 1985) shows the atmospheric transmission at sea level for a 300 m path. Although this is much longer than the 60 m maximum path (< 20 m distance to the target for most measurements) in this study, I recognize that the amount of absorptive gases in the path is probably much greater in the volcanic environment where measurements were made than is typical for areas at sea level.

The equation which Planck used to describe blackbody curves has an interesting feature in that the shape of each temperature curve across the electromagnetic spectrum is different from the shapes of other curves exhibiting different temperatures. Wien's

Law, which can be used to calculate the maximum flux emitted by a blackbody of any given temperature, shows that the cooler a blackbody gets, the farther out into the infrared the wavelength of maximum emission occurs. The properties of blackbodies are such that the shape of a blackbody curve or the ratio of fluxes at any two given wavelengths is unique for each emitting object exhibiting a different temperature, or:

$$K_{12} = B(\lambda_1,T)/B(\lambda_2,T) \qquad (8)$$

where $B(\lambda_1,T)$ and $B(\lambda_2,T)$ are the radiance values of a blackbody exhibiting temperature T at wavelengths λ_1 and λ_2, respectively, and K_{12} is the ratio of these values. K_{12} is unique for each object at wavelengths λ_1 and λ_2 at any temperature T. The use of ratios is also beneficial in that only changes in emissivity and atmospheric transmission with wavelength (which are both negligible) would have an effect on the numerical model. In this study, the accurate measurement of absolute fluxes would have been extremely difficult due the number of calibrations involved and the automatic gain change feature of the spectroradiometer. However, the relative fluxes are all that are necessary for flux ratios such as equation 8. Due to the repeatability of the calibration measurements, I can be sure that the relative fluxes obtained are very accurate.

In each of the numerical models listed below, I have assumed that the number of temperature-exhibiting emitters is limited to the number listed in a particular model. This means that in the 2-component model, I have assumed that there are only two separate areas (A_h, 1 - A_h) radiating at two separate temperatures (T_h, T_c). The result is that the radiative flux as measured by the spectroradiometer at a particular wavelength is the sum of two components exhibiting different radiative temperatures.

Using equations 5 – 7, one can solve the system of equations simultaneously in order to determine the three unknowns in the 2-component problem: A_h, T_h, and T_c.

The numerical model used in this study uses the characteristics of blackbody curves exhibited in equation (8) to solve for the three unknowns in the 2-component case. Four wavelengths, each located in atmospheric windows, were chosen to represent the spectrum. Some of the wavelengths most commonly used for model calculations in this chapter were 1.23, 1.24, 1.25, 1.53, 1.62, 1.66, 1.70, 2.08, 2.10, and 2.25 μm. The corrected flux values at these wavelengths were used to calculate the following flux ratios (K):

$$K_{21} = (F(\lambda_2)/F(\lambda_1)); \quad (9)$$

$$K_{31} = (F(\lambda_3)/F(\lambda_1)); \quad (10)$$

$$K_{41} = (F(\lambda_4)/F(\lambda_1)); \quad (11)$$

where $F(\lambda_2)$, for instance, is the data corrected flux recorded for a particular spectrum at wavelength λ_2. Thus, K_{21}, K_{31}, and K_{41} represent the ratio of fluxes recorded at wavelengths λ_2, λ_3, and λ_4 to the flux recorded at λ_1, respectively, for the 2-component model. The "K" values are calculated directly from the corrected spectral data.

An iterative method is used to find theoretical values which match K_{21}, K_{31}, and K_{41} as closely as possible. The corrected flux values at λ_1, λ_2, λ_3, and λ_4 are entered into a program which calculates the K-value data-derived flux ratios. Next, using Planck's Law (eq. 2), the iterative model generates theoretical (Planck-derived) flux ratios to most closely match those generated by the data. This is accomplished by

supplying a hot temperature (T_h), representing the temperature of molten magma, and a relatively cooler temperature (T_c), representing the temperature of the lake surface crust. The amount of flux emitted by objects (T_c) radiating at T_h and T_c at wavelengths λ_1, λ_2, λ_3, and λ_4 is then calculated using Planck's Law (eq. 2). This yields eight values h_1, h_2, h_3, h_4, c_1, c_2, c_3, c_4, which are the fluxes generated by an object radiating at temperature T_h at wavelengths 1 to 4, and an object radiating at temperature T_c at wavelengths 1 to 4, respectively.

The next step is to find the area of the hot emitting object which results in the flux ratios that most nearly match the values found from the data-derived ratios, K_{21}, K_{31}, and K_{41}. First, a value of 0.90 of the total area is assigned to the hot emitter (radiating at T_h) with the remainder of 0.10 of the total area occupied by the cold portion (radiating at T_c). Equation 5 is an example of the equations used to calculate the total flux, at wavelengths 1 to 4, emitted by the area occupying the field of view of the spectroradiometer. This results in a set of theoretical total flux values at wavelengths 1 to 4. Equations 9 to 11 are then used to calculate the theoretical K values for the parameters of T_h, T_c, and A_h.

The data-derived K values and the theoretical K values are then compared by the following calculation:

$$E_{21} = (K_{21d} - K_{21t}) / K_{21d} \qquad (12)$$

where E_{21} is the weighted error of the data-derived flux differential (K_{21d}) minus the theoretically-derived flux differential (K_{21t}) divided by the data-derived flux

differential. Weighting is necessary to insure that the errors calculated are not biased toward the larger flux differentials but are dependent on the goodness of the overall fit to the data.

An error value (such as E_{21}) is calculated for each pair of data-derived and theoretical K values. The errors are summed, which gives a quantity that expresses the overall fit to the data. The smaller the total or summed error, the better the fit between the actual data and the computer-generated model.

A minimum total error is then found for the temperature of the hot radiating area. First, A_h, or the hot emitting fractional area, which is set at 0.90 of the total area, is decreased by 0.10 until 0.10 is reached, then the subtracted increment becomes 0.01, and so on until a minimum total error is reached. The region in which the minimum total error occurs is found when the next calculation done for a given T_h and T_c with a decreasing A_h results in a greater total error than in the previous calculation. The subtracted increment is divided by ten and a search is done between the values for A_h which bound the region where the total minimum error occurs. The final result is a value for A_h which returns the minimum error value for T_h and T_c.

Once a minimum total error is found for a given T_h and T_c by varying A_h, the whole process is repeated after T_c is decreased by an increment, ΔT_c, which is usually 10°C in a general search, and 2°C when the general search narrows down a particular temperature range for T_c where the total error is at or near a minimum. At the end of the iterative search, the numerical model returns values of T_c and A_h for a given T_h which are the best fit to the flux ratios (K) obtained from the spectral data.

Total errors for various T_h, T_c, and A_h parameter sets may be compared to find the optimum fit to the spectral data. Best-fit values for T_h, T_c, and A_h are compared by observing the individual errors (E_{21}, E_{31}, E_{41}) which are added together to give the total error. This can be very useful for identifying how well the model fits the spectral data at different wavelengths.

3.2.2 The three-component model

A critical question addressed by the spectroradiometer approach is whether or not a 2-component model is an accurate representation of the lava lake surface. By increasing the number of discrete-temperature radiating areas from two to three or four components and observing the behavior of the resulting fit to the data, one can find the number of radiating areas which most accurately represents the spectral data.

To find out if solving for a greater number of radiating areas results in a better fit to the spectral data, a numerical model based on the 2-component model was developed for a 3-component system. In the 3-component case, equation 5 becomes:

$$F(\lambda_1) = ET(A_h B(\lambda_1,T_h) + A_m B(\lambda_1,T_m) + (1-(A_h + A_m))B(\lambda_1,T_c) \quad (13)$$

where $F(\lambda_1)$ is the measured flux from all three radiating areas at wavelength, λ_1; A_m is the mid-temperature radiating area; and $B(\lambda_1,T_m)$ is the Planck-Law-calculated radiative flux at wavelength, λ_1, of an object at temperature T_m. The number of wavelengths used for the study was increased from four for the 2-component model to six for the 3-component model. The 3-component model flux ratios were calculated as follows:

$$K_{21} = F(\lambda_2)/F(\lambda_1); \quad (14)$$

$$K_{43} = F(\lambda_4)/F(\lambda_3); \quad (15)$$

$$K_{65} = F(\lambda_6)/F(\lambda_5); \quad (16)$$

$$K_{31} = F(\lambda_3)/F(\lambda_1); \quad (17)$$

$$K_{51} = F(\lambda_5)/F(\lambda_1); \quad (18)$$

$$K_{53} = F(\lambda_5)/F(\lambda_3); \quad (19)$$

where K_{21}, for example, is the ratio of the flux recorded at wavelength λ_2 to the flux recorded at wavelength λ_1.

The analysis of the 3-component model is very similar to that described above for the 2-component case. The exceptions are that flux values must be calculated for six wavelengths rather than four, and that an additional area, A_m, radiating at temperature T_m will combine to yield ten more Planckian blackbody values (h_5, h_6, m_1, m_2, m_3, m_4, m_5, m_6, c_5, and c_6) to the calculations. The execution of the 3-component model is the same as that of the 2-component model except two loops are added which vary T_m and A_m in the same manner that was described above for T_c and A_h.

The total error which measures the goodness of the numerical fit to the data is now the sum of six individual error values which were each calculated in the exact manner as in equation 12 except for using the Planck-generated and spectrum-generated flux ratios listed in equations 14-19. The total error may be expressed for the 3-component model as

$$E_{total} = E_{21} + E_{43} + E_{65} + E_{31} + E_{51} + E_{53} \quad (20)$$

As mentioned in regards to the two-temperature model, the total error as expressed in equation 20 was the primary method for determining the best fit for a given set of spectral data.

3.3 Model Results for Kupaianaha Lava Lake Spectral Data

The spectral determination of the two and three thermal components of selected areas of crust at the Kupaianaha lava lake are most significant when considered according to the three Stages of activity seen in the concurrent video data. For the purposes of this study, spectra were characterized, according to the observations described in Chapter 2, section 4, as belonging to Stage 1 (active overturning or fountaining of magma), Stage 2 (limited rifting), or Stage 3 (solid crust). The results of the numerical models were studied to identify any radiative similarities in Stages 1, 2, and 3 to try to determine representative radiative temperatures.

3.3.1 Stage 3: two-component results

I will consider the results of Stage 3 (the solid crust) first, since it represents the easiest stage to measure thermally with the spectroradiometer as the temperature of the solid crust did not vary greatly during the duration of a measurement. Also, as a result of plates of crust buckling together, the movement of the lake surface frequently slowed to a standstill, which allowed a measurement to be completed on the same piece of crust from start to finish.

Figure 3.2 shows a typical spectrum collected of Stage 3 quiescent crustal activity. During our two days of observations, thirteen spectra were collected of Stage 3 activity. Of this number, eleven were collected on 10/12/87, and two were collected on 1/23/88. A "neutral" density filter used on 1/23/88 to prevent saturation of the detectors when viewing Stage 1 (active fountaining) unfortunately proved to be too absorptive in the infrared region to collect data of Stage 3 activity; consequently, the one

pair of useful Stage 3 spectra were collected before the neutral density filter was placed over the entrance port of the spectroradiometer.

In order to more fully appreciate how the 2-component model determines a result for a given hot temperature and set of spectral parameters, I present the abbreviated results of a typical run (Figure 3.3) using spectral data from Figure 3.2. In this case, the temperature for the hotter portion of the surface of the lake being measured was set at 1100°C. As seen in Figure 3.3, the surface of the quiescent lake is remarkably cool. The best fit matches with a surface crust having a radiative temperature of 264°C with glowing cracks at 1100°C comprising only 0.0015% of the total viewing area. As can be determined from the errors, the choice of the correct background temperature for the model is very important as the error for numerical fits increases 18-fold if the background temperature is 50°C too hot or too cold.

Lastly, Figure 3.3 identifies a curious aspect of the blackbody temperatures and the numerical model developed to fit the data. One would expect, for a given fraction of the crust and the crack temperature, T_h, that as the model sets the background temperature colder, the hot area should increase. Thus the flux from the hotter surface would make up for the decreased flux from the colder surface. Actually, the results presented in Figure 3.3 are correct even though they may be at first counter-intuitive. Since each area exhibiting a different temperature has a blackbody curve of a specific shape, as the background gets colder two things happen: 1) the shape of the background blackbody curve shifts toward longer wavelengths, and, as a result, 2) the sum of the two curves shifts towards longer wavelengths which alters the ratio of fluxes between points. The numerical model works with flux ratios between certain wavelengths so that the shape of the summed curve may be fitted. The absolute flux values at each

wavelength do not matter. What does matter is that the ratios of fluxes be kept as close as possible to the spectroradiometer-measured values. Thus, as the background temperature becomes colder, the hot area must decrease so that the contribution from the crack temperature, T_h, becomes less with increasing wavelength to make up for the background curve which is shifting to longer wavelengths. In this way, the flux ratios between wavelengths can be kept close to the spectroradiometer-measured values. If the hot area were allowed to increase with decreasing background temperature, the whole summed curve would shift to longer wavelengths which would result in a greater difference between the spectroradiometer-measured flux ratios and the model generated ratios, thus, increasing the error.

Figure 3.4 shows the results of the 2-component best fits to the spectrum presented in Figure 3.2 for hot component temperatures of 900°C, 950°C, 1000°C, 1050°C, 1100°C, 1130°C, 1150°C, 1200°C, and 1250°C. The best fit result of T_h = 900°C and T_c = 260°C is plotted in terms of radiance in Figure 3.5. The results of Figure 3.4 are typical for most of the other Stage 3 examples in that the crack temperature, T_h, could vary from 900 - 1250°C with little effect on the surface crust temperature, T_c, or the hot area, A_h (Flynn et al., 1990). For the range of magmatic temperatures chosen, T_c varies by only 10°C. The solid crust temperature of the lava lake may be summarized as 265 ± 5°C and include all of the best fit results. With the hot cracks making up only 5.0×10^{-5} of the total pixel, the surface crust (T_c = 260°C) contributes > 50% of the total flux after 1.49 μm for T_h = 900°C (see discussion below). The best fits for the model give almost the same all-important solid crust

temperature (T_c), irrespective of what hot component temperature is chosen between 900 - 1250°C. The error values obtained from the best fits in Figure 3.4 were all very low (< 0.001), which means that all fits were good and again suggests that for Stage 3 quiescent crustal activity, the accurate determination of T_c is most important.

Table 3.1 includes a summary of all 2-component Stage 3 measurements and shows the time that each Stage 3 measurement was taken, any distinguishing characteristics of the surface of the lava lake, and the best fits for each of the spectral measurements. Some of the measurements were recorded within minutes of one another while viewing the same plate of crust on the surface of the lake. Spectra 1 and 2, and spectra 3 and 4 were pairs of measurements taken with the spectroradiometer pointed at the same section of crust. Slight movements of the nearly stagnant crust prevent me from being absolutely certain that the same piece of crust occupied the field of view for both sets of measurements, but it is certain that the measurements were completed within three minutes of one another, and that the target areas were very close to one another (≤1 m). Of course, the two beams of the spectroradiometer provided two spectra which were taken simultaneously of portions of crust that were separated by only 0.68 m and 1.05 m on 10/12/87 and 1/23/88, respectively. Examples which were collected simultaneously can be found in Table 3.1 by looking for matching times of acquisition (e.g., examples 1 and 2).

Upon first glance at the two temperature best fits in Table 3.1, it seems that the magma filling the cracks in the surface plates exhibited a temperature, T_h, in many cases of 900°C. This number is a bit misleading. For twelve out of the thirteen model results shown for Stage 3 activity, T_h could be varied from 900 to 1250°C with a

corresponding range in the solid crust temperature T_c of less than 10°C. Best fit numerical model results 2 - 5, 7 - 9, and 11 in Table 3.1 showed variances in T_c of 4°C or less with corresponding changes in the best fit errors of less than 6% for T_h varying between 900 – 1250°C. This means that for these eight observations of Stage 3 activity where Kupaianaha was covered by a solid crust, a particular value for T_h was not important in reducing the error of the fit to the spectral curve. On the other hand, small variations in T_c would result in large increases in the error values (Figure 3.3). T_c is the most important parameter when determining the best fits to the Stage 3 spectral data. For each of the best fit examples listed in Table 3.1, the fractional area of the hot radiator, A_h, of all of the numerical model fits (900 - 1250°C in each example) varied by less than one order of magnitude from the fractional area of the best fit.

3.3.2 Stage 3: three-component results

Before discussing the 3-component results for Stage 3 activity, I would like to note that the errors listed for 3-component best fits are in no way correlatable with the errors calculated for the 2-component models. The 3-component model uses six ratios producing six individual error values which are summed to get a total error (equation 20). The 2-component model uses three ratios to produce three individual error values which are summed to get a total error. It is not easy to compare the two best fit error quantities of the 2- and 3-component models for the same spectrum. A further discussion of best fit errors and the factors which influence them will be detailed below (section 3.4.2).

Three-component numerical model best fit results for sample magmatic temperatures of 900°C, 950°C, 1000°C, 1050°C, 1100°C, 1150°C, 1200°C, and 1250°C using input spectral data from Figure 3.2 are given in Figure 3.6. These model results contain a number of trends that were present in the majority of the Stage 3 numerical model best fits. In most cases, T_m and T_c both showed little change regardless of the magmatic temperature chosen for T_h. In all examples of Stage 3 activity, T_m varied by 30°C or less while T_c exhibited a change of $\leq$ 30°C in 9 out of 13 examples. What is most significant is that the difference between T_m and T_c was found to be $\leq$ 20°C in only 3 of 13 examples. For the other 10 examples, the difference between T_m and T_c was > 90°C. Examples of these statistics (e.g., Figure 3.6), show that the range of values (with T_h = 900 – 1250°C) for T_m is 45°C, the range for T_c is 185°C, and the range of the difference ($T_m - T_c$) is $\geq$ 65°C for all the sample magmatic temperatures chosen. Table 3.2 includes the 3-component numerical model best fits for Stage 3 activity.

Numerical model solutions for examples of Stage 3 activity show that the temperature, T_h, of the magma in microcracks approaches 1100°C (Table 3.2). However, as was the case for the 2-component Stage 3 results, this outcome is a bit misleading. In 10 out of 13 examples, any value for T_h between 900 – 1250°C would result in a best fit with an error within 5% of the errors listed in Table 3.2 and all showed error values that were less than 10% higher than the lowest error value.

The difference between the two solid crust temperature components, T_m and T_c, is greater than 90°C in 10 best fit examples for Stage 3 activity (Table 3.2). For these

examples there is such a large temperature difference between T_m and T_c that two radiating areas exhibiting two temperatures may result in an inadequate fit to the spectral data. For these cases, a 3-component model may be necessary. In 10 out of 13 examples, T_m and T_c were also > 90°C apart for all best fits between 900 – 1250°C suggesting that a wide range of possible magmatic temperatures, T_h, may be substituted into the numerical model without changing the result that a 2-component model would be inadequate to solve these cases.

It would seem that for Stage 3 activity, the radiating area of the warmer solid crust component, A_m is a critical factor in determining the best fit to the spectral data. However, in 3 cases, the difference between T_m and T_c was < 30°C, suggesting that a third radiative component was unnecessary. For most cases, the temperatures of the two solid crust components are so far apart (> 90°C) that three areas, one representing hot microcracks in the surface, one representing thinner crust (possibly over annealed cracks) and the other the thick solid crust, may be a necessary solution for most Stage 3 examples.

Some general characteristics of Stage 3 activity may be derived from the numerical model results (Tables 3.1 and 3.2). The choice of a particular temperature representing microcracks in the surface of the solid crust plates, T_h, did not seem to be an important factor in determining the best fit to the data points chosen for the numerical model. The fractional radiating area of the microcracks, A_h, was 10^{-5} or less of the total measured area for both the 2- and 3-component models. For many of the best 3-component solutions, the difference between T_m and T_c was very large (>90°C)

suggesting that a 2-component solution may provide an inadequate fit to the data. The largest change in the error value occurred in all Stage 3 examples when T_m and T_c were allowed to vary from the best possible numerical fit values. The proper choice of the surface crust temperatures T_m and T_c was most important governing factor which resulted in the lowest possible error value. Typical values of T_c for Stage 3 for both models were generally found to be between 80 - 350°C with most solutions near 220 - 275°C.

3.3.3 Stage 2: two-component results

As described in Chapter 2, section 4, Stage 2 was defined to occur when many long, narrow fissures form in the surface of the lava lake exposing magma which quickly solidifies. Stage 2 was more difficult to measure with the spectroradiometer since the activity was continuous with fresh crust forming from recently erupted magma. The three examples of Stage 2 activity (Table 3.3) were taken on October 12, 1987 of developing rifts which were stationary on the surface of the lake. Distinct differences can be seen in the shapes of the spectral curve collected for Stage 3 (Figure 3.2) and Stage 2 (Figure 3.7). Stage 2 rifting spectra show much higher fluxes in the 1.5 - 1.8 μm region relative to Stage 3 spectra. Also, the ratios of measured fluxes between 1.5 - 1.8 μm to the fluxes between 2.0 - 2.25 μm are less in the Stage 2 spectra relative to Stage 3 spectra. It can also be seen that reflected sunlight contributes a smaller percentage of the measured flux in Stage 2 activity than in Stage 3 activity. At 1.53 μm, reflected sunlight contributes only 4% of the total measured flux in Stage 2 examples.

A summary of the best 2-component numerical model fits to the data presented in Figure 3.7 for magmatic temperatures ranging from 900 - 1250°C is given in Figure

3.8. The best fit result of T_h = 1000°C and T_c = 262°C is plotted in terms of radiance (Figure 3.9). Unlike in the Stage 3 example (Figure 3.4), the temperature of the solid crust, T_c, varies considerably depending on the magmatic temperature, T_h, chosen for the numerical model (Figure 3.8). Over the range of values for Th, the best fit for Tc varies by 210°C. The best fit errors for Stage 2 2-component models (Table 3.3) also show wide differences of up to 1100% depending on the value for T_h chosen for the model. As would be expected, the hot emitting area, A_h, for rifting Stage 2 activity increased relative to quiescent Stage 3 activity.

3.3.4 Stage 2: three-component results

The 3-component best fit results for Figure 3.7 are given in Figure 3.10. Upon inspection of Figure 3.10, it is obvious that the temperatures of the two solid crust components, T_m (the temperature of the medium component) and T_c (the temperature of the relatively cold component), vary considerably depending on the value chosen for the hot component temperature, T_h. However, the results of Figure 3.10 show that the difference between T_m and T_c is 40°C or less for most best fits between 900°C and 1250°C. This trend was not consistent for the other two examples (Table 3.3) where the difference between T_m and T_c was $\geq$ 80°C. Again, this suggests that a 2-component solution would be sufficient to describe the surface activity in the spectroradiometer field of view for the spectral data presented in Figure 3.7, but would be inadequate for the other two examples of Stage 2 activity. The best fit errors (Figure 3.10) for T_h of $\leq$1050°C were much larger than those fits derived with higher T_h values.

Some very general assumptions about rifting events on the lava lake surface associated with Stage 2 may be gained from our examples (Table 3.3). For the 3-component best fit examples, the difference between T_m and T_c was small enough in one case that a 2-component model would be sufficient to describe the radiative characteristics of the lake surface. Solid crust temperatures (T_m and T_c) ranged from 100 - 340°C, with most crust temperatures falling between 210 and 290°C. Hot component temperatures, T_h, of 900 - 1100°C gave the best model solutions in all cases. The area radiating at magmatic temperatures, A_h, was on the order of 10^{-4} - 10^{-6} for all Stage 2 examples.

3.3.5 Stage 1: two-component results

In chapter 2, section 4, I defined Stage 1 to occur when the surface of the lava lake experiences rapid, wide rifting exposing fresh magma and is marked by the effervescence of gas bubbles and small (3 m high) fountaining events as segments of the lake surface subduct. Sixteen spectra of Stage 1 activity were collected at Kupaianaha. Of these spectra, eight were collected while the spectroradiometer was aimed at very active rifting and fountaining events, and eight were collected while the instrument was pointed at a glowing lava tube or vent at an edge of the lake. Stage 1 events proved to be the most difficult to measure in the field using the spectroradiometer. Fountaining or large-scale rifting events were extremely transient. The duration of these events (less than a second to a few seconds long) was frequently much less than the time that the instrument required to complete a measurement (at least 30 seconds, for the most rapid

presented a problem as the amount of fresh magma occupying the field of view varied continuously. In addition, after the first day of data collection, it became apparent that the extremely high infrared flux exhibited by Stage 1 activity frequently saturated the spectroradiometer detectors. Thus, a neutral density filter was introduced to reduce this flux to measurable levels. Unfortunately, the neutral density filter, which was simply a piece of photographic film exposed for a certain amount of time, proved to be less than neutral, as is shown by the new instrument response normalizations (Table 3.4). Table 3.4 lists instrument response normalizations with and without the neutral density filter, and shows that the neutral density film used to cover the entrance aperture of the spectroradiometer was extremely absorptive in the infrared (>99% at 0.988 μm and longer wavelengths!).

Table 3.4 was generated using data from Figures 3.11 and 3.12, which show the filtered target and reference beam spectral responses to the Infrared Industries, Inc. 900°C blackbody source. Comparing Figures 3.11 and 3.12 with Figures 2.15 and 2.16 (which are the 900°C blackbody curves measured by the spectroradiometer without the filter) show the effects of the neutral density filter used to collect spectral data on 1/23/88. It is especially striking to look at the instrument spectral response after 1.66 μm relative to the visible wavelengths. Again, the extreme absorptivity of the filter longward of the visible wavelengths made measurements of anything cooler than Stage 1 targets impossible. Figures 3.11 and 3.12 provide the normalizations for Stage 1 spectral data collected on 1/23/88.

An example of Stage 1 activity as viewed through the filter detailed above is given in Figure 3.13. Small peaks in the flux measured at certain wavelengths seem to be superimposed upon a much smoother curve. These peaks may be due, in part, to small

eruptions of magma which increased the hot fractional area for very short periods of time. However, upon inspection of the other examples taken with the filter, it was discovered that the small peaks appear in all examples at roughly the same wavelengths. It seems highly unlikely that fountaining events occurred at the same time during the acquisition of each spectrum using the filter. It must be assumed that some or many of these small peaks are less absorptive regions of the filter. In any case, the instrument response normalizations, which were calculated from spectra taken of blackbody standards using the same filter that was used at Kupaianaha (Figures 3.11 and 3.12), should correct for inconsistencies in the filter.

Figure 3.13 displays the data file collected while observing a fountaining region on the surface of the lava lake. At the time that the spectrum was collected, the whole of the lake surface was cloud covered. Note the low reflected sunlight peak (~0.554 μm) which appears as a result of a combination of clouds and autoscaling with the very large fluxes measured at longer wavelengths.

Due to the small features appearing throughout Stage 1 spectra, I was somewhat apprehensive about using numerical models on these data. Errors in these models can be particularly large due to two factors: 1) the high normalizations (5.47×10^{-4} at 0.554 μm versus 3.41 at 2.13 μm) required to correct the data would accentuate small anomalous features, and 2) the amount of flux emitted at a given wavelength may change rapidly due to the activity in the field of view. With these possible problems in mind, Figure 3.14 summarizes the numerical model best fits for Figure 3.13. The best fit of Th = 900°C and Tc = 546°C is plotted in terms of radiance in Figure 3.15. This numerical model contains some of the highest temperatures for the solid crust, T_C, that have been found in this study. This was to be expected when considering that a

fountaining event and very fresh crust occupied the field of view. The fractional hot area, A_h, was also very large when compared to the other data. According to the numerical model, about 1.5% of the area measured by the spectroradiometer was covered by magma. The errors were moderately high, suggesting that the numerical fit was not entirely satisfactory for the data points chosen from Figure 3.13.

For the 2-component Stage 1 best fit results, examples 22 to 27 and 30 to 32 in Table 3.5 illuminate yet another problem with observing fountaining or very active regions. Not only are the events temporally brief, they also tend to be very limited in spatial extent. Examples 22 to 27 were collected while the field of view of the spectroradiometer was pointed at a glowing lava tube situated at one end of the lava lake. Examples 22 to 24 were collected within six minutes of one another with no visible apparent change in activity during the time that the measurements were collected. However, the result for example 22 suggests that the crust of the lake was much warmer than it was when examples 23 and 24 were collected only moments later. There could be two plausible reasons for this discrepancy. The first is that the lake surface actually did cool dramatically in the intervening 4 minutes, although this conclusion is not supported by the video observations taken of the area at the time. The second reason is that the spectroradiometer could have been pointed at the edge of an area of intense activity in example 22, and that the activity or the field of view of the spectroradiometer had moved slightly in the 4 minutes between measurements so that examples 23 and 24 were actually collected while observing a cooled (220°C and 292°C respectively) portion of crust. Examples 25 - 27 were spectra of the same lava tube taken 30 - 65 minutes after examples 23 and 24. The video record shows that the tube became very active during this time. Examples 25 - 27 reflect this. However, it must be recognized that

example 26 which was taken with the reference beam of the spectroradiometer was over 200°C cooler than examples 25 and 27. Examples 25 and 26 were collected at the same time and the spots viewed on the lake surface were within 1.05 m of one another. These examples show the spatially limited extent of Stage 1 activity.

A similar result can be seen for examples 30 and 31 which were collected at the same time with the target and reference beams of the spectroradiometer, respectively. The best fit results suggest that example 31 was taken of a very active area including fresh magma and newly formed crust. The area of example 30 which was no more than 1.05 m away from the area where example 31 was collected matches the temperatures observed for Stage 3 activity, although the area of the hot radiator, A_h, does seem to be more characteristic of Stage 2 activity. The cooler of the two spectral measurements is confirmed by a second target beam measurement (example 32) of the same area of crust only 3 minutes after example 30 was collected.

3.3.6 Stage 1: three-component results

Table 3.5 includes the three component model results for two examples of Stage 1 activity. Unfortunately, the remainder of the examples were taken with the neutral density filter covering the entrance port of the spectroradiometer. Since the instrument response corrections and possible errors were so enormous for these spectra, I did not feel that extending these data to the 3-component model was justified. However, the two 3-component best fit examples for Stage 1 activity which were taken without the filter give results that are consistent with the 2-component models. The difference between T_m and T_c in example 17 is 210°C, which definitely suggests that a 3-component model may be a better fit to these data than a 2-component model.

Table 3.5 includes the best fit results for the sixteen examples of Stage 1 activity that were collected on the two days. Considering the above explanation for the cooler solid crust temperatures derived for examples 19 - 21, 23, 24, 26, 30, and 32, Stage 1 characteristics may be summarized as areas displaying actively overturning crust or magma fountains. The results of this study suggest that Stage 1 areas exhibit solid crust temperatures (T_m and T_c) between 370°C - 570°C, and hot radiating fractional areas of greater than 10^{-3} of the viewing area. However, some of these results have high errors which may be due to the inability of the spectroradiometer to record temporally brief and spatially limited events, or due to the high normalization required to correct the effects of the filter used on January 23, 1988.

3.3.7 Special case - stage 1 and stage 2

One particular set of data collected on 10/12/87 did not neatly fit into any of the three stages mentioned above. The spectrum (Figure 3.16) was collected while a moving spreading center passed through the field of view of the spectroradiometer. A large spike occurring at 2.00 – 2.08 μm shows where the instrument detector was saturated by a burst of radiative flux from the lava lake surface. This large spike is almost certainly due to a fresh batch of erupting magma which entered the field of view as the instrument was collecting data in the 18 channels between 2.00 – 2.08 μm. Since this spectrum was collected while the instrument was set at a 70-second (speed factor 3) measurement time, this eruptive event must have been present in the field of view for only ~1.25 sec (assuming that each of the 1000 channels in the spectrum took an equal time to collect). Less obvious is the arrival of the recently formed crust from the spreading center (Stage 2) in the field of view. Relatively small amounts of flux were

detected shortward of 1.6 μm, after which the amount of flux increased very rapidly. Although not as dramatic as the spike at 2.00 μm, the event recorded longward of 1.6 μm also represents a change in the radiative output of the lake surface.

At the bottom of Table 3.5, I give the 2 and 3-component fits (example 33 in both cases) to Figure 3.16. The data chosen are located in two atmospheric windows between 1.61 - 1.77 μm and 2.08 - 2.23 μm; hence, it is the arrival of the recently formed crust near the spreading center which is crossing the field of view that is being modeled. Both 2 and 3-component results show that the surface of the lake was relatively hot when this part of the spectrum was recorded. The area exhibiting magmatic temperatures of 1100°C occupied 13% of the field of view. As a result, the hot component dominates the radiative flux coming from the surface of the lake for almost the entire wavelength range of the study (Figure 3.17). The 3-component fit shows that 29% of the surface radiated at 1100°C, 45% of the surface radiated at 790°C, while 36% radiated at 200°C. Both numerical fits are rather poor considering that the data chosen to represent the spectrum were relatively close together in two atmospheric windows (1.5 - 1.8 μm and 2.0 - 2.4 μm).

3.4 Discussion of Kupaianaha Results

There are many important results with direct implications for satellite remote sensing which can be extracted from the data collected with the spectroradiometer on the days of 10/12/87 and 1/23/88. These ideas are subdivided into separate discussion topics as follows:

1) Cool surface crust temperatures (T_c). Perhaps the most striking discovery in the results of this Chapter is the relatively cool surface temperatures derived

from the numerical models for Stage 3 spectra. Transfer of energy from the surface of the lava lake to the atmosphere must have been very rapid since the plates of crust which were being measured were less than 0.5 hours old, which was the total transit time for a plate of crust across the surface of the lava lake. This result is very important for satellite studies of lava lakes since it shows that "cool" surface crusts can mask volcanic activity from satellite sensors.

2) Small fractional hot areas, A_h. The second important result was the very small hot-component radiating areas found for all stages. Some of these fractional areas would have been undetectable in Landsat TM pixels (Oppenheimer, 1991, reports that the lowest detectable fraction of a hot pixel radiating at approximately 1130°C is 10^{-5} of the total pixel). Although the hot areas were small, they did dominate the spectral flux in the visible to near-infrared wavelengths depending on the temperature of the crust in the filed of view and the fractional area of the hot radiator. Wavelengths representing both hot and cold components were chosen as input for the numerical models.

4) The reflected sunlight component. The spectral data which were acquired at Kupaianaha were unique in that the data collected in the visible wavelengths allowed for the determination of the amount of contamination due to reflected solar flux in each of the collected spectra. Typical percentages of the total flux for each stage of activity which were solar radiation are listed below.

5) Characterization of stages of activity by radiant energy. Finally, the spectral data set collected on the two trips to Kupaianaha provide a wide range of values for the average flux density and the total energy budget of the lava lake. Combining the coverage of the video data with average results obtained for the three stages of

activity yielded energy budget calculations which show that the radiative flux emitted by the lava lake could double on short time scales (minutes) depending on the proportions of stages occupying the surface of the lava lake. This time scale is extremely short when compared with the elapsed time between possible successive satellite acquisitions (every 16 days for the Landsat satellite, and every few hours for the Advanced Very High Resolution Radiometer).

3.4.1 Cool surface crust temperatures

Remote sensing studies of active volcanoes using Landsat TM data (Rothery et al., 1988; Glaze et al., 1989; Pieri et al., 1990) conflict with one another over the lower temperature limit of detection using bands 5 and 7. Rothery et al. (1988) claim that the lowest temperature that may be derived using the dual-band method on Landsat TM bands 5 and 7 is 160°C. Glaze et al. (1989) assume a background temperature of 100°C in their study because this is the lowest detection limit of TM band 7. Conversely, Pieri et al. (1990) use 125°C as a background temperature because they claim that it is the "detection threshold for thermally emitting pixels". Looking closely at these studies, we conclude that the lowest derivable temperature using TM bands 5 and 7 is 160°C. The choice of a background temperature in the other two studies depends on the lowest DN (digital number) value that is considered to be significant above the background DN. Tables 3.1 and 3.2 show that the Kupaianaha lava lake exhibited solid crust Stage 3 temperatures of 80 - 345°C, which means that parts of solid crust would not appear to be thermally significant in TM band 5 (> 225 - 270°C to be detectable [Glaze et al., 1989]), and a dual-band method temperature for the background crust could not be

derived under some conditions, especially if the radiant pixels including the lava lake included significant portions of the surrounding non-thermally radiant terrain.

During field and video observations, I observed that the margins of the lake were most likely to experience Stage 1 and Stage 2 activity, due to the vertical fluctuations in the level of the lake. Rothery et al. (1988) claim that a 30 m TM pixel, when blurred by radiance "bleeding" into the adjacent pixel and geometric-correction effects, will actually be ~40 m in size. Thus it is conceivable (but unlikely) that a TM pixel occupying the center of the lava lake would show little or no activity if it were covered by common, thick, Stage 3 crust, while the pixels representing the fringes of the lava lake would show hot anomalies due to fountaining or rifting events. Using TM data, one may easily seriously underestimate the activity in the scene. This study suggests that future satellites designed to observe active volcanoes should have increased sensitivity to be able to unequivocally detect 100°C anomalies. In order to achieve this, more spectral data in the 2.0 - 5.0 μm range, where the radiative flux from the cooler crust dominates that of the small fraction radiating at near magmatic temperatures, must be collected. In addition to this, future satellite sensors should have a greater dynamic range than 255 of Landsat TM, for instance. A combination of these two improvements over that which the current generation satellites has to offer will allow for the solution of multiple sub-pixel radiating areas with greater precision and accuracy than is presently possible. Instruments such as MODIS-N (Salomonson et al., 1989) and especially ASTER and HIRIS (Goetz and Herring, 1989) on the EOS platforms will provide these capabilities.

3.4.2 Choice of wavelengths for study and effect on errors

All of our radiative results from Kupaianaha suggest that the fractional area of the magmatic radiator was very small. Stage 3 activity exhibited hot areas of $\leq 5 \times 10^{-5}$ of the total viewing area. Many examples of Stage 3 activity exhibited a fractional hot area an order of magnitude lower than the lowest derivable fractional hot area using the dual-band method with data from Landsat TM bands 5 and 7 (which is 10^{-5} of the total pixel for a hot area radiating at ~1100°C, Oppenheimer, 1991). Video observations collected at Kupaianaha include frequent periods of tens of minutes duration in which the lava lake is covered by Stage 3 crust, which means that it is probable that a Landsat TM data acquired over Kupaianaha lava lake would not be suitable for dual-band calculations because of the very small hot fractional areas of the crusted surface.

Another consideration which has to be taken into account is that Stage 3 fractional hot areas are so small that in the case of the field of view of the spectroradiometer, this amounts to a magmatic area of ≤ 2.3 mm^2 and ≤ 5.5 mm^2 for 10/12/87 and 1/23/88, respectively. This is almost non-existent, and one has to consider whether or not a 2- or 3-component solution using lower than magmatic temperatures would result in better fits to the spectral data. In addition, many of the best fit results occur for hot component temperatures of 900 or 950°C, which again suggests that temperatures below 900°C may provide better 2- and 3-component solutions. Stage 1 activity showed the highest fractional hot areas to be ~0.3 of the total area.

While the areas exhibiting magmatic temperatures are very small in most cases, the radiation emitted by these sources dominates the total flux in the visible to the near-infrared wavelengths, after the reflected sunlight component is removed from the data. At some point of the collected spectrum, the magmatic cracks and the solid crust

will both contribute approximately equal amounts of flux to the total radiant flux. I have chosen to name the wavelength at which the crust and hot components are both contributing equal amounts to the radiative flux the transition wavelength because it marks the point in the collected spectrum where, at shorter wavelengths, the magmatic component is contributing more of the total radiant flux, while at longer wavelengths, the solid crust will be contributing more of the total radiant flux. Figures 3.5, 3.9, 3.15, and 3.17 are interesting in that they show the best fit 2-component radiance curves which are summed to match the collected spectra. For the 2-component best fit model to a Stage 3 example (Figure 3.2), the contribution from magmatic microcracks dominate the radiative flux up to approximately 1.49 μm (Figure 3.5). For the Stage 2 example (Figure 3.7), the flux from the magmatic rift crack contributes more to the total flux up until about 1.99 μm (Figure 3.9). In this Stage 1 example of magma fountaining (Figure 3.13), the hot component dominates the total flux up to 1.27 μm (Figure 3.15). The transition wavelength occurred between 1.25 μm and 2.00 μm in all examples, except example 33 in which the magmatic component filled almost 13% of the field of view, and the transition wavelength is located at 2.20 μm (Figure 3.17).

The wavelengths used in the models for this study were chosen to most accurately represent the magmatic component, the solid crust component(s), and the summation of the two curves. The 3-component model requires six flux values at certain wavelengths while the 2-component model requires four. Input data for the numerical models were chosen from atmospheric windows in the 1.2 - 1.3 μm (magmatic component), 1.5 - 1.8 μm (transition wavelength zone), and 2.0 - 2.5 μm (solid crust component) ranges. Ideally, for the 3-component model, two data were chosen to represent each of the three windows mentioned above. In the 2-component case, a number of combinations of input

data were tried with the best result that, if possible, one input datum each should be chosen from 1.2 - 1.3 μm and 1.5 - 1.8 μm, with the remaining two coming from the 2.0 - 2.5 μm range.

Errors should be viewed only as a rough relative indicator of comparable goodness of fit. It was not possible to use the same wavelengths for all examples in this study because of the relatively large reflected sunlight component in Stage 3 examples at wavelengths < 1.5 μm and because of the effects of the filter on spectra of Stage 1 activity collected on 1/23/88. For these reasons and because of the fact that the 3-component model had both more data points and more ratios to match successfully to lower error values, the 2- and 3-component model errors are not correlatable between examples or between 2- and 3-component models for the same example. Errors are only an indicator of fit for a given set of data input values. In a very general sense, error values between measurements for the same component model may be compared. For instance, a 2-component best fit error of 0.0047 (Example 1, Table 3.1) certainly fits the data values chosen for one spectrum better than a 2-component best fit error of 0.3205 (Example 8, Table 3.1), but one factor which must be considered is whether the wavelength distributions of chosen data were the same in both cases. The low error may be due to the fact that only data values which were close together in wavelength space could be used, thus making it easier to fit a curve to these data. A case in point is example 33, which exhibited moderate error values for both 2- and 3-component best fits. However, data values used for this example were taken from 1.62, 1.66, 1.70, 2.10, 2.18, and 2.23 μm because, as pointed out above, a spreading center (rift) entered the field of view as the instrument was collecting data. This event, which manifested itself in the spectrum as a rapid increase in flux longward of 1.60 μm,

limited which wavelengths could be used in the numerical models for that particular example.

3.4.3 Reflected sunlight in measurements

Earlier, on the basis of the Stage 3 test case, I showed that the amount of radiation from reflected sunlight dominated the measured flux at 0.554 μm, but I must now prove that this is also valid for Stage 1 and 2 activity. The Stage 2 example with the largest fractional magmatic radiating area (example 14, Table 3.3) exhibited a radiant flux at 0.554 μm of 1.2×10^{-4} mW cm^{-2} μm^{-1} sr^{-1}, which is still only about 0.2% of the flux from the reflected solar component. The Stage 1 example with the highest radiance at 0.554 μm (example 18, Table 3.5) was 2.6×10^{-3} mW cm^{-2} μm^{-1} sr^{-1} which is about 3.5% of the flux from the reflected solar component. However, I can safely say that the error due to this amount is negligible since the amount of reflected sunlight at the wavelengths used for Stages 1 and 2 in this study were at most only 5% and 10% of the total flux, respectively. This works out to be an error in the estimate of the subtracted reflected solar flux on the order of 0.1% at most. Thus, the assumptions that were made in Chapter 2, section 6 concerning the flux at 0.554 μm being entirely reflected sunlight are still valid arguments.

One factor in particular that made it difficult to choose data values representative of the magmatic component was the amount of reflected sunlight present in the data. Especially for Stage 3, where the radiative contribution of the magmatic component was very small, the flux of reflected sunlight frequently dominated the total radiative flux at wavelengths < 1.5 μm. Thus, in some Stage 3 cases, it was impossible to choose data where the hot component dominated as input for the numerical model. Figure 3.18

shows the effect of reflected sunlight on examples of the various stages identified in this study. As a comparison between the different stages of activity, reflected sunlight comprises 13% of the thermal flux at 0.988 μm for Stage 1, 12% at 1.23 μm for Stage 2, and 19% at 1.70 μm for Stage 3. Even more surprising is the fact that in the 1.2 - 1.3 μm window, from which input data representing the magmatic radiators were chosen, reflected sunlight makes up only about 3.5% of the total radiative flux for Stage 1, on the order of 10% for Stage 2, and above 90% for Stage 3. Stage 3 solid crust activity exhibits hot areas of 10^{-5} or less, which is 2 to 3 orders of magnitude below that found for Stage 1 activity. Since the amount of sunlight reflecting off of Kupaianaha was fairly constant on October 12, 1987, and examples of all three stages were collected on this date, the radiative area of the magmatic component made a critical difference in my ability to reliably choose input data from the 1.2 - 1.3 μm window.

3.4.4 Average radiative flux and total energy budget of lake

Recent studies (e.g. Glaze et al., 1989; Pieri et al., 1990; Oppenheimer and Rothery, 1991) of active volcanoes using Landsat TM data have attempted to quantify the total energy budget, Q, of volcanic areas. The 2-component equation for the total energy budget, as discussed in Pieri et al. (1990), is:

$$Q = (e\sigma T_h^4) \times Area_h + (e\sigma T_c^4) \times Area_c \qquad (21)$$

where Q is the total energy flux (in W/m^2); e is the emissivity; σ is the Stefan-Boltzmann constant; T_h and $Area_h$ are the temperature (in K) and area (in m^2) of the magmatic cracks, respectively; and T_c and $Area_c$ are the temperature and area of the solid crust, respectively.

This study provides important additional data to the growing information on Q values for active volcanoes. Since the spectroradiometer's field of view was very limited (< 0.6 m^2) compared to the 900 m^2 covered by Landsat TM pixels (bands 1 - 5 and 7), the question of calculating the total energy budget of Kupaianaha on the days when observations were made will be considered in two ways. First, the average flux density, (Q/A), as discussed in Glaze et al. (1989) and Pieri et al. (1990), has been calculated for each of the best fit examples listed in Tables 3.1, 3.2, 3.3, and 3.5. This allows the results of this study to be directly compared with the results of the larger-scale Landsat studies mentioned above. Next, using the video of the lake recorded on both days, I have calculated values for the total energy budget of Kupaianaha by assigning fractional areas of the lake to the various Stages observed.

Tables 3.1, 3.2, 3.3, and 3.5 list the 2- and 3-thermal-component average flux densities for the three Stages of activity observed at Kupaianaha. I assumed an emissivity of 0.995 given the result that was found for fresh basalt samples. Two-component average flux densities for quiescent periods (Stage 3, Table 3.1) ranged from 3.0 x 10^3 - 6.3 x 10^3 W/m^2 with an average of 4.9 x 10^3 W/m^2. Three-component (Table 3.2) average flux densities for quiescent periods ranged from 1.9 - 6.2 x 10^3 W/m^2 with an average of 3.4 x 10^3 W/m^2. Two-component and 3-component average Q/A values for rifting (Stage 2, Table 3.3) events are almost identical at 5.3 x 10^3 W/m^2 and 4.8 x 10^3 W/m^2, respectively. Two-component average flux densities for active overturning and magma fountaining events (Stage 1, Table 3.5) were between 9.8 x 10^3 and 3.0 x 10^4 W/m^2 (excepting examples 19 – 21, 23, 24, 26, 30 and 32 which, as discussed above, were not representative of Stage 1 activity) with an average of 2.4 x 10^4 W/m^2.

The contribution of the hot area to the average flux density was found to be very small for all three stages of activity. Radiating microcracks in Stage 3 activity accounted for only about 5 W/m^2 of the total average flux density. Larger rifting cracks characteristic of Stage 2 contributed up to 50 W/m^2 which was less than 1.5% of the total average flux density. Magma fountains and larger overturning events of Stage 1 contributed on the order of 100 - 1000 W/m^2 to the total average flux density. Example 33 in Table 3.5 exhibited the highest proportional hot area (~13% of the total field of view) in this study. In this case, the area radiating at magmatic temperature accounted for 36% of the average flux density. For all examples of all Stages of activity, the background or solid crust radiated most of the flux detected by the spectroradiometer.

The average flux density values calculated from the spectral measurements of this study are consistent with but higher than values derived for other volcanoes using Landsat TM data. Glaze et al. (1989) report a Q/A range of 0.7 - 2.2 x 10^3 W/m^2 for 10 Landsat images collected over Lascar volcano, Chile, between December 1984 and November 1987. This set of average flux densities is lower than the range found from the 3-component results of this study for Stage 3 activity. Of particular relevance to this study, Glaze et al. (1989) also report Q/A values of 1.6 and 2.3 x 10^3 W/m^2 for the active basaltic lava lakes of Erebus and Erta Ale volcanoes, respectively. In our Kupaianaha study, these values were found to be slightly lower than those representative of Stage 3, quiescent activity. Pieri et al. (1990) calculate an average flux density for a 1984 active lava flow on Etna of 1.5 x 10^3 W/m^2 which also falls slightly below the range of values that this study identified for Stage 3 crusted surfaces. The only other study to calculate a Q/A value for a terrestrial volcanic thermal source is that of

Oppenheimer and Rothery (1991), who used Cyclops thermometers to measure brightness temperatures of a 40 m-long fumarole at Vulcano, Italy. They reported an average flux density of 23 W/m^2 for this type of activity, which is two orders of magnitude lower than the average flux densities calculated for Stage 3 in this study.

The total energy budget, Q, is also an important parameter when discussing the level of activity of a particular erupting volcano. I calculated Q-values for stage of activity distributions identified in the video record (Table 3.6). More than 90% of the time, the lava lake surface could be described by the first three examples in Table 3.6. In other words, for the majority of the time, the lava lake was very quiescent with very limited rifting occurring between massive plates in the center of the lake and very limited < 1 m high fountains erupting along the perimeter of the lake. Thus, according to my numerical model fits to the spectral data, more than 90% of the time Kupaianaha would have exhibited a Q value of $1.1 - 1.2 \times 10^7$ W. However, the lava lake did experience periods of increased radiative output, both through rifting events and large scale subducting (one plate sliding beneath the other) events. Examples 4 – 10 summarize some of the typical stage distributions observed for these temporally limited events. Increased Stage 1 activity was always accompanied by increased Stage 2 activity as is suggested by the examples in Table 3.6. The most active period (example 10) observed at Kupaianaha occurred on October 12, 1987, when a large (3 - 4 m high and occupying ~ 50 m^2) fountain erupted from between two plates near the center of the lake while a large subducting event was exposing even more fresh magma near the edge of the lake. Even with these relatively large events occurring at the same time, Stage 1 could not have an area of greater than 15% of the total lake surface and a momentary Q value of 1.8×10^7 W. However, these instances of large increases in the surface

activity of the lava lake show that Q for Kupaianaha could almost double in the span of seconds. It would be very difficult to argue that the Landsat satellite, which acquires repeat images every 16 days, would be capable of measuring typical Q-values for volcanoes, since the span of time between successive acquisitions is large enough that multiple changes in factors affecting the radiative characteristics of volcanoes (such as the distribution of surface flows or the size and convective pattern of a lava lake) would occur.

A number of previous studies have attempted to quantify Q for volcanic sources. Le Guern et al. (1979) which reported a Q value of 1.13×10^8 W for the two lava lakes (total area = 3800 m^2) of Erta Ale during 1973. Le Guern (1987) reports Q values for Nyiragongo of 5.4×10^8 W (area of anomaly = 13,125 m^2) and 1.22×10^{10} W in 1959 and 1972 respectively. These lava lakes were reported to be much larger than Kupaianaha at the time of our visits. Oppenheimer and Rothery (1991) quote a Q for a fumarole at Vulcano, Italy, of 37 kW, placing this type of low thermal activity in a category of its own as far as remote measurements of Q are concerned.

Several investigators have explored the potential for satellite measurements of Q. Glaze et al. (1989) used Landsat TM data to derive Q values of $0.3 - 7.6 \times 10^7$ W for Lascar, 5.8×10^7 W for Erebus and 6.9×10^7 W for Erta Ale volcanoes, respectively. These values for basaltic lava lakes (Erebus and Erta Ale) are almost an order of magnitude greater than my estimates for Kupaianaha, but are actually consistent with my results since the surface area of Kupaianaha was an order of magnitude smaller than these other thermal anomalies. Further Landsat TM results presented in Pieri et al. (1990) calculate a Q value of 12.5×10^7 W for a June 1984 lava flow on Mt. Etna,

which is again higher than my estimates for Kupaianaha because of the larger radiating surface presented during that eruption.

It is important to note that comparing values Q and Q/A of basaltic, andesitic, and rhyolitic volcanic activity may not be straightforward since these calculations depend on an accurate estimate of the emissivity of the fresh lava crust. My measurements of basalt samples have shown that the reflectance (and hence, emissivity) of fresh basalt across the 0.4 - 2.5 μm spectral region is less than 0.5% and is very featureless. Thus, in calculations of Q and Q/A presented in this chapter, the emissivity may be treated as a constant in the spectral region of this study. However, I would caution against extending this assumption to rhyolitic or andesitic crusts without first measuring the emissivities of fresh (days old) samples. Rothery et al. (1988) assume, based on their own unpublished data, that the emissivities of volcanic rocks is 0.6 in bands 5 (1.55 - 1.75 μm) and 7 (2.08 - 2.35 μm), and 0.8 in band 4 (0.76 - 0.90 μm). These estimates are very much lower than those which I measured for basalt. In a recent study of lava flows from Volcan Lonquimay, Oppenheimer (1991) assumes an emissivity of fresh andesite of 0.95, which is much closer to my measurements of the emissivities of volcanic rocks.

The investigations of the total energy budgets and the average flux densities of the observations presented in Chapter 3 have led me to an important conclusion. Both quantities are important in describing the activity of a volcanic eruption. While Q provides a comparable estimate of the overall activity of the volcano (Glaze et al., 1989), I have found that the average flux density Q/A measures the intensity of the eruptive phenomenon. My calculations of Q are about an order of magnitude lower than other reported Q values for active eruptions. However, when Q/A values are compared,

the results for Stage 3 activity are consistent with those results obtained for the Landsat TM studies mentioned above. Volcanic areas covered primarily by magma fountaining events or other Stage 1 activity would exhibit Q values much higher than those reported. Thus, I would point out that while Q is an important indicator of the volume and subareal extent of an eruption, Q/A is critical to the understanding of the intensity of the ongoing eruption. Furthermore, remotely sensed estimates of Q depend on the accurate determination of the overall size of the radiative anomaly, which, as shown above, can be arbitrary depending on the assumed background temperature. Q/A can be calculated on an individual pixel basis and only depends on the fractional area of the emitting blackbodies. Thus, even when the total extent of an eruption cannot be determined (due to partial cloud cover, for instance), Q/A, calculated from thermally emitting pixels, can provide comparable estimates of the degree of severity of an eruption. However, any satellite estimate of Q or Q/A should be regarded with caution, because, as have shown in this Chapter, the radiated energy from volcanic areas is extremely variable on a time scale of minutes.

3.5 Conclusions

Spectral data collected on October 12, 1987 and January 23, 1988 have been analyzed using numerical models in which the ratios of fluxes at wavelengths chosen from atmospheric windows were matched to theoretical values at the same wavelengths for two and three blackbody curves. This method is innovative in that it attempts to match the shape of the spectral curve as closely as possible. For many of the spectra analyzed, I determined that a 2-component model would be insufficient in describing the radiative output of the lava lake, since the two surface crust components of the three

component model varied by 90°C or more. For these spectra, a numerical model of 3 or more radiative components is necessary.

With the help of the video film obtained while the spectral data were collected, I have been able to identify three characteristic stages of activity for the Kupaianaha lava lake. Stage 1, characterized by magma fountaining and overturning events exhibited the hottest crust temperatures (> 370°C) and largest fractional hot areas (> 10^{-3}) and may require a 3-component thermal model to accurately describe the 0.4 - 2.5 μm spectrum. Stage 1 average flux densities were about 2.4 x 10^4 W/m^2, the highest recorded for the three stages of activity that were observed. Stage 2, marked by rifting events between plates of crust, exhibited crust temperatures between 100 – 340°C with fractional hot areas about an order of magnitude lower than those found for Stage 1. Average flux densities calculated for the three examples of Stage 2 activity were typically 5.3 x 10^3 W/m^2. Stage 3, quiescent periods when the lake was covered by a thick crust, dominated the activity on the surface of the lake both temporally and spatially over 90% of the time. Numerical model results for Stage 3 suggest characteristic crust temperatures of 80 - 345°C with fractional hot areas of 10^{-5} or less of the total viewing area. The hot fractional areas representative of stage 3 were so small that the reflected solar flux dominated the total thermal flux up to about 1.5 μm and the variation of the hot component temperature between 900°C and 1250°C did not have a significant effect on the solution of the crust temperature (Flynn et al., 1990). Average flux densities for Stage 3 averaged 4.9 x 10^3 W/m^2.

The results and the discussion presented in Chapter 3 represent an important part of this dissertation. The spectral data set collected at Kupaianaha represents the first hyperspectral data set having more than spectral channels per measurement. It also is

the first field study carried out using a spectroradiometer capable of collecting 200 data which can be used for calculations of the radiative components of small (< 0.6 m^2) target areas. It is also the first study to recognize and analyze the different stages of activity for an active volcanic source. The spectral data collected are the first to allow for the accurate removal of the flux from sunlight reflecting off of a thermally radiant lava crust, and the first to estimate the degree of solar contamination with wavelength depending on the type of volcanic activity present. Finally, the video record combined with the spectral examples of each stage of activity are the first to allow a study of the change in the energy budget of an entire lava lake on time scales of minutes to hours. These calculations have major implications for satellite observations of volcanic thermal anomalies. MODIS and ASTER will be used on EOS (Mouginis-Mark et al., 1991) for this application, and it is crucially important that both the spectral and temporal content of these temperature measurements are considered.

Perhaps the most difficult and time-consuming problem with reducing the spectra in Chapter 3 was calculating the flux in the spectral data due to reflected sunlight. Solar contamination prevented me from using wavelengths at < 1.5 μm for numerical models of Stage 3, by far the dominant activity of the surface of Kupaianaha lava lake. Stage 3 results suggest vanishingly small hot fractional areas. For this type of activity, a 2- or 3-component model using temperatures which are lower than those used for the hot component temperature in this chapter may give better fits to the spectral data, since the component radiating at magmatic temperatures is so small. To be able to use spectral data in the numerical models where the magmatic component is dominant, I would have to acquire the data at night. In Chapter 4, a new nighttime field study using the GER

spectroradiometer introduced in Chapter 2 is described, thus, eliminating the flux due to reflected sunlight.

The purpose of this next chapter is to answer some questions which remain after the results of Chapter 3 have been analyzed and to extend some concepts on the rate of cooling of lava flows. Some of these questions are what are numerical model results for lava crusts (Stage 3) using data at < 1.5 μm (previously swamped by over 90% reflected sunlight); what does the radiative emission from an active volcanic source look like without solar contamination; how does the emitted radiance of a recently emplaced lava flow change with time; and how do the derived crust temperatures, hot fractional areas and energy budget (Q) of the lava flow behave after emplacement.

References

Dozier, J., A method for satellite identification of surface temperature fields of subpixel resolution, *Remote Sens. Environ., 11,* 221 - 229, 1981.

Flynn, L. P., P. J. Mouginis-Mark, and J. C. Gradie, Radiative Temperature Measurements of Kilauea Volcano, Hawaii, paper presented at International Volcanological Congress, *Int. Assoc. Volcanol. Chem. Earth's Interior,* Mainz, Germany, Sept. 3-8, 1990.

Glaze, L., P. W. Francis, and D. A. Rothery, Measuring thermal budgets of active volcanoes by satellite remote sensing, *Nature, 338,* 144 - 146, 1989.

Goetz, A. F. H., and M. Herring, The high resolution imaging spectrometer (HIRIS) for EOS, *IEEE Trans. Geosci. Remote Sens., 27,* 136 - 144, 1989.

Jones, A. C., L. Wilson, and H. Pinkerton, Surface temperature measurements of active Hawaiian lava flows, paper presented at International Volcanological Congress, *Int. Assoc. Volcanol. Chem. Earth's Interior,* Mainz, Germany, Sept. 3-8, 1990.

Le Guern, F., Mechanism of energy transfer in the lava lake of Niragongo (Zaire), 1959 - 1977, *J. Volcanol. Geotherm. Res., 31,* 17 - 31, 1987.

Le Guern, F., J. Carbonelle, H. Tazieff, Erta ' Ale lava lake: Heat and gas transfer to the atmosphere, *J. Volcanol. Geotherm. Res., 6,* 27 - 48, 1979.

Matson, M. and J. Dozier, Identification of subresolution high temperature sources using a thermal IR sensor, *Photogramm. Eng. Remote Sens., 47,* 1311 - 1318, 1981.

Mouginis-Mark, P., *et al.*, Analysis of active volcanoes from the Earth Observing System, *Remote Sens. Environ., 36,* 1 - 12, 1991.

Oppenheimer, C., Lava flow cooling estimated from Landsat Thematic Mapper infrared data: the Lonquimay eruption (Chile, 1989), *J. Geophys. Res., 96,* 21,865 - 21,878, 1991.

Oppenheimer, C. M. M., and D. A. Rothery, Infrared monitoring of volcanoes by satellite, *Journal of the Geological Society, London, 148,* 563 - 569, 1991.

Pieri, D. C., L. S. Glaze, and M. J. Abrams, Thermal radiance observations of an active lava flow during the June 1984 eruption of Mount Etna, *Geology, 18,* 1018 - 1022, 1990.

Rothery, D. A., P. W. Francis, and C. A. Wood, Volcano monitoring using short wavelength infrared data from satellites, *Journal of Geophysical Research, 93,* 7993 - 8008, 1988.

Salomonson, V. V., W. L. Barnes, P. W. Maymon, H. E. Montgomery, and H. Ostrow, MODIS: Advanced facility instrument for studies of the Earth as a system, *IEEE Trans. Geosci. Remote Sens., 27,* 145 - 153, 1989.

Wiesnet, D. R., and J. D'Aguanno, Thermal imagery of Mt. Erebus from the NOAA-6 satellite, *Antarct. J. U.S., 17,* 32 - 34, 1982.

Wolfe, W. L., and G. J. Zissis, *The Infrared Handbook*, Infrared Information and Analysis (IRIA) Center, Environmental Research Institute of Michigan, Ann Arbor, Michigan, 1985.

Table 3.1

Summary of the 2-component model best fits of Stage 3 spectra obtained at Kupaianaha lava lake on 10/12/87 and 1/23/88. Under "Time (HST)" are listed the example number which is used for referencing in the Chapter 3, along with the time (Hawaii Standard Time) that the measurement was started. An asterisk after the time denotes a measurement acquired on 1/23/88. Activity is a short description of the lake surface in the spectroradiometer's field of view at the time of the measurement. T_h(°C) and T_c(°C) are the best fit radiative temperatures of the magmatic and solid crust components, respectively. A_h is the fraction of the measured area exhibiting the radiative temperature, T_h, with the remainder radiating at T_c. Error (a unit-less quantity) refers to lowest the sum of the three individual flux ratio errors (eq. 12, Chapter 3, section 3.2.1) obtained by the model and is the criterion by which the model determines the best fit. Q/A is the average flux density radiated by a surface exhibiting the parameters (T_h, T_c, and A_h) of the best fit.

	TIME(HST)	ACTIVITY	T_h(°C)	T_c(°C)	A_h	ERROR	Q/A(Wm^{-2})
1.	13:57:40	crust near rift	900	260	5.0×10^{-5}	0.0047	4.6×10^3
2.	13:57:40	crust near rift	900	304	3.5×10^{-6}	0.0075	6.3×10^3
3.	13:59:40	plate crust	950	236	2.9×10^{-5}	0.0413	3.8×10^3
4.	13:59:40	plate crust	950	238	3.0×10^{-5}	0.0150	3.9×10^3
5.	14:01:40	fresh crust	1100	302	1.4×10^{-5}	0.0669	6.2×10^3
6.	14:01:40	fresh crust	950	256	2.0×10^{-5}	0.0495	4.4×10^3
7.	14:10:30	plate crust	950	294	6.8×10^{-6}	0.0263	5.9×10^3
8.	14:10:30	plate crust	900	210	3.7×10^{-6}	0.3205	3.1×10^3
9.	14:13:30	plate crust	900	270	5.7×10^{-6}	0.0636	4.9×10^3
10.	14:16:30	plate crust	1250	280	1.4×10^{-5}	0.0512	5.3×10^3
11.	14:16:30	plate crust	900	208	9.4×10^{-7}	0.3261	3.0×10^3
12.	12:45:00*	crust near rift	1100	296	8.7×10^{-6}	0.0900	5.9×10^3
13.	12:45:00*	crust near rift	1150	294	2.0×10^{-5}	0.0074	5.9×10^3

Table 3.2

Summary of the 3-component model best fits to the Stage 3 spectra obtained at Kupaianaha lava lake on 10/12/87 and 1/23/88. Examples are presented in the same order as in Table 3.1. Column headings are consistent with those described for Table 3.1, with the exceptions of T_m and A_m which refer to the temperature and fractional area, respectively, of the component radiating at a temperature between that of the other two components. Error (a unit-less quantity) refers to the lowest sum of the six individual flux ratio errors of the 3-component model and is the best fit criterion. Q/A is the average flux density radiated by a surface exhibiting the parameters (T_h, T_m, T_c, A_m, and A_h) of the best fit.

EXAMPLE	T_h(°C)	T_m(°C)	T_c(°C)	A_h	A_m	ERROR	Q/A(W/m^2)
1.	950	270	138	1.3×10^{-5}	0.29	0.0371	2.6×10^3
2.	900	305	125	2.2×10^{-6}	0.99	0.0647	6.2×10^3
3.	1100	275	270	9.7×10^{-7}	0.95	0.6350	5.1×10^3
4.	1100	285	275	2.2×10^{-8}	0.62	0.4733	5.3×10^3
5.	1100	345	245	6.4×10^{-8}	0.30	0.2076	5.3×10^3
6.	1100	280	170	8.3×10^{-8}	0.35	0.3958	3.4×10^3
7.	1100	300	170	4.6×10^{-7}	0.40	0.0828	3.7×10^3
8.	1100	220	80	8.5×10^{-7}	0.95	0.6015	3.2×10^3
9.	900	270	180	4.2×10^{-8}	0.30	0.3180	3.1×10^3
10.	1100	280	160	9.4×10^{-6}	0.30	0.1074	3.0×10^3
11.	900	180	80	2.2×10^{-6}	0.70	0.7731	1.9×10^3
12.	1100	215	195	5.0×10^{-6}	0.10	0.3133	2.8×10^3
13.	1100	295	155	1.1×10^{-5}	0.40	0.0379	3.5×10^3

Table 3.3

Summary of the 2- and 3-component model best fits to the Stage 2 spectra obtained at Kupaianaha lava lake on 10/12/87 and 1/23/88. Example numbers listed are the same as those referred to in Chapter 3. Column headings are consistent with either those described for Table 3.1 for the 2-component best fits or those described for Table 3.2 for the 3-component best fits.

Two-component model

	TIME(HST)	ACTIVITY	T_h(°C)	T_c(°C)	A_h	ERROR	Q/A(Wm^{-2})
14.	14:21:00	beginning rift	1000	262	3.9×10^{-4}	0.0081	4.7×10^3
15.	14:21:00	beginning rift	1100	210	1.2×10^{-4}	0.0900	3.1×10^3
16.	14:25:00	active rift	900	340	6.1×10^{-6}	0.1168	8.0×10^3

Three-component model

EXAMPLE	T_h(°C)	T_m(°C)	T_c(°C)	A_h	A_m	ERROR	Q/A(W/m^2)
14.	1100	290	285	3.0×10^{-4}	0.30	0.1130	5.6×10^3
15.	1100	200	120	1.3×10^{-4}	0.15	0.1503	1.6×10^3
16.	1100	340	100	3.7×10^{-6}	0.90	0.4682	7.3×10^3

Table 3.4

Normalized instrument response corrections for each wavelength (first column) used in numerical model calculations in Chapter 3. At a given wavelength, the spectroradiometer measured value, minus the offset, multiplied by the instrument response yields the actual amount of radiation originating from the lava lake surface. The second and third columns list instrument response corrections for target and reference spectra taken without the neutral density filter. The fourth and fifth columns show the instrument response corrections for target and reference spectra taken with the neutral density filter (examples 19 - 32). Without the filter, the ratio of the correction at 2.10 μm to that of 0.554 μm is ~0.66. With the filter in the field of view of the spectroradiometer, the ratio of the correction at 2.115 μm to that of 0.554 μm is ~5900. This shows that the neutral density filter was extremely absorptive in the infrared.

Wavelength (μm)	Normalization (no filter)		Normalization (with ND filter)	
	Target	Reference	Target	Reference
0.554	0.35915	0.34834	5.4704×10^{-4}	5.5623×10^{-4}
0.973	- - - - - - -	- - - - - - -	0.37961	- - - - - - -
1.013	- - - - - - -	- - - - - - -	0.50091	- - - - - - -
1.09845	1.00000	1.00000	1.00000	1.00000
1.175	- - - - - - -	- - - - - - -	- - - - - - -	1.31789
1.23	0.73229	0.69677	1.47395	- - - - - - -
1.24	0.64845	0.62274	- - - - - - -	- - - - - - -
1.25	0.58549	0.55681	- - - - - - -	- - - - - - -
1.27	- - - - - - -	- - - - - - -	1.46498	1.61720
1.296	- - - - - - -	- - - - - - -	1.42370	1.53344
1.506	- - - - - - -	- - - - - - -	2.01209	- - - - - - -
1.512	- - - - - - -	- - - - - - -	- - - - - - -	2.15786
1.53	0.40320	0.37527	2.17517	2.17144
1.57	- - - - - - -	- - - - - - -	2.16742	2.31026
1.62	0.41360	0.38072	- - - - - - -	- - - - - - -
1.625	- - - - - - -	- - - - - - -	2.47801	- - - - - - -
1.64	- - - - - - -	- - - - - - -	2.46832	- - - - - - -
1.66	0.41878	0.38682	- - - - - - -	- - - - - - -
1.673	- - - - - - -	- - - - - - -	- - - - - - -	2.95954
1.68	- - - - - - -	0.36303	- - - - - - -	- - - - - - -

Table 3.4 (continued)

Normalized instrument response corrections for each wavelength (first column) used in numerical model calculations in Chapter 3. At a given wavelength, the spectroradiometer measured value, minus the offset, multiplied by the instrument response yields the actual amount of radiation originating from the lava lake surface. The second and third columns list instrument response corrections for target and reference spectra taken without the neutral density filter. The fourth and fifth columns show the instrument response corrections for target and reference spectra taken with the neutral density filter (examples 19 - 32). Without the filter, the ratio of the correction at 2.10 μm to that of 0.554 μm is ~0.66. With the filter in the field of view of the spectroradiometer, the ratio of the correction at 2.115 μm to that of 0.554 μm is ~5900. This shows that the neutral density filter was extremely absorptive in the infrared.

Wavelength (μm)	Normalization (no filter)		Normalization (with ND filter)	
1.70	0.42399	0.39428	2.88804	-------
1.73	-------	-------	-------	3.16857
2.03	-------	-------	2.83843	2.84957
2.067	-------	-------	2.90237	2.98608
2.08	0.23929	0.23147	-------	-------
2.083	-------	-------	2.96981	3.13088
2.10	0.23832	0.23281	-------	-------
2.115	-------	-------	-------	3.30513
2.13	-------	-------	3.41472	3.63500
2.18	0.24111	-------	-------	-------
2.25	0.25171	0.26484	-------	-------

Table 3.5

Summary of the 2- and 3-component model best fits to the Stage 1 spectra obtained at Kupaianaha lava lake on 10/12/87 and 1/23/88. The special case example (number 33, discussed in Chapter 3, section 3.3.7) of Stage 1 and Stage 2 activity is also listed here. Example numbers listed are the same as those referred to in Chapter 3. Column headings are consistent with either those described for Table 3.1 for the 2-component best fits or those described for Table 3.2 for the 3-component best fits. Note that there is only one pair of Stage 1 spectra which could be used for 3-component calculations.

Two-component results

TIME(HST)	ACTIVITY	T_h(°C)	T_c(°C)	A_h	ERROR	Q/A(Wm^{-2})
17. 14:03:40	very active	900	400	9.1×10^{-3}	0.0491	1.3×10^{4}
18. 14:03:40	very active	1100	572	3.1×10^{-3}	0.1060	3.0×10^{4}
19. 12:50:00*	near rift	900	348	1.5×10^{-4}	0.1613	8.4×10^{3}
20. 12:55:00*	near rift	900	216	7.1×10^{-5}	0.0167	3.2×10^{3}
21. 12:55:00*	nearrift	1200	198	1.8×10^{-6}	0.0212	2.8×10^{3}
22. 13:14:00*	lava tube	900	370	1.3×10^{-3}	0.3845	9.8×10^{3}
23. 13:18:00*	lava tube	950	220	1.3×10^{-4}	0.0042	3.4×10^{3}
24. 13:18:00*	lava tube	1250	292	6.3×10^{-5}	0.0440	5.8×10^{3}
25. 13:48:00*	lava tube	1000	564	8.7×10^{-3}	0.0671	2.9×10^{4}
26. 13:48:00*	lava tube	950	282	1.5×10^{-4}	0.1217	5.4×10^{3}
27. 14:23:00*	lava tube	900	490	8.1×10^{-3}	0.1245	2.0×10^{4}
28. 14:30:00*	active vent	900	528	1.9×10^{-2}	0.0055	2.5×10^{4}
29. 14:30:00*	active vent	900	528	2.1×10^{-2}	0.0997	2.5×10^{4}
30. 14:35:00*	fountain	900	278	7.0×10^{-4}	0.0888	5.3×10^{3}
31. 14:35:00*	fountain	900	546	1.5×10^{-2}	0.1977	2.7×10^{4}
32. 14:38:00*	hot surface	900	332	3.2×10^{-3}	0.1269	7.9×10^{3}
STAGE 1 and STAGE 2						
33. 14:25:00	active rift	1100	710	1.3×10^{-1}	0.2054	7.2×10^{4}

Table 3.5 (continued)

Summary of the 2- and 3-component model best fits to the Stage 1 spectra obtained at Kupaianaha lava lake on 10/12/87 and 1/23/88. The special case example (number 33, discussed in Chapter 3, section 3.3.7) of Stage 1 and Stage 2 activity is also listed here. Example numbers listed are the same as those referred to in Chapter 3. Column headings are consistent with either those described for Table 3.1 for the 2-component best fits or those described for Table 3.2 for the 3-component best fits. Note that there is only one pair of Stage 1 spectra which could be used for 3-component calculations.

Three-component results

ACTIVITY	T_h(°C)	T_m(°C)	T_c(°C)	A_h	A_m	ERROR	Q/A(W/m^2)
STAGE 1							
17.very active, magma	900	390	180	5.5×10^{-4}	0.05	0.1332	2.9×10^3
18.very active, magma	1100	550	270	8.4×10^{-4}	0.30	0.2640	1.1×10^4
19 - 32	no result						
STAGE 1 and STAGE 2							
33.active rift, magma	1100	790	200	2.9×10^{-1}	0.45	0.3666	9.1×10^4

Table 3.6

Calculations of the total energy budget, Q, of Kupaianaha lava lake using video and spectral data collected on 10/12/87 and 1/23/88. Stage 1(%), Stage 2(%), and Stage 3(%) refer to the percentage of the total surface area occupied by one of the three types of activity. Total Q/A is the overall average flux density radiated by the lava lake exhibiting the specified distribution of activity. Q is the total energy budget of the lava lake and is the product of the overall average flux density and the total radiating surface of the lava lake. Since the lake was roughly 50 m in diameter with a 30 m x 10 m channel, I have assumed a total area of 2300 m^2. Video observations suggest that the activity of Kupaianaha could be best described by one of the first three examples 90% of the time.

Example	Stage 1(%)	Stage 2(%)	Stage 3(%)	Total Q/A (W/m^2)	Q(x 10^7 W)
1	0	0	100	4.9×10^3	1.1
2	0	10	90	4.9×10^3	1.1
3	1	5	94	5.1×10^3	1.2
4	1	10	89	5.1×10^3	1.2
5	5	10	85	5.9×10^3	1.4
6	5	20	75	5.9×10^3	1.4
7	5	25	70	6.0×10^3	1.4
8	10	20	70	6.9×10^3	1.6
9	10	25	65	6.9×10^3	1.6
10	15	20	65	7.8×10^3	1.8

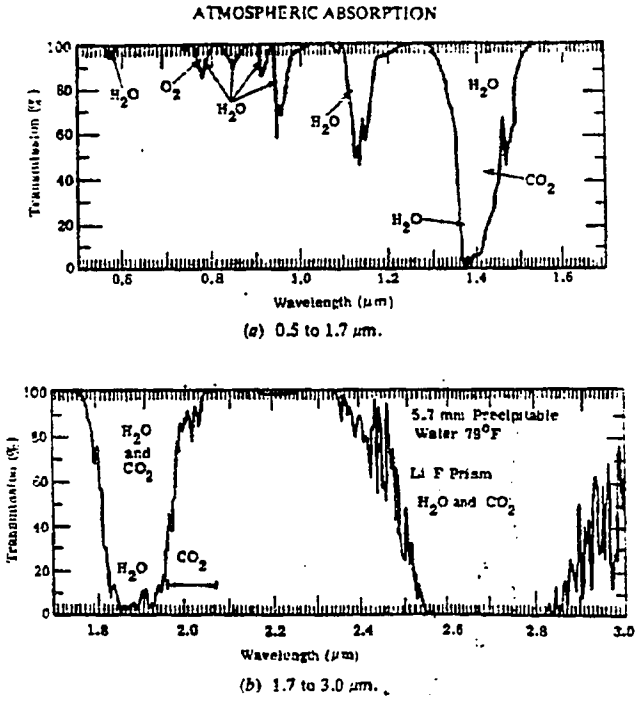

Figure 3.1. Atmospheric transmission for path length of 300 m at sea level, taken from Wolfe and Zissis, 1985.

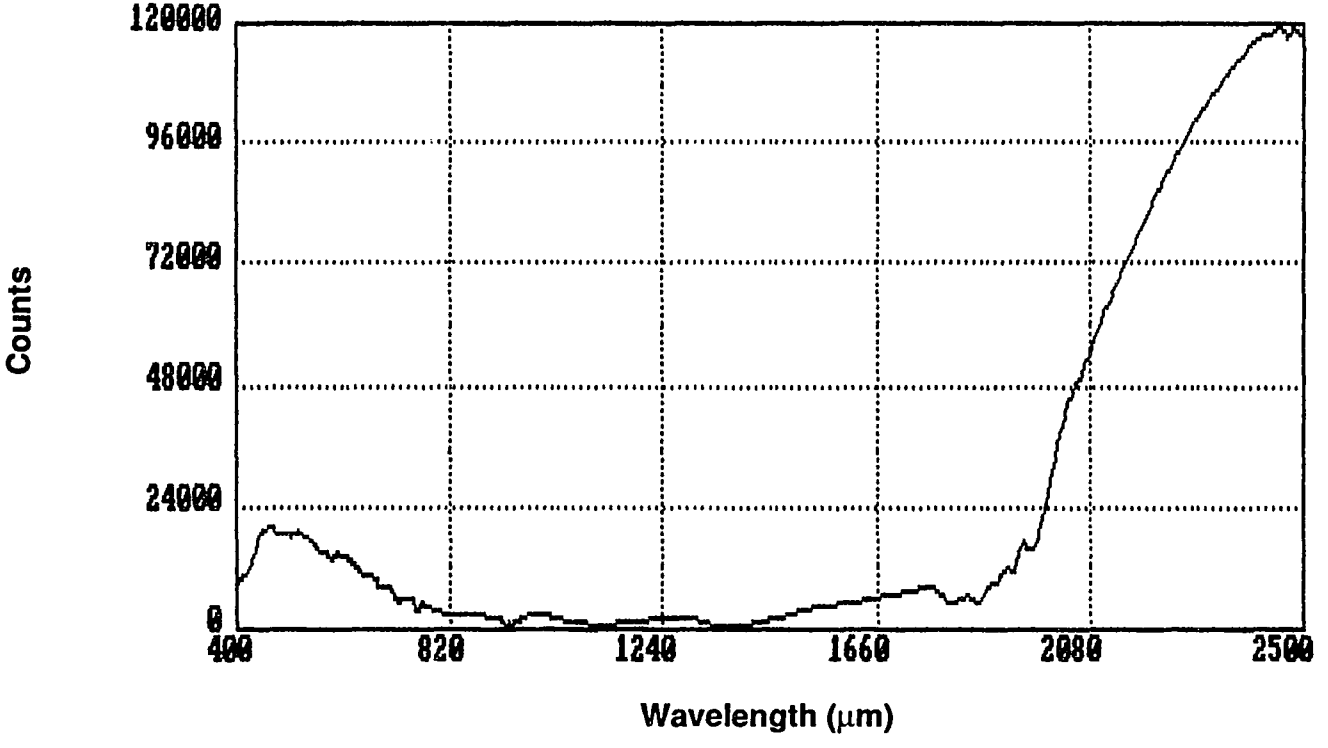

Figure 3.2. An example of Stage 3 raw data, corrected for automatic gain change, collected with the spectroradiometer at the Kupaianaha lava lake on October 12, 1987. The lake was in a quiescent state when these data were collected. Horizontal axis plots wavelength between 0.4 and 2.5 μm. Vertical axis is in number of counts, which varied for each spectrum that was collected due to the automatic gain feature of the GER spectrometer. Although data was collected to 3.0 μm, large water and carbon dioxide absorption features occupying 2.5 - 3.0 μm severely limited the usefulness of this data for this study.

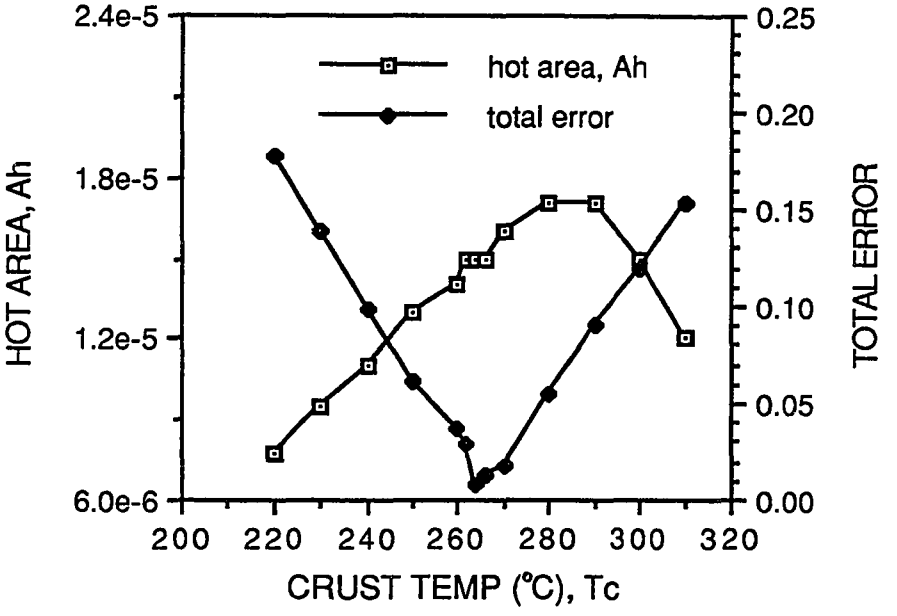

Figure 3.3. Example of the 2-component numerical model, using spectral data from Figure 3.2, with hot temperature set to 1100°C. Crust temp, T_C, refers to the background or solid crust temperature within the viewing area. Hot area, Ah, is the fraction of the viewing area radiating at the hot temperature. Total error is the sum of weighted individual flux ratio errors described above and is the criterion by which the model determines the best possible fit to the data points chosen. Note that the minimum error in the model occurs at a solid crust temperature of 264°C.

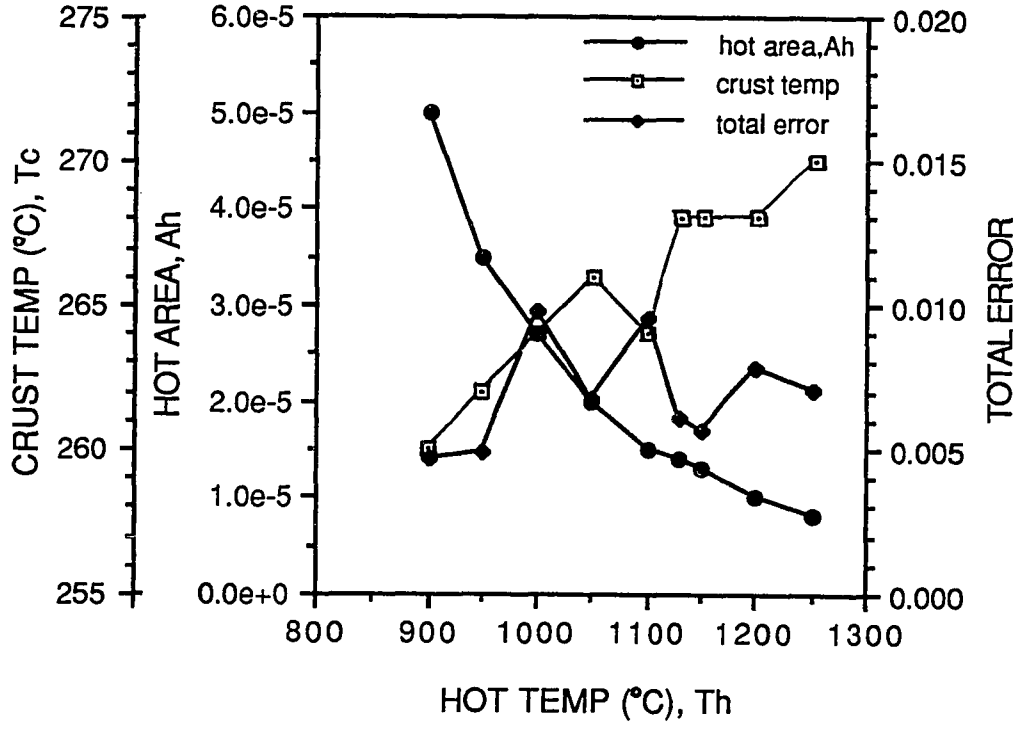

Figure 3.4. Stage 3 (Figure 3.2) 2-component model results for hot temperature starting conditions between 900 - 1250°C. Lines connecting data points illustrate trends in solutions; however, data points have only been calculated for the hot temperatures mentioned in the text. Only these data points are actual results. Hot Temp, T_h, is the temperature of magma in cracks on the viewed surface; Crust Temp, T_c, is the surface crust temperature; and Hot area, A_h, is the fraction of the viewing area that is occupied by material at T_h, with the remainder exhibiting T_c. "Total error" is the sum of the weighted differences between the data derived flux ratios and the model generated flux ratios, and measures the quality of the model fit to the spectroradiometer data.

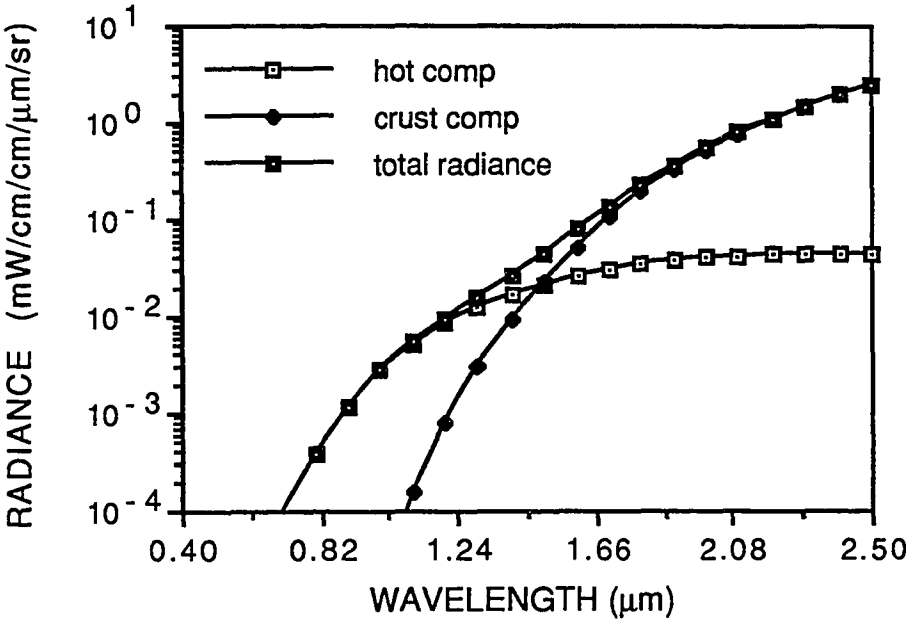

Figure 3.5. Radiance contributions of the best fit 2-component model for Figure 3.2. The hot component represents magmatic microcracks in the surface crust radiating at 900°C and occupying 0.0050% of the field of view. The crust component represents the thick surface crust radiating at 260°C occupying the remainder of the field of view. Note that the transition wavelength where the crust contributes more flux than the magmatic cracks occurs at 1.49 μm.

Figure 3.6. Stage 3 (Figure 3.2) 3-component model results for hot temperature starting conditions between 900 - 1250°C. Style of presentation of results is the same as that used in Figure 3.4. T_h, T_m, and T_c represent the temperatures of magmatic microcracks in the surface of the solid plates, of recently formed solid crust, and of older thicker crust, respectively. Hot area and Medium area identify the fractions of the measurement area exhibiting temperatures of T_h and T_m, respectively. The remainder of the measurement area radiates at temperature T_c. T_m was allowed to vary by a minimum increment of 5°C in all numerical simulations, while T_c was allowed to vary by a minimum of 2°C.

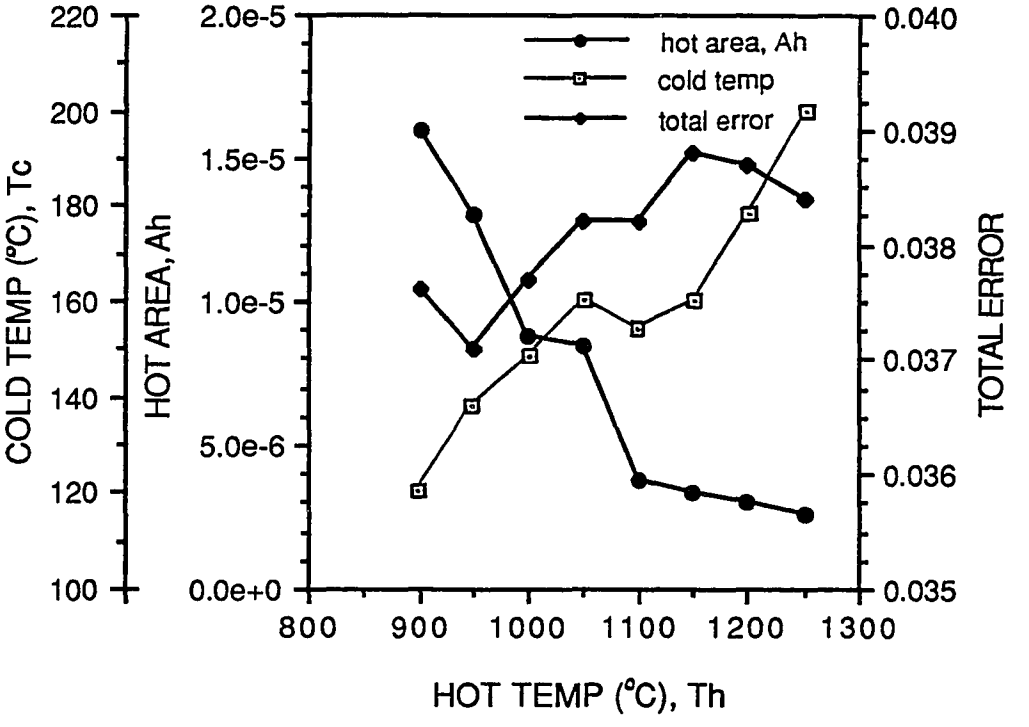
220
200
180
160
140
120
100
COLD TEMP (°C), Tc
2.0e-5
1.5e-5
1.0e-5
5.0e-6
0.0e+0
HOT AREA, Ah
0.040
0.039
0.038
0.037
0.036
0.035
TOTAL ERROR
hot area, Ah
cold temp
total error
800
900
1000
1100
1200
1300
HOT TEMP (°C), Th

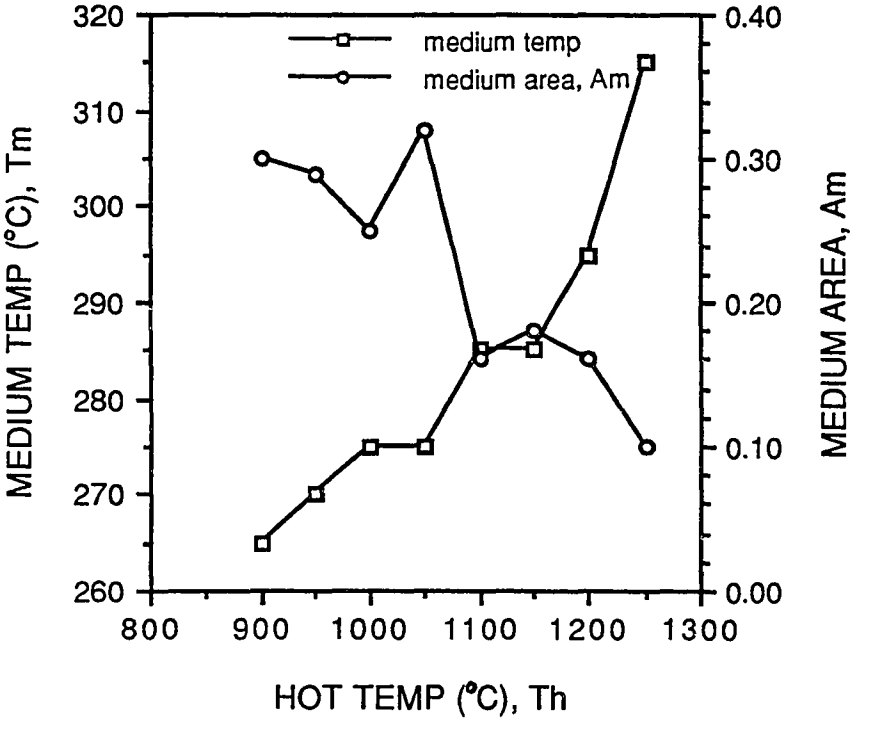
320
310
300
290
280
270
260
MEDIUM TEMP (°C), Tm
0.40
0.30
0.20
0.10
0.00
MEDIUM AREA, Am
medium temp
medium area, Am
800
900
1000
1100
1200
1300
HOT TEMP (°C), Th

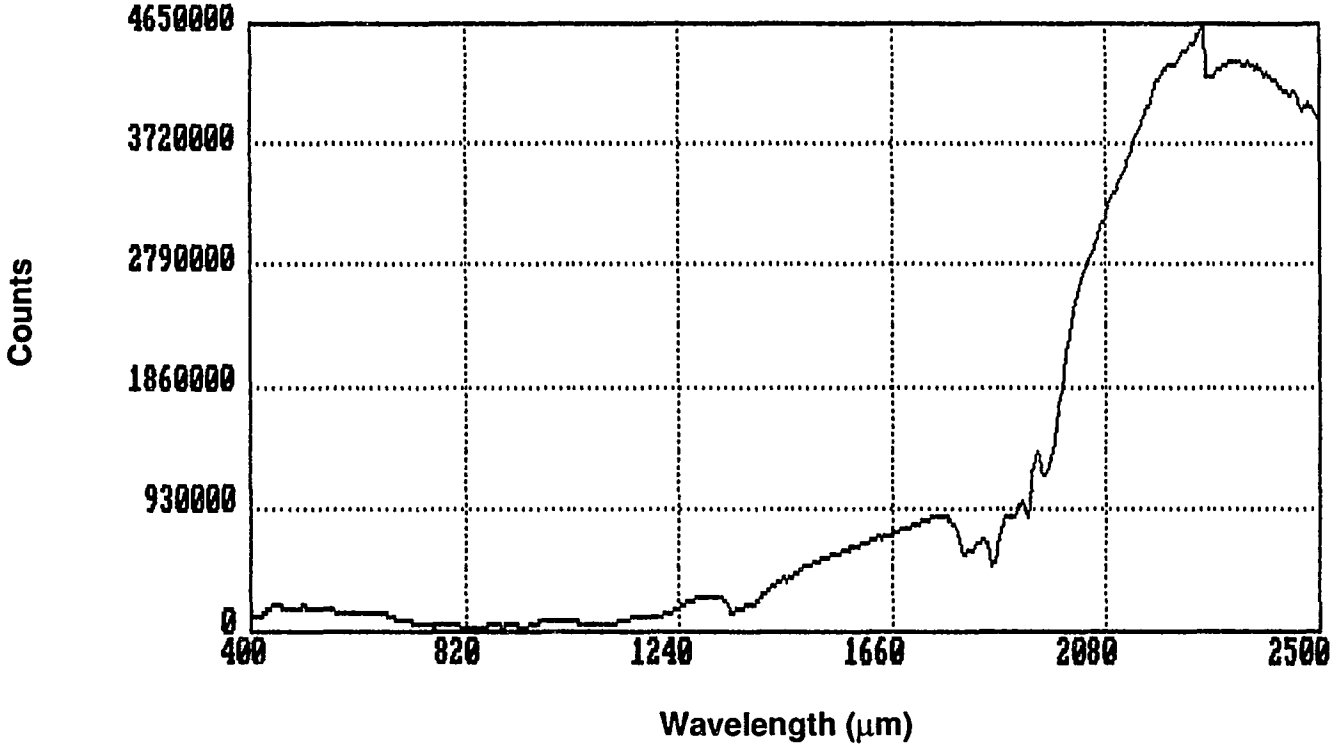

Figure 3.7. An example of Stage 2 data collected on October 12, 1987. Data format is the same as that in Figure 3.2. The horizontal axis is plotted with respect to wavelength from 0.4 - 2.5 μm, while the vertical axis is plotted in counts.

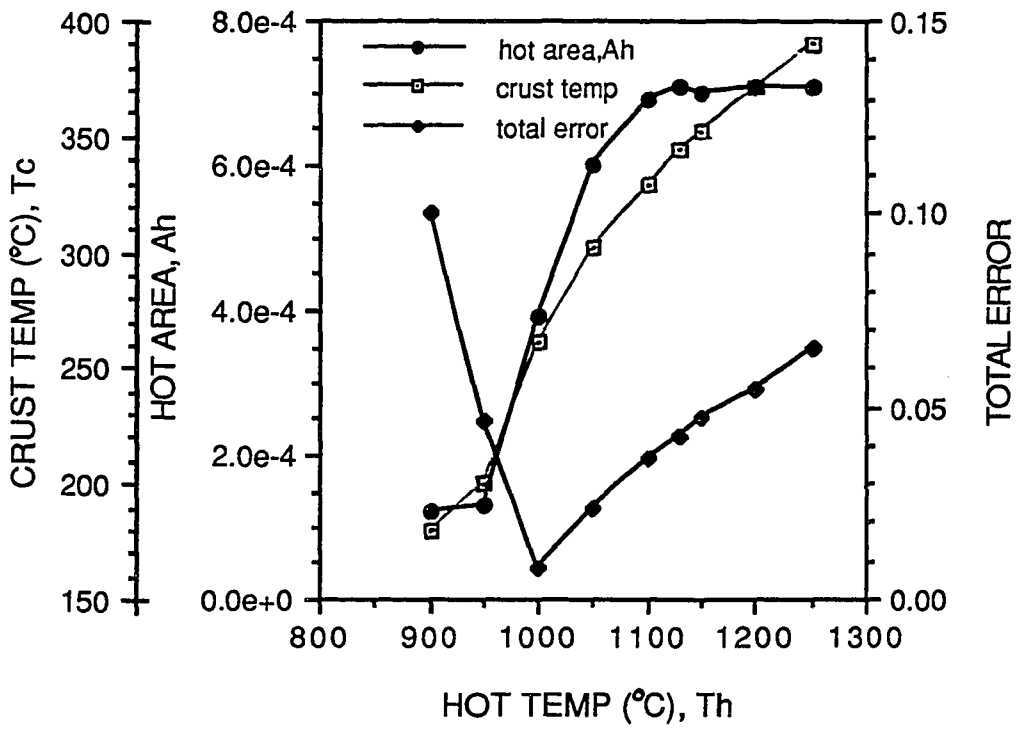

Figure 3.8. Two component temperature model for Stage 2 activity (data presented in Figure 3.7). Format for the presentation of the data is the same as Figure 3.4. Note that in this case, the minimum error occurs at a hot temperature of 1000°C.

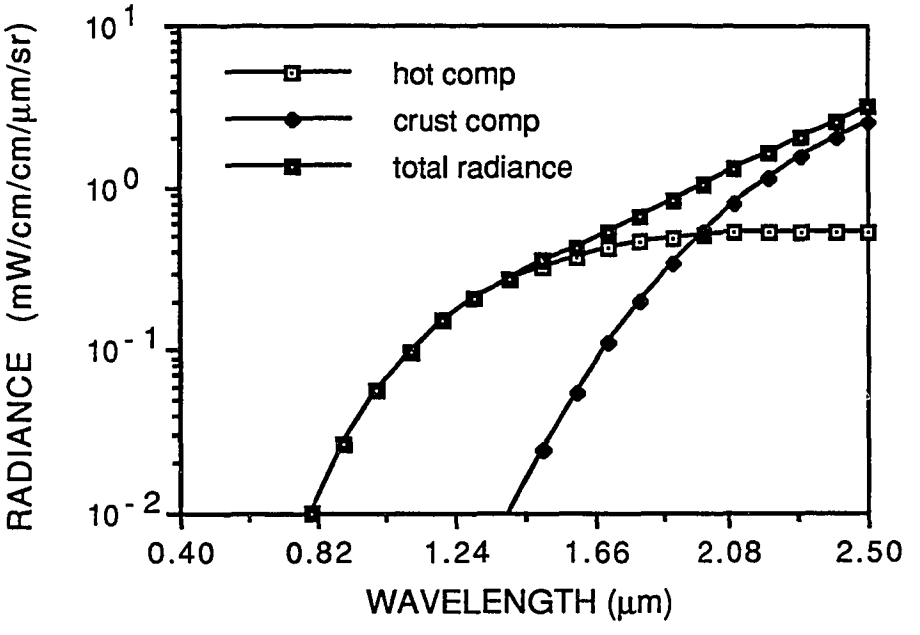

Figure 3.9. The radiance contributions of the best fit 2-component model to Figure 3.7. The hot component, T_h = 1000°C, represents the flux of the magma coming from the rifting crack. The cold component, T_c = 262°C, represents the flux from the newly formed crust near the rift. The transition wavelength (see Chapter 3, section 4.2) occurs at 1.99 μm in this example.

Figure 3.10. Stage 2 3-component temperature model for Stage 2 activity for data presented in Figure 3.7. Format for presentation is same as Figure 3.6. Note that in this case the error values were extremely high when the hot temperature was set above1000°C.

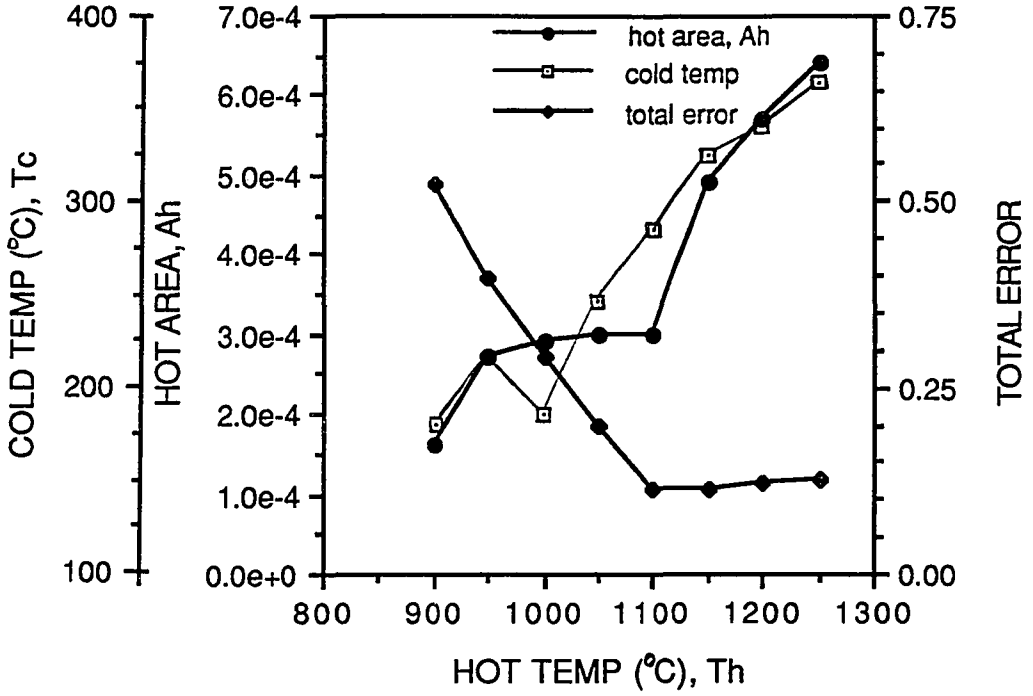
400
300
200
100
COLD TEMP (°C), Tc
7.0e-4
6.0e-4
5.0e-4
4.0e-4
3.0e-4
2.0e-4
1.0e-4
0.0e+0
HOT AREA, Ah
0.75
0.50
0.25
0.00
TOTAL ERROR
hot area, Ah
cold temp
total error
800
900
1000
1100
1200
1300
HOT TEMP (°C), Th

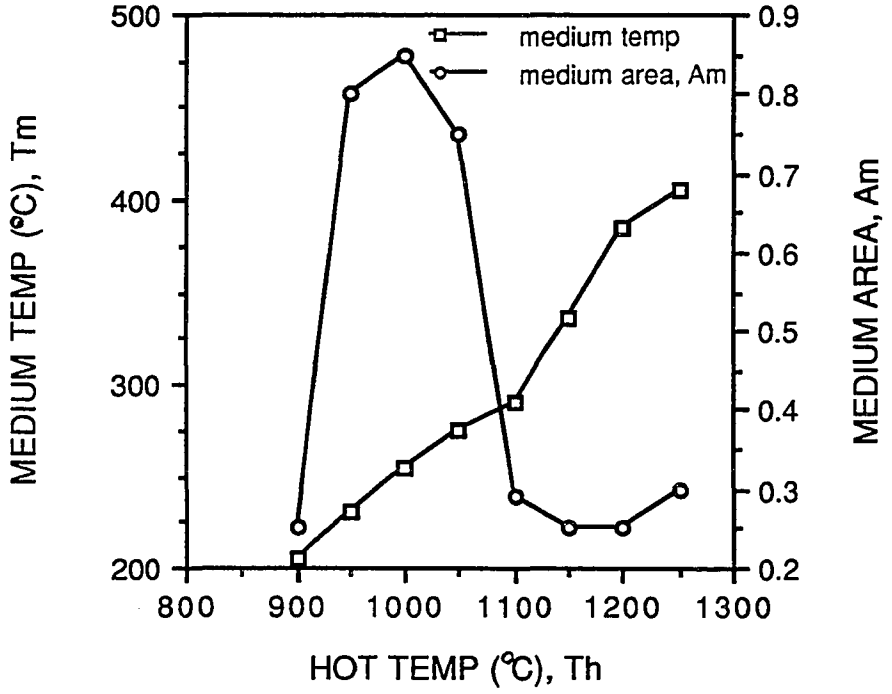
500
400
300
200
MEDIUM TEMP (°C), Tm
0.9
0.8
0.7
0.6
0.5
0.4
0.3
0.2
MEDIUM AREA, Am
medium temp
medium area, Am
800
900
1000
1100
1200
1300
HOT TEMP (°C), Th

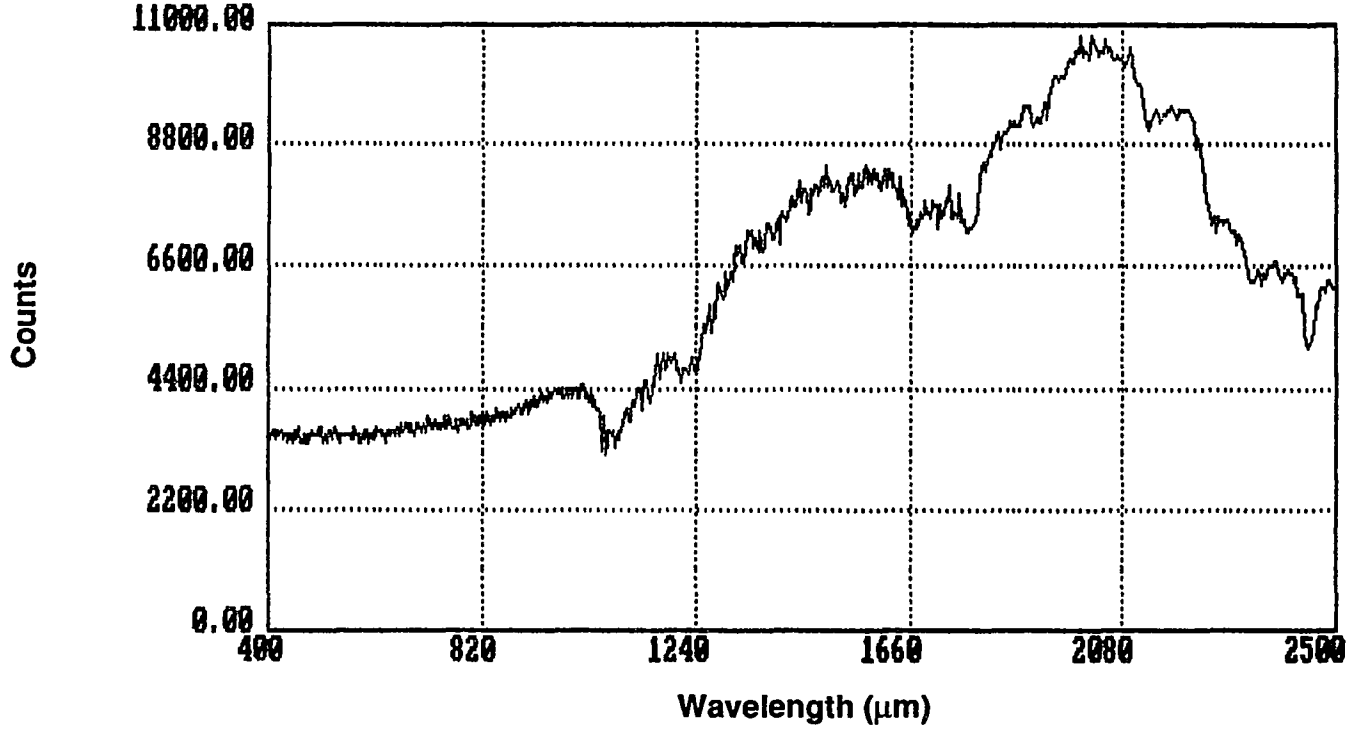

Figure 3.11. An example of a calibration spectra (for the target beam) used to correct the lava lake data for instrument response while the neutral density filter covered the entrance port of the spectroradiometer (see Chapter 3, section 3.5). The Infrared Industries blackbody simulator was set at 900°C and had an error of 0.5°C according to laboratory supplied calibrations. Data are presented in the same format as Figure 3.2. Contrast this spectrum with that of Figure 2.15, which was collected with the same operational set-up on the same day, except that the neutral density filter was removed from the target beam.

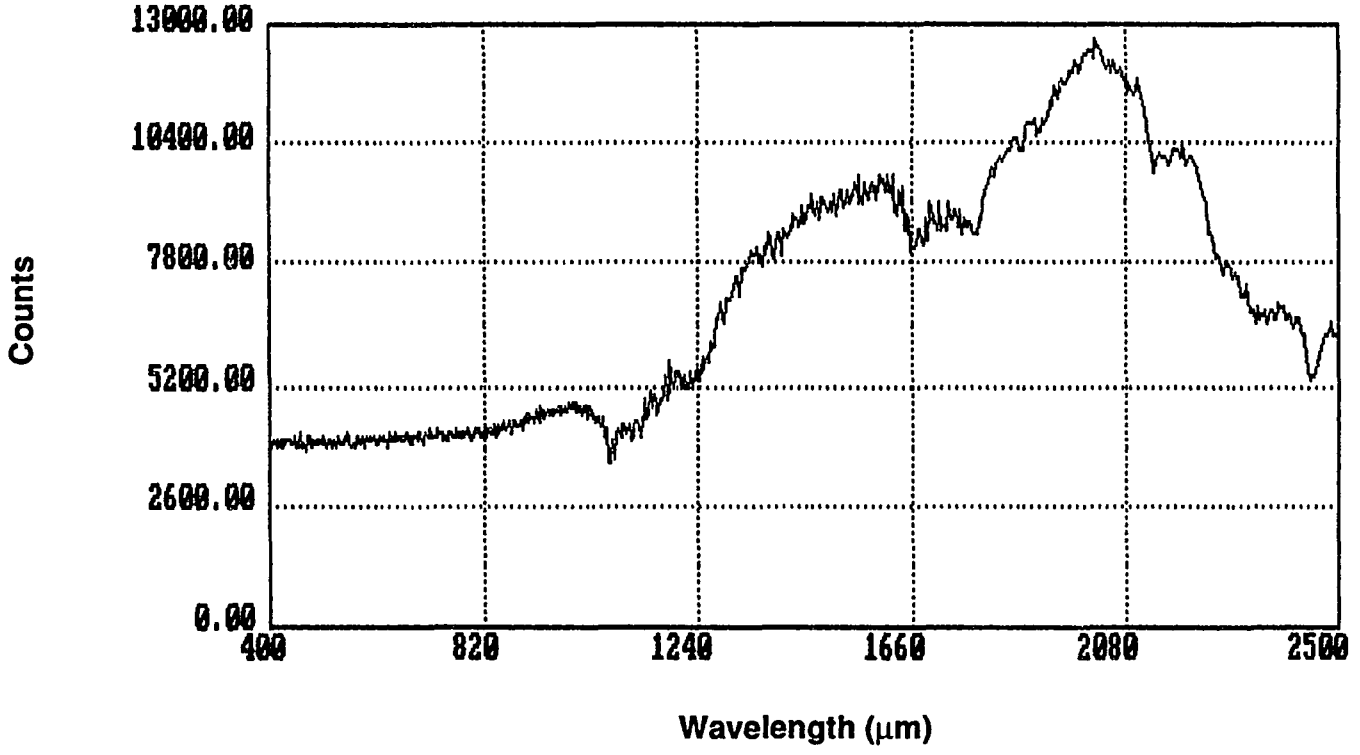

Figure 3.12. An example of a calibration spectra (for the reference beam) used to correct the lava lake data for instrument response while the neutral density filter covered the entrance port of the spectroradiometer (see Chapter 3, section 3.5). The Infrared Industries blackbody simulator was set at 900°C and had an error of 0.5°C according to laboratory supplied calibrations. Data are presented in the same format as Figure 3.2. Contrast this spectrum with that of Figure 2.16, which was collected with the same operational set-up on the same day, except that the neutral density filter was removed from the target beam.

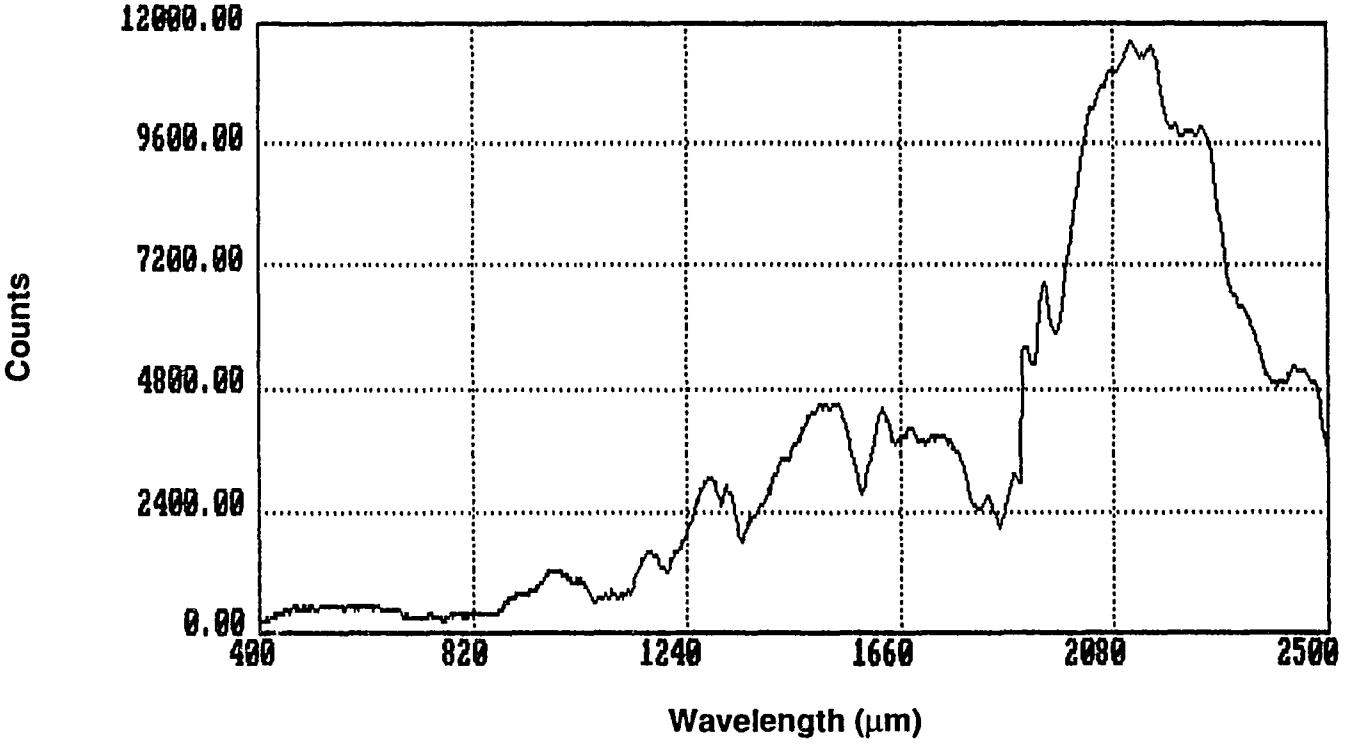

Figure 3.13. Spectrum of an example of Stage 1 activity, collected on January 23, 1988, presented in the same format as Figure 3.2. "Flickering" in the shape of the spectrum at both a small scale (a few counts) and large scale (thousands of counts) between 0.82 - 2.10 μm is interpreted to be due to temporal variations in the level of activity of the lake during the time interval that the spectrum was collected (~30 seconds).

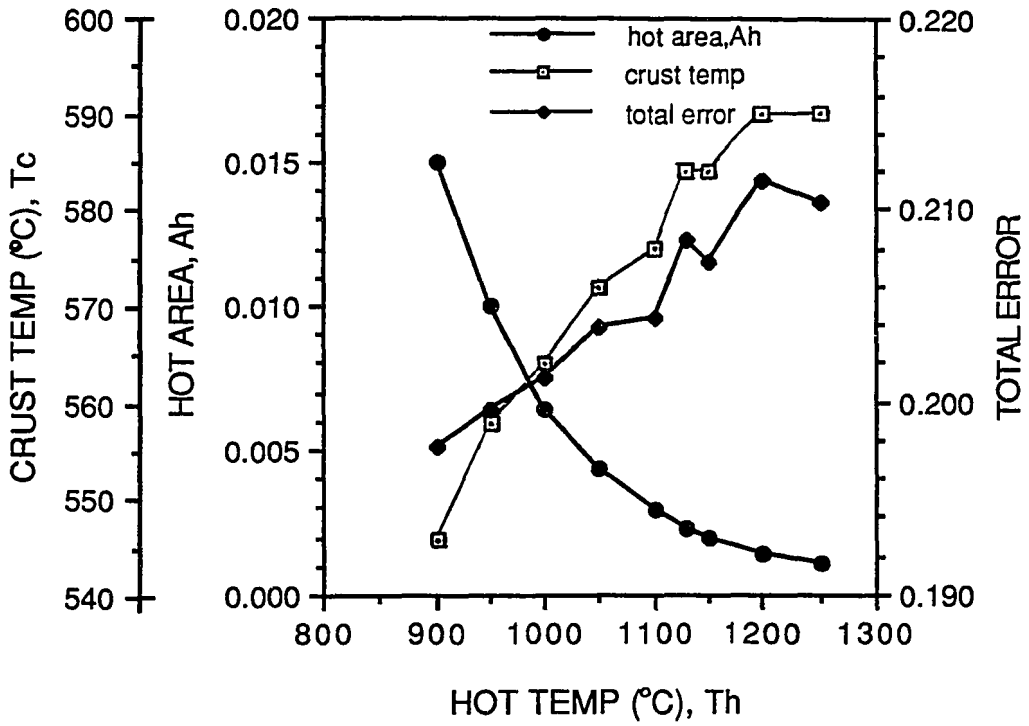

Figure 3.14. Two component temperature model for Stage 1 activity (data presented in Figure 3.13). Format for the presentation of the data is the same as Figure 3.4. Note that in this case, the error increases from a minimum at a hot temperature of 900°C.

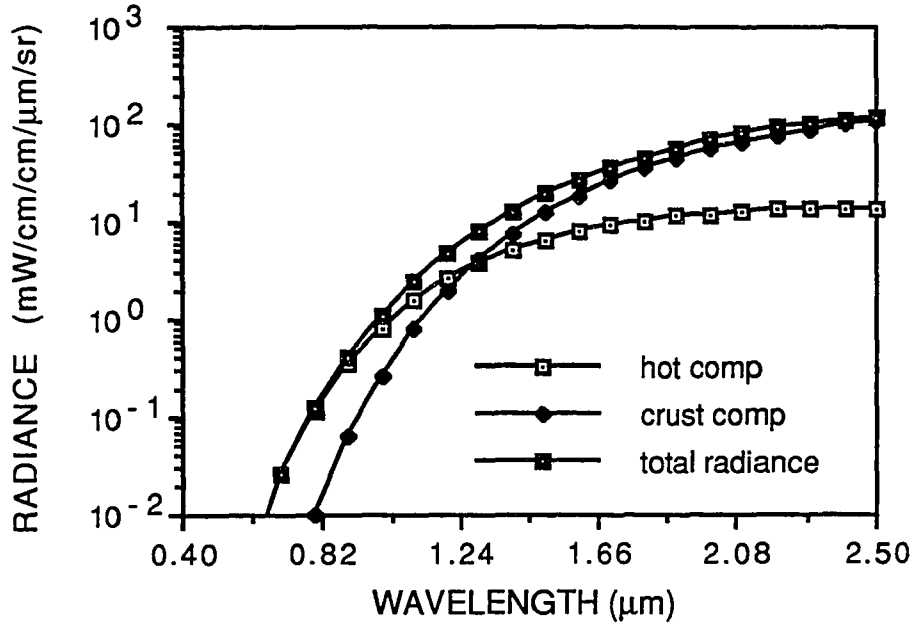

Figure 3.15. Radiance contributions of the 2-component best fit for Figure 3.13. The hot component represents the flux from erupting molten magma at 900°C occupying 1.5% of the field of view. The newly formed surface crust occupying the rest of the field of view is represented by the crust component at 546°C. The transition wavelength occurs at 1.27 µm.

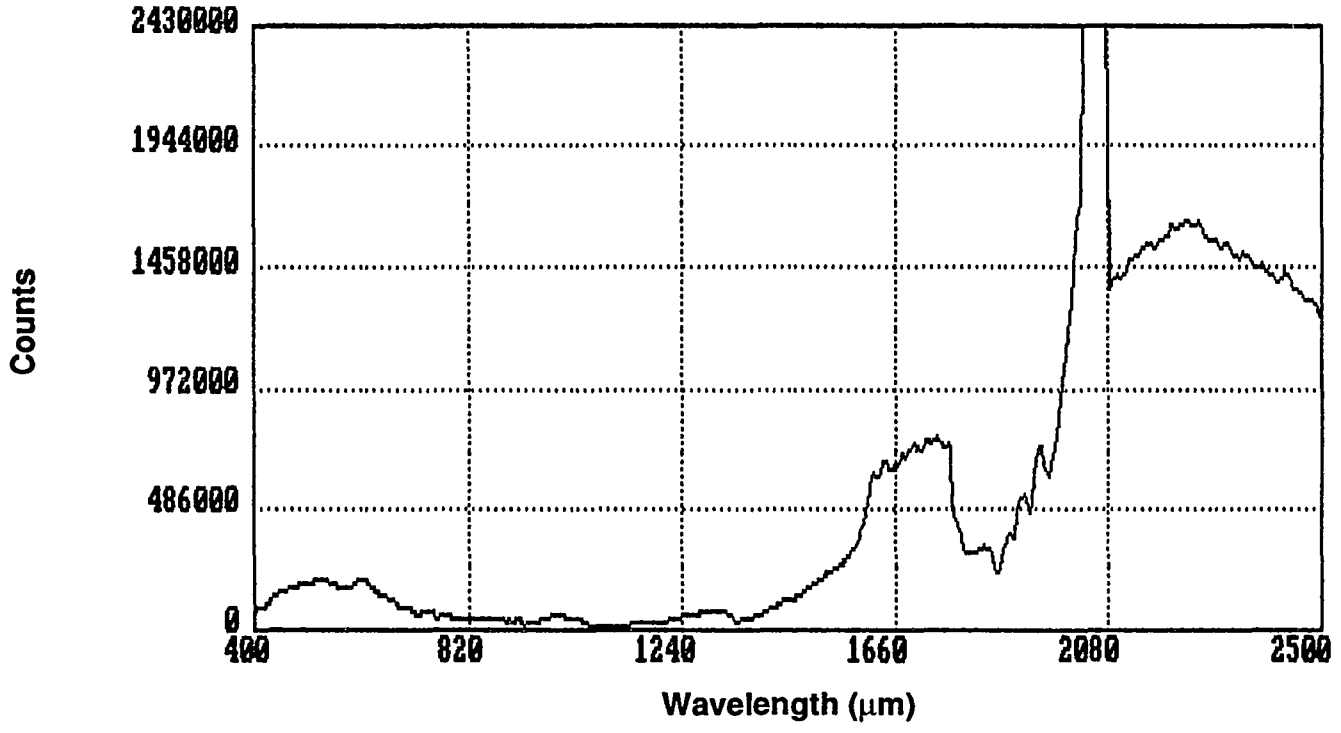

Figure 3.16. Spectrum of Stage 1 and Stage 2 activity occurring almost at the same time. The rapid increase in flux at 1.6 μm represents the arrival of an active rift (Stage 2) in the spectroradiometer's field of view. Saturation of the instrument detectors occurred at 2.00 - 2.08 μm due to an eruption of magma (Stage 1). This is an excellent example of the transient nature of Stage 1 events.

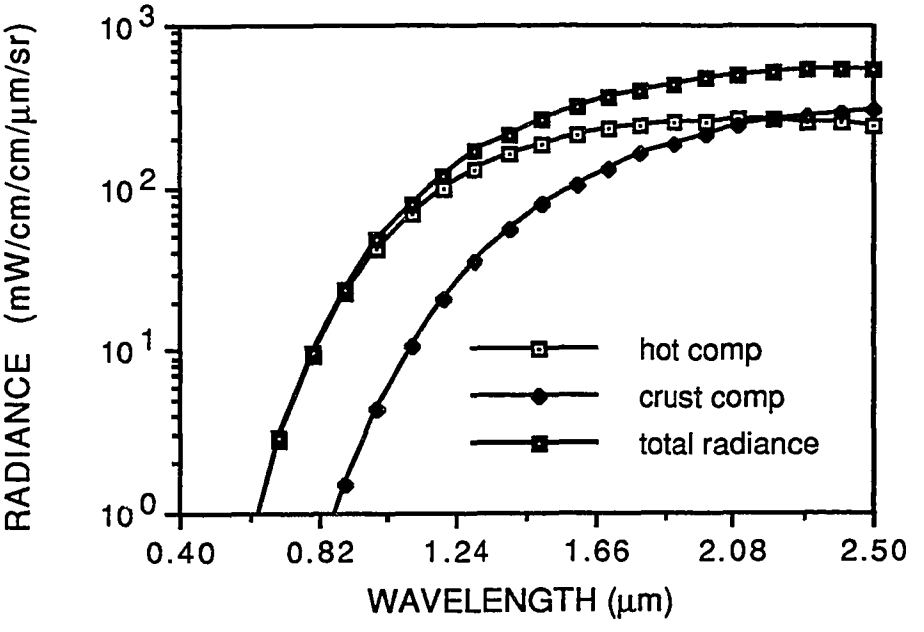

Figure 3.17. Radiative contributions of 2-component best fit for Figure 3.16. The hot component represents the flux emitted by the rift radiating at 1100°C and occupying 13% of the field of view. The flux of the newly formed crust is represented by the crust component radiating at 710°C occupying the remainder of the field of view. Due to the relatively high fraction of the hot component, the transition wavelength is at 2.2 µm.

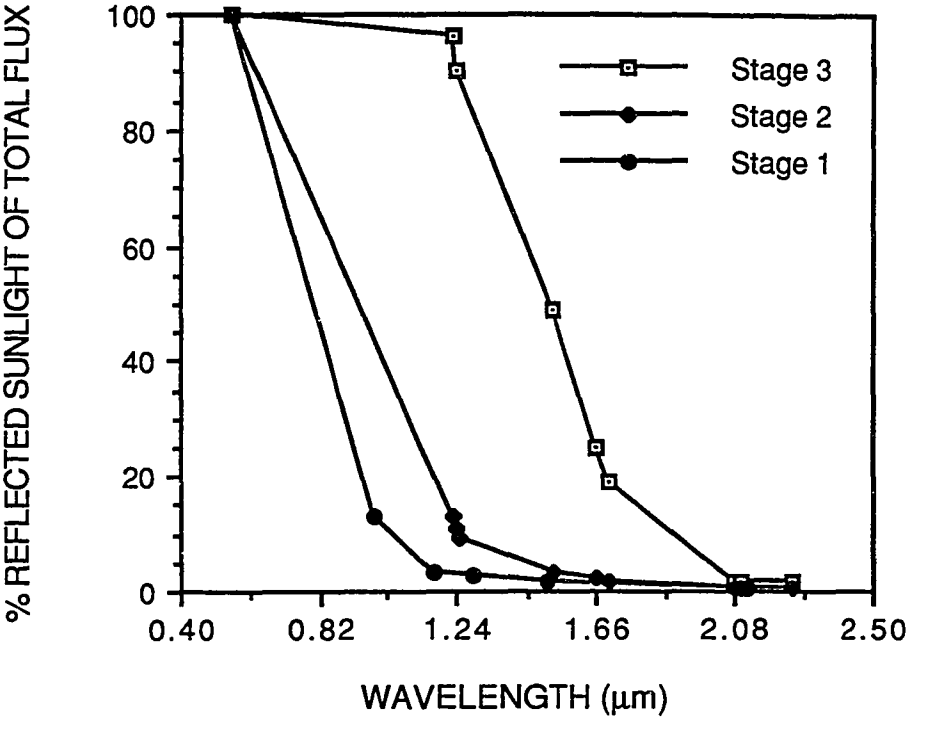

Figure 3.18. Effect of reflected sunlight on the three stages of activity present at Kupaianaha lava lake. The horizontal axis is plotted with respect to wavelength (0.4 - 2.5 μm), while the vertical axis is plotted in percent of the total measured flux which was contributed by sunlight reflecting off of the surface of the lava lake. Data points are actual amounts of reflected sunlight extracted from the spectra presented in Figures 3.2, 3.7 and 3.13.

Chapter 4: Spectral Data of Phase 50 of the Puu O'o Eruption Collected at Night

4.1 Introduction

Bearing in mind the results of the study presented in Chapters 2 and 3, namely, the overwhelming effects of reflected sunlight at less than 1.6 μm for Stage 3 activity and the very small proportion of the total field of view occupied by lava radiating at molten magma temperatures, two of my dissertation advisors (Peter Mouginis-Mark and Jonathan Gradie) and I decided that it would be very important to acquire spectral data at night. The two primary aims of this second study, which comprises Chapter 4, are to accurately determine the radiative role, if any, of the magmatic component in eruptive activity and to study the distribution of lava temperature for an active erupting area without being hampered by the reflected sunlight component in the data.

The results of the first study (Chapter 3) suggest fractional areas for the magmatic component of Stage 3 (solid crust) which were far below values (1 - 3 orders of magnitude) expected from previous studies using satellite data (e.g. Rothery et al.,1988; Glaze et al., 1989; Pieri et al., 1990; and Oppenheimer, 1991). The need for accurate ground-truth measurements of the fractional hot area (A_h) of the hot component has been recognized in theoretical models of lava flow emplacement (e.g. Crisp and Baloga, 1990) and remotely-sensed satellite observations (Rothery et al., 1988; Oppenheimer, 1991).

Previous field studies (Jones et al., 1990; Oppenheimer, 1991) of the radiative porperties of lava flows have used single wavelength band field radiometers which are unable to identify a hot fractional area for a lava crust. This is due to the lack of multiple spectral channels per measurement, which allows the determination of only a

single brightness temperature for the instrument's field of view. The brightness temperature is the equivalent of reporting a pixel-integrated temperature for radiant pixel in satellite data. The actual temperature of the lava crust in both cases is lower than the pixel-integrated temperature and can be much lower if the fractional area of the hot cracks are significant (Oppenheimer, 1991). In addition to this, since the total energy emitted by the surface depends on T^4 (Glaze et al., 1989), it is very important to be able to accurately identify the crust temperature of lava flows in order to be able to study changes in the radiative energy output of the flow with time. In this Chapter, I use hyperspectral data to measure the cooling rate of a lava flow at night. I do this by studying the temporal change in radiant energy, radiative crust temperature, and fractional area of the hot component. An important component of this chapter is the analysis of nighttime spectral data.

4.2 Field Area and Experiment Description

The original targets of this study were to have been the numerous easily-accessed flows from phase 49 of the Puu O'o/Kupaianaha eruption which were advancing over the Pali and onto the plain east of the Royal Gardens subdivision. Unfortunately, by the time this study got off the ground in early November, 1991, the activity on the lower slopes of Kilauea had ceased. However, reports by geologists from the Hawaii Volcano Observatory claimed that there was volcanic activity in the form of an active lava lake in Puu O'o crater.

On November 13, 1991, Jonathan Gradie, Harold Garbeil, Peter Mouginis-Mark, and myself headed to the Kilauea with the intent of acquiring nighttime spectra of the activity in Puu O'o crater. Unfortunately, the attempt at data acquisition on this date was

unsuccessful. After an arduous midday trek through the rainforest from Glenwood to a position about 1.5 km north of Puu O'o, it became readily apparent by the reddish glow east of our position in the fading light of the afternoon that an eruption of fairly large size was taking place between Puu O'o and Kupaianaha. Puu O'o was covered with a thick haze that would have made hiking treacherous and spectral observations impossible. An aborted (read: painful) attempt was made to cross ~2 km of aa, which would have made an incredible roughometer data set, but, with light fading fast, it was decided that for safety reasons, that we should return the way that we had come. What we had seen on the horizon was the last major outburst of phase 49 of the Puu O'o eruption.

After a bit of a recovery period for all of the particpants of the first trip, a second trip to study lava flows at night was planned for the first week of February, 1992. Unfortunately, at this time there was not much activity on Kilauea, and plans for a trip had to be postponed until the third week in February. The day before (February 18, 1992) the next expedition to Puu O'o was to set out, I contacted Frank Trusdell of the Hawaii Volcano Observatory who had been communicating with Peter Mouginis-Mark about the activity on Kilauea. Thanks to Frank, I learned that a 150 m east - west fissure had opened up on the west side of Puu O'o and was disgorging magma at the rate of approximately 1.2 - 1.5 million cubic meters per day. Surface flows were reportedly forming in an area west of the eruption site. In the early afternoon of February 19, 1992, an expedition of Peter Mouginis-Mark, Harold Garbeil, Henning Haack, Marc Norman, two geologists from the Hawaii Volcano Observatory, and myself set out from the Mauna Ulu trail on the Chain of Craters Road to collect spectral measurements of phase 50 of the Puu O'o eruption. When we arrived at the eruption site (just uprift of the Puu O'o cone, close to the August 1985 eruption site), we discovered that the rift

eruption was feeding an area of active flows west of Puu O'o cone that was approximately 1 km x 1 km in size (Figure 4.1, see Figure 2.2 for the location of Puu O'o on the East Rift Zone of Kilauea).

As the first field site for the spectroradiometer, we selected a 15 m high nob on the west side of Puu O'o. It provided an excellent site to make spectral measurements of a 20 m wide x 60 m long lava channel in which magma with a partially solidified crust was moving at approximately 2 m/s away from the spectroradiometer (Figure 4.2). The 1.5° x 3.0° projected area of the target and reference beams of the spectroradiometer on the lava channel surface was approximately 18 m^2 because the instrument was located 60 m from the activty and the declination angle of the optical head was only 15° from the horizontal. Unfortunately, this was the best operational set-up that could be managed because the steep slopes of Puu O'o made deployment of the instrument hazardous. I attempted to collect 20 spectral pairs of various areas within the lava channel between 18:30 and 19:30 HST after the sun set behind Mauna Loa. A ten-minute video record and numerous photographs by Peter Mougins-Mark, Henning Haack, and Marc Norman were collected while spectra were being acquired. At 18:41 HST, after 6 spectral pairs had been acquired (some of which are the subject of section 4.3.3), the spectroradiometer detectors became saturated with radiance from the lava channel on every attempt to make a measurement between that time and 19:30 HST. Inspection of photographs taken by Henning Haack show that the activty in the channel became much more turbulent with time. The emitted radiance from exposed, fresh magma is much greater than that of lava crust, which is the reason that the detectors saturated. Since I was no longer collecting any useful data with the spectroradiometer, and the real purpose of the expedition had

been surface flows, I decided to move the spectroradiometer to a location which would permit observations of cooling flows.

The second site of spectral measurements was located 1 km southwest of the active rift on a wide, flat plate of recently-cooled lava (It was still hot to sit on, and a crack toasted a sandwich in my pack!) about 20 m away from a 3 m high, steep (~80°), magma-covered slope. This slope faced toward the spectroradiometer (Figure 4.3), resulting in a beam size of ~0.55 m^2. What was important about the geometry of this site was that lava flows cascading over the edge of the slope presented a small-scale analog for satellite observations, since the horizontally pointed spectroradiometer and the near vertical slope combined to simulate near "nadir" viewing for this study. Sixty-five spectral pairs (a total of 130 spectra) were collected at this location during the hours of 20:40 - 23:00 HST. Concurrent with these measurements, a video record and a photo record (1 photo taken by Peter Mouginis-Mark about every minute) were obtained for the spectral targets. Spectral observations were made for a variety of flow activities including long term (~ 1 hour between pulses of new batches of magma) records of solidifying flow lobes, small active flow channels, and glowing cracks in older flows. The former of these is the subject of section 4.3.2.

4.3 Model Results for Spectral Data Collected During the Phase 50 Puu O'o Eruption

The purpose of this section is to present two kinds of spectra, which were collected at the Puu O'o Phase 50 rift eruption during the evening of February 19, 1992. These spectra are very important in that (to my knowledge) they represent the only hyperspectral ground-truth data set collected at night to date. The value of this data set can not be adequately stressed since it is the only ground-truth data which can

unequivocally show the radiant contribution of the hot component to the total flux of a volcanic thermal anomaly in the 0.4 - 2.5 μm range. This range of wavelengths is of particular value to Landsat TM studies (e.g. Oppenheimer, 1991) since it covers the spectral range of bands 1 - 5 and 7. The data set is also invaluable as input to 2-component numerical models of lava flow emplacement (e.g. Crisp and Baloga, 1990) since it is the only ground-based hyperspectral data set available that can accurately determine the fractional hot areas of the core component without contamination by radiance from reflected sunlight. For comparative purposes with satellite results, I use the two-component model detailed in Chapter 3, section 2.1 to generate temperatures and areas of anomalies.

I will start by comparing the features (or lack of features) in the nighttime spectral data versus that for daylight measurements presented in Chapter 3. Next, I present a series of 13 spectra collected of a cooling lava surface over the time span of 59 minutes. As a result of the high quality of the spectral data, I am able to accurately show temporal variations in the temperature of the solid crust, the area of the hot component, and perhaps most importantly, the emitted energy of the cooling flow. Finally, I present spectral data collected of the vigorously active lava channel, which gave the highest crust and fractional hot areas observed in either of the two data sets presented in Chapters 3 and 4. The spectra are also unique in that they show the distribution of radiance with wavelength of an anomaly having a high fractional hot area.

4.3.1 A comparison of daytime versus nighttime spectral features

The differences between spectra of solidfied lava crusts collected with and without the presence of sunlight are easily recognized. Figure 4.4 is a spectrum of Stage 3

activity (solid crust) taken at the Kupaianaha lava lake on 10/12/87 at 13:57:40 HST while there were no clouds obscuring the sun. As I have pointed out in Chapter 2 section 6, the radiance from sunlight reflecting off of the surface of the lava lake is apparent by the curve having a peak at about 0.55 μm. The radiative component resulting from the thermally emitting lava lake surface did not begin to become significant until 1.24 μm and not obvious until about 1.5 μm. I compare this spectrum with the spectrum of a cooling lava surface acquired at our second site (1 km west of Puu O'o cone) at night (Figure 4.5). The differences are immediately noticeable. In the nighttime spectrum there is no reflected sunlight peak at 0.55 μm, nor are there any minor solar peaks at ~1.0 μm as there are in Figure 4.4.

The only radiance which was measured in the nighttime spectra were thermal contributions from the hot volcanic surfaces in the field of view of the spectroradiometer. Data reduction was greatly facilitated with nighttime data. Chapter 2 section 6 lists the corrections and approximations which were necessary to remove the solar component from the lava lake spectra. The solar spectrum was obviously not a problem when data were collected at night. The only correction which had to be done for the nighttime spectra was to correct for the instrument response of the spectroradiometer. The only features of Figure 4.5 and the rest of the nighttime spectra are features due to absorptions by atmospheric constituents. Since I use data in atmospheric windows for calculations of temperature and area, this does not present a problem. Figure 4.5 and the rest of the nighttime spectra are very important because they show the distribution of radiance with wavelength in the absence of radiative contamination from sunlight. I did not have to be concerned whether or not half of the

radiance at 1.66 μm was from solar contamination as I did with data such as that presented in Figure 4.4 (see also the discussion in Chapter 3, section 4.3).

4.3.2 Temporal cooling measurements of lava flows

A total of 25 spectral pairs were collected during a 59-minute period between successive flows of fresh lava over an area (Figure 4.6) on the slope which was 20 m away from the spectroradiometer. Figure 4.6 is a chronological sequence of photographs recording the emplacement of the lava flow which is the subject of this study. Of these 25, 13 were chosen to represent the cooling of the lava surface. An example spectrum, collected at 21:27 HST, is given in Figure 4.7. The shape of the spectral curve suggests that a very hot anomaly occupied the target beam because the radiance in the 1.5 - 1.7 μm atmospheric window is elevated. This spectrum shows that thermal flux was detectable by the spectroradiometer at 0.9 μm. The rapid increase in flux in the 1.20 - 1.27 μm range also suggests that the hot component in the target beam was much larger than those observed for Stage 3 activity at Kupaianaha (for example, Figure 4.4). Using the model that I developed in Chapter 3, the 2-component best fit results (Figure 4.8) for this spectrum (Figure 4.5) are plotted for hot component temperatures between 900 and 1250°C (at 50°C intervals). The best fit results were typical for those calculated for the other 12 spectra in the series in that the crust temperature varied by more than 50°C over the temperatures chosen to represent the hot component. This result shows that the radiance contributed by the hot component was a sizeable part of the total spectral radiance at the wavelengths (1.53, 1.70, 2.08, and 2.25 μm) chosen to represent the spectrum in the 2-component model. A best fit having a hot component temperature of 1150°C, a crust temperature of 768°C, and a hot fractional radiating

area, A_h, of 3.6×10^{-2} of the total area measured was returned by the 2-component model.

Before I present the set of 13 spectra as a whole, as a means of comparison, I would also like to show a spectrum (Figure 4.9) taken of the same target 32 minutes after Figure 4.7. The differences between the two spectra are entirely the result of a decrease in emitted radiance due to the cooling of the lava surface. Becasue the spectral data were collected at night and the instrument response was constant for all of the collected spectra, I can extract qualitative information by looking at the shape of the spectral curve. Figure 4.9 suggests that a cooler crust occupied the target beam than that of Figure 4.7 because the large peak in radiance, which increases tremendously after 2.0 μm in both cases, is shifted more toward the infrared in Figure 4.9 than in Figure 4.7. Hotter crusts shift this curve towards the visible region of the spectrum, while cooler crusts shift the peak toward the infrared. Another feature to look for which gives a qualitative idea of the magnitude of the hot component is the size of the spectral response in the 1.24 - 1.70 μm region relative to the large peak which occurs after 2.0 μm. A quick look at Figure 4.7 shows that the spectral response at 1.66 μm is about 25% of the peak radiance measured at about 2.15 μm. On the other hand, Figure 4.9 shows that the radiance at 1.66 μm is 20% of that measured at 2.3 μm where the peak occurs. Since the spectral radiance at 1.66 μm is less (relative to that after 2.0 μm) for Figure 4.9, I know that either the hot fractional area is smaller or that the radiating temperature of the hot component is lower than that of the surface represented in Figure 4.7. These qualitative approximations could not be attempted with any reasonable accuracy for spectra acquired in daylight because of the variable and sometimes

dominant effect that the reflected sunlight component has at wavelengths of less than 1.66 μm.

The qualitative conclusions that I pointed out above for the shapes of the spectra are borne out in Figure 4.10, which gives the 2-component best fit results for Figure 4.9. I would note again that the temperature of the crust component varies by 28°C over the range of hot component temperatures which suggests that the radiance from the hot component was significant. The best fit hot component temperature in this example was 950°C. The hot fractional area of Figure 4.9 is 39% of the size of the best fit hot fractional area for Figure 4.7. The best fit crust temperature of Figure 4.9 is 224°C cooler than that of Figure 4.7.

The best fit results for the 13 spectral examples, along with the times when the spectra were collected, are listed in Table 4.1. A gap in the collection of spectra of 20 minutes occurred between the acquisition of the first spectrum and that of the second, because spectral data were being collected of other targets during this time period. Almost all of the best fit results, with the exception of the first, fourth and seventh examples in the series, occurred for hot component temperatures of 900 or 950°C. It is interesting to note that examples 2 - 6 did not show any significant cooling over the 5 minutes that they were collected. This means that the radiance of the surface did not change appreciably as one would expect for a cooling lava flow. One of the possible explanations for the lack of cooling could be that the flow was in a state of dynamic thermal equilibrium, because the flow may have been filling with magma as the surface radiated heat. This kind of action in which the cooling lava flow fills with magma is the same type of action ("lava inflation") suggested by Hon and Kauahikaua (1991) for Kilauea flows and by Self et al. (1991) for the Columbia River Flood Basalt, but here I

witnesed the activity on a much more limited scale. I also noted periods of activity when a thin layer (~10 - 20 cm) of crust would slough off leaving very hot (glowing) core material exposed (over 3 - 5 m in width and ~ 2 m in height).

Figure 4.11 is a plot of the temporal variation of the fractional hot component area and the solid crust temperature of the cooling lava flow. Figure 4.11 shows that both crust temperature and hot fractional area generally decrease over the 59 minutes that spectra were acquired. Note that with the arrival of the next flow crossing part of the field of view at ~54 minutes, the crust temperature increases by 104°C. At 59 minutes, the hot fractional area increases 5-fold from the previous datum, but the crust temperature is less than that derived for the spectrum collected at 52 minutes, which again suggests that the new flow did not completely occupy the filed of view or else these radiative values would be consistent with those modeled for the first spectrum of the series at T=0 minutes.

As a final note, the radiative temperatures identified with the 2-component model for the cooling lava flow in this study are at least 100°C hotter and have hot fractional areas 100 times greater than those derived for Stage 3 crusts of the active Kupaianaha lava lake (Chapter 3). Surface crust temperatures for the Kupaianaha lava lake which were measured with the spectroradiometer minutes after being erupted from rifts were still, on average, at least 100°C cooler than the crust temperatures derived for the cooling flow in this chapter. Since the lava lake crusts were forming on, literally, a lake of magma, I interpret the hot crust temperatures and fractionally large hot component areas to be a sign that the cooling flow was actually being heated from within, perhaps by magma injection.

4.3.3 Spectral observations of the lava channel

Theoretical 2-component models of lava flow emplacement (Crisp and Baloga, 1990) and satellite studies of lava flows (Pieri et al., 1990; and Oppenheimer, 1991) require information from field studies to provide radiative ground-truth measurements of active volcanic areas. My objective in this section was to measure the radiative temperatures and areas of a very hot volcanic target to provide a hot end-member estimate for these studies, as well as providing data to be compared with the results obtained for Stage 1 activity in Chapter 3.

The first location of the field spectroradiometer was on a 15 m high hill overlooking the phase 50 eruption. A 100 m long fissure which was fountaining magma to a height of 3 - 5 m fed a channel of magma which was ~20 m wide by 60 m long. About 5 - 10 m from the active fountaining a solidifying lava crust was already visible on the surface of a turbulent, overturning river of magma (Figure 4.2). The thin crust covered about 5 - 10 m of the center of the flow and looked like rope coiled together on the surface of the moving magma. I held little hope that the spectroradiometer would actually collect a spectral measurement without saturating the detectors.

Of the 20 attempts to collect spectra of the lava channel (between 18:30 and 19:30 HST), only 6 pairs were successfully acquired. Many times, especially after 19:14 HST on February 19, 1992, the instrument detectors became saturated. Peter Mouginis-Mark had thought that it would have been beneficial to have a series of spectral measurements along the flow channel, but unfortunately, this was impossible because the detector saturation. As I mentioned earlier, upon examining photographs taken of the channel by Henning Haack, it became apparent that the magma in the channel had become more turbulent, perhaps as a result of an increase in the eruption rate from

the vent. In any case, the character of the surface changed and prevented further measurements from being taken.

The lava channel was centered in the target beam of the spectroradiometer with the reference beam covering an area near the channel boundary. In Figure 4.2, the target beam measured a surface in the center of the channel on the boundary between the crusted and incandescent parts. A sample of one of the target beam spectra is given in Figure 4.12. The acquired spectrum suggests a lava surface which is very hot, since the radiance peak after 2.0 μm (in this case, ~2.09 μm) is shifted toward the visible wavelengths. The fractional hot area or the hot component temperature must also be very great, since the flux in the 1.5 - 1.7 μm window is very large. The 2-component best fits for hot component temperatures of 1000 - 1250°C all resulted in crust temperatures of ~970°C, with the hot fractional area decreasing as the hot component temperature was set to the higher values. The best fit for the spectrum presented in Figure 4.12 was a hot component having a temperature of 1100°C and a fractional area of 0.10 of the total pixel, and a surface crust temperature of 970°C. However, model fits for hot component temperatures of ≥ 1000°C had total errors within 3 % of the best fit error. The fractional hot area and the surface crust temperature are among the most elevated radiance values measured with the spectroradiometer of any volcanic thermal anomaly in this dissertation. The crust temperature is so high that it dominates emitted radiance after 0.5 μm. The radiance emitted by the hot component is one-tenth that of the crust component at 2.5 μm. The results presented above are consistent with other measurements made with the target beam of the center of the lava channel. For instance, a spectrum collected 2 minutes previous to Figure 4.12 yielded a best fit hot fractional area of 0.16, a crust temperature of 900°C, and a hot component temperature of

1100°C. However, the same conclusion cannot be reached for spectra acquired at the same time centered 6 m away from the center of the target beam. The reference beam spectrum, collected at the same time as that in Figure 4.12, is presented in Figure 4.13. The surface covered by the reference beam included the dark strip of fresh crust running parallel to the channel boundary and furthest from the spectroradiometer as seen in Figure 4.2. The reference spectrum contains a cooler surface and a smaller fractional hot area than the target spectrum because the large peak after 2.0 μm is shifted further toward the infrared signifying cooler crust temperatures. The emitted thermal radiance from 1.2 - 1.7 μm is smaller in the reference spectrum than in the target spectrum, which means it has a smaller hot radiative component. Figure 4.14 presents the 2-component best fit results for Figure 4.13 which confirms my qualitative analysis of the two spectra. The best fit for the reference beam was a hot fractional area of 9.6 x 10^{-3} radiating at 1200°C, and a crust temperature of 610°C. The reasons for the great difference between the results for the target and reference beam measurements of the lava channel, which were consistent for all spectral pairs, is the subject of section 4.4.1 below.

The temperatures and hot fractional areas measured with the spectroradiometer of the lava channel were some of the highest measured in the entire dissertation and provide important estimates of the characteristics of lava channels. Hot fractional areas of the surface are greater than 10% of the total surface area measured. The surface crust, which only formed 2 - 6 seconds before passing through the area within the target beam, had already cooled to ~970°C which suggests that a very fresh thin crust had formed on the surface of the channel. Difficulty with the acquisition of spectra after 19:14 HST implies that the surface characteristics of the lava channel had changed.

Since the area that I measured was approximately in a dynamic equilibrium (there were no sudden peaks in the acquired spectra as there were for Stage 1 activity in Chapter 3), I can assume that the change in the radiative character of the surface could have been a result of an increase in the eruption rate of the rift with the resultant decrease in the rate of cooling of magma at our observation site.

4.4 Discussion

I will present a series of discussions on the important points which can be gained from the spectral data collected on February 19, 1992 and presented in the section (4.3) above. I discuss some of the problems associated with the acquisition of the lava channel measurements because of the shallow (with respect to the horizontal) angle that the optical head was depressed at to collect the spectra. Next, I would like to present a study of the changes in radiant energy of the crust and hot components for the 13 spectra collected of the cooling lava flow.

4.4.1 Spectral measurements at high incidence angles

Some of the best fit results which were presented in section 4.3.3 of the lava channel of the phase 50 eruption seem, at first, to be rather low estimates when compared to the activity that our field party observed on the ground (Figure 4.2). Since there was no reflected sunlight component in the data, and thus, there was no incorrect subtraction of a reflected sunlight component as there could have been in Chapter 3, I have to assume that the radiance measured by the spectroradiometer is accurate and that there is some other discrepancy between the visual and spectral observations.

Although photographs taken while the spectral measurements were being acquired show that a crust covered much of the surface area of the lava channel, the reason why the spectral estimates of the radiant characteristics of the channel are low (< 15%) is probably the result of the geometry of the spectral acquisition. The optical head of the spectroradiometer was depressed at 10 -15° from the horizontal, meaning that spectral observations of the lava channel were made at a high grazing angle. (Unfortunately, I was limited in the choices of where I could safely set up the spectroradiometer, and this was the best that could be done under the circumstances.) Measurements made at this angle greatly change the spot size falling within the beam of the spectroradiometer. At 60 m distance from the lava channel, the spot size for nadir viewing compared to that of 15° from the horizontal (75° from the vertical or nadir position) is ~4.5 m^2 and 18m^2, respectively. The difference between the two areas means that it was entirely possible that part of the beam of the spectroradiometer may have fallen outside of the lava channel, which would have depressed the temperature and area results considerably. This is probably the principal reason why the 2-component fits for the target and reference beams were different; the reference beam was centered more toward the edge of the lava channel meaning that more of the inactive area outside of the channel was included in reference measurements.

The other optical effect which results from spectral measurements made at high incidence angles is that the hotter molten material in the beam may have been obscured by the recently formed and slightly elevated crust. Instead of measuring the hot, molten material within the cracks and fissures on the recently formed crust, the spectroradiometer measured most crust which was elevated with respect to the molten material. This effect produced by high incidence angle measurements has been reported

in two other cases. A study (Mouginis-Mark et al., 1991) done with AVHRR images taken of the East Rift Zone of Kilauea concurrent with a Landsat TM scene acquisition show that measurements made at off-nadir angles have the possibility of missing important radiative information. An AVHRR scene collected at near-nadir viewing geometry showed that Puu O'o crater was active, while an off-nadir scene showed an inactive crater because the activity was located too deep within the crater for it to be measured by the spacecraft at a high viewing angle. In another interesting case, measurements made of the Jovian moon, Io, have shown that active volcanoes located on or near the terminator are undetectable until the planet actually rotates to allow for "nadir" viewing conditions (William Sinton, personal communication).

I have to conclude that the radiance measured by the spectroradiameter was consistent for the activity in its field of view and that low estimates of radiative characteristics of this anomaly are due to two geometric effects of high incidence angle measurements, which are the increased spot size, which may have resulted in areas outside of the channel being measured, and the elevated cooled surface crust which obscured the molten material.

4.4.2 Temporal changes in radiant energy from cooling lava flows

While crude estimates of flow cooling have been done in the past (e.g. Jones et al., 1990), they have not had the benefit of multispectral data, which allows for the identification of components radiating at core and crust temperatures (Oppenheimer, 1991). The data presented in section 4.3.2 of this chapter allow for the first accurate estimate of the temporal changes of radiative contributions of the solid crust and hot components of a cooling flow to date.

Table 4.2 shows the change of the emitted energy with time of the lava flow studied in section 4.3.2 of this chapter. This table was produced by calculating the total emitted energy at all wavelengths of each of the 13 best fits for the examples in Table 4.1. A spot size of 0.55 m^2 and an emissivity of 0.995 were used to generate these values. What is immediately evident is the low percentage (< 11.5% in all cases) of the total radiant energy which comes from the radiator of magmatic temperature (consistent with the Landsat TM result reported in Oppenheimer, 1991). Actually, the main reason why the hot component shows up prominently in these data is because the peak of its characteristic blackbody curve (~2.1 μm for an object radiating as a 1100°C blackbody) is within the spectral region of our study. On the other hand, the peak of the blackbody curve (~3.3 μm for an object radiating as a 600°C blackbody) for the crust component is outside of the range of our study, meaning that the majority of the flux emitted by the crust is further out in the infrared.

The total energy budget of the lava flow is dependent on the temperature of the crust component (Glaze et al., 1989). This is borne out by Table 4.2 which shows that only a small fraction of the total emitted energy is from the hot component.

4.5 Conclusions

The nighttime hyperspectral measurements presented in Chapter 4 represent the only field hyperspectral measurements of lava flows acquired at night to date. The spectral data are extremely easy to work with since there is no contamination from reflected sunlight. Estimates of the hot fractional area of the core component as identified in studies by Crisp and Baloga (1990) and Oppenheimer (1991) can only be approximated. With the spectral data which I presented in this Chapter, I was able to

accurately determine the hot fractional area of a cooling flow to be on the order of 10^{-2} - 10^{-3} while hot fractional areas of lava channels had a lower boundary (due to geometrical effects) of 10% of the total area viewed.

Comparing these field results with those predicted by the Crisp and Baloga (1990) 2-component theoretical model for the emplacement of lava flows, the hot fractional areas observed for the cooling flow fell within the lower limit (~0.001) of those calculated by the model. Using their model and information from the episode 4 and 18 Puu O'o flows, Crisp and Baloga (1990) predicted hot fractional areas for those flows of 0.5%. These estimates match those calculated at roughly 29 - 52 minutes. I must conclude that the 2-component theoretical model of Crisp and Baloga (1990) yields consistent results with those obtained for lava flows with the field spectroradiometer. The hot fractional area of the lava channel that was reported in this chapter was ~0.10 of the total surface area in the field of view which falls within the range of values (0.1 - 0.001) predicted for lava flows with the Crisp and Baloga (1990) model. However, I would also point out that Crisp and Baloga (1990) considers a two-component model necessary when the rate of core heat loss (proportional to $A_h T_h^4$) divided by the rate of crust heat loss (proportional to $[1-A_h]T_c^4$) is between 0.1 and 10. These conditions were met for the target beam examples acquired of the center of the lava channel (~0.17), but not for all of the examples of the cooling lava flow (< 0.05 in 11 cases, 0.14 and 0.24 for the first and last example, respectively).

The average flux densities measured in both locations on February 19,1992, were much greater than those reported for Stage 3 activity at the Kupaianaha lava lake in Chapter 3. The average flux densities of the cooling flow ranged from 1.3 - 7.2 x 10^4 W/m^2 which was what was reported for Stage 1 activity in the previous chapter. The

average flux density of the lava flow channel was greater than 1.4 x 10^5 W/m^2, which was definitely out of the range of any activity that was measured for Kupaianaha. I put a lower bound estimate on the total emitted power of the phase 50 lava channel at an incredible 1.7 x 10^8 W for a 20 m x 60 m area, which for that limited area, is about 136% of the total power output reported for a Mt. Etna lava flow (which had a surface area of ~8 x 10^4 m^2 [Pieri et al., 1990]).

The results of this chapter form an important part to this dissertation in that they provide spectral measurements of lava flows to compliment the acquisitions of chapter 3. The benefits of nighttime spectral acquisition can be fully appreciated after dealing with the problems associated with the removal of the reflected sunlight component (Chapter 3). Chapter 4 forms an important bridge between Chapters 3 and 5 in that it uses the field technique first shown in Chapter 3 to measure lava flows which are by far the dominant form of volcanic activity in Hawaii, which is the topic of Chapter 5. The data presented here for lava flows will be important as ground-truth measurements for satellite studies (Oppenheimer, 1991) of surface crust temperature and fractional hot area of lava flows. What is missing from all of the field spectroradiometer data that I have presented so far in this dissertation is any easy way to assess the spatial variability of hot volcanic targets. This aspect of the problem is considered in Chapter 5, which presents temperature measurements of Kilauea that were derived from Landsat Thematic Mapper (TM) data.

References

Crisp, J., and S. Baloga, A model for lava flows with two thermal components, *J. Geophys. Res., 95*, 1255 - 1270, 1990.

Glaze, L., P. W. Francis, and D. A. Rothery, Measuring thermal budgets of active volcanoes by satellite remote sensing, *Nature, 338,* 144 - 146, 1989.

Hon, K., and J. Kauahikaua, The importance of inflation in the formation of pahoehoe sheet flows, Abstracts of the Fall 1991 American Geophysical Union Conference, *EOS supplement*, 557, 1991.

Jones, A. C., L. Wilson, and H. Pinkerton, Surface temperature measurements of active Hawaiian lava flows, paper presented at International Volcanological Congress, *Int. Assoc. Volcanol. Chem. Earth's Interior,* Mainz, Germany, Sept. 3-8, 1990.

Mouginis-Mark, P. J., S. K. Rowland, H. Garbeil and P. Flament, AVHRR Observations of the Kupaianaha Eruption, Hawaii, Abstracts of the Fall 1991 American Geophysical Union Conference, *EOS supplement*, 562, 1991.

Oppenheimer, C., Lava flow cooling estimated from Landsat Thematic Mapper infrared data: the Lonquimay eruption (Chile, 1989), *J. Geophys. Res., 96,* 21,865 - 21,878, 1991.

Pieri, D. C., L. S. Glaze, and M. J. Abrams, Thermal radiance obseravtions of an active lava flow during the June 1984 eruption of Mount Etna, *Geology, 18,* 1018 - 1022, 1990.

Rothery, D. A., P. W. Francis, and C. A. Wood, Volcano monitoring using short wavelength infrared data from satellites, *Journal of Geophysical Research, 93,* 7993 - 8008, 1988.

Self, S., S. Finnemore, T. Thordarson, G. P. L. Walker, Importance of compound lava and lava-rise mechanisms in the emplacement of flood basalts, Abstracts of the Fall 1991 American Geophysical Union Conference, *EOS supplement*, 63, 1991.

Table 4.1

Summary of 13 spectra of cooling lava flow. TIME(HST) refers to the time that the measurement was taken. T_h is the temperature of the hot component. T_c is the temperature of the crust component. A_h is the fractional hot area. ERROR is the best fit error value.

TIME(HST)	T_h(°C)	T_c(°C)	A_h	ERROR
1. 21:27	1150	768	3.6×10^{-2}	0.0181
2. 21:47	900	604	1.0×10^{-2}	0.0082
3. 21:48	950	626	1.4×10^{-2}	0.0034
4. 21:49	1150	626	1.1×10^{-2}	0.0084
5. 21:50	950	610	1.4×10^{-2}	0.0073
6. 21:52	900	594	1.0×10^{-2}	0.0166
7. 21:56	1100	550	5.2×10^{-3}	0.0078
8. 21:59	950	544	1.4×10^{-2}	0.0091
9. 22:08	900	454	9.3×10^{-3}	0.0161
10. 22:16	900	454	8.1×10^{-3}	0.0258
11. 22:19	900	410	5.3×10^{-3}	0.0194
12. 22:21	900	514	4.6×10^{-3}	0.0418
13. 22:26	900	390	2.1×10^{-2}	0.0292

Table 4.2

Temporal variation of emitted energy from the hot (Q_{hot}) and crust (Q_{crust}) components of the cooling lava flow. Q_{total} gives the total energy emitted by the flow from an area of 0.55m^2. Results are presented in the same order as Table 4.1.

Time (minutes)	Q_{hot}(W)	Q_{crust}(W)	Q_{total}(W)
0	4580	35128	39708
20	587	18173	18760
21	972	19984	20956
22	1400	20045	21445
23	972	18599	19571
25	587	17358	17945
29	574	14162	14736
32	972	13631	14603
41	546	8587	9133
49	476	8597	9073
52	311	6717	7028
54	270	11851	12121
59	1458	5870	7328

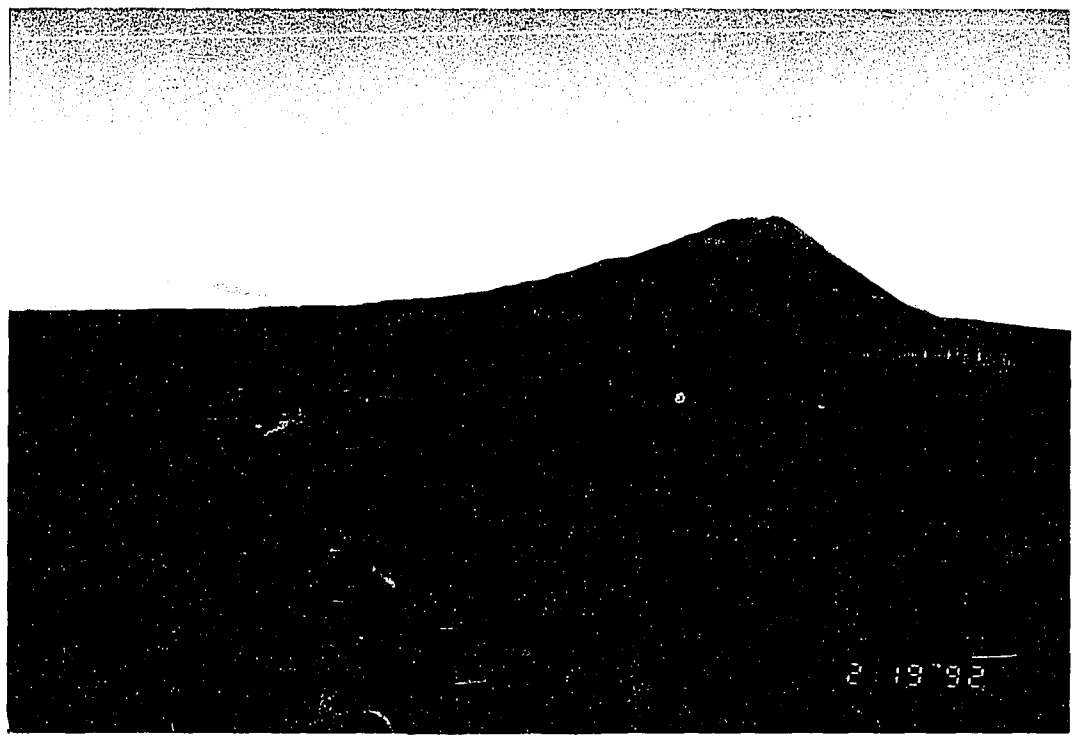

Figure 4.1. Photo of the Phase 50 Puu O'o eruption as seen from 5 km west of the rift eruption. Smoke rising from the base of Puu O'o marks the location of the rift. The lava channel spectra were acquired of the activity in this region. Smoke rising from recently erupted flows can be seen in the foreground and to the left of Puu O'o. An area of active flows in the general direction of the withered trees between the position where this photo was taken and the active rift was the site of the cooling lava flow study.

Figure 4.2. Observational set-up of the spectroradiometer above lava channel of the phase 50 Puu O'o eruption. The active rift is to the right in this picture. The spectroradiometer optical head, which was depressed at a ~15° angle, can be seen above the group of observers to the left. The lava channel is 60 m from the spectroradiometer which resulted in a target spot of 18 m^2.

Figure 4.3. Area of cooling lava flows which were the subject of this study. This photograph was taken 8 minutes after the start of the spectral study of the cooling flow. The spectroradiometer was set up approximately 20 m from a 75 - 80° slope. The effective target size was 0.55 m^2. The target area was a spot below the bright incandescent part of the flow which runs from the center of the photo to the right side of the picture.

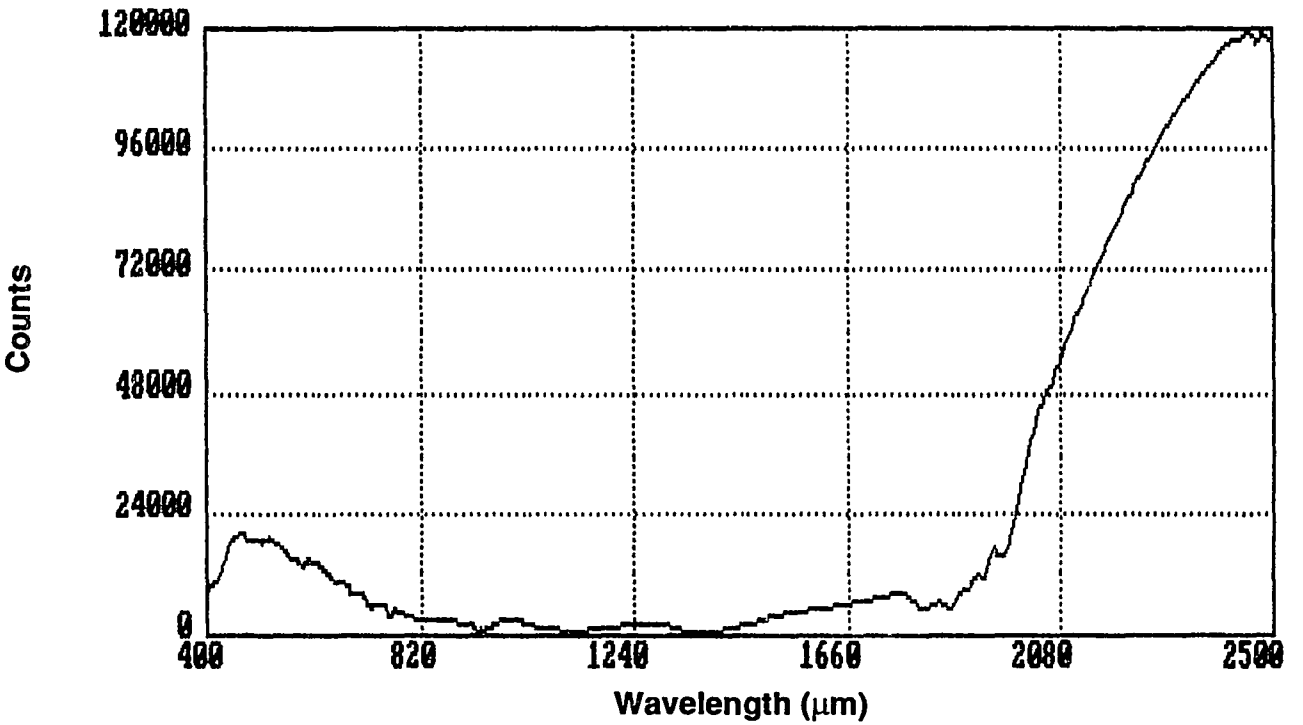

Figure 4.4. An example of Stage 3 raw data, corrected for automatic gain change, collected with the spectroradiometer at the Kupaianaha lava lake on October 12, 1987. The lake surface was covered by plates of crust when this spectrum was collected. Horizontal axis plots wavelength between 0.4 and 2.5 μm. Vertical axis is in number of counts, which varied for each spectrum that was collected due to the automatic gain feature of the GER spectroradiometer. Note the spectral features at 0.4 - 0.9 μm which are due to reflected sunlight contamination.

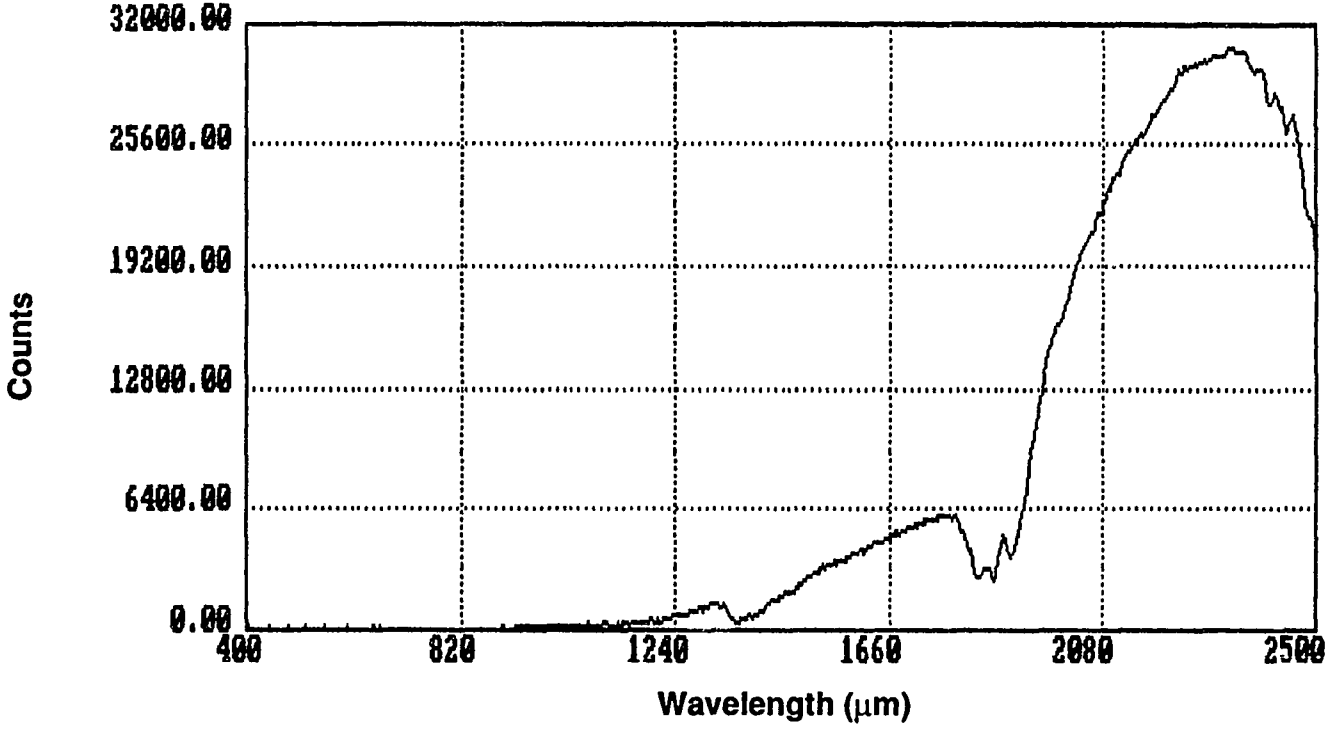

Figure 4.5. Spectrum of cooling lava flow taken at night. Data format is the same as that in Figure 4.4. The lava flow had cooled for 52 minutes by the start of the acquisition of this data, and appeared to have formed a crust similar to that observed for Stage 3 activity in Chapter 3 (Figure 4.4). The measured flux is entirely due to thermal radiators in the field of view of the spectroradiometer. Compared to Figure 4.4, note the lack of features due to reflected sunlight at 0.4 - 0.9 μm.

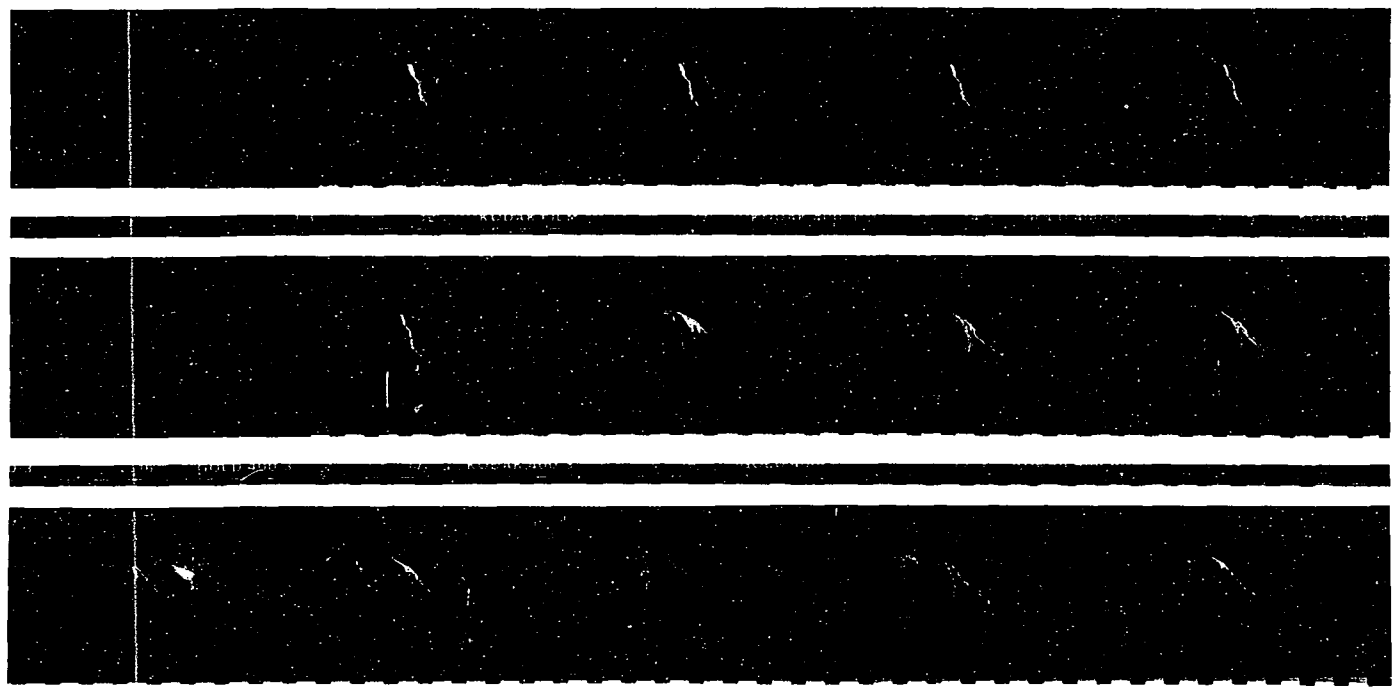

Figure 4.6. Time elapsed photos of the emplacement of the lava flow which was the subject of this study. Photos were acquired once every 1 - 2 minutes. The first spectrum of the cooling lava flow study was acquired at 21:27 HST which corresponds to the second to the last picture in this series. The target area of the spectral study was the upper part of the left lobe of the branching lava flow which is located in the center of the photo.

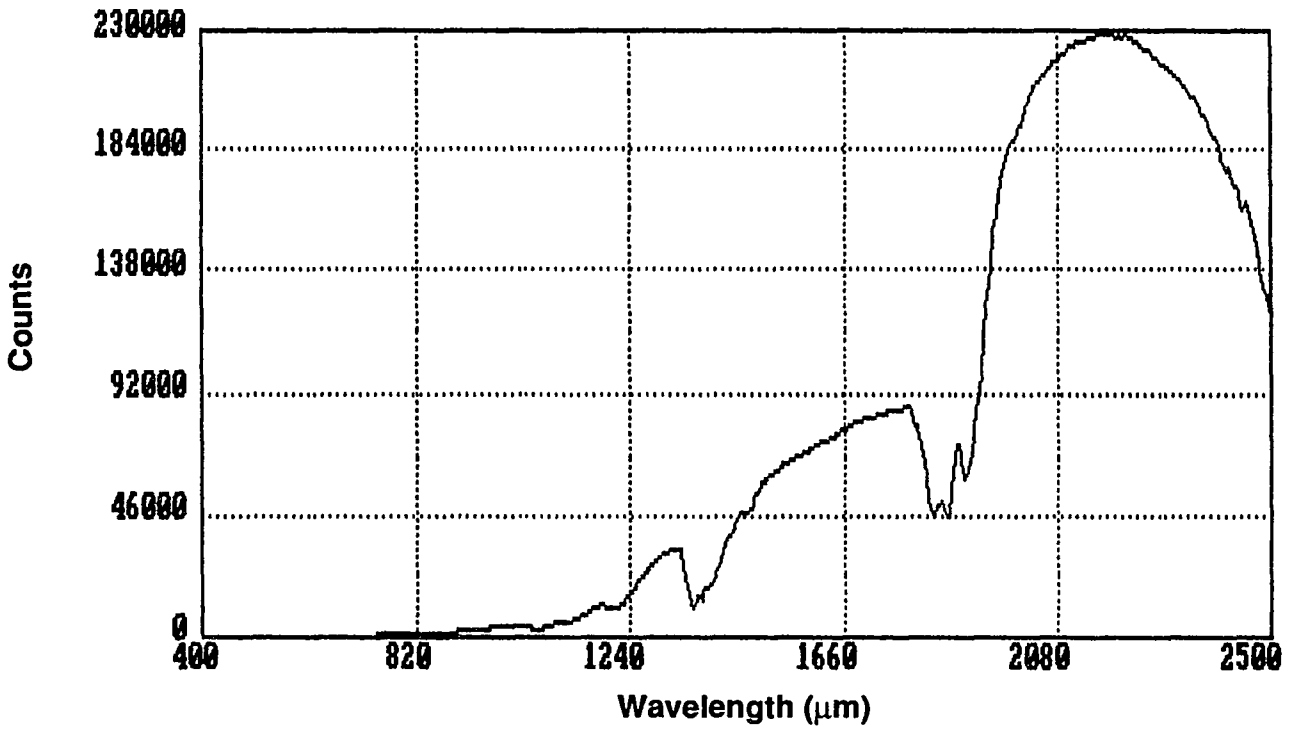

Figure 4.7. Spectrum of the recently emplaced lava flow. Data format is the same as that in Figure 4.4. This is the first spectrum of the lava flow study acquired at 21:27 HST. The high fluxes in the 1.2 - 1.7 μm range suggest large hot fractional areas and high surface crust temperatures.

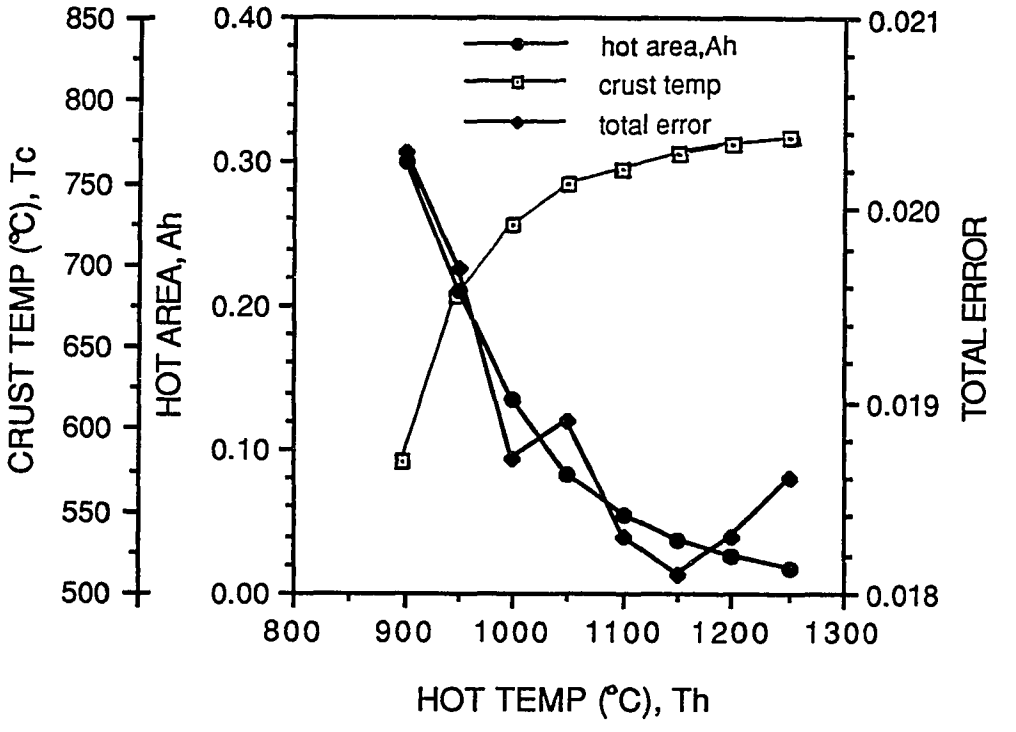

Figure 4.8. Two-component best fits to spectrum collected at 21:27 HST and presented in Figure 4.7. Best model results for hot temperature starting conditions between 900 - 1250°C. Lines connecting data points illustrate trends in solutions; however, data points have only been calculated for the hot temperatures at 50°C intervals between and inclusive of 900 and 1250°C. Only these points are actual results. Hot temp, T_h, is the temperature of magma in cracks on the viewed surface; Crust Temp, T_c, is the surface crust temperature; and Hot Area, A_h, is the fraction of the viewing area that is occupied by material at T_h, with the remainder exhibiting T_c. "Total Error" is the sum of the weighted differences between the data derived flux ratios and the model generated flux ratios, and measures the quality of the model fit to the spectroradiometer data.

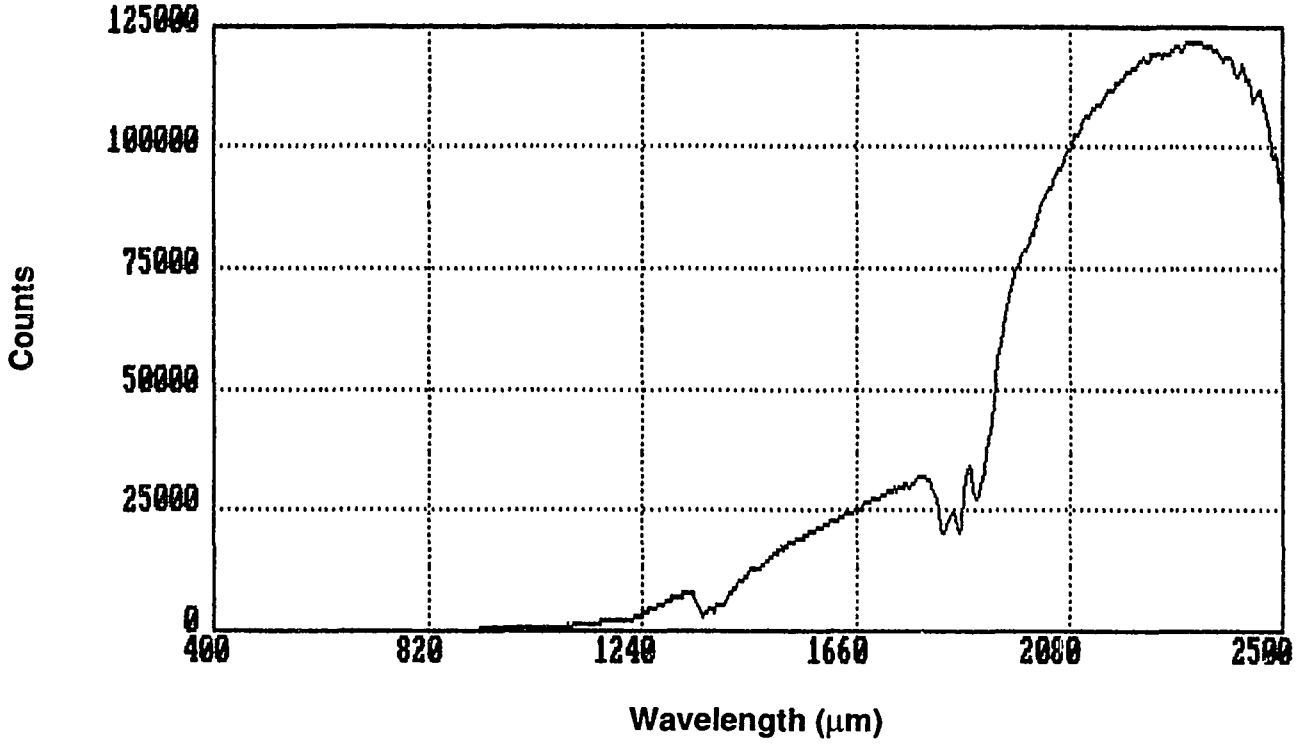

Figure 4.9. Spectrum of cooling lava flow 32 minutes after emplacement. Data format is the same as that in Figure 4.4. Compared with Figure 4.7, the low relative fluxes in the 1.2 - 1.7 μm spectral range suggest that the fraction of the target area radiating at hot (near magmatic) temperatures had dropped significantly from that observed for Figure 4.7. Note that the slope of the spectral curve which marks a rapid rise in flux after 2.0 μm is shifted further into the infrared relative to that of Figure 4.7, which suggests a cooler crust temperature for this spectrum.

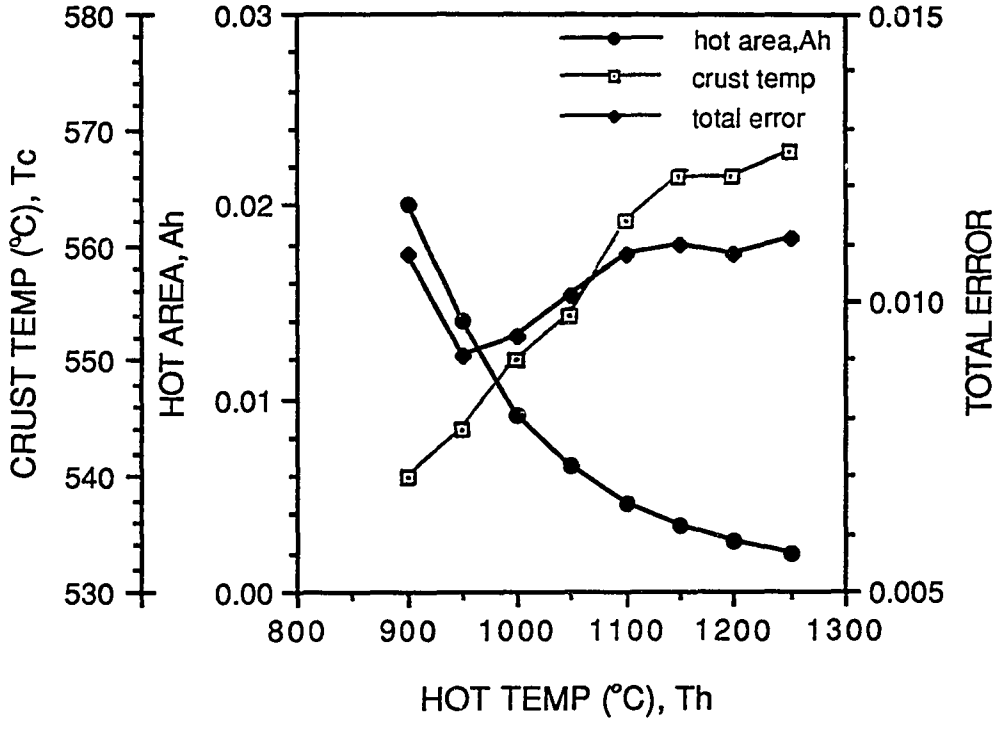

Figure 4.10. Two component model best fit results for lava flow 32 minutes after emplacement (Figure 4.9). Format for presentation of the data is the same as Figure 4.8. In this case, the minimum error occurs at a hot temperature of 950°C.

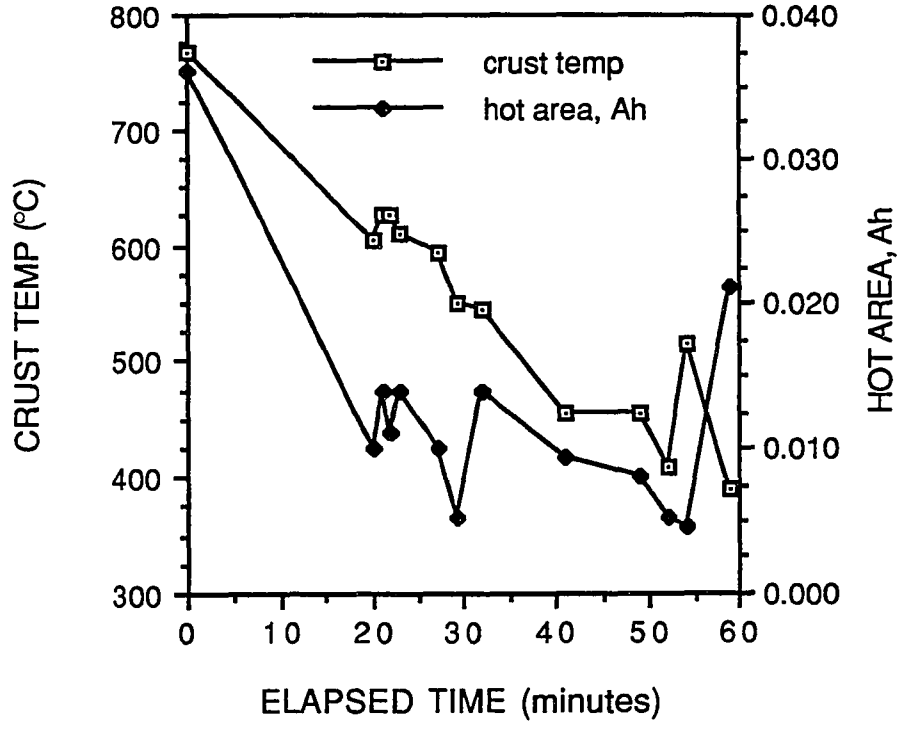

Figure 4.11. Temporal variations of a cooling of lava flow. The 13 examples show the changes in hot fractional area and crust temperature with time. Note that examples 2-6 show an brief increase in crust temperature which may be due to an injection of magma under the cooling crust.

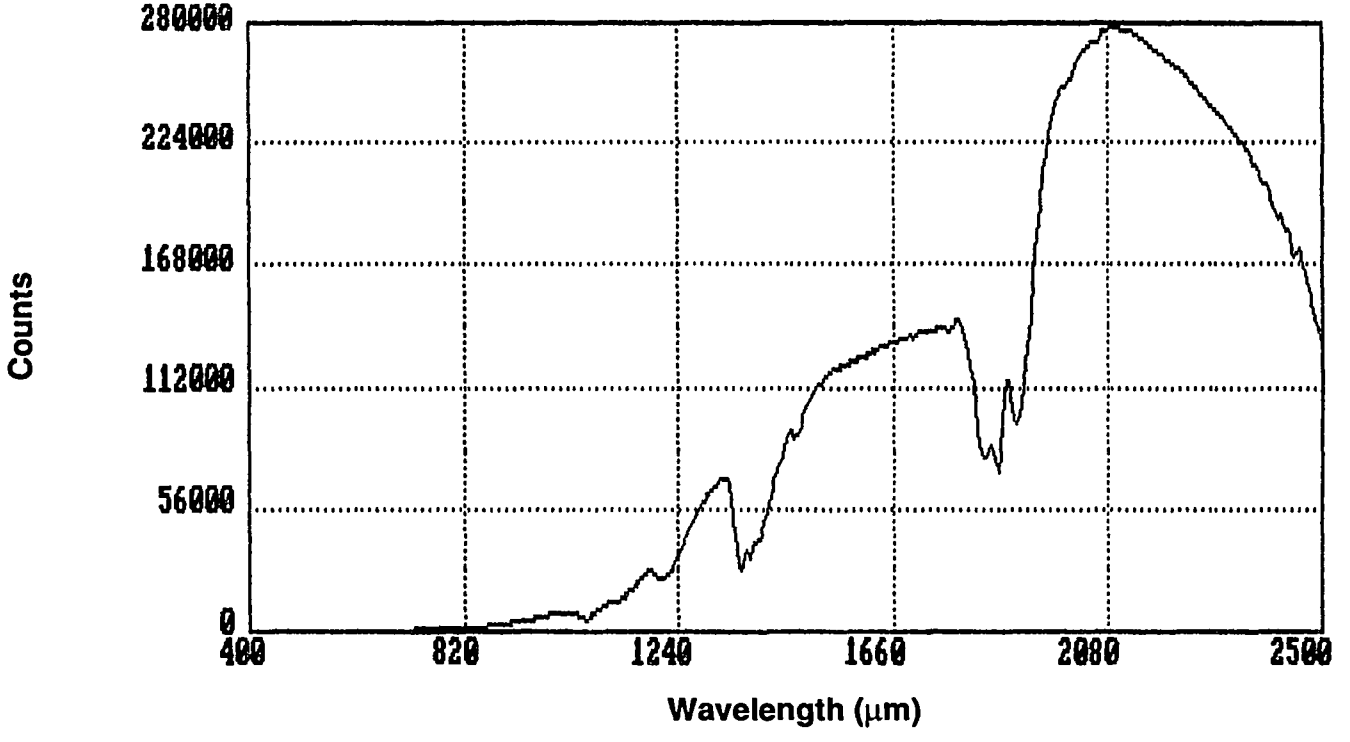

Figure 4.12. Spectrum of the center of the lava channel. Data format is the same as that in Figure 4.4. The high flux values in the 1.2 - 1.7 μm range suggest a large fractional area for the hot component.

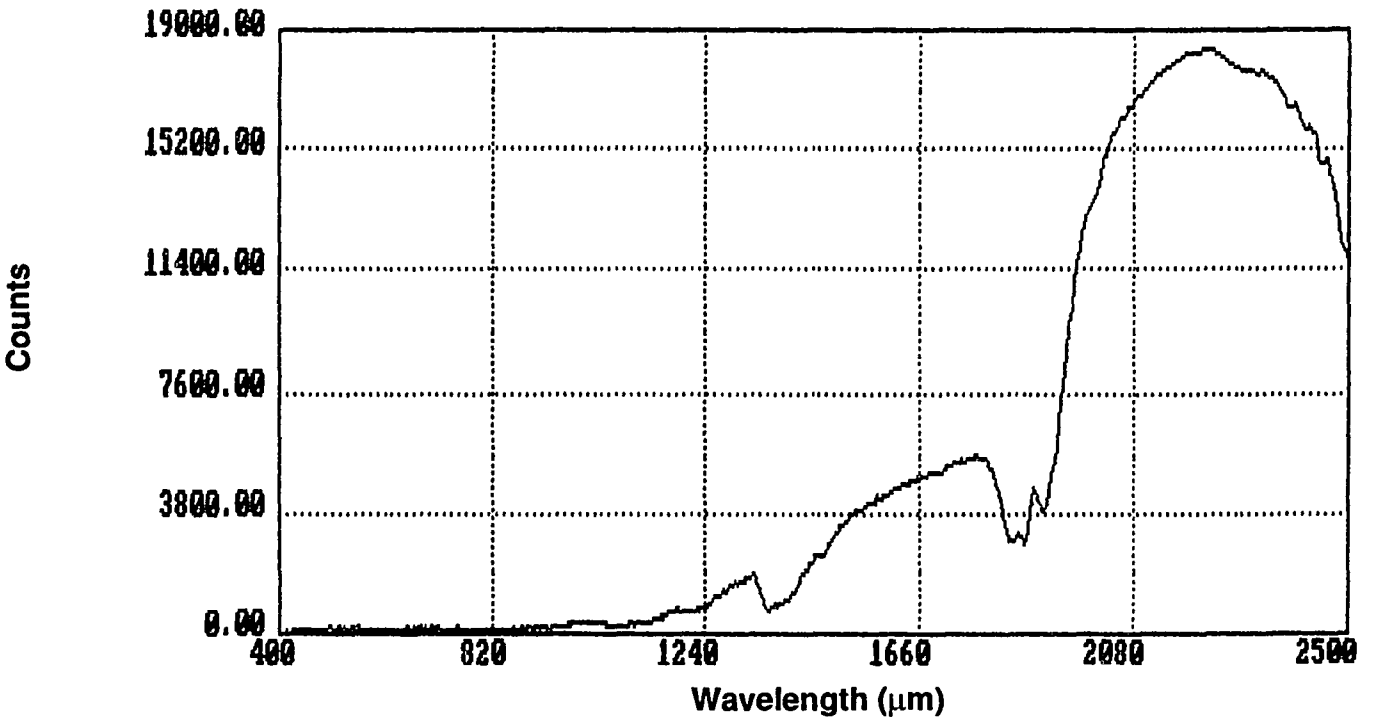

Figure 4.13. Reference beam spectrum acquired at the same time as the target beam spectrum of Figure 4.12, but of an area closer to the far boundary of the lava channel. Data format is the same as that in Figure 4.4.

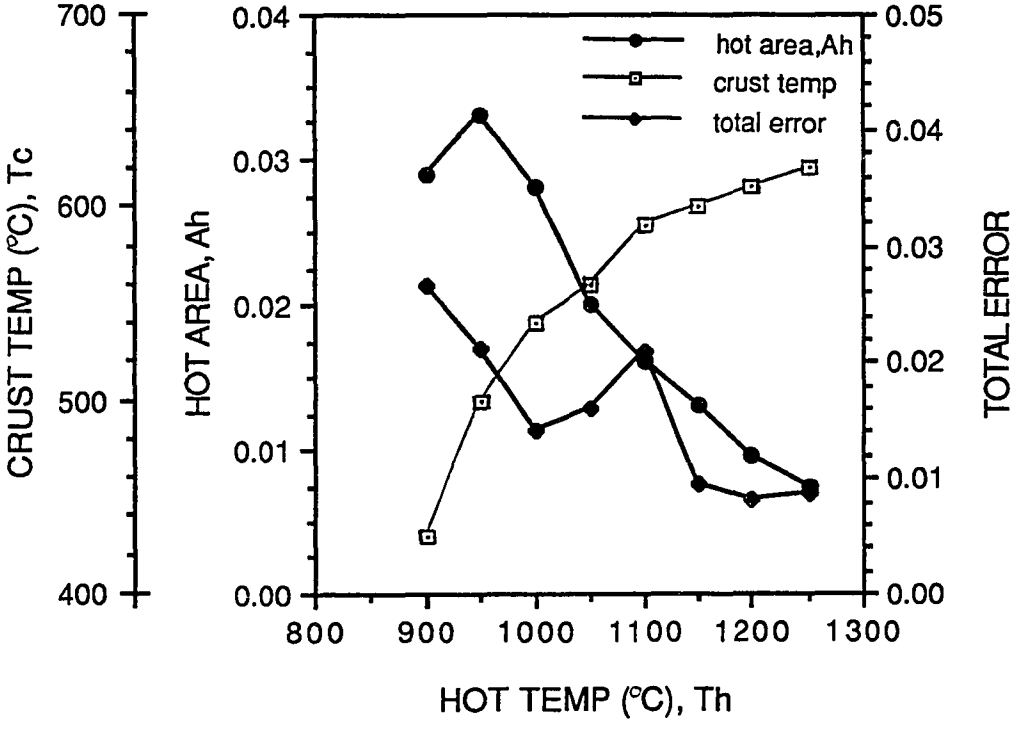

Figure 4.14. Two component model best fit results for edge of lava channel (Figure 4.13). Format for presentation of the data is the same as Figure 4.8. In this case, the minimum error occurs at a hot temperature of 1200°C.

Chapter 5: Comparison of A- and P-Format Landsat Thematic Mapper Images of Kupaianaha/Puu O'o Eruption Taken on July 23, 1991.

5.1 Introduction

The focus of this dissertation has been to study the sizes and radiative temperatures of volcanic anomalies. The previous chapters (3 and 4) have presented results of field studies of radiative temperature which could be used as ground truth measurements for active volcanoes. While detailed in the thermal information that they provide, those field measurements lack any spatial information on the characteristics of the eruption. Chapter 5 presents a Landsat Thematic Mapper (TM) data set acquired on July 23, 1991 over the East Rift Zone of Kilauea Volcano. At the time of acquisition, Kilauea exhibited a variety of volcanic activity including a small (< 5 m in diameter by helicopter pilot reports) lava lake in the crater of Puu O'o; numerous small (less than the 30 m x 30 m dimensions of a Landsat TM pixel), hot skylights; surface flows both on the top of the Pali near the Royal Gardens subdivision and further down slope on the plain before the ocean; and two areas where tubes are emptying magma into the ocean. Thanks to a grant from the W. M. Keck Foundation, both A- (uncorrected) and P- (geometrically corrected) data were purchased from the Earth Observation Satellite Company (EOSAT) so that I could not only study the radiative signatures of different types of volcanic activity but could also weigh the benefits against the drawbacks of using each type of data. A comparison between the radiance characteristics of A- and P-format data for the different types of volcanic anomalies in the scene is presented here along with estimates of the average flux densities of areas and the energy budgets of active areas of the volcano.

The utility of satellite data for making radiative temperature measurements was first realized in Matson and Dozier (1981) and Dozier (1981). In those studies, a calculation, later known as the dual-band method, was introduced which used data from two Advanced Very High Resolution Radiometer (AVHRR) wavelength bands to approximate the temperature and area of a relatively hot thermal subarea in individual pixels. This method was later adapted by Rothery et al. (1988) for the detection of hot volcanic thermal anomalies using Landsat TM data. Landsat and the NOAA weather satellites provide the only current means of studying volcanoes remotely from space, and each has certain advantages and disadvantages. The number of NOAA satellites (4 spacecraft, each in 12-hour repeat orbits) combined with an effective swath width of 2700-km means that the AVHRR can be used to acquire data over most areas of the world every few hours; however, the image resolution is fairly coarse (~1km) for radiative studies of volcanoes. Nevertheless, Mouginis-Mark et al. (1991) have shown that the AVHRR can be particularly useful for monitoring the short- and long-term presence of volcanic activity. They have shown that the AVHRR can be used as a relatively inexpensive (compared to the image costs of Landsat TM data) tool to monitor gross changes in eruptive phenomena.

More frequently, studies of active volcanoes are carried out using Landsat TM data. The major advantage of Landsat TM data over that of AVHRR is that of pixel resolution (~30 m for Landsat TM versus 1 km for nadir AVHRR). Studies using Landsat TM data suffer from the fact that consecutive images may only be obatined over an active volcano once every 16 days. Even assuming that the lack of clouds permits scenes to be obtained on successive overpasses, the intervening period of time between measurements is more than sufficient to allow for undetected large-scale changes in eruptive activity (Glaze et

al., 1989). Thus, although the finer details of active eruptions (such as flow sizes and locations) may be mapped more adequately using Landsat TM data, AVHRR provides the higher temporal resolution data which would be required for a global volcano-monitoring alarm system.

The Landsat TM "snapshots" of active volcanoes of previous studies (Rothery et al., 1988; Glaze et al., 1989; Pieri et al., 1990; Andres and Rose, 1991; and Oppenheimer, 1991) have shown the usefulness of 30 m resolution data when mapping the distribution of active areas on a volcano. The wavelength bands of the Landsat TM instrument are given in Table 5.1. Band 7 is particularly useful in that detectors covering this range of the short wavelength infrared are sensitive to the thermal emissions of erupting volcanoes. Since many volcanic thermal anomalies are limited spatially (generally subpixel-size for skylights, for instance), it is of vital importance to be able to identify the radiance of individual pixels to accurately map and attempt to calculate the radiative characteristics of those anomalies.

The two types of data used for Landsat studies of active volcanoes have been raw data (A-format) which have not been corrected for the parallelogram shape of the collected pixels, and data which have undergone cubic convolution. These data have been resampled (P-format) to correct for the geometric distortion of pixels due to the movement of the satellite during data acquisition. The advantage of A-format data over P-format data is that the radiance values in all bands of individual pixels are maintained; however, the data have been regarded by some authors (e.g. Rothery et al.,1988) as difficult to work with. I can only assume that the difficulty mentioned by other authors is due to rows of data being shifted an unspecified (by EOSAT) amount of pixels to the right or left, which requires a bit of image reconstruction to shift the rows

into matching columns. (For the A-format image collected over Kilauea, this process was simple because there were many anomalies whose boundaries were continuous after the alignment process.) The advantage of P-format data over that of A-format is that the geometric correction process makes features in the scene more continuous with smoother boundaries.

However, when dealing with the radiative characteristics of volcanic anomalies, the resampling process which creates the smoother boundaries of P-format images tends to smear anomalously high pixel radiance values into surrounding pixels. Numerous previous studies (e.g. Rothery et al., 1988; Glaze et al.,1989) have hinted that A-format (uncorrected, raw data) Landsat TM data may eliminate the effects of pixel "smearing" found in P-format (corrected) data. In this chapter, I calculate radiative temperatures and areas using the dual-band method (Dozier,1981) with both A- and P-format TM data collected over the East Rift Zone of Kilauea on July 23, 1991. I use the Rothery et al. (1988) method of using the midpoint of the wavelength band for calculations, and I explore the possibilities of using another method which takes into account the distribution of thermal energy across the wavelength band. I compare A- and P-format temperature and area results of a number of different active centers including the Puu O'o cone, hot skylights, and extensive (~500 pixels or 0.5 km^2 in total area) active lava flow fields. Next, I compare average flux densities and the energy budgets of a number of areas for both data sets. I then calculate and compare the total energy budget, Q, for the entire area using both sets of data. Finally, I discuss the spatial distribution of temperatures that can be inferred from these image data.

5.2 Field Area, Data Acquisition, and Data Formats

The area used as a test site for this study was the active East Rift Zone of Kilauea Volcano, Hawaii. The Puu O'o eruption which has lasted from January 1983 to the present, provided an excellent research target for the study of an active volcano using satellite remote sensing. Unlike previous studies of active volcanoes, such as that for Lascar volcano, Chile (Glaze et al., 1989) and Mount Erebus, Antarctica (Rothery et al., 1988), Puu O'o and the East Rift Zone of Kilauea Volcano are readily accessible both by car/hike and, for more elaborate field efforts, by helicopter. Its accessibility for ground truth measurements combined with its well-recorded history, courtesy of the scientists at the Hawaii Volcano Observatory, made it an excellent choice for a field study involving the comparison of corrected and uncorrected format Landsat TM images.

In January, 1989, I contacted EOSAT with the intent of acquiring a Landsat Thematic Mapper (TM) quarter scene (Path 62 Row 47 Quadrant 1) over the East Rift Zone of Kilauea Volcano, Hawaii. The purpose of the original study was to study the response of the Landsat TM senors to the surface activity of the then still-active Kupaianaha lava lake. Every 16 days, from March, 1989 to June, 1990, a field team including myself and one or two of numerous other participants (Peter Mouginis-Mark, Scott Rowland, Duncan Munro, and Scott Moncrief) were ready to travel to Kupaianaha to record with a video camera the surface activity of Kupaianaha when the Landsat satellite passed overhead at 10:16 HST. Inclement weather conditions forced the cancellation of trips on (conservatively) 80% of the possible target dates (roughly 26 in all) for acquisition. Of the six dates when conditions were predicted to be favorable for satellite data acquisition, four (late 1989 - March, 1990) were very promising, with clear skies over the East Rift Zone, up until about an hour before the satellite overpass.

Cumulus clouds formed in the vicinity of Kapoho and Kalapana quickly spread up slope to cover Kupaianaha. On one occasion, there were no cumulus clouds in the immediate area, but there were extensive layers of high wispy cirrus clouds patching the sky. Finally, on one of the last field trips (with Scott Moncrief) in April 1990, the forcast by the National Weather Service in Hilo, Hawaii was highly questionable, when a report of "clear skies" resulted in torrential rains over all of Kilauea Volcano from Kalapana upslope past Kupaianaha and Puu O'o to Mauna Loa!

Although the six expeditions to Kupaianaha failed to achieve coincident satellite and video data, they did give me a unique opportunity to record the evolution of Kupaianaha and to witness the growth of Kilauea Volcano by observing some of the numerous flows which covered the upper slopes (in some places up to 3 - 4 m in depth between March, 1990 and April, 1990) below Kupaianaha. These trips were very important in helping to gain insight in the dynamics of Kupaianaha lava lake and of lava flow emplacement. During the months of May - August, 1990, Kupaianaha drained and partially filled with magma a number of times. The anomaly which the lava lake would have presented in terms of Landsat TM pixels rapidly diminished. The initial experiment to obtain Landsat TM data over an active Kupaianaha lava lake was abandoned in August, 1990 because there was no longer any lake to image!

Thirteen months after my last trip to Kupaianaha and eleven months after the lava lake drained for the final time, the Landsat satellite overflew the East Rift Zone on a day when clouds were scattered in a pattern that did not substantially interfere with the acquisition of data. On July 23, 1991 at 10:16 HST a useful TM image (Figure 5.1) was finally collected for the East Rift Zone of Kilauea Volcano (Path 62 Row 47 Quad 1). While the lava lake ceased to exist, there were numerous large (> 0.5 km^2) active

surface flows apparent on the image, as well as hot spots in Puu O'o cone, two small hot areas which were probably skylights, and two places where magma was pouring into the ocean. Each of these areas will be discussed in detail below, but first I would like to introduce the model which was used to fit temperatures and areas to thermally radiant pixels.

5.3 Dual-band Method Computer Model

Before any method can be used to calculate radiative temperatures using Landsat TM data, the digital number (DN) of a given pixel, which represents the smallest increment of energy that the sensor of a particular band can descriminate and has a range for Landsat TM of 0 to 255, must be converted to units of radiance (W m^{-3} sr^{-1} or mW cm^{-2} μm^{-1} sr^{-1}). Fortunately, the conversions for each band are simple and more than adequately detailed in Markham and Barker (1986).

As first noted in Chapter 2, section 6, the distribution of radiant energy across the electromagnetic spectrum from an object exhibiting characteristics of a blackbody emitter is given by Planck's Law:

$$B_\lambda(T) = \frac{2hc^2}{\lambda^5} \frac{1}{e^{(hc/\lambda kT)}-1} \qquad (5.1)$$

where $B_\lambda(T)$ is the power at wavelength λ radiated per unit wavelength per unit solid angle into a small cone from a piece of the surface of an opaque body with uniform temperature T (in Kelvin), with the piece having unit area in the projection perpendicular to the axis of the cone; h is Planck's constant (6.63 x 10^{-34} J s); c is the speed of light (3.00 x 10^8 m s^{-1}); and k is Boltzmann's constant (1.38 x 10^{-23} J K^{-1}) (Shu, 1982). Assuming that a single pixel radiates at a uniform temperature, I

can calculate the radiative pixel-integrated temperature by switching around Planck's Law:

$$T(K) = \frac{hc}{k\lambda} \frac{1}{\ln([ET2hc^2/\lambda^5 B] + 1)} \qquad (5.2)$$

where all variables and constants are the same as those described above for equation 5.1 with the exceptions that E and T are the emissivity of the surface and the atmospheric transmissivity at wavelength λ, respectively. As discussed in Rothery et al. (1988), most active volcanic surfaces exhibit at least two subareas having different temperatures, and a pixel-integrated temperature of such a surface would be a value between the end-member temperatures in the pixel. This could result in a considerable error when extending this calculation to estimate the total radiant energy flux, which varies directly as T^4.

If the blackbody curve of one temperature is not sufficient to describe the radiant energy from a pixel, then the next logical step is to attempt to fit two blackbody curves to the data. The number of variables in the 2-component case increases to three, which are the temperature of the hot component (T_h), the temperature of the cooler component (T_c), and the fractional area of the hot component (A_h), with the fractional area of the cooler component as the remainder of the pixel or ($1 - A_h$). I would like to point out that these variables are the same as those of listed in previous studies, but may have been assigned different symbols (T_c, T_s, and f for the hot temperature, cool temperature, and hot fractional area, respectively in Crisp and Baloga [1990] and Oppenheimer [1991]).

The equations which are used to solve the 2-component or "dual-band" problem were adapted from Matson and Dozier (1981), and are listed below

$$F(\lambda_1) = ET(A_h B(\lambda_1, T_h) + (1-A_h)B(\lambda_1, T_c)) \quad (5.3)$$

$$F(\lambda_2) = ET(A_h B(\lambda_2, T_h) + (1-A_h)B(\lambda_2, T_c)) \quad (5.4)$$

where $F(\lambda_1)$ and $F(\lambda_2)$ are measured radiance values of different Landsat TM bands, leaving A_h, T_h, and T_c as the quantities which must be solved for. E and T are the emissivity and the atmospheric transmissivity, respectively. In this study, E was assigned a value of 0.995 based on my (with the help of Paul Lucey) measurements of fresh (< 3 days old) Kilauea basalt flow samples provided by Alun Jones. I recognize that the emissivity of basalt may change with time as the cooled flow surface weathers and erodes (Kahle et al.,1986); however, the thermally radiant pixels which are the target of this study were probably not old enough to have undergone sufficient erosion to change the emissivity significantly from the laboratory measured value. An atmospheric transmittance of 0.95 was assumed based on the value estimated in Oppenheimer (1991) from LOWTRAN 7 atmospheric transmission model.

The solution of two equations (eq. 5.3 and 5.4) having three variables (A_h, T_h, and T_c) requires that a value for one of the variables must be chosen. Earlier studies (Rothery et al., 1988; Glaze et al.,1989; and Pieri et al., 1990) have chosen a cool component temperature and have solved the dual-band equations for the hot component temperature and hot fractional area. These studies have led to inadequate estimates of the total energy radiated by an active volcano since this quantity has been shown (Glaze et al., 1989) to be essentially dependent on the cooler, much-larger, radiating area. Data

for Stage 3 (solid crust) activity obtained at Kupaianaha and reported in Chapter 3, suggest that the fractional radiating area of the hot component is extremely small (10^{-5} - 10^{-7}) when compared to that of the cooler component. A recent study by Oppenheimer (1991) solves the dual-band equations by estimating the hot component temperature from thermocouple measurements acquired during the Landsat-imaged eruption of Volcan Lonquimay, Chile. The Lonquimay study argues that the cooler solid crust component should be solved for since its contribution dominates the total energy flux emitted by active volcanoes. I agree with this conclusion and also assume a hot temperature in the dual-band calculations for the TM data results listed below.

Another problem that the Oppenheimer (1991) study points out is that the dual-band method is only successful when the range of radiance coverage of two bands overlap so that temperature and area solutions may be the same for both channels. The two bands with the largest useful overlap are bands 5 and 7. Bands 4 and 5 overlap very briefly if the hot component temperature is high enough. Oppenheimer (1991) found that although bands 3 and 4 have an area of overlap, the temperatures and areas required in a pixel for a dual-band fit were not met with the Volcan Lonquimay data set. The dual-band method is most successfully employed using data from TM bands 5 and 7.

The Landsat TM scene that I use here contains such a large number (> 1300) of thermally emitting pixels (anomalously high values in bands 5, 7 or both) that I developed an iterative program to handle dual-band solutions for arrays of pixels. In my program, the hot component temperature, the emissivity of the surface and the atmospheric transmissivity must be entered by the operator and are assumed to not change significantly over the set of pixels used as input.

Upon inspection of the dual-band equations (eq. 5.3 and 5.4), I found that A_h must be less than the measured pixel radiance in each band divided by the product of the hot component blackbody radiance in the band, the emissivity of the surface and the atmospheric transmissivity; otherwise, the radiance contribution from the cool component would have to be negative which is physically impossible. In the form of an equation, the highest value for A_h which will yield a dual-band method fit is

$$A_{lim} = F(\lambda)/(ET[B(\lambda)_{1130}]) \qquad (5.5)$$

where A_{lim} is the upper limit of the hot area which will still give a dual-band solution; $F(\lambda)$ is the DN-derived radiance from the band in question; E and T are the emissivity and atmospheric transmissivity, respectively; and $B(\lambda)_{1130}$ is the radiance calculated for a blackbody radiating at the temperature chosen for the hot component (which in this study was 1130°C).

Both the A- and P-format data for the same scene were processed using the computer program described in Appendix 1. A hot component temperature of 1130°C was assumed. First, the P-format data set was processed completely, then the A-format data were dealt with. I did not attempt to compare DN values between data sets while processing either of the two data sets, so that I could remain as objective as possible in identifying the distribution of thermal anomalies. The results of this study are listed in the next section.

5.4 Comparison of A- and P-format Data Using Volcanic Anomalies

There are many ways to compare the characteristics of the A- and P-format Landsat TM data. I will begin by separating the radiative activity of the volcano into

categories, which are Puu O'o crater, skylights, lava flows in sunlight, lava flows in the shadow of clouds, and lava tubes discharging magma into the ocean. For each of the activities, I point out the band 7 A- and P-format response to the anomaly, and point out differences between the numbers of saturated pixels in each case. Next, I present a representative cross-section of the active area that gives the DN values (which is directly proportional to the radiance) of bands 5 and 7 (and 4 if bands 5 and 7 are saturated). I report the results of the dual-band calculations by presenting a temperature and area map of the thermally enhanced pixels. Finally, I compare the average flux density for each area calculated from the A- and P-format data.

5.4.1 Puu O'o crater and vicinity

A-format (Figure 5.2) and P-format (Figure 5.3) band 7 Landsat TM images of Puu O'o crater taken on July 23, 1991, show that the crater was active on this date. Both the uncorrected (Figure 5.2) and corrected (Figure 5.3) band 7 images have areas with anomalously high pixel values west to south of the crater. The half-halo to the south and west of the crater is an optical effect which is probably a result of scattering of light due to particles in the atmosphere. This effect has been observed in the past for Kilauea eruptions (Oppenheimer, 1991). The anomalously high pixel values which trail to the south of the crater in both images are also present in the same area in bands 3, 4 and 5 (Bands 1 and 2 were not important for this study.), but not in band 6. If the area south of Puu O'o crater were radiating significantly in the infrared, I would expect to find elevated pixel values in band 6. However, since this is not the case, I assume that the anomalously high pixel values in bands 4, 5, and 7 is an optical effect due to haze reflecting sunlight back to the Landsat TM sensors. A look at the bigger picture of the

area around Puu O'o (Figure 5.1) shows that the haze produced by Puu O'o is floating south and southwest of the volcano.

The greatest difference between the A- and P-format results for Puu O'o is the size of the anomaly. Using band 7 as an example and neglecting anomalously high pixels due to haloes, haze, or detector saturation (a single row of saturated pixels having their origin in a saturated area and extending into areas which are not thermally emitting), the P-format data set (Figure 5.3) includes 15 saturated pixels and 31 pixels with DN values of 200 or greater. The P-format size of Puu O'o crater, assuming that the crater contains only saturated pixels (DN of 255), is approximately 180 m east to west and 150 m north to south. These dimensions increase to 210 m x 210 m if pixels having DN's $\geq$ 200 are considered to fall within the crater. On the other hand, the A-format data covering Puu O'o and vicinity (Figure 5.2) includes 24 saturated pixels and 26 pixels with DN values $\geq$ 200. The A-format size of Puu O'o crater, assuming that the crater contains only saturated pixels, is approximately 180 m x 180 m. The size of the crater does not increase when taking into consideration pixel values of 200 or greater. These statistics suggest that the cubic convolution process which is performed on A-format data to produce P-format data significantly changes the radiance values originally recorded by the detector. The correction process also tends to increase the size of the anomaly as can be seen by comparing the size of Puu O'o crater (pixels with DN's $\geq$ 200) in the uncorrected and corrected images.

This conclusion is reinforced when north - south cross-sections of DN values are veiwed for both formats of data taken across Puu O'o crater. The A-format cross-section (Figure 5.4) exhibits more abrupt and larger-scale increases and declines in DN across the anomaly than does the smoother P-format cross-section (Figure 5.5). Bands 5 and 7

of the A-format data (Figure 5.4) have more saturated pixels than the same column after cubic convolution is performed (Figure 5.5).

The differences in DN values for both A- and P-format images should be apparent in the results of dual-band calculations. Since there were no reports of surface flows or activity outside of the crater and there was a considerable amount of haze present, I have chosen to report results for only a 210 m x 270 m area which contains Puu O'o crater. Unfortunately, since most pixels within Puu O'o crater are saturated in TM bands 5 and 7, but not significantly greater than the background of band 3, dual-band calculations using either bands 5 and 7 or bands 3 and 4 can not be performed for the data collected of Puu O'o crater. In the instances where band 5 is saturated, I have listed the band 5 pixel-integrated temperature of 425°C. This should be regarded as potentially very inaccurate approximation, since the cool component temperature could be below this value if the radiance contribution by the hot component is large (Oppenheimer, 1991), or it could be above this value if the pixel radiance in band 5 is much greater than the saturation level of the detector.

Bearing these approximations in mind, I present the temperature and area results for the Puu O'o crater and vicinity for both the A- (Table 5.2) and P-format (Table 5.3) data. Of the 63 pixels presented for the uncorrected A-format data (Table 5.2), 15 were saturated in bands 5 and 7, preventing dual-band calculations with these channels. Unfortunately, attempts to use bands 3 and 4 for dual-band calculations were also unsuccessful because either the cool temperatures calculated from each band did not converge, or the pixel radiance in band 3 was not significant. Eight pixels returned a band 7 pixel-integrated temperature of 271°C, and should be regarded with caution since this represents the highest pixel-integrated temperature that could be derived

from band 7. For most of these pixels, band 7 was saturated, and the radiance from band 5 was too high for dual-band calculations, which meant that a band 7 pixel-integrated temperature was reported. Twenty-three pixels exhibited radiances in bands 5 and 7 which allowed for dual-band fits. However, the temperatures and areas reported for pixels south of the saturated area in Table 5.2 should be viewed with caution since there is a considerable amount of haze trailing to the south of the crater. The remainder of the pixels were fit with band 7 pixel-integrated temperatures since the radiances of bands 5 and 7 were not favorable for dual-band calculations.

Temperature and area statistics for the P-format data (Table 5.3) were different from those listed above for the A-format data. Only 7 pixels were saturated in both bands 5 and 7. For 7 pixels, a maximum band 7 pixel-integrated temperature of 266°C was reported. (The difference between this number and that of 271°C for the A-format data is a result of the different background radiances assumed in each case.). Thirty pixels exhibited radiances in bands 5 and 7 which could be used for dual-band calculations. For the remainder of the pixels a band 7 pixel-integrated temperature was reported.

Due to the limitations of the Landsat TM data collected over Puu O'o crater, it is extremely difficult to extract much information from the temperatures and areas presented here. The most interesting radiating pixels in regard to this study would be those within Puu O'o crater. Unfortunately, the large gap between dual-band solutions possible for bands 5 and 7 and bands 3 and 4 (Oppenheimer, 1991) prevents me from investigating this area with any accuracy. I have to conclude that any calculations involving the emitted energy of the Puu O'o crater would involve potentially very large errors due to the inability to derive temperature and hot fractional area solutions for

saturated pixels, and due to the inability to accurately estimate the effect that haze has on calculations for pixels south of the crater.

On a more qualitative level, observations of the results obtained for both A- and P-format data show that the cubic convolution process which is used to produce P-format data does tend to smooth (i.e. lower) pixel values at the edges of highly radiant anomalies such as Puu O'o crater. This directly affects the temperature and area pixel calculations which can result in changes in the interpreted size of an anomaly. For instance, if all band 5 and 7 saturated pixels fall within Puu O'o crater (which is a reasonable assumption since there were no reports of activity outside of the crater) then the A-format data would suggest a crater size of about 180 m x 120 m, while the P-format data of the same scene would give a crater size of 90 m x 90 m. However, these sizes could be exaggerated if radiance from especially bright pixels is affecting adjacent pixels (Rothery et al., 1988).

The radiative characteristics of Puu O'o are difficult to identify due to the limitations imposed by the Landsat TM data. I can qualitatively claim that if a lava lake of significant size had been present in Puu O'o then pixels containing this type of anomaly would be saturated in bands 5 and 7 due to the high radiant fluxes in these channels. In comparison, the two lava lakes of Erta'Ale registered on a January, 1986 Landsat TM P-format scene as a 60 m x 60 m anomaly for the nothern lake and 120 m x 150 m for the central lake. The central anomaly exhibited 5 pixels which were saturated in band band 7 and one of those was also saturated in band 5, while the Puu O'o P-format data of this study exhibited 7 pixels which were saturated in bands 5 and 7. This suggests that the Puu O'o anomaly was hotter that of the central lake at Erta'Ale. Lava lakes would also show elevated pixel values in band 4, but not necessarily in band

3, unless the band 3 pixel-integrated temperature was greater than 765°C. Given the amount of haze trailing south of the crater and knowing from personal experience the amount of outgassing which can occur at Puu O'o, I would say that it is entirely possible that many of the saturated pixels within the crater could have been a result of sunlight reflecting off of a thick haze. However, band 6 is also saturated in the area covering Puu O'o crater, which suggests that a thermal anomaly of unknown dimensions did occupy the crater.

5.4.2 Skylights

About 4 km ENE of Puu O'o crater (Figure 5.1) are two small groups of pixels having anomalously high pixel values in bands 4, 5, and 7 in both the A- and P-format data. I have assumed that these clusters are skylights since they are small enough to not cause a significant increase in the radiance measured in the 120 m pixels of band 6; yet, the areas are hot enough to show up in band 4. I chose the north-western-most of the two anomalies to study the differences between A- and P-format data.

Figures 5.2 and 5.3 show the distribution of the radiant energy from the skylight in the uncorrected and the corrected band 7 images, respectively. Skylights are normally small (< 5 m in diameter) when compared to the 30 m size (except band 6 which has a pixel size of 120 m) of a Landsat TM pixel. However, a number of effects may cause subpixel-sized hot radiators, such as skylights, to appear to cover a larger areal extent than they actually do. One consideration is that the skylight may be positioned near the "edge" of a pixel so that the radiance emitted by the skylight is divided between adjacent pixels (Rothery et al., 1988). The other consideration is that the radiant flux emitted by the skylight may be great enough so that the radiance emitted

in the area covered by one pixel may be registered in adjacent pixels (Rothery et al., 1988). It is difficult to determine the exact physical distribution of the thermally distinct areas in the group of "hot" pixels included in Figures 5.2 and 5.3. The high pixel DN's could result from numerous skylights or one large skylight which is either near the boundary between pixels or is radiant enough to affect the adjacent pixels. In any case, the initial distribution of energy for the A- and P-format cases are the same, since it is the same image, and differences in radiance are due to the corrections performed to produce the P-format data.

Keeping in mind the effects that small hot radiators have on TM pixels (Rothery et al., 1988), the size of the anomalous area is according to the P-format data is contained within a single pixel or within a 60 m x 60 m area depending on if saturation or if DN's $\geq$ 200 are the reguating criteria, respectively. The A-format data exhibits 3 saturated pixels in a 60 m x 60 m area, and 4 pixels have DN's > 200 in a 90 m east - west by 60 m north to south area. As I found for the previous section, the P-format correction process altered the radiances of the emitting pixels.

Histograms of DN's taken of the hot anomaly for both the A- (Figure 5.6) and P-format (Figure 5.7) data again show that the cubic convolution process tends to smear the boundaries of anomalies. The A-format data exhibit sharp boundaries, while the P-format data show the effects of smoothing that is a result of the correction process. I will note also that the histograms show that the two saturated pixels of band 7, in the A-format data (Figure 5.4) have been altered by the correction process to be reported as within the range of the band 7 sensor! This is a potentially large source of error when calculating temperatures and areas of subpixel-sized anomalies since saturation in bands means that the detected radiance is above the limit of the sensor by an unknown

amount; thus, the magnitude of the error introduced in this example by the correction process can not be determined.

Using the model outlined in section 5.4, I calculated temperature and area results for thermally emitting pixels contained within the skylight area shown in Figures 5.2 and 5.3. In both cases, if the thermal radiance was not significant (i.e., the DN value for the pixel minus the background DN value was less than 5) in the pixel a temperature of 40°C is reported. The temperature and area results for the A-format data (Table 5.4) show that a dual-band calculation was possible for 10 out of 30 pixels in the vicinity of the skylight(s). Two central pixels, which were saturated in bands 5 and 7, were not radiating above the background in band 3, so that a dual-band calculation using bands 3 and 4 could not be attempted. The remainder of the pixels were either radiating at the background temperature, or were fit with a band 7 pixel-integrated temperature which gives the upper temperature limit of the cool component within the pixel. The distribution of pixel temperatures (Table 5.4) was what I expected since the radiant temperature of the pixels increased nearer to the skylight(s).

The temperature and area results for the corrected, P-format data are given in Table 5.5. Of the 35 pixels investigated, 9 could be used for dual-band calculations using bands 5 and 7, 2 pixels were saturated in bands 5 and 7 and were assigned a pixel-integrated temperature of 425°C, and the rest of the pixels were either fit with band 7 pixel-intgerated temperatures or were assigned the background temperature. It is interesting to note that due to the correction process, one of the thermally emitting pixels was saturated in band 5, but not saturated in band 7. This result is not possible if the background component has been successfully compensated for and the rest of the radiance is only due to areas of the pixel emitting as blackbodies. It is a result that is

contrary to the boundary conditions of our problem (hot temperatures < 1130°C) and Planck's Law.

Comparing the A- and P-format dual-band calculations (Tables 5.4 and 5.5, respectively) for the same pixels, I found a range of the quality of correlations between temperatures and areas. Some of the dual-band results for the same pixel could have cool temperatures which were 30°C different and A-format hot fractional areas which were twice that of the P-format data.

The average flux density of a 120 m x 180 m area containing the skylight was calculated to be 2.9 x 10^3 W/m^2 for both data types. The total energy budget of the skylight for both formats of data were also very close at 6.3 x 10^7 W for the A-format data and 6.2 x 10^7 W for the P-format data. Although the pixel values were changed when the geometric correction process was applied to the A-format data, it did not seem to affect the outcome of energy calculations for this example of volcanic activity.

Using the two examples of skylights that I have identified in the TM images, I will note some of the general characteristics of skylights in terms of their radiative signature in Landsat TM data. Skylights are small, subpixel-sized anomalies which are very radiant in bands 4, 5, and 7. Due to their position within a pixel or the great amount of energy in the short wavelength infrared that they radiate, skylights may register as thermal anomalies in more than one adjacent pixel. However, skylights are small enough that they do not significantly elevate the radiance of band 6 above background levels.

5.4.3 Lava flows

Lava flows were by far the greatest source of thermally emitting pixels in the Landsat image collected on July 23, 1991. There were 3 areas (a total of 1.3 km^2) on the slopes of Kilauea which were covered by active flows. The breakout which occurred highest on the slopes of Kilauea began about 6.5 km due east of Puu O'o crater (see Figure 5.1) and extended 1.5 km east-south-east. This general area seems to mark the place where the tube system bifurcates to the south, feeding at least one flow area near the Royal Gardens subdivision. A second tube system evidently headed more to the south east, fed magma to five breakouts of various sizes.

The lava flows which will be investigated in this section are the flows which were 6.5 km east of Puu O'o and extended 1.5 km downslope towards the coast. A- (Figure 5.2) and P-format (Figure 5.3) band 7 images show that the 1.5 km active flow had a maximum flow width of about 0.5 km. Unlike skylights, lava flows cover large areas (many pixels) and high fractions of individual pixels, which is why they are also easily traced through band 6 data. Unlike volcanic craters, such as the Puu O'o lava lake, active lava flows do not necessarily have an ovoid shape, and generally do not have to have very distinct boundaries if the more recently erupted flows are surrounded by older thermally emitting flows.

The band 7 A-format image (Figure 5.2) of the up slope flow area (total size of 570 pixels or roughly 0.5 km2) contains 68 pixels with DN's of ≥200, including 52 pixels which are saturated. The band 7 P-format image (Figure 5.3) of the up slope flow area contains 108 pixels with DN's ≥ 200, including 63 saturated pixels. Close inspection of Figure 5.2 reveals that the up slope flow area may be roughly divided into two flows with each flow having a central area which saturates the band 7 sensor. The

central saturated pixels of the western most of the two flows seems to follow a NW to SE direction. These saturated pixels could either represent a central channel with smaller flows radiating away from the center, or this area may have a higher concentration of flows than the outer, less thermally distinct areas. The saturated area in the center of the westernmost flow is probably a little less than 240 m long and generally 90 m in width at the ends, but 180 m in width in the middle. Including the nonsaturated but thermally distinct pixels, the total flow width is probably about 0.5 km. The saturated center of the easternmost of the two flows is larger in length (300 m) and width (240 m in the middle) than the western flow. The saturated pixels of this flow follow a NW to SE trend. Including the nonsaturated but thermally distinct pixels, the total flow width is probably again roughly 0.5 km. These two flows may mark the area where the lava tube(s) from Puu O'o via Kupaianaha branch into two to feed the lava flows at the base of the Pali. The interpretation of trends in the P-format data is the same except that widths of the central saturated zones are smaller (up to 150 m for the western flow, up to 180 m for the eastern flow) and the total flow widths are about 0.1 km wider than those derived from the A-format data.

The cross-sections of the lava flow for A- (Figure 5.8) and P-format (Figure 5.9) data show similar trends to those of previous sections. The northern boundary of the active flow in both cases is sharp and distinct, but it is more abrupt for the A-format data. The pixels in bands 5 and 7 north of the saturated pixels in these cross-sections are definitely radiating above the background (DN of 13 for band 7, DN of 20 for band 5), which suggests that a younger lava flow may be covering a slightly older flow that is still hot enough to radiate energy in bands 5 and 7. Otherwise, these DN distributions could mark a central shallow (or exposed) flow channel that is < 150 m in

width with smaller flows and toes extending away from the central channel to a distance of about 90 m. In either case, the cross sections show that the pixels south of the saturated central pixels have higher DN's in band 5 than in band 7. Situations where band 5 is more radiant than band 7 are not realistic in terms of the Planck's Law. A similar trend was found for the other lava flows also, in that the pixels south of the main channel (saturated pixels) were anomalously hgh in band 5 relative to band 7. The reason for this may be easily explained in that the degassed haze was floating to the south when this scene was acquired, and had more of an effect on band 5 than it did on band 7.

The next step was to use the A- and P-format data to generate temperature and area fits to the thermally distinct pixels marking the extent of the lava flow. The results of the A-format study are given in Figures 5.10 and 5.11 (for crust temperatures and hot fractional areas, respectively). Of the 570 pixels examined for the flow in this study, 9 were saturated in bands 5 and 7 requiring a maximum pixel-integrated band 5 estimate of 425°C (Figure 5.10). These saturated pixels occurred in the central channels of both flow areas, signaling areas of intense activity, possibly located over active lava tubes. For the A-format data, 234 of the 570 pixels exhibited suitable radiances which could be used for band 5 and 7 dual-band calculations. The remainder of 327 pixels were either fit with band 7 pixel-integrated temperatures or radiated at the background temperature of 40°C because they were not thermally significant. The results for the P-format data (Figures 5.12 and 5.13, crust temperatures and hot fractional areas, respectively) were similar with the exception that only 4 pixels were saturated in both bands 5 and 7. Band 5 and 7 radiances of 250 pixels could be used for dual-band calculations, with the remainder at band 7 pixel-integrated temperatures or at the background temperature.

Both temperature and hot fractional area results for the A- and P-format data seem to include inconsistancies, in that as the center of the flow is approached from its edge, the pixel temperatures increase and then discontinuously drop to a lower value and then increase again. This drop in temperature corresponds to the boundary between pixels which may be used for dual-band calculations and those pixels which can not be used. In almost all circumstances, the pixels which are thermally significant in band 7 along the outer flow margins are not suitable for dual-band calculations, so that a pixel-integrated temperature is generated to represent these pixels. The pixel-integrated temperatures generally show increasing values towards the center of the flow (Figures 5.10 and 5.12). At the boundary where pixel-integrated temperatures are replaced by dual-band calculations, the dual-band temperature is lower because it represents the radiative temperature of only the solid crust or cool component temperature. The pixel-integrated temperature on the other hand represents both the solid crust and the hot fractional area which could not be separated due to the limitations of the data.

Analysis of the crust temperature and hot fractional area data obtained using both types of data (A- and P-format, Figures 5.10 and 5.11, and 5.12 and 5.13, respectively) for the 0.5 km^2 lava flow shows that there definitely was not an even distribution of energy emitted across the flow surface. Crust temperature (Figures 5.10 and 5.12) and hot fractional area (Figures 5.11 and 5.13) increased away from the flow boundaries and continued to increase until the center of the flow (marked by saturated pixels) was reached. This observation was valid both across the flow and along the length of the flow. The active center of the lava flow seems to have been divided into two parts separated by about 450 m from the end of the first branch to the beginning of

the next branch. These could mark the two tubes feeding extensive flows to the south and south east. If I consider pixel-integrated temperatures of > 200°C to mark the active flow, then the western flow was approximately 540 m long (NW to SE) and 260 m wide at its widest point. The eastern flow began about 150 m east of the western active flow center and ran east for about 300 m before following a SE direction for the remainder of its 800 m total length. The eastern flow was about 190 m at its widest cross-section. The two flow areas may have been joined by a narrow (60 m) east-west corridor of activity. Surrounding the more active parts of the flow field are areas (at least 90 m wide) where thermal radiance was measurable above background levels signifying that either cooling inactive flows or less concentrated active flows occupied these areas. Thus, for this flow field there were no abrupt increases in crust temperature at the margins of the flows which would suggest a large advancing flow front, for example.

I calculated the average flux density and the total energy budget of the entire flow (see Chapter 3, section 4.4 for how average flux densities and total energy budgets are calculated) using results from the A- and P-format data. The results were very consistent in that the average flux density of the flow for both A- and P-format data were 2.6×10^3 W/m^2. The total energy budget of the 0.5 km^2 flow was 1.3×10^9 W for both types of data. This result suggests that while the correction process (A- to P-format) does alter the DN values of pixels which are adjacent to other pixels having greater or lesser DN values, this correction does not have a significant effect on the estimation of the energy output of the anomalous surface.

Lava flow radiative characteristics determined from the image used in this study may be summarized as follows. Unlike that found for Puu O'o crater (section 5.4.1) or skylights (section 5.4.2), lava flows do not exhibit sharp pixel to pixel radiance

differences from a background DN to a saturated DN value. Lava flows tend to show a steady increase in radiance in bands 5 and 7 as the center of the flow was approached from the margin. Lava flows tended to be much greater in size (tens to hundreds of pixels versus less than 10 pixels for most other activity) than any of the other volcanic anomalies studied here. Lava flows erupted along noticeable trends suggesting the presence of underground feeder tube systems.

5.4.4 Lava flow in cloud shadow

I was very fortunate in that the image of Kilauea obtained on July 23, 1991, included some relatively small lava flows in the shadow of clouds. The background DN of all bands except 6 in the areas under clouds were lower because the amount of reflected sunlight detected by the Landsat TM was less in these areas than the areas in full sunlight. Boundaries between flows and the background were much more distinct for the flows in the cloud shadow. The flow that I have chosen to compare A- and P-format results is located about 10 km east south east of Puu O'o and is the largest bright area which can be seen at this location in the cloud shadow (Figure 5.1). Band 7 A-(Figure 5.2) and P-format (Figure 5.3) images suggest that the flow erupted along a west to east trend. Elevated pixel values from the A-(Figure 5.2) and P-format (Figure 5.3) data suggest that the lava flow was ~ 300 m west to east by 180 m north to south. Perhaps the greatest difference between the two sets of data are the pixel values which cover the same areas in the A- and P-format images. The A-format uncorrected data contains 12 saturated pixels and 17 pixels having DN's $\geq$ 100. On the other hand, the P-format, corrected data contains only 9 saturated pixels and has 21 pixels that have DN's greater than 100. This is a difference is a result of the correction process used to produce

P-format data. I interpreted the A-format anomaly to be a fairly substantial, very recent (due to the number of saturated pixels) lava flow, but the correction process has smeared the original anomaly, and I would interpret the P-format image as a smaller flow which had either cooled significantly or occupied only fractions of pixels at high temperatures.

Cross-sections of the flow reinforce the point that the correction process has smeared the original data. The A-format (Figure 5.14) cross-section has distinct flow boundaries and saturated band 7 pixels in the center of the flow. The P-format data (Figure 5.15) shows the effects of the correction process because flow boundaries are less distinct due to the smearing of pixel values.

The results of temperature and area calculations on the thermally bright pixels are given in Tables 5.6 and 5.7 for the A-format and P-format data, respectively. Results for the central pixels where band 7 was saturated are roughly consistent. Of the 54 A-format pixels representing the flow, 24 had band 5 and 7 radiances which were suitable for dual-band calculations. The P-format data (Table 5.7) results included 32 pixels for which dual-band calculations were possible. The temperatures and hot fractional areas obtained from the dual-band fit was roughly (within 14°C) consistent in most cases, although some pixels exhibited larger differences (up to 37°C).

Calculations of the average flux density for this lava flow yielded 2.5×10^3 W/m^2 for the A-format case and 2.7×10^3 W/m^2 for the P-format case. These values bracket those found for the flow in the previous section. The total energy budget of the flow was 1.2×10^8 W in the A-format case and 1.3×10^8 W in the P-format case. These values are consistent with one another but contain potentially large errors due to the uncertainty of the numbers approximated without the dual-band method.

The radiance contributions from thermal anomalies were considerably easier to identify in the case of the lava flow in the cloud shadow rather than that of the previous case where the lava flow was in sunlight. The A-format data exhibited a slightly larger core of saturated pixels than the P-format data. This is assumed to be an effect of the data smoothing which, when using the data to calculate radiative temperatures, is an unwanted attribute of the correction process.

5.4.5 Lava tubes at coast

Another type of volcanic activity that was present in the Landsat TM scene was a series of active lava tubes pouring magma into the ocean. Two areas occupying only a few pixels mark areas where the tube systems supplying the flow branches described in section 5.5.3 emptied lava into the ocean. I will choose the larger of the two anomalies which was situated at the end of the westernmost flow branch. In Figure 5.1, this area is 10 km south east of Puu O'o.

Band 7 images of the area in both A- (Figure 5.2) and P-format (Figure 5.3) reveal that there were actually two tube exit points located about 180 m apart. The A-format image (Figure 5.2) yields a saturated band 7 pixel value at the tube furthest to the east, which seems to be the larger of the two exit points because of the cluster of 4 high pixel values. A total of 4 pixels have DN's ≥100 in the A-format image. Details in the P-format image (Figure 5.3) are somewhat smeared. There are no saturated pixels, but there are 6 pixels with DN's ≥ 100.

Looking at the cross-sections through the larger tube for both data types (Figures 5.16 and 5.17), one can see the effects of the correction process on the P-format data. The A-format data exhibits much more distinct boundaries than the P-format data. Pixel

values for the P-format data are smeared relative to those in the uncorrected A-format case. This is especially evident when comparing the cross-section DN values for band 5 of both data types. The A-format data returns a high band 5 DN value in the fourth pixel of the cross-section, which is smeared out (almost halved) in the P-format data.

A comparison of the temperature and area fits to the pixel values of both types of data yields consistent results. Of the 32 pixels in the study area, 5 A-format pixels (Table 5.8) and 6 P-format pixels (Table 5.9) exhibited radiances in bands 5 and 7 which allowed dual-band calculations. The dual-band results obtained for both sets of data were consistent. The remainder of the pixels were either not radiating significantly above the background or were fit with band 7 pixel-integrated temperatures. Average flux densities calculated for four radiant pixels forming a 60m x 60m square around each of the tube sites yielded values of 3.3×10^3 W/m^2 for the A-format case and 3.2×10^3 W/m^2 for the P-format case. These values translate into total energy budgets of 2.4×10^7 W and 2.3×10^7 W for the A-format and P-format data respectively.

Open ended lava tubes pouring magma into the ocean were conspicuous in this data set because they are small, yet highly radiant anomalies. Average flux densities of these anomalies are high relative to that of lava flows, but their small size means that their energy budgets are negligible when compared to the total energy budget of the actively erupting volcano.

5.4.6 The total energy budget for Kilauea

Given the results obtained in the 5 previous sections as well as temperature and hot fractional area data for all of the thermally radiant areas of the volcano, I present a breakdown of the energy budgets (Table 5.10) of each of the anomalies identified on the

slopes of Kilauea using both A- and P-format data. These results are only an approximation at best, since many pixels were saturated in bands 5 and 7 and could not be fit using the dual-band method. Many more pixels were fit using a band 7 pixel-integrated temperature which may have been either a high or low estimate depending on whether or not band 7 was saturated for the given pixel. In addition to this, because the radiances of lava flow margins tended to grade into background radiances gradually rather than abruptly, I admit that the placement of flow boundaries is somewhat subjective.

As shown in Table 5.10 the total energy budget for the volcano was 3.8 x 10^9 W for both formats of data. By far, the largest contributors to the total energy budget of the volcano were the three large areas of flows on the slopes of Kilauea. A number of previous studies have attempted to quantify Q for different volcanic sources, which are summarized in Chapter 3, section 4.4. However, of particular interest are the results of other Landsat surveys. Glaze et al. (1989) used Landsat TM data to derive Q values of 0.3 – 7.6 x 10^7 W for Lascar, 5.8 x 10^7 W for Erebus and 6.9 x 10^7 W for Erta Ale volcanoes, respectively. Further Landsat TM results presented in Pieri et al. (1990) calculate a Q value of 12.5 x 10^7 W for a June 1984 lava flow on Mt. Etna. These results are at least an order of magnitude lower than the result that I have found here. This is in part due to the fact that the Mt. Etna lava flow (Pieri et al., 1990) was about 8 x 10^4 m^2, while the upper slope flow (section 5.4.3) alone covered a much larger area (5.1 x 10^5 m^2). Comparing the average flux densities of the two flows reveals that the Kilauea flows emitted more power per unit area (2600 W/m^2) than the Mt. Etna flow (1500 W/m^2, Pieri et al., 1990). Again, I would caution against the absolute

reliability of energy budget calculations of Landsat TM data due to the unsuitability of the data.

5.5 Discussion

There are a number of questions which arose while I was processing both types of data for the available Landsat TM image. I will state them here and discuss them in separate sections below.

1) How can I determine which pixels have elevated radiances due to haze rather than thermal radiators within a given pixel?

2) In a similar fashion, any Landsat TM image acquired during daylight hours will have an amount of reflected sun in each pixel that has a variable effect on the data depending on the amount of emitted radiance from the pixel. This was considered in Chapter 4, but for satellite data how can this component be accounted for?

3) Is the central wavelength in a given TM band the most accurate to use for dual-band calculations?

4) How do the results obtained with Landsat TM data compare with those reported for Kupaianaha lava lake in Chapter 3 and the flow activity in Chapter 4?

5.5.1 Reflected component due to haze

While trying to fit temperatures and areas using bands 5 and 7 to A- and P-format pixel values, it immediately became obvious that something was causing anomalously high radiances in band 5 south of active areas which was not present in pixels to the north of the anomaly. This phenomenon was particularly apparent for the data collected

in the vicinity of Puu O'o crater. Pixel values south of the crater were elevated in all bands except band 6. In the A-format data, band 6 showed saturated DN values for only a very small area (240 m x 120 m, or two band 6 pixels). The rest of band 6 did not show any anomaly. Even more suspect was the discovery that band 3 and 4 pixel values were also elevated south of the crater but not north of the crater. Finally, there were no reports of activity on the slopes of Puu O'o or in the vicinity of Puu O'o other than within the crater. For these reasons, it seems logical to assume that the elevated radiances south of Puu O'o crater are entirely due to haze which was reflecting significant amounts of sunlight back to the Landsat satellite.

To my knowledge, there have not been any studies using Landsat TM data which have attempted to model the effects of haze in thermally radiant, volcanologically active areas, although Abrams et al. (1990, unpublished) have attempted haze removal for airborne Thematic Mapper Simulator data of Kupaianaha. The magnitude of the haze component should decrease with distance from the source vent as the wind disperses gas and particles. However, for areas such as Puu O'o crater where it is known that considerable outputs of haze are common, and the crater itself is frequently filled with haze, it may be extremely difficult to separate the haze component from the thermally emitted radiance. While it is imposssible to be absolutely convinced that the haze component is removed from the data, one method which would be most useful in removing most of the haze component would be a line by line background estimation for each line containing thermally radiant pixels, such as that described in Oppenheimer (1991). This method would lessen the contamination of haze in the data by treating it as a background component which could be removed. If the layer of haze was not sufficiently

opaque in the infrared, band 6 could also be used to detect pixels which are both covered with a layer of reflective haze and emitting thermal energy.

5.5.2 The reflected sunlight component

The background radiance for thermally emitting pixels may be determined from nearby pixels which are not thermally radiant. To accurately estimate the background radiance, the slope incline on which the active surface lies (Rothery et al.,1988) and haze characteristics should be consistent if possible for both the thermally radiant pixels and the pixels used to estimate the background radiance.

Background radiance comes from two sources, thermal radiation which is emitted as a result of absorbed solar radiation, and the reflection of sunlight off of the observed surface. If I can identify and separate the radiance contributions of these two background components then I would be able to model the distribution of background radiance across the Landsat TM bands. In the available Landsat TM image, there are a variety of pixels which are located in cloud shadows. I know that the background radiance in sunlight minus the background radiance under a cloud is part of the radiance from reflected sunlight. Now I can determine the distribution of energy across the wavelength band for a given amount of sunlight.

Using data for the irradiance of the sun at 1 optical depth presented in Wolfe and Zissis (1985), I can crudely approximate the distribution of reflected sunlight across bands 5 and 7. The amount of reflected sunlight decreases linearly across the bands so calculation of the reflected solar energy at the ends of the wavelength bands (1.55 and 1.75 μm for band 5, and 2.08 and 2.35 μm for band 7) is all that is required. For band 5, the solar irradiance decreases from 19 to 8 mW cm^{-2} μm^{-1} at 1.55 - 1.75 μm.

For a surface having only 0.5% reflectance, this translates into a reflected solar component of 1 x 10^{-2} to 4 x 10^{-3} mW cm^{-2} μm^{-1} sr^{-1} across band 5. These numbers are 5 orders of magnitude above the radiance produced by a surface radiating at 40°C due to solar warming. For band 7, the solar irradiance decreases from 7 to 2 mW cm^{-2} μm^{-1} at 2.08 - 2.35 μm. For a surface having only 0.5% reflectance, this translates into a reflected solar component of 4 x 10^{-3} to 1 x 10^{-3} mW cm^{-2} μm^{-1} sr^{-1} across band 7. These numbers average an order of magnitude above the radiance produced by a surface radiating at 40°C due to solar warming.

The results of these calculations show that the reflected solar energy component which makes up the majority of the background radiance is significantly higher at the beginning of bands 5 and 7 than at the end of the bands. Depending on the magnitude of the thermal anomaly within a given pixel, this could have a profound effect on the thermal distribution of energy for the pixel.

5.5.3 The wavelength to use for dual-band calculations

Previous studies (Rothery et al., 1988; Glaze et al.,1989; Pieri et al.,1990; and Oppenheimer, 1991) using Landsat TM data have chosen the central wavelength in the band as the optimal wavelength for the study. Oppenheimer (1991) states that for channels of narrow spectral width this approximation should not have a significant effect on temperature and area calculations. However, given the distribution of reflected sunlight from the background component (calculated in the previous section) and the distribution of radiance across a band due to the crust temperature, I can show that the latter wavelengths are much more accurate choices for dual-band or pixel-integrated temperatures.

Figures 5.18 and 5.19 plot the emitted energy of lava crusts radiating at typical dual-band temperatures found in this study for bands 5 and 7, respectively. From this information, I can calculate the ratio of emitted radiance at the end of the band compared with that at the beginning of the band. The ratios show that 5.14 to 6.73 times more energy is emitted at the longward end of band 5 than at the beginning of band 5 for crust temperatures between 150 and 200°C. Similar calculations for band 7 show that 2.83 - 3.42 times as much energy is emitted at the longward end of band 7 than at the beginning. This would support my idea that the center of the wavelength band is not the most accurate wavelength to choose for dual-band or pixel-integrated calculations.

However, when a hot fractional radiating area is present in the pixel, such as that found for dual-band fits to pixels, the problem becomes much more complex. The reason for this is shown in Figures 5.18 and 5.19. The emitted energy of a very small fractional hot area (having a blackbody temperature of 1130°C) identified in this study (9.0×10^{-6}) is plotted in Figure 5.18 for band 5. This shows that in almost all dual-band solutions identified in this study that the hot fractional area radiates the majority of the emitted energy in band 5, and that this contribution is fairly uniform across the band.

The emitted energy of sample fractional hot areas (having blackbody temperatures of 1130°C) identified in this study (9.0×10^{-6} and 6×10^{-4}) are plotted in Figure 5.19 for band 7. This shows that in the dual-band solutions identified in this study that the hot fractional area radiates a significant (and in some cases dominant) amount of the emitted energy in band 7. Again, as was the case for band 5, the emitted energy from the hot component in band 7 is fairly constant across the wavelength band.

The results of this exercise are not surprising when viewed in the context of the Chapter 3 and 4 results. In Chapter 3, section 4.2, I showed that the hot radiance component dominated that of the solid crust at < 1.49 μm for Stage 3 (solid crust) activity on the surface of Kupaianaha lava lake, and in Chapter 4, the radiance of the hot component dominated that of the crust at < 1.00 μm (I use temperature and area model results from Figure 4.7 for this calculation). The values that I calculated for the hot fractional areas in Chapter 3 were generally an order of magnitude less than the lowest detectable using the dual-band method, but the fractional hot area values for the cooling lava flow in Chapter 4 were, for the most part, within the range or higher than those derivable with the dual-band method. Thus, the result discovered for band 5 above is confirmed by observations in Chapters 3 and 4. On the other hand, depending on the hot fractional area and the temperature of the crust, Figure 5.19 shows that the radiance from the hot fractional area can be a very small or dominant part of the total pixel radiance in band 7.

I conclude that because of the highly variable radiance contribution which the hot fraction contributes to band 7 and, because of the subordinate to negligible amount of radiance that the crust component contributes in band 5, that choosing another representative band wavelength other than the central wavelength would be difficult even on a pixel by pixel basis without first knowing the crust temperature and fractional hot area. I would also stress that the hot fractional area and, hence, the hot temperature are very important contributors to the total radiance. This is a point that seems to be neglected in previous studies (Glaze et al., 1989; Oppenheimer, 1990), which are quick to assume that the crust component dominates the short wavelength infrared spectrum.

To summarize, my measurements of lava crusts in Chapter 3 showed that the fraction radiating at the core temperature was low enough that sunlight dominated the wavelengths below 1.55 μm. The Landsat data that I studied here returned dual-band calculations of between 100 - 270°C with hot fractions varying between 6×10^{-4} and 9×10^{-6}. Given these areas, the hot component can contribute anywhere between 10% and 90% of the total radiance of the emitting pixel. This result is intensified by the fact that some solutions to the dual-band problem are given as lower limits (Oppenhiemer, 1991) because band 7 saturates and the radiance from band 5 is too great for dual-band calculations.

When the DN value in band 5 or band 7 is small enough to necessitate a pixel-integrated temperature calculation, caution should be excersized to take into account the distribution of reflected sunlight across the wavelength band. This may lead to a significant shift in the wavelength chosen to do the pixel integrated temperature fit. The shift will be toward longer wavelengths, since both bands 5 and 7 have decreasing contamination from sunlight with wavelength.

5.5.4 A comparison with the lava lake data

Values for the average flux densities of lava flows identified using Landsat TM data are consistent with some results found for Stage 3 (quiescent crust) activity of Kupaianaha lava lake in Chapter 3. An unreliable (due to the limitations of the Landsat TM data) estimate of the average flux density for Puu O'o crater was about 6.0×10^3 W/m^2, which would have been consistent with stage 2 activity at Kupaianaha. I would like to point out that, if Puu O'o crater exhibited a high average flux density such as that calculated here, it would have had to have an actively overturning lava lake covering the

much of the crater floor! Since this is highly unlikely and is not supported by helicopter pilot reports over the area, I must assume that some potentially large fraction of the total energy calculated for Puu O'o is actually due to sunlight reflecting off of the haze collected within the crater. Finally, estimates of the total energy budget of the volcano using Landsat TM data are over an order of magnitude above those calculated for Kupaianaha, but this is a result of the enormous size difference between the volcanic anomalies.

5.6 Conclusions

This chapter compared the radiative charcteristics of A- and P-format Landsat Thematic Mapper data for several types of activity on Kilauea volcano on July 23, 1991. A-format data are the raw data collected by the satellite which have not been geometrically corrected. P-format data have been geometrically corrected by a process known as cubic convolution which resamples neighboring pixels. The results of this study suggest that the process which produces P-format data tends to smear the boundaries of distinct anomalies. An example of this (although not for a thermally emitting source) may be observed in the boundaries between pixels covered by clouds and those that are not. Cross-sections perpendicular to cloud boundaries show how A-format data (Figure 5.20) preserves a sharp and distinct boundary in bands 4, 5, and 7 between cloud-covered and non-cloud-covered pixels. On the other hand, it is difficult to determine where the clouds begin in the P-format data (Figure 5.21) because the sharp cloud boundary is smeared by the averaging process.

While the DN values of individual pixels and, hence, the radiance values of those pixels were altered by the geometric correction process, this did not have a noticeable

effect on calculations of either the average flux density or the total energy budget of the thermally emitting areas. Any small differences between the energy calculations for the A- and P-format data are minute compared to the potential arrors that I was forced to accept due to the limitations of the data and the large numbers of pixels for which pixel-integrated temperatures were the only possible fit.

I conclude from this study that while Landsat TM data are particularly useful for mapping volcanic activity at a reasonably fine scale of 30 m, they are hopelessly inaccurate as a means for calculating the temperatures, fractional hot areas, or energies of active eruptions. The relatively small set of pixel values for which dual-band calculations are feasible forced me to approximate fits of radiant pixels with pixel-integrated temperatures, which could result in very large errors in the average flux density and the total energy budget of the volcano. Instances where bands 5 and 7 are both saturated, such as that for Puu O'o crater, led to particularly frustrating situations, since these areas which are the most thermally apparent can not be successfully fit with either a temperature or a fractional hot area.

With these comments in mind, I have to conclude that the A-format data are the lesser of two evils. While it is not geometrically correct, individual pixel DN's and, hence, radiances are maintained allowing for more accurate mapping of the boundaries of thermal anomalies. The Earth Observation Satellite Company has begun to offer Landsat TM data which have been nearest-neighbor resampled (Andre Kiebuzinski, personal communication, 1992), which preserves individual pixel values and corrects for geometric distortion. This format of data seems to offer the benefits of the A- and P-format data and should be considered in further studies of active volcanoes.

In this chapter, I calculated the radiative energy budget of volcanic activities and used it as a criterion to judge the usefulness of Landsat TM data for monitoring volcanoes. However, as I have pointed out, Landsat TM data may be used to accurately map volcanic activity. I would also propose that this type of data could be used to *predict* the location of certain volcanic landforms. For instance, the location of tumuli (Walker, 1991) may or may not correspond to the saturated pixels of the lava flow field which signify intense activity. It is also possible to predict the locations of lava tubes if there are enough skylights and active flows to serve as markers (There were ample in this data set).

What is really required for further studies of active volcanoes are new satellite instruments which have more bands of narrower spectral width. If possible, these bands should also have greater dynamic ranges than the present generation of sensors. A combination of these attributes will allow for the solution of two or more radiating subareas in a single pixel. The future generation satellite instruments of the Earth Observation System, more specifically HIRIS, MODIS, and ASTER should be more than capable of allowing for accurate studies of the radiative properties of volcanoes. Radiative temperature measurements with field spectroradiometers, such as that reported in Chapters 3 and 4 provide the only accurate measurements of the energy budget of *any* volcanic anomalies to date.

References

Andres, R. J. and W. I. Rose, Detection of Thermal Anomalies Associated with the Santiaguito Dome, Guatemala With Landsat Thematic Mapper Imagery Abstracts of the Fall 1991 American Geophysical Union Conference, *EOS supplement*, 523, 1991.

Crisp, J., and S. Baloga, A model for lava flows with two thermal components, *J. Geophys. Res., 95*, 1255 - 1270, 1990.

Dozier, J., A method for satellite identification of surface temperature fields of subpixel resolution, *Remote Sens. Environ., 11,* 221 - 229, 1981.

Glaze, L., P. W. Francis, and D. A. Rothery, Measuring thermal budgets of active volcanoes by satellite remote sensing, *Nature, 338,* 144 - 146, 1989.

Kahle, A. B., Gillespe, A. R., Abbott, E. A., Abrams, M. J., Walker, R. E., Hoover, G. and J. P. Lockwood, Relative dating of Hawaiian lava flows using multispectral thermal infrared images: a new tool for mapping young volcanic terranes. *J. Geophys. Res., 93*, 15239 - 15251, 1988.

Markham, B. L., and J. L. Barker, Landsat MSS and TM post-calibration dynamic ranges, exoatmospheric reflectances and at-satellite temperatures, *EOSAT Tech. Notes 1*, pp. 3 - 8, Earth Obs. Satell. Co., Lanham, Maryland, 1986.

Matson, M. and J. Dozier, Identification of subresolution high temperature sources using a thermal IR sensor, *Photogramm. Eng. Remote Sens., 47,* 1311 - 1318, 1981.

Mouginis-Mark, P. J., S. K. Rowland, H. Garbeil and P. Flament, AVHRR Observations of the Kupaianaha Eruption, Hawaii, Abstracts of the Fall 1991 American Geophysical Union Conference, *EOS supplement*, 562, 1991.

Oppenheimer, C., Lava flow cooling estimated from Landsat Thematic Mapper infrared data: the Lonquimay eruption (Chile, 1989), *J. Geophys. Res., 96,* 21,865 - 21,878, 1991.

Pieri, D. C., L. S. Glaze, and M. J. Abrams, Thermal radiance obseravtions of an active lava flow during the June 1984 eruption of Mount Etna, *Geology, 18,* 1018 - 1022, 1990.

Rothery, D. A., P. W. Francis, and C. A. Wood, Voicano monitoring using short wavelength infrared data from satellites, *Journal of Geophysical Research, 93,* 7993 - 8008, 1988.

Shu, F. H., *The Physical Universe: An Introduction to Astronomy*, University Science Books, Mill Valley, California, 1982.

Walker, G. P. L., Structure, and origin by injection of lava under surface crust, of tumuli, "lava rises", "lava-rise pits", and "lava-inflation clefts" in Hawaii, *Bull Volcanol, 53,* 546 - 558, 1991.

Wolfe, W. L., and G. J. Zissis, *The Infrared Handbook*, Infrared Information and Analysis (IRIA) Center, Environmental Research Institute of Michigan, Ann Arbor, Michigan, 1985.

Table 5.1

Landsat Thematic Mapper bands and corresponding spectral ranges. Bands 5, 6, and 7 were most useful for this study. Bands 5 and 7 were used for dual-band calculations.

Band number	Spectral Range
1	0.45 - 0.52 μm
2	0.52 - 0.60 μm
3	0.63 - 0.69 μm
4	0.76 - 0.90 μm
5	1.55 - 1.75 μm
6	10.4 - 12.4 μm
7	2.08 - 2.35 μm

Table 5.2

Crust temperature and hot fractional area dual-band method results for Landsat TM bands 5 and 7 A-format spectral data for an area surrounding Puu O'o crater. Columns and rows are listed in bold and are underlined. Top number in each row and column pair is either the dual-band crust temperature solution or pixel-integrated band 7 crust temperature in °C. The hot fractional area for the pixel radiating at 1130°C is listed below the crust temperature. Entries of "0" denote pixel-integrated calculations in which it was not possible to separate the hot and crust components. Numbers other than zero are the dual-band calculated hot fractional areas. Actual values for the fractional hot areas are the listed value multipied by 10^{-4}. In instances where both bands 5 and 7 were saturated (raw DN = 255), the pixel-integerated upper temperature limit of band 5 has been listed (425°C). Note that there were 8 saturated pixels in a 90 m x 90 m area according to the A-format results presented here.

	1	2	3	4	5	6
1	162	152	209	212	208	209
	0.38	0	0	0.10	0.27	0.22
2	204	205	244	238	197	209
	0.34	2.87	2.07	0	0	0
3	232	127	266	264	155	256
	0	5.77	0	0	5.11	0.46
4	263	266	425	425	266	137
	0	0	0	0	0	4.76
5	266	266	425	425	425	263
	0	0	0	0	0	0
6	245	266	425	425	425	262
	1.48	0	0	0	0	0
7	227	208	266	265	190	214
	0	2.81	0	0	3.55	4.27
8	196	219	232	240	238	234
	0	0.31	1.84	1.04	0.42	2.18
9	157	170	216	213	217	221
	1.21	1.44	0.37	0.97	2.13	1.89

Table 5.3

Crust temperature and hot fractional area dual-band method results for Landsat TM bands 5 and 7 P-format spectral data for an area surrounding Puu O'o crater. Style of presentation is the same as that of Table 5.2. Actual values for the fractional hot areas are the listed values multipied by 10^{-4}. Area of coverage is the same as that of Table 5.2. Note that there were 14 saturated pixels in a 120 m x 240 m area according to the P-format results presented here. The difference in saturated pixels between the results presented in Tables 5.2 and 5.3 is due to the geometric correction process which "smears" anomalies in P-format data.

	1	2	3	4	5	6
1	216	187	174	226	229	230
	0	0	1.56	0	0	0
2	217	165	176	196	141	230
	0	2.80	5.99	4.19	1.63	0
3	219	248	425	425	271	231
	0	2.63	0	0	0	3.97
4	425	425	425	425	425	271
	0	0	0	0	0	0
5	271	425	425	425	425	425
	0	0	0	0	0	0
6	228	246	271	425	425	271
	0.98	2.94	0	0	0	0
7	203	226	148	271	242	198
	0.69	0.41	6.30	0	0.69	5.49
8	173	185	182	214	197	171
	0.91	1.60	2.91	2.26	3.72	4.46
9	229	230	225	225	246	252
	0	0	0	0	0	0

Table 5.4

Crust temperature and hot fractional area dual-band method results for Landsat TM bands 5 and 7 A-format spectral data for an area containing one or more skylights. Style of presentation is the same as that for Table 5.2. Actual values for the fractional hot areas are the listed values multipied by 10^{-4}.

	1	2	3	4
1	128 0	40 0	127 0.51	40 0
2	216 0.37	233 3.96	188 0	158 0
3	246 1.53	425 0	425 0	152 0
4	176 0.25	168 1.09	191 0	98 0.15
5	120 0	128 0	163 0.67	128 0.45
6	40 0	120 0	156 1.33	194 0

Table 5.5

Crust temperature and hot fractional area dual-band method results for Landsat TM bands 5 and 7 P-format spectral data for an area containing one or more skylights. Style of presentation is the same as that for Table 5.2. Actual values for the fractional hot areas are the listed values multipied by 10^{-4}. Area of coverage is the same as that of Table 5.4. Results are consistent with those obtained for the A-format data listed in Table 5.4

	1	2	3	4
1	149 0	181 0	184 0	40 0
2	203 0.75	201 5.25	237 0	149 0
3	235 2.06	425 0	425 0	189 0
4	151 0.27	165 0.85	136 0.80	124 0.21
5	40 0	40 0	138 0.62	140 0.50
6	40 0	40 0	203 0	204 0

Table 5.6

Crust temperature and hot fractional area dual-band method results for Landsat TM bands 5 and 7 A-format spectral data for an area of lava flows in the shadow of a cloud. Style of presentation is the same as that for Table 5.2. Actual values for the fractional hot areas are the listed values multipied by 10^{-4}. Background DN values were less than half that of areas exposed to sunlight at the time of acquisition. A central core of hotter crust temperatures may represent an area of concentrated flow activity.

	1	2	3	4	5	6	7	8	9
1	120 0	161 0	149 0	145 0	149 0	155 0	120 0	40 0	120 0
2	161 0	189 0.07	199 0.06	197 0.18	225 0.75	181 0.54	128 0	135 0	40 0
3	166 0	222 0.25	229 4.45	229 4.45	259 1.21	213 5.28	201 0.40	190 0	163 0
4	173 0	268 0.65	201 5.72	273 0	249 2.98	273 0	176 6.29	156 6.53	40 0
5	152 0	212 0.10	234 1.01	232 0.96	204 0.69	244 1.20	231 1.08	247 3.05	150 1.21
6	40 0	161 0	168 0	161 0	161 0	149 0	170 0	140 0	158 0

Table 5.7

Crust temperature and hot fractional area dual-band method results for Landsat TM bands 5 and 7 P-format spectral data for an area of lava flows in the shadow of a cloud. Style of presentation is the same as that for Table 5.2. Actual values for the fractional hot areas are the listed values multipied by 10^{-4}. Background DN values were less than half that of areas exposed to sunlight at the time of acquisition. A central core of hotter crust temperatures may represent an area of concentrated flow activity. These results are roughly consistent with those presented in Table 5.6

	1	2	3	4	5	6	7	8	9
1	120 0	161 0	166 0	155 0	166 0	173 0	155 0	120 0	120 0
2	149 0	178 0.19	201 0.40	201 0.46	210 0.86	222 1.00	188 0.24	128 0	140 0
3	135 0	210 0.16	215 4.09	218 5.09	258 1.85	229 4.51	228 2.45	189 0.07	187 0
4	40 0	251 0.65	215 5.21	273 0	232 4.32	273 0	153 6.59	225 4.70	2.54 1.02
5	128 0	212 0.22	228 1.21	233 1.48	218 0.95	224 1.52	238 1.34	232 2.84	239 2.39
6	40 0	161 0	177 0.08	180 0	172 0	166 0.08	173 0.08	170 0.26	166 0.14

Table 5.8

Crust temperature and hot fractional area dual-band method results for Landsat TM bands 5 and 7 A-format spectral data for an area of lava tubes emptying magma into the ocean. Style of presentation is the same as that for Table 5.2. Actual values for the fractional hot areas are the listed values multipied by 10^{-4}.

	1	2	3	4	5	6	7	8	9
1					400	400	158	189	128
					0	0	0	0.07	0
2					1400	400	210	234	192
					0	0	0.16	3.72	0
3					1700	400	195	271	152
					0	0	2.77	0	0
4	1350	1550	1490	1750	2060	1840	2060	1770	400
	0	0	0	0	0	0	0	0	0
5	1121	2500	1600	1400					
	1.45	0	0	0					
6	2050	2120	400	400					
	0	0	0	0					

Table 5.9

Crust temperature and hot fractional area dual-band method results for Landsat TM bands 5 and 7 P-format spectral data for an area of lava tubes emptying magma into the ocean. Style of presentation is the same as that for Table 5.2. Actual values for the fractional hot areas are the listed values multipied by 10^{-4}.

	1	2	3	4	5	6	7	8	9
1					400	400	170	197	170
					0	0	0	0.47	0.14
2					1200	400	188	239	169
					0	0	0.24	2.80	0.44
3					400	199	228	186	40
					0	0	2.45	4.97	0
4	40	120	152	188	196	197	153	212	40
	0	0	0	0	0	0	6.59	0	0
5	235	206	140	163					
	0	0	0	0					
6	40	202	40	40					
	0	0	0	0					

Table 5.10

The total energy budget (Q) of eruptive features calculated using dual-band fits where possible and band 7 pixel-integrated temperatures where dual-band fits were not possible. Energy Budget (A) are energy estimations using A-format data. Energy Budget (P) are energy estimations using P-format data. Results are similar for both data sets.

Eruptive Feature	Energy Budget (A)	Energy Budget (P)
1. Puu O'o crater	2.4×10^8 W	2.9×10^8 W
2. Skylights	8.0×10^7 W	8.1×10^7 W
3. Lava flows		
Upper flow on Pali	1.3×10^9 W	1.3×10^9 W
Western flow system	3.4×10^8 W	3.3×10^8 W
Eastern flow system	1.8×10^9 W	1.8×10^9 W
4. Tubes at coast	3.0×10^7 W	2.9×10^7 W
TOTAL FOR ERUPTION	3.8×10^9 W	3.8×10^9 W

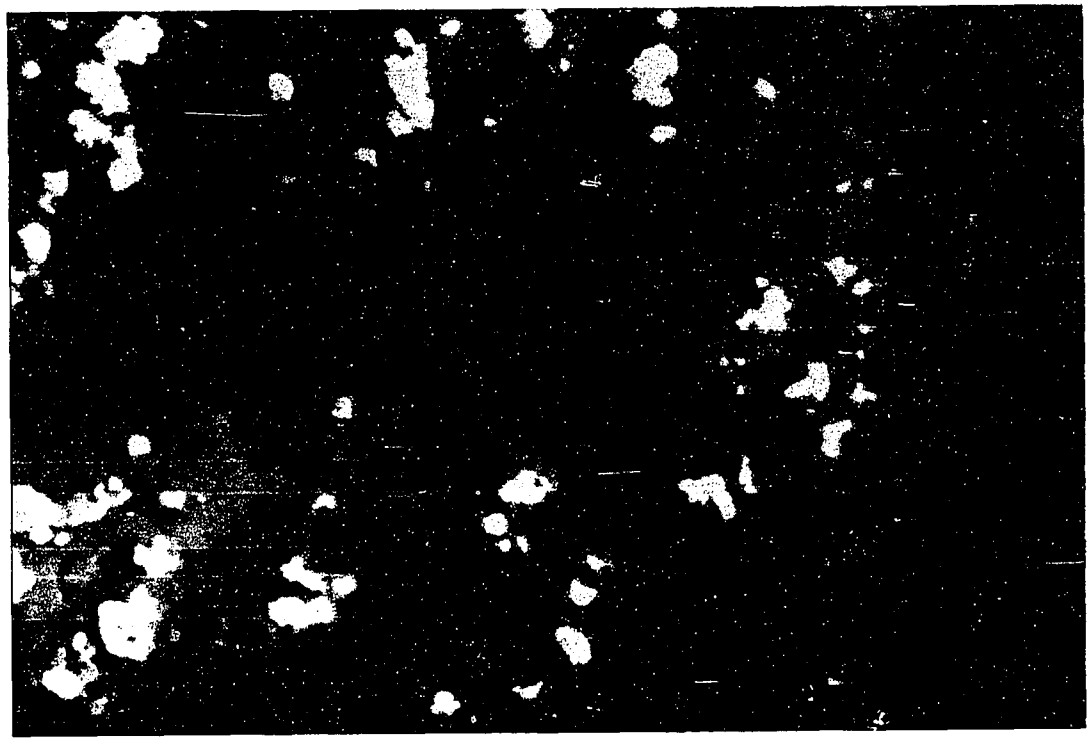

Figure 5.1. Landsat TM false-color composite of the Puu O'o - Kupaianaha eruption acquired on 7/23/91. Bands 7, 4, and 6 were used to make this composite. North is to the top of the photograph. Width of image is ~20 km. The areas which are radiating significant amounts of infrared energy appear reddish-purple in the scene. Puu O'o cone is the bright pink feature in the right center of the photograph. About 3 - 4 km east north-east of Puu O'o is a series of hot spots which are probably skylights. To the south-east of the skylights are a series of lava flows which extend to the ocean. Two areas of bright pixels on the coast mark where lava tubes were emptying magma into the ocean.

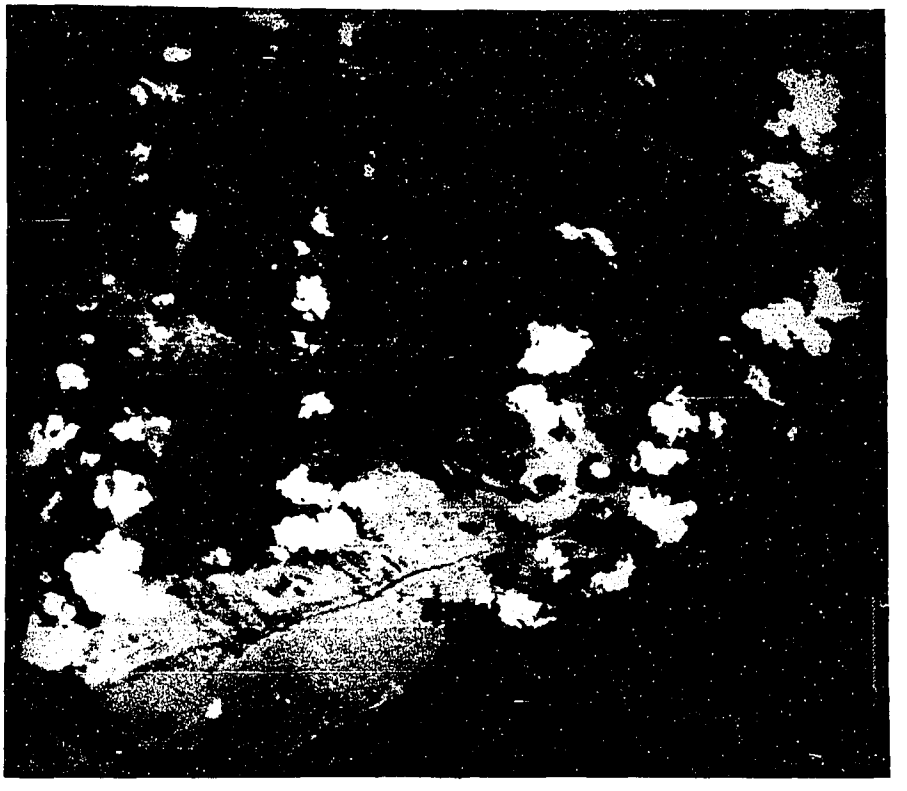

Figure 5.2. A-format band 7 close-up of the study area used to compare the radiative differences recorded by A- and P-format Landsat TM data for a variety of volcanic anomalies. North is to the top of the scene. Width of the image is ~16 km. Bright areas either mark areas radiating a significant amount of infrared energy, or are areas covered by clouds or haze. Puu O'o crater is toward the upper left corner of the image and is a bright spot with a black line (from detector saturation) extending due west. The bright pixels which were identified as skylights in this study are about 3 - 4 km east-north-east of Puu O'o. The area of active lava flows which was a subject of this study is ~5 km south-east of the skylights and due east of Puu O'o. Further to the south-east is the bright area in a cloud shadow which was analyzed in this study. To the south of this area, at the coast, are the lava tubes which were also a subject of this chapter. Overall, the A-format data shows sharp boundaries between volcanic anomalies and the surrounding terrain.

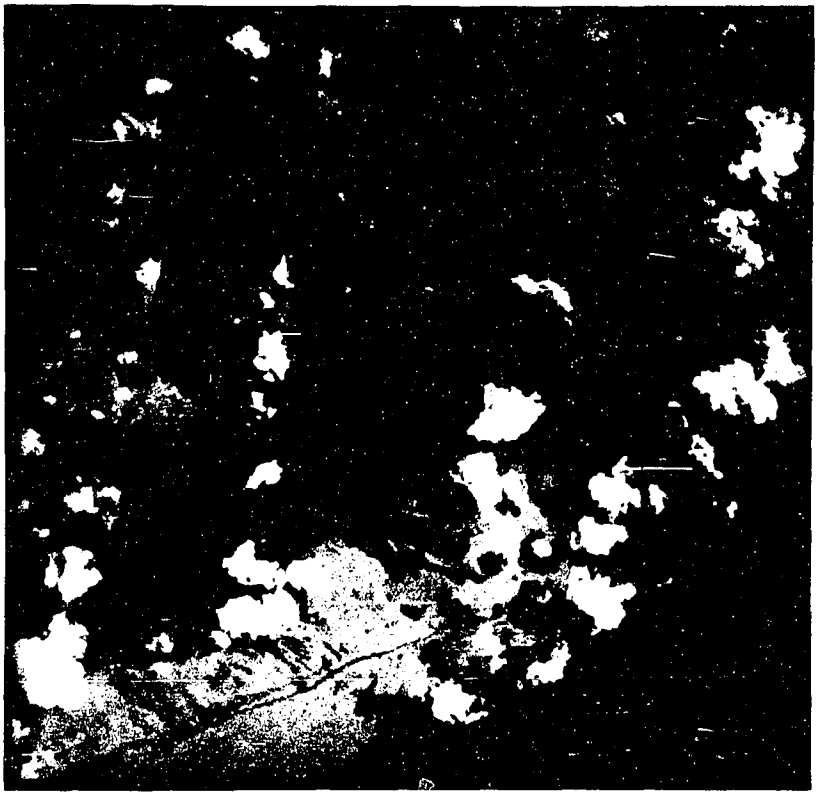

Figure 5.3. P-format band 7 close-up of the study area used to compare the radiative differences of A- and P-format Landsat TM data for a variety of volcanic anomalies. North is to the top of the scene. Width of the image is about 14 km across. At this scale, in a comparison between the A- and P-format data, it is difficult to recognize any differences in surface phenomena.

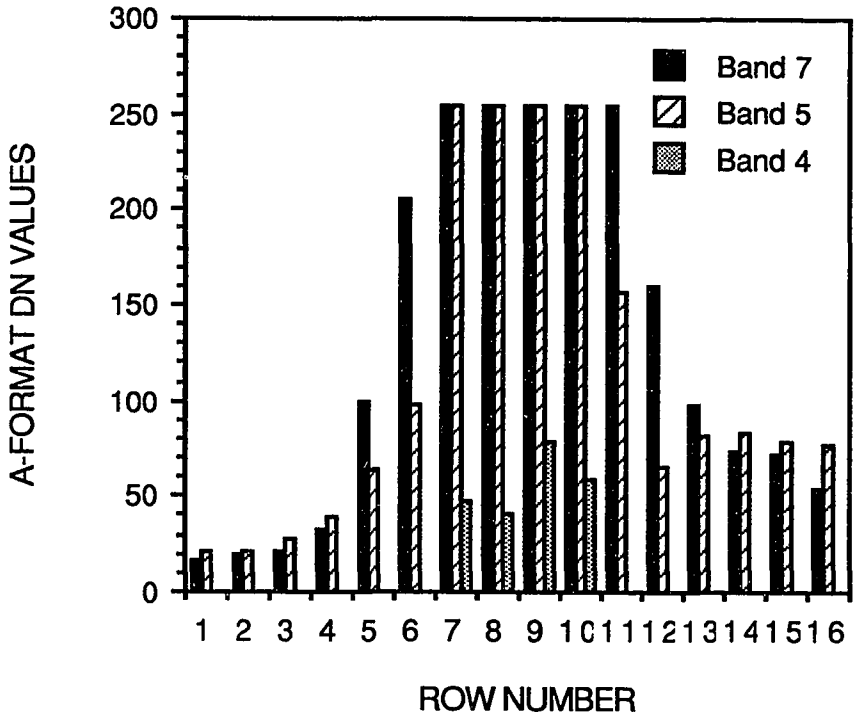

Figure 5.4. Histogram of A-format raw band 5 (stripe) and 7 (solid) DN pixel values across Puu O'o crater. The possible range of DN values is 0 - 255. For pixels in which both bands 5 and 7 are saturated (DN = 255), the band 4 DN values (stippled) are also shown. Histogram shows fairly sharp boundaries of the Puu O'o anomaly.

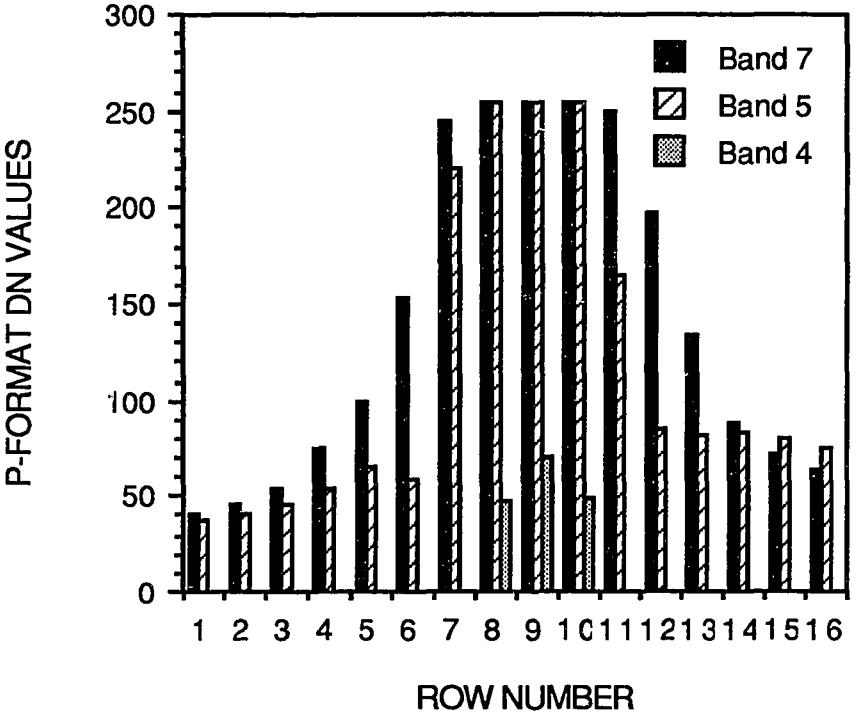

Figure 5.5. Histogram of P-format raw band 5 (stripe) and 7 (solid) DN pixel values across Puu O'o crater. The possible range of DN values is 0 - 255. For pixels in which both bands 5 and 7 are saturated (DN = 255), the band 4 DN values (stippled) are also shown. Compared to the A-format cross-section (Figure 5.4), the boundaries of the P-format anomaly are smeared.

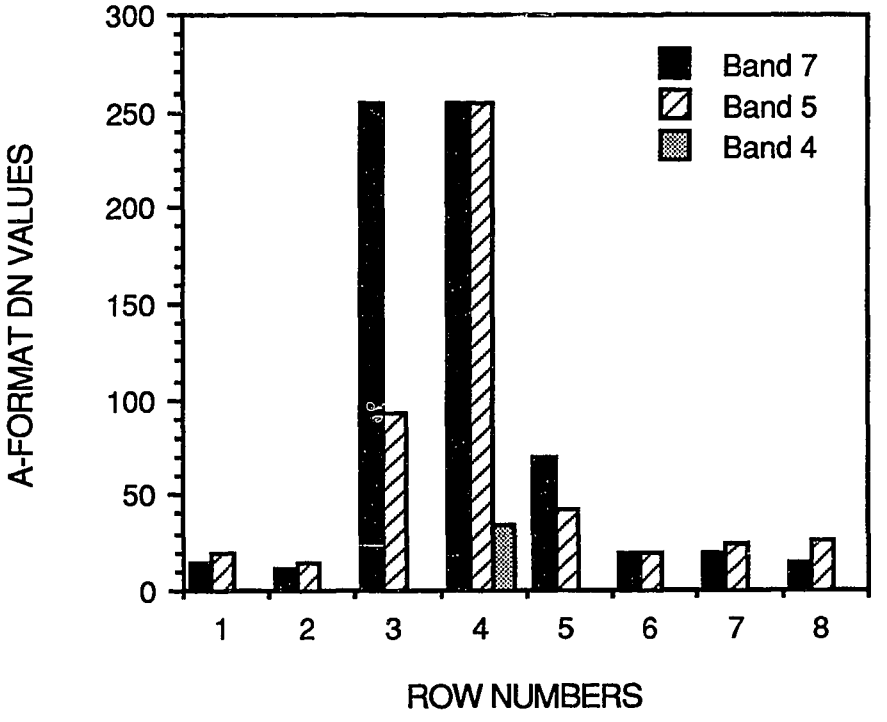

Figure 5.6. Histogram of A-format raw band 5 (stripe) and 7 (solid) DN pixel values across the skylights. The possible range of DN values is 0 - 255. For the pixel in which both bands 5 and 7 are saturated (DN = 255), the band 4 DN value (stippled) is also shown. Histogram shows very sharp radiant boundaries of the skylight.

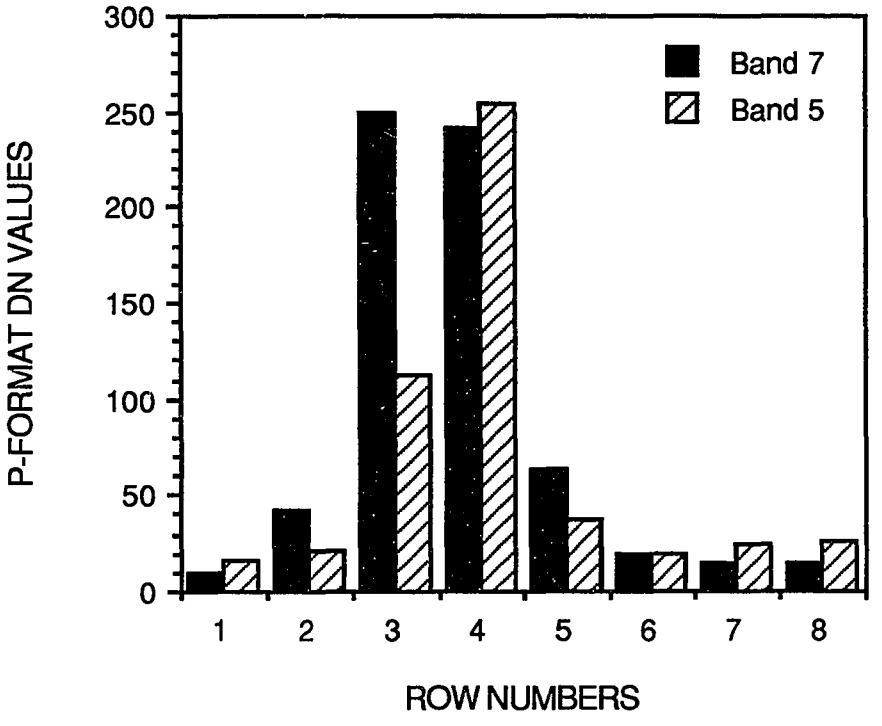

Figure 5.7. Histogram of P-format raw band 5 (stripe) and 7 (solid) DN pixel values across the skylights. The possible range of DN values is 0 - 255. Histogram shows less sharp radiant boundaries than the A-format cross-section (Figure 5.6).

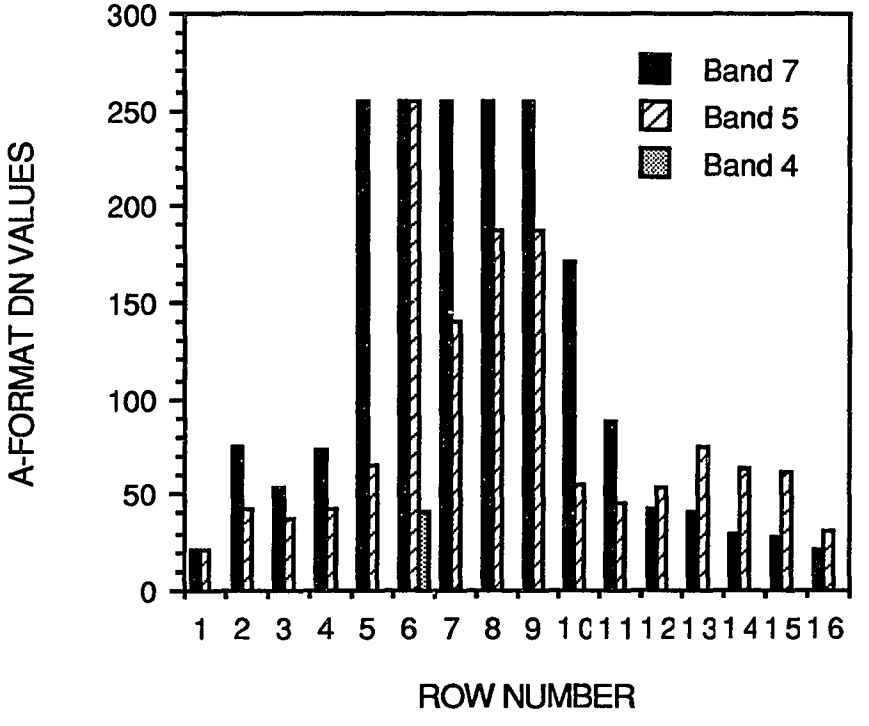

Figure 5.8. Histogram of A-format raw band 5 (stripe) and 7 (solid) DN pixel values across the lava flow which was a subject of this study. The possible range of DN values is 0 - 255. For the pixel in which both bands 5 and 7 are saturated (DN = 255), the band 4 DN value (stippled) is also shown. Histogram shows very sharp radiant boundaries of the skylight.

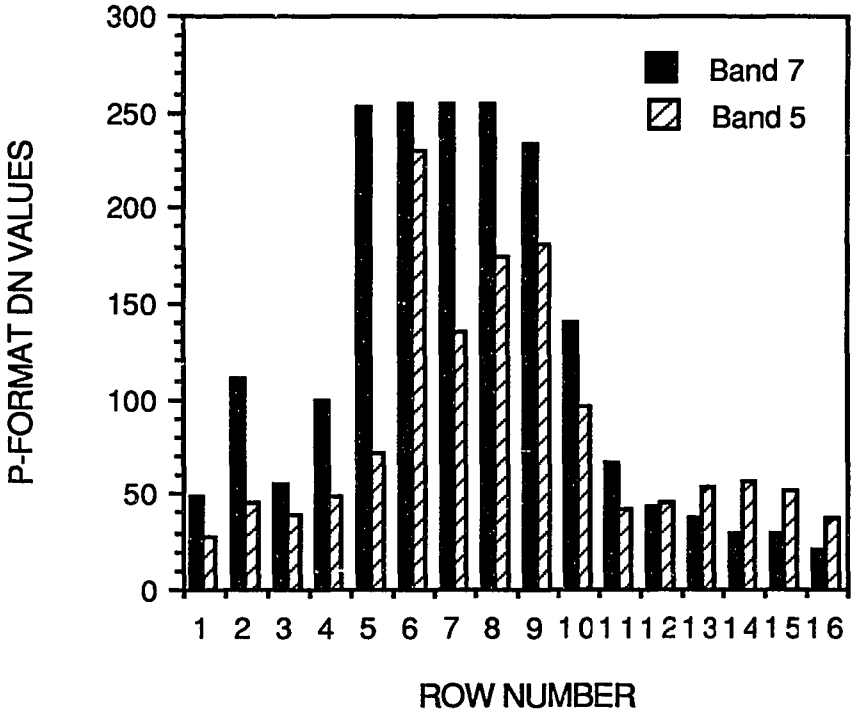

Figure 5.9. Histogram of P-format raw band 5 (stripe) and 7 (solid) DN pixel values across the lava flow which was a subject of this study. The possible range of DN values is 0 - 255. Histogram shows less sharp radiant boundaries than the A-format cross-section (Figure 5.8). The cross-section was taken from north to south across the flow. Note the haze trailing to the south of the flow which manifests itself in the histogram as elevated band 5 DN values.

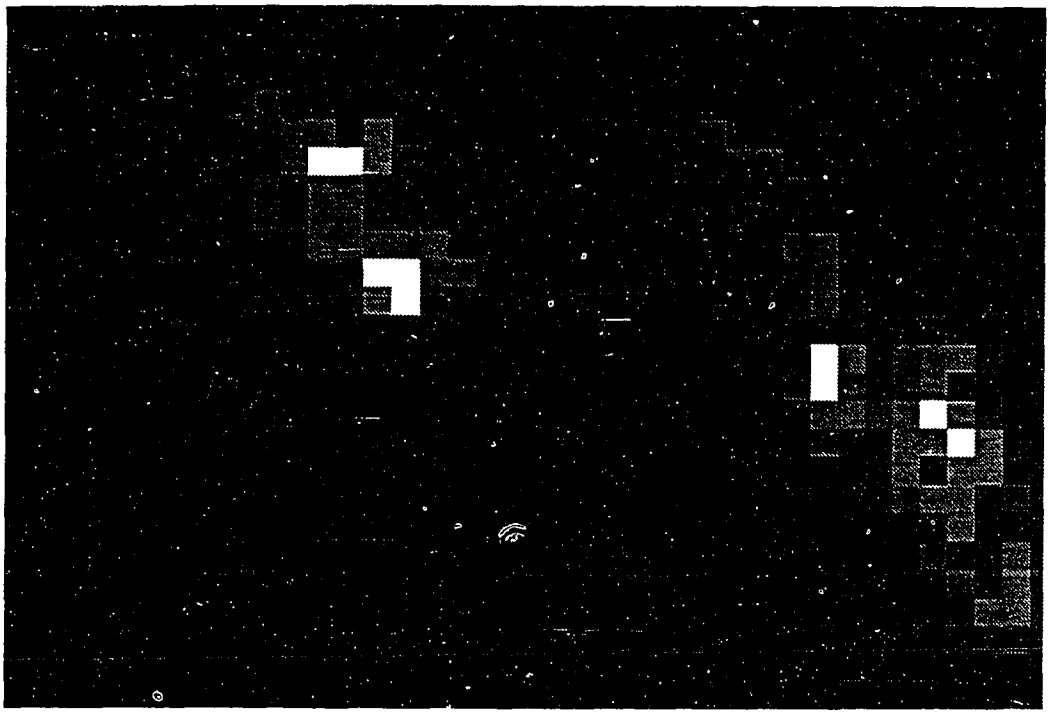

Figure 5.10. Dual-band method and pixel-integrated crust temperature results for A-format data of the active lava flow of this study. North is toward the top edge of the figure. Each square represents one 30 m x 30 m Landsat TM pixel. White pixels represent areas where both bands 5 and 7 were saturated (DN = 255) with radiance from the flow. Black pixels did not exhibit elevated radiances in either bands 5 or 7 and were assigned a background temperature of 40°C. Gray pixels represent either pixel-integrated or dual-band method crust temperatures, which ranged from 90 - 273°C in this example. The temperature map clearly shows two areas of elevated temperatures centered around the saturated pixels. Both flow centers are oriented in a NW - SE direction.

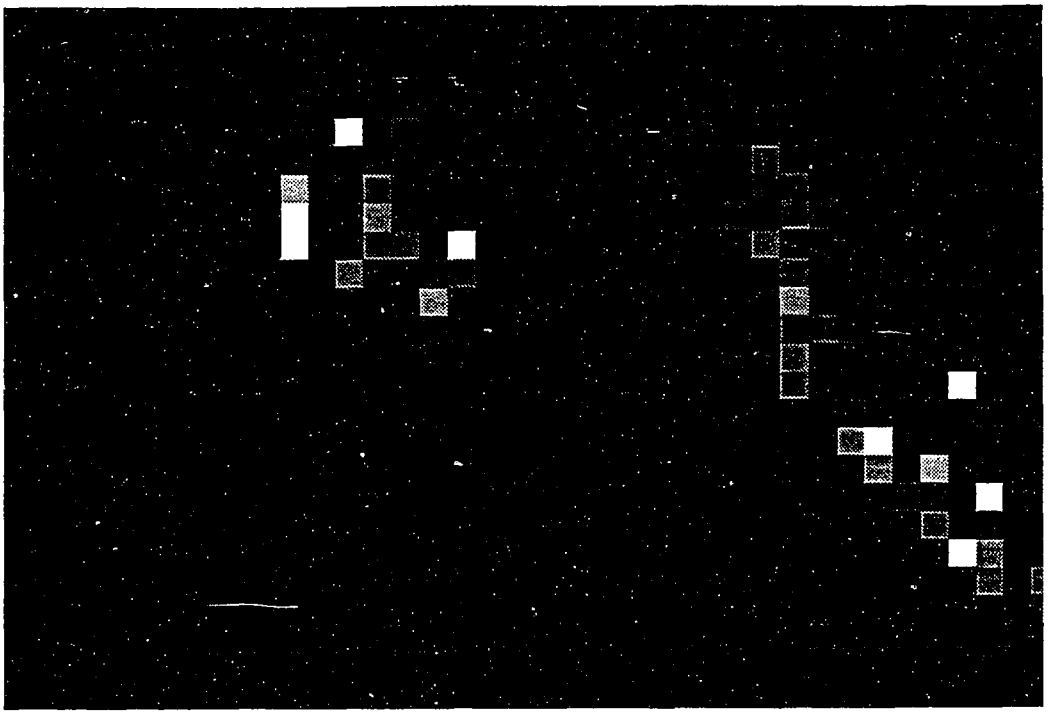

Figure 5.11. Hot fractional radiating areas of pixels of the active lava flow using A-format Landsat TM data. The area of coverage and orientation of the data is identical to that of Figure 5.10. Black pixels represent areas where dual-band calculations were not possible or where the thermal radiance was not significantly above that of the background. White pixels represent areas which exhibited the highest hot fractional area derivable with the dual-band method, which was 0.064% of the total pixel radiating at 1130°C. The figure clearly shows two distinct areas of activity.

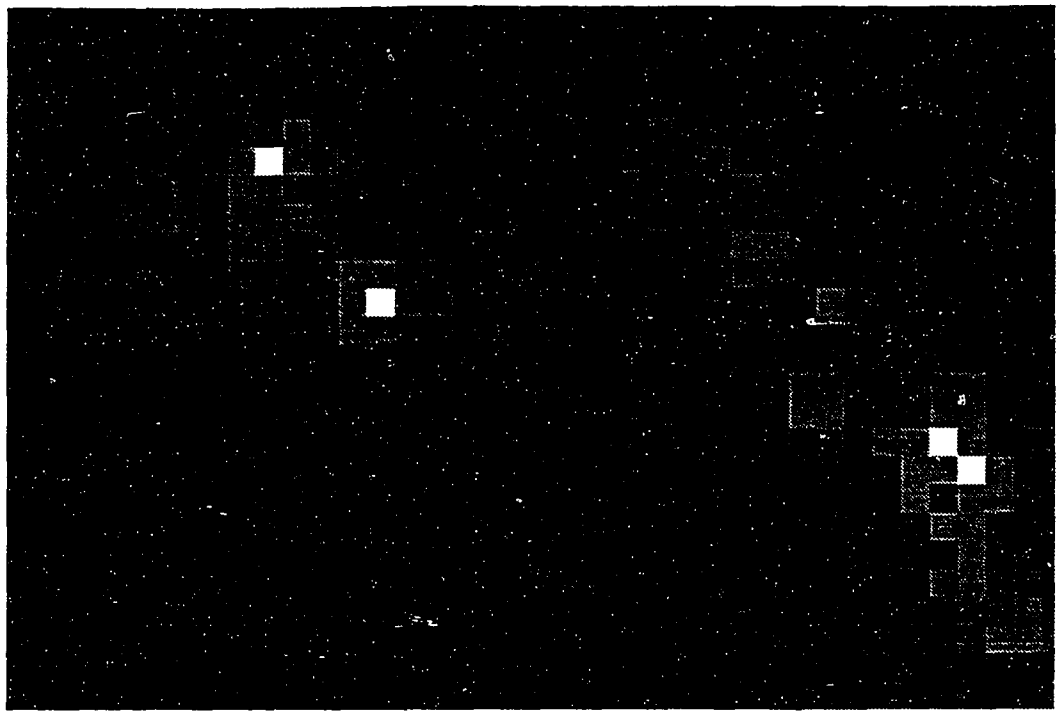

Figure 5.12. Dual-band method and pixel-integrated crust temperature results for P-format data of the active lava flow of this study. Area of coverage, figure orientation, and pixel temperature limits are the same as that in Figure 5.10. The temperature map clearly shows two areas of elevated temperatures centered around the saturated pixels. Both flow centers are oriented in a NW - SE direction. Comparing this temperature map with that of Figure 5.10 shows the effects of radiance smearing due to the geometric correction process. There are less saturated pixels in Figure 5.12 than in Figure 5.10, but temperature boundaries are less distinct in the P-format data.

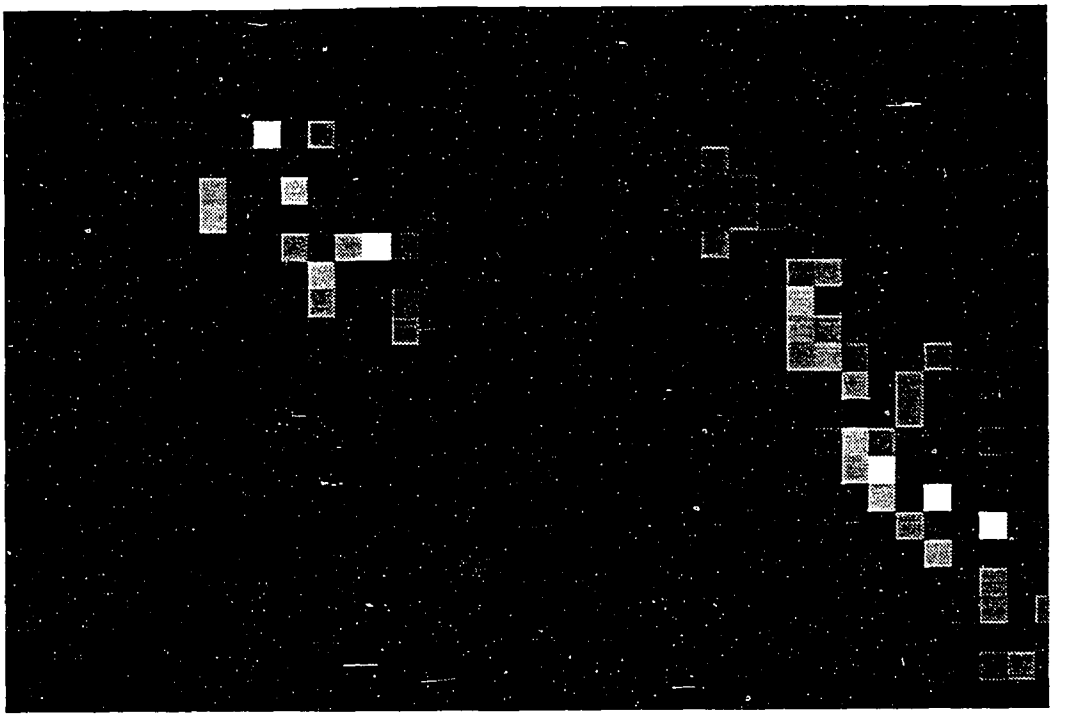

Figure 5.13. Hot fractional radiating areas of pixels of the active lava flow using P-format Landsat TM data. The area of coverage and orientation of the data is identical to that of Figure 5.10. Black pixels represent areas where dual-band calculations were not possible or where the thermal radiance was not significantly above that of the background. White pixels represent areas which exhibited the highest hot fractional area derivable with the dual-band method, which was 0.064% of the total pixel radiating at 1130°C. The figure clearly shows two distinct areas of activity. Careful inspection of Figures 5.11 and 5.13 shows that hot fractional area results are smeared in the P-format data relative to the A-format data

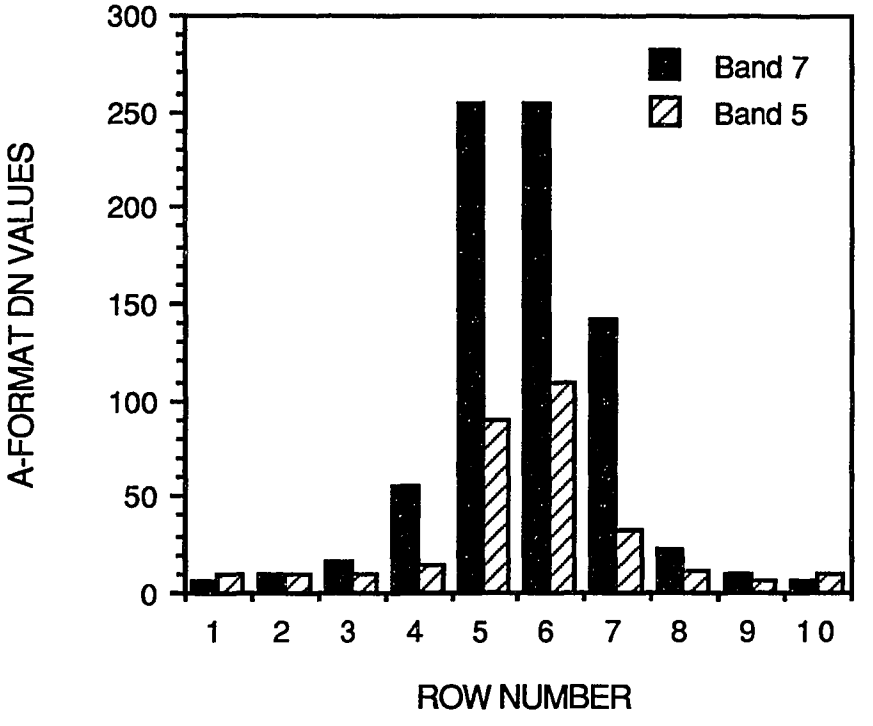

Figure 5.14. Histogram of A-format raw band 5 (stripe) and 7 (solid) DN pixel values across the lava flow in the shadow of the cloud. The possible range of DN values is 0 - 255. Histogram shows very sharp radiant boundaries of the lava flow. Background DN pixel values for bands 5 and 7 in the cloud shadow are one-third the background DN values of pixels in sunlight.

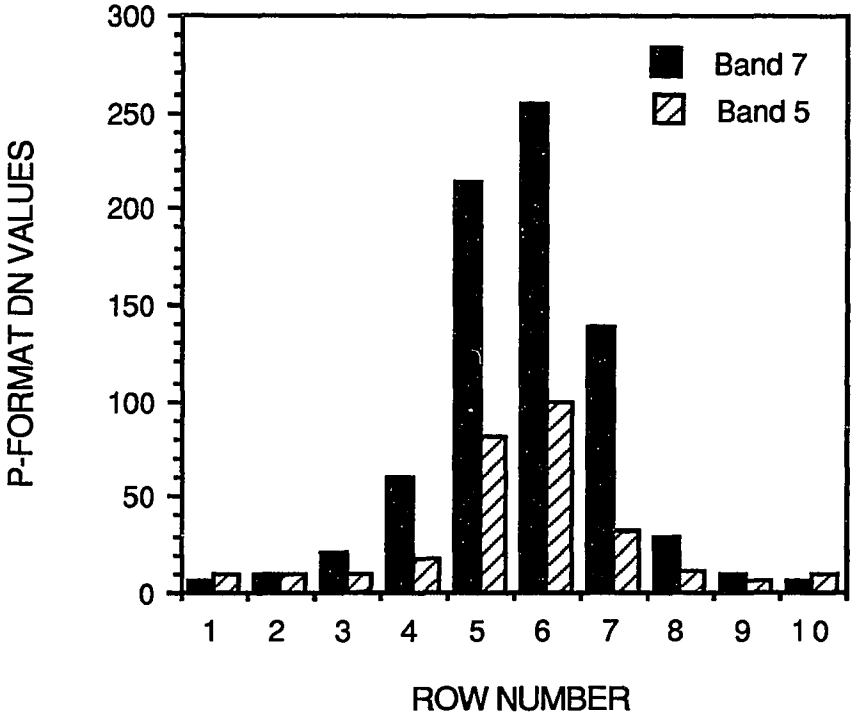

Figure 5.15. Histogram of P-format raw band 5 (stripe) and 7 (solid) DN pixel values across the lava flow in the cloud shadow. The possible range of DN values is 0 - 255. Histogram shows very sharp radiant boundaries of the lava flow. Background DN pixel values for bands 5 and 7 in the cloud shadow are one-third the background DN values of pixels in sunlight.

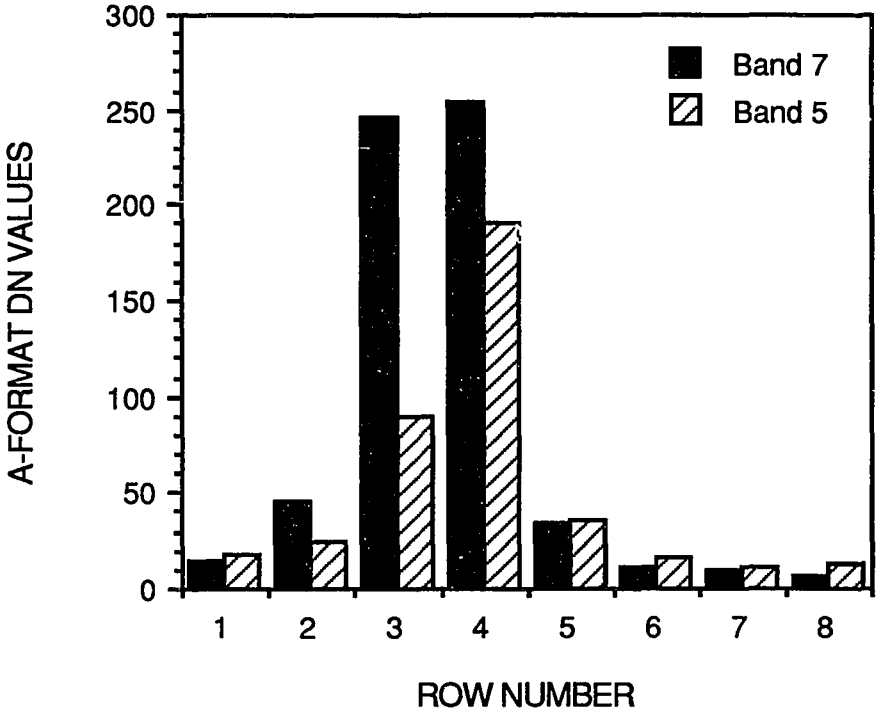

Figure 5.16. Histogram of A-format raw band 5 (stripe) and 7 (solid) DN pixel values across the lava tube at the coast. The possible range of DN values is 0 - 255.

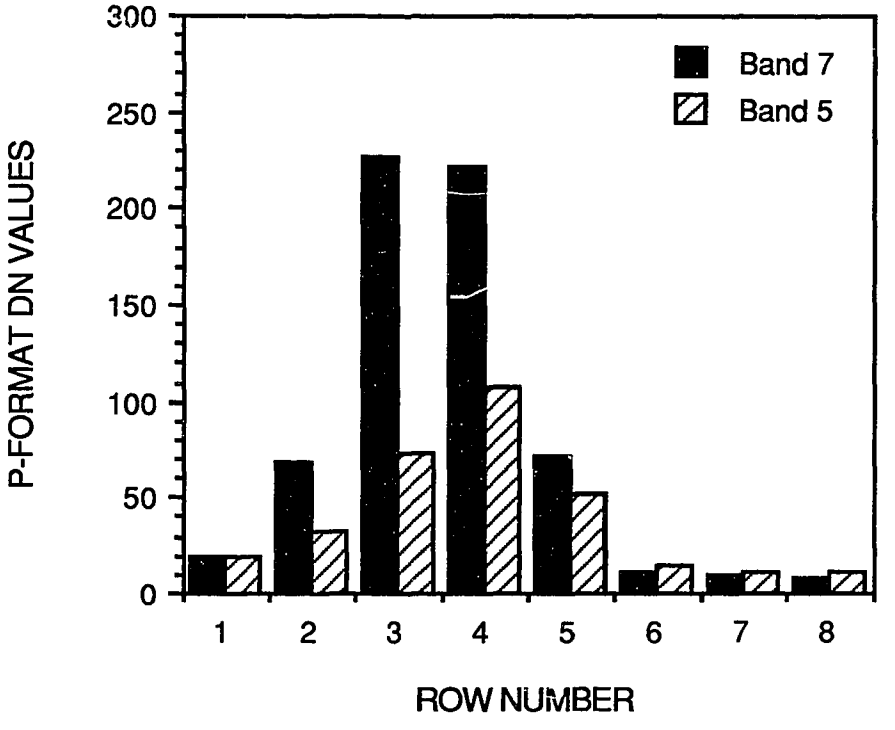

Figure 5.17. Histogram of P-format raw band 5 (stripe) and 7 (solid) DN pixel values across the lava tube at the coast. The possible range of DN values is 0 - 255.

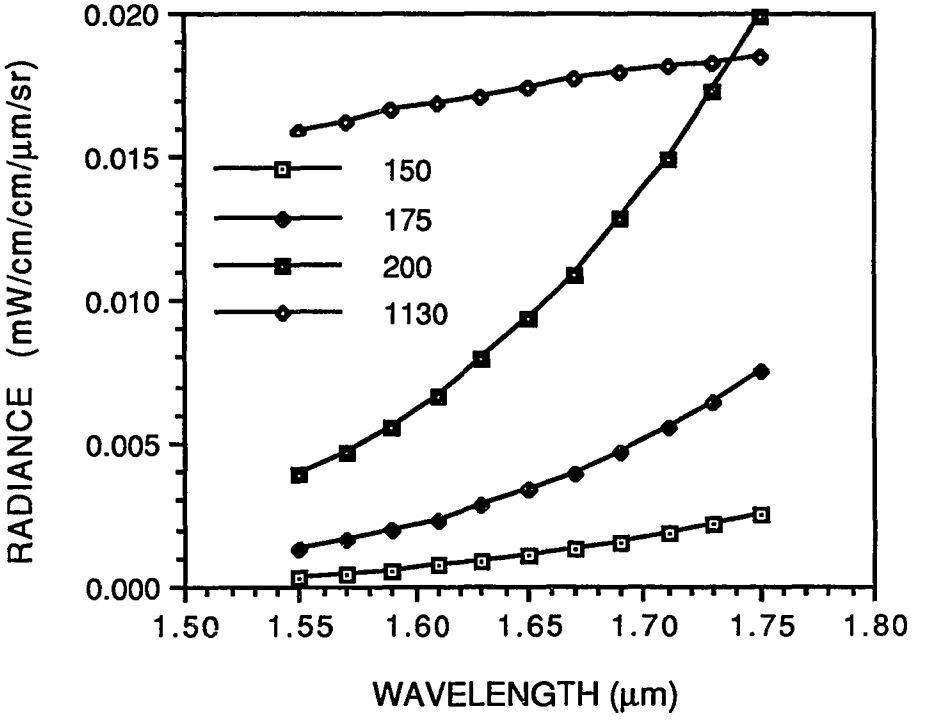

Figure 5.18. Distribution of radiance across band 5 for typical dual-band solutions. The horizontal axis is plotted with respect to wavelength in microns. The vertical axis is plotted in terms of radiance (mW cm^{-2} μm^{-1} sr^{-1}). Note that for most dual-band solutions, the radiance from the hot fraction is dominant over that of the crust across most, if not all, of band 5.

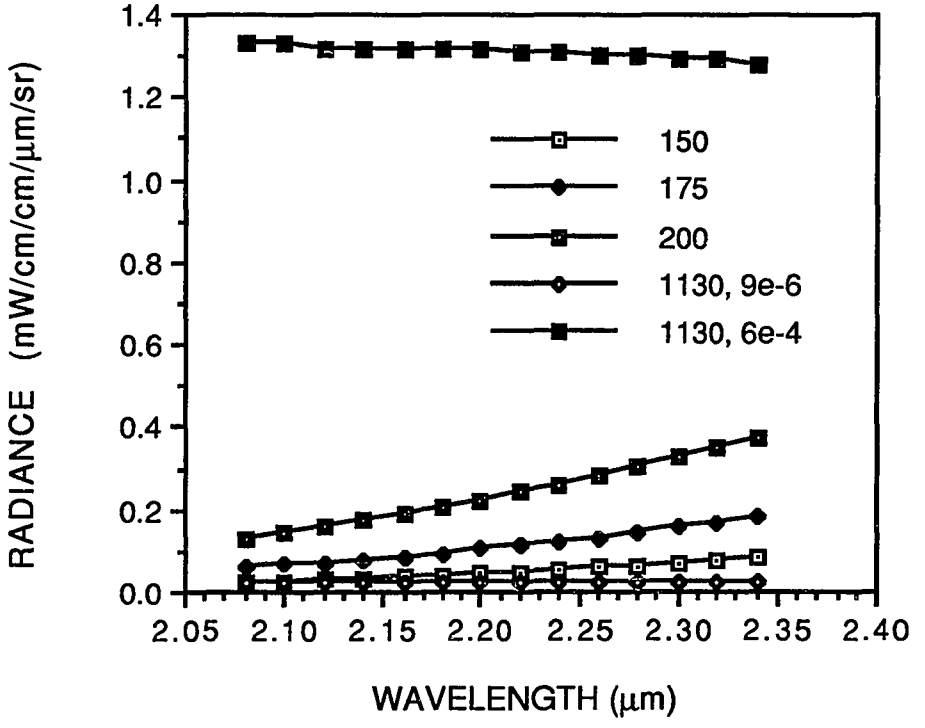

Figure 5.19. Distribution of radiance across band 7 for typical dual-band solutions. The horizontal axis is plotted with respect to wavelength in microns. The vertical axis is plotted in terms of radiance (mW cm^{-2} $\mu m^{-1} sr^{-1}$). For some dual-band solutions the amount of radiant energy from the crust and hot components are comparable. However, for the larger hot fractional areas calculated with the dual-band method, the radiance of the hot component is dominant.

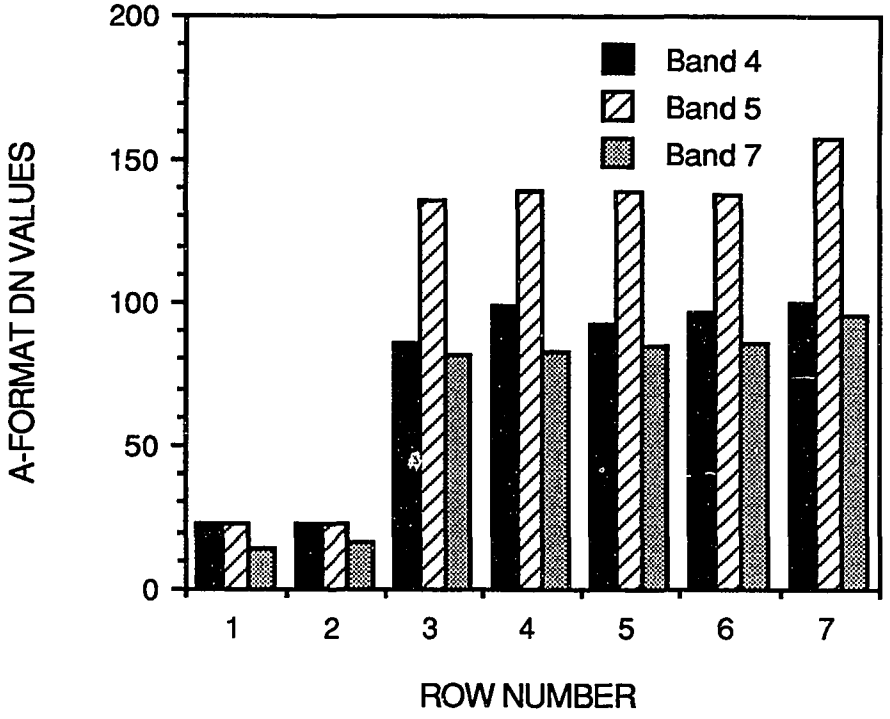

Figure 5.20. Histogram of A-format band 4 (stippled), 5 (stripe), and 7 (solid) DN pixel values across the edge of a cloud. The possible range of DN values is 0 - 255. Note the immense drop in DN from the cloud (row 3) to the ground (row 2).

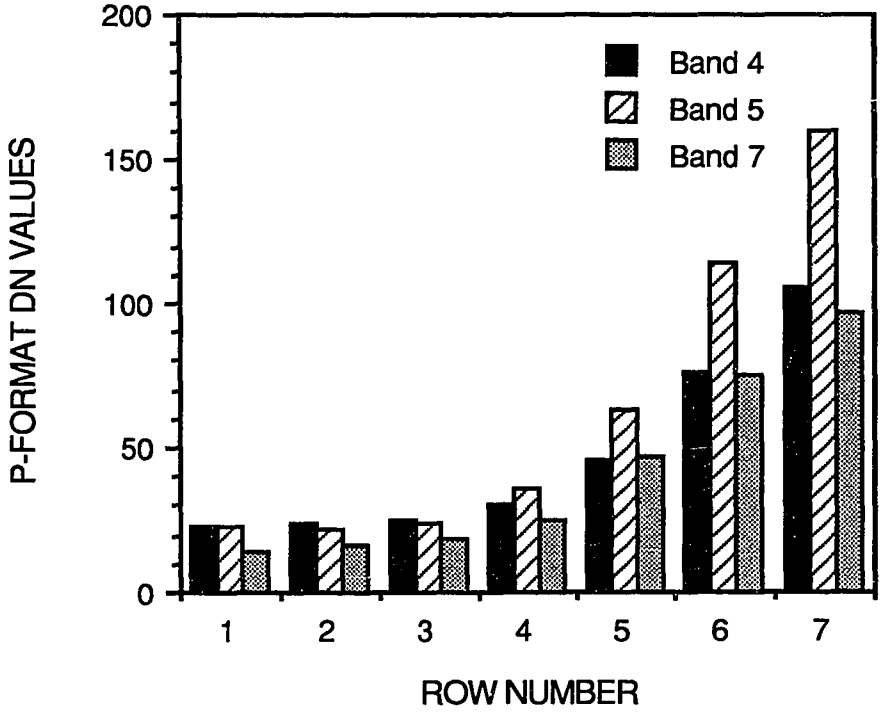

Figure 5.21. Histogram of P-format band 4 (stippled), 5 (stripe), and 7 (solid) DN pixel values across the edge of a cloud. The position of the cross-section is the same as that for Figure 5.20. Note the dramatic change in DN across the cloud edge in Figure 5.20 has been smeared out completely by the geometric correction process, as is shown in this graph.

Chapter 6: Conclusions

The spectroradiometer data presented in Chapters 3 and 4 provide the most complete multispectral field analysis of the thermal radiative properties of lava lakes and flows that has been done to date. However, as has been noted by Oppenheimer and Rothery (1991), further instrument developments will have to be made before satellite observations of thermal anomalies can become adequate for the complete description of surface temperatures of volcanic phenomena. For instance, the data that I have presented in Chapters 3 and 4 lack the spatial information of the thermal anomalies. Although the two spectroradiometer beams provide some information on the variability of surface temperatures at a separation of ~1 meter or less, this information lacks the synoptic view afforded by satellite data (Chapter 5) to completely describe the thermal structure of either a dynamic lava lake or a moving lava flow. Another problem with the spectroradiometer involves the time that is required to collect a spectrum. Transient Stage 1 events are manifested in the spectral data as flickering lasting fractions of seconds or as large spikes lasting on the order of 1 second (Chapter 3). I used the most rapid method of data collection with the spectroradiometer, which was 1000 data points in approximately 30 seconds, but this was still far too slow to record some events when data were collected in the 0.4 - 2.5 μm range. Instruments with more rapid data collection (<1 sec), perhaps having fewer very narrow channels located in atmospheric windows, are required to provide the speed and volume of data necessary to describe transient fountaining events or quickly cooling lava flows.

The instrument of the future for radiative field studies of active volcanoes is the imaging spectroradiometer. In this dissertation, I have produced a number of pairs of point measurements (one radiance value per channel per field of view) of active volcanic

areas which have hinted at the spatial variability of lava lakes (Chapter 3) and lava channels (Chapter 4). These data are not adequate to describe the temporal radiative evolution of volcanic areas. The instrument that is required for the next generation of studies, the imaging spectroradiometer, would collect a continuous array of pixels, each of which contains many channels so that multiple radiative subareas within a single pixel may be identified. Ideally, the imaging spectroradiometer should collect data in all pixels and in all channels simultaneously, or as rapidly as possible, to prevent significant changes in the radiative character of the surface in the field of view while a measurement is in progress.

The spectroradiometer data also show some of the potential problems in using infrared thermometers operating in the 0.8 - 1.1 μm range (Oppenheimer and Rothery, 1991; Jones et al., 1990), or using Landsat bands 4 (0.76 - 0.90 μm) and 5 (1.55 - 1.75 μm), to study active lava flows and lakes. Solar contamination of the spectrum may be greater than 12% of the total flux at wavelengths shorter than 1 μm for even highly active Stage 1 events (Chapter 3). Even worse, the flux from reflected sunlight increases rapidly at shorter wavelengths making estimations of the effects of reflected sunlight difficult for Landsat band 4, and almost impossible for the automatic infrared thermometers. In both cases, the distribution of reflected sunlight shortward of 1 μm suggests that brightness temperatures measured with infrared thermometers (operating at 0.8 - 1.1 μm) or calculated using Landsat TM band 4 will result in higher temperatures than are actually present. A similar problem could be present when using TM band 5 to estimate the temperatures of the surface crust (Stage 3 and to a lesser extent Stage 2) on lava lakes and lava flows. The raw spectral data of numerous examples of quiescent activity suggest that reflected sunlight contributes a significant

percentage of the total radiative flux at 1.55 - 1.75 μm (Landsat TM band 5, discussion in Chapters 3 and 5). Again, the amount of flux due to reflected sunlight decreases with increasing wavelength and has been shown (Chapter 3) to be about 50% of the total radiative flux at 1.55 μm and 19% at 1.70 μm. This uneven distribution of flux from reflected sunlight would again adversely affect dual-band solutions using TM bands 5 and 7 (Chapter 5). Nighttime measurements, such as those presented in Chapter 4, are the best method to avoid these solar contamination issues. The spectra collected in Chapter 4 show that qualitative information may be gained directly from the data, since the measured thermal radiance is only from the volcanic anomaly in the field of view of the instrument.

If I had to collect data for this dissertation again, I would have supplemented the lava lake data with spectral measurements acquired at night at this site. The nighttime data in Chapter 4 was much easier to work with and produces a much more accurate result due to the absence of sunlight.

As noted by Rothery et al. (1988) in the case of Landsat data, it is important to use non-geometrically corrected data (A-format) for the temperature determinations, because pixel resampling will destroy the radiometry of each pixel. In Chapter 5, I explored this issue and arrived at the conclusion that A-format data was much better for mapping boundaries of thermal sources than P-format data which contained "smeared" pixel radiances due to the correction process. However, I found that energy budget calculations using both types of data were consistent for many different volcanic anomalies. Perhaps the most frustrating aspect of working with Landsat TM data of active volcanoes is that the radiance overlap between bands, which determines whether or not dual-band calculations may be performed, is severely limited (essentially only

bands 5 and 7 are useful). Thus, the hottest pixels of the anomaly can not be accurately fit with characteristic temperatures and areas. Nighttime TM acquisitions would help in that very low thermal radiances from band 3, which were undetectable from the background in the data presented in Chapter 5, would be more significant without contamination from sunlight. With nighttime data, perhaps more of the hot pixels (saturated in bands 5 and 7) could use bands 3 and 4 for dual-band fits. The drawback of nighttime Landsat TM data is that the identification of reference points in the image, where most objects in the nighttime scene are dark, makes the comparison between the thermal properties and the morphology of the flow a difficult task.

Finally, advances in satellite equipment development must also be made which take advantage of the data collecting ability of the spectroradiometer. Imaging spectrometers, such as the airborne Advanced Visible and Infrared Imaging Spectrometer (AVIRIS) or the HIRIS instrument planned for the Earth Observing System (EOS) (Goetz and Herring, 1989), will prove to be much more useful in the study of active volcanoes than the currently available Landsat TM. These new instruments collect spectral data in 192 channels between 0.4 - 2.5 μm, and have a spatial resolution of ~30 m/pixel. What AVIRIS and HIRIS both lack is the temporal resolution that a field instrument can provide. The fact that the spectroradiometer data show radiative thermal changes in the area of the lake that is characterized as Stage 1 (Chapter 3) over timescales of at most a few tens of seconds and in surface flows (Chapter 4) which are cooling over tens of minutes indicates that an instantaneous view of a lava lake is not sufficient to determine the level of activity that an observer would find on the ground. Fortuitous satellite observations of overturning events on the lava lake surface could lead to an overestimation of the normal representative total energy budget from the lake, whereas

an episode of Stage 3 activity may be interpreted as an inactive lake. For example, the Landsat TM measurements of the total energy budget, Q, that were determined by Glaze et al. (1989) indicated changes in Q for Lascar volcano, but these changes are partially due to the varying size of the anomaly and could equally well be related to short-term (minutes to hours) variations in the thermal characteristics of the volcano. Even when the EOS is deployed and operational, this lack of temporal coverage will still exist. Only measurements made from an as-yet unapproved geostationary platform, or from a sensor in a Molniya orbit (i.e., an orbit that is highly elliptical, and that enables the spacecraft to "hang" over a particular spot on the Earth's surface for several hours each orbit) will be able to address this dynamic aspect of the total energy budget of a volcano (Peter Mouginis-Mark, personal communication, 1991).

This dissertation represents only a small primitive part of what may be accomplished using the instruments described above in future studies. In the field, imaging spectroradiometers may be used to calculate the subpixel-sized temperatures and areas of active volcanic anomalies on scales of less than a square meter. Detailed studies of the spatial and temporal variations of volcanic anomalies such as these will provide information which will allow more accurate models to be developed. Future satellites will provide many narrow spectral channels which may be used to solve for many radiative subareas within a single pixel. The greatest benefit of this will be the ability to model at least three radiative areas (a hot core component, a surface crust component, and the non-thermally radiant background) which will allow for more accurate mapping of flow boundaries and the identification of active (hotter) and inactive (cooler, but radiating above the background) flow units. Fumarolic activity may be recorded after each successful acquisition, since the availability of multiple spectral

channels and greater sensor dynamic ranges will allow for the detection of changes in the radiative characteristics of currently undetectable early-warning, sub-pixel anomalies. Continuous monitoring of active potentially active volcanoes with these improved satellites will truly provide an early warning system for oncoming eruptions.

References

Glaze, L., P. W. Francis, and D. A. Rothery, Measuring the thermal budgets of active volcanoes by satellite remote sensing, *Nature, 338,* 144 - 146, 1989.

Goetz, A. F. H. and M. Herring, The high resolution imaging spectrometer (HIRIS) for EOS, *IEEE Trans. Geosci. Remote Sensing, 27*, 136 - 144, 1989.

Jones, A. C., L. Wilson, and H. Pinkerton, Surface temperature measurements of active Hawaiian lava flows, paper presented at International Volcanological Congress, *Int. Assoc. Volcanol. Chem. Earth's Interior,* Mainz, Germany, Sept. 3-8, 1990.

Oppenheimer, C. M. M., and D. A. Rothery, Infrared monitoring of volcanoes by satellite, *Journal of the Geological Society, London, 148,* 563 - 569, 1991.

Rothery, D. A., P. W. Francis, and C. A. Wood, Volcano monitoring using short wavelength infrared data from satellites, *Journal of Geophysical Research, 93,* 7993 -8008, 1988.

Appendix

The program used to generate temperatures and hot fractional radiating areas is listed here in the Appendix. I will elaborate on the general flow of the code here. First, the operator must enter values for the atmospheric transmissivity, the emissivity of the surface, the hot component temperature, the background DN values for bands 4, 5, and 7, the size of the pixel array, as well as the band 4, 5, and 7 pixel DN values for the array. Next, the radiance of each band in each pixel is calculated by subtracting the background DN value from the pixel DN of each band. When the procedure *Radiance* is called, the radiance of each pixel from thermal sources is calculated using the conversions listed in Markham and Barker (1986).

Each pixel is then processed individually with cool temperatures, T_c and hot fractinal radiating areas A_h being stored to separate arrays. First, within the procedure *Temparea*, the hot fractional area limits are calculated for bands 4, 5, and 7 using equation 5.5. Next, if the DN values obtained for the pixel are less than five greater than the background values for each band, I assume that there is not an anomaly in that pixel and a background temperature and area are reported. If the radiance of band 7 is higher than that of the background but not saturated (the DN value input for the pixel was less than 255) and the radiance of band 5 is not significant (i. e., greater than the background of band 5) then a pixel-integrated temperature using the radiance of band 7 and a fractional hot area of zero are reported. If the radiances of bands 5 and 7 are significant but band 5 is not saturated and the hot fractional area limit of band 7 is greater than that of band 5, then a dual-band solution using bands 5 and 7 is calculated. I

will note here that this program includes one of the conventions first used in Oppenheimer (1991) in that in some cases where band 7 is saturated a dual-band solution may still be derived which should be regarded as a lower limit for the cooler temperature and an upper limit to the hot fractional area. If the three radiance values for the given pixel do not satisfy any of the conditions listed above, then a dual-band solution using bands 4 and 5 is attempted, if band 7 is saturated, band 5 is significant, but not saturated, and the hot fractional area limit of band 5 is greater than that of band 4. Otherwise, if band 5 is not saturated and the hot fractional area limit of band 5 is greater than that for band 7, then the pixel-integrated temperature for band 7 is calculated but the hot fractional area is assigned 5 to signify that the radiance of band 5 was anomalously high when compared to that of band 7. Lastly, if none of the above conditions are satisfied and band 5 and 7 are both saturated, then the cool temperature is set equal to the pixel-integrated saturation limit of band 5 (425°C) and the hot fractional area is set at 0, but this must be recognized as a crude approximation at best.

The procedure *Dualband* is called if a dual-band calculation is possible. The fractional hot area highest limits are calculated for the two bands using equation 5.5. Half of the lowest of the two band limits is then used as a fractional hot area to calculate the cool component temperature for each of the bands. The two numbers are compared, and if they match, then the cool component temperature and fractional hot area are saved in an array. If the two cool temperatures of each band do not match, then two thirds of the lowest of the two band limits is used as the fractional hot area, and so forth, with the numerator and denominator of the fraction multiplying the lowest band limit until the two calculated cool temperatures match. The method of multiplying the fractional hot

area limit by an increasingly large fraction insures that the iterations may get very close to but never actually reach the fractional hot area limit of either of the two bands.

The results are reported in the output form of two arrays, one of which contains the crust temperatures for the input pixel values, and the other of which contains the respective hot fractional areas.

```
{Luke Flynn, 1/14/92}
{This program uses Landsat TM bands 4, 5, and 7 DN values as input data in the form of
arrays.}
{Next, the raw DN's are converted to radiance in W m-3 sr-1 for convenience}
{Each pixel is fit with a crust temperature and hot radiating area using dual-band
method.}
{If fit is not possible, a lower limit temperature is listed for the pixel.}
{Data output is two arrays, one for temperatures and one for hot areas.}
Program LandsatTM;
    type DNarea=array [1..30,1..30,1..3] of integer;
         radarea=array [1..30,1..30,1..3] of real;
         Crusttemp=array [1..30,1..30] of integer;
         fraction=array [1..30,1..30] of real;
   var DNvalue,DNcorrect:DNarea;
      pixrad:radarea;
      tempcold:Crusttemp;
      hotarea:fraction;
          bkgr4,bkgr5,bkgr7,bkgrtemp,temphot,i,j,k,xmax,ymax,band:integer;
         transmissivity,pixtemp,emissivity:real;
  {This procedure calculates the radiance value for a band DN}
   procedure Radiance(bandDN,bandnum:integer;var pixrad:real);
    var radmax,radmin:real;
  begin
    radmin:=0;
    radmax:=0;
    if bandnum=4 then
    begin
          radmin:=(-0.150000);
         radmax:=(20.620000);
     end;{if}
    if bandnum=5 then
      begin
           radmin:=(-0.0370000);
          radmax:=(2.7190000);
       end;{if}
    if bandnum=7 then
       begin
            radmin:=(-0.0150000);
           radmax:=(1.4380000);
       end;{if}
          pixrad:=(radmin+(((radmax-radmin)/255.00000)*bandDN));
      if (pixrad<0) then pixrad:=0.0000
         else pixrad:=(pixrad*10000000)
  end;{Radiance}
    {Dualband takes two input radiance values, matches a cold area and temperature to
those values.}
procedure Dualband(firrad,secrad,a1lim,a2lim,emissiv:real;fband,sband,hottemp:
      integer; var tempC:integer; var hota:real);
      var tcone,tctwo,anum,aden:integer;area,onehrad,twohrad,rohot,rthot:real;
```

```
begin {Dualband}
  rohot:=0;
  rthot:=0;
  anum:=1;
  aden:=2;
    area:=((a1lim*anum)/aden);
     writeln('the two limits are',a1lim,a2lim);
  onehrad:=0;
  twohrad:=0;
  tcone:=20;
  tctwo:=0;
    if((fband=4)and(sband=5)) then
  begin
     while((tcone-1)>tctwo) do
   begin
              rohot:=((1.5148E14*emissiv)/(exp(17365.11/hottemp)-1));
              rthot:=((9.7581E12*emissiv)/(exp(8735.18/hottemp)-1));
            onehrad:=((firrad-(area*rohot))/(1-area));
            twohrad:=((secrad-(area*rthot))/(1-area));
              tcone:=(round(17365.11/ln(((1.5148E14*emissiv)/onehrad)+1)));
               tctwo:=(round(8735.18/ln(((9.7581E12*emissiv)/twohrad)+1)));
      anum:=(anum+1);
     aden:=(aden+1);
       area:=((a1lim*anum)/aden)
   end{while}
  end;{if}
    if((fband=5)and(sband=7)) then
  begin
     while((tcone-1)>tctwo) do
   begin
              rohot:=((9.7581E12*emissiv)/(exp(8735.18/hottemp)-1));
              rthot:=((2.238E12*emissiv)/(exp(6507.02/hottemp)-1));
            onehrad:=((firrad-(area*rohot))/(1-area));
            twohrad:=((secrad-(area*rthot))/(1-area));
              tcone:=(round(8735.18/ln(((9.7581E12*emissiv)/onehrad)+1)));
               tctwo:=(round(6507.02/ln(((2.238E12*emissiv)/twohrad)+1)));
      anum:=(anum+1);
     aden:=(aden+1);
       area:=((a1lim*anum)/aden)
   end{while}
  end;{if}
   tempC:=(tcone-273);
  hota:=area;
 end;{Dualband}
{Temparea identifies the two bands to be used for the dual-band method.}
{Temparea also assigns precalculated values for saturated pixels.}
procedure Temparea(b4,b5,b7,emis:real; DN4,DN5,DN7,DNc4,DNc5,DNc7,thot:
    integer; var cold:integer; var harea:real);
     var a4lim,a5lim,a7lim:real;band1,band2:integer;
```

```
const BACKGROUND=40;
      SATURATE=425;
       HIGHTEMP=425;
begin
   a4lim:=0;
   a5lim:=0;
   a7lim:=0;
  band1:=0;
  band2:=0;
          a4lim:=(b4/((1.5148E14*emis)/(exp(17365.11/thot)-1)));
          a5lim:=(b5/((9.7581E12*emis)/(exp(8735.18/thot)-1)));
          a7lim:=(b7/((2.2383E12*emis)/(exp(6507.02/thot)-1)));
       writeln('a4limit,a5limit,a7limit  are',a4lim,a5lim,a7lim);
  if (((DNc7<5) and (DNc5<5)) and (DNc4<5)) then
 begin
  cold:=BACKGROUND;
    harea:=0;
  end {if monitoring background}
  else if (((DNc7>4) and (DN7<255)) and (DNc5<5)) then
 begin
   harea:=0;
            cold:=(round(6507.02/ln(((2.238E12*emis)/b7)+1)));
     cold:=(cold-273)
 end
   else if ((((DN5<255) and (DNc5>4)) and (DNc7>=5)) and (a7lim>a5lim))then
 begin
  band1:=5;
  band2:=7;
      Dualband(b5,b7,a5lim,a7lim,emis,band1,band2,thot,cold,harea)
 end
     else if (((DN7>=255) and (((DN5<255) and (DNc5>=5)) and (a5lim>a4lim)))
and (DNc4>4)) then
 begin
  band1:=4;
  band2:=5;
      Dualband(b4,b5,a4lim,a5lim,emis,band1,band2,thot,cold,harea)
 end
   else if ((DN5<255) and (a5lim>a7lim))then
 begin
     if (b7<0.1) then
      begin
         harea:=0;
       cold:=BACKGROUND
      end
    else begin
      harea:=5;
            cold:=(round(6507.02/ln(((2.238E12*emis)/b7)+1)));
       cold:=(cold-273)
  end
```

```
      end
        else if ((DN7=255) and (DN5=255)) then
       begin
        cold:=SATURATE;
         harea:=0
        end{if}
      else begin
        cold:=HIGHTEMP;
         harea:=0
        end{if}
    end;{Temparea}
begin{LandsatTM, main program section}
  pixtemp:=0;
   {Initialize arrays to zero}
  for i:=1 to 30 do
    for j:=1 to 30 do
      for k:=1 to 3 do
            pixrad[i,j,k]:=0;
  for i:=1 to 30 do
    for j:=1 to 30 do
      for k:=1 to 3 do
           DNvalue[i,j,k]:=0;
   for i:=1 to 30 do
    for j:=1 to 30 do
      for k:=1 to 3 do
            DNcorrect[i,j,k]:=0;
  for i:=1 to 30 do
    for j:=1 to 30 do
         tempcold[i,j]:=-1;
  for i:=1 to 30 do
    for j:=1 to 30 do
        hotarea[i,j]:=0;
    transmissivity:=0;
   emissivity:=0;
  band:=0;
   bkgr4:=0;
   bkgr5:=0;
   bkgr7:=0;
  temphot:=0;
  xmax:=0;
  ymax:=0;
  {Ask for constants to be used in calculations.}
    writeln('What is the emissivity of the surface?');
    readln(emissivity);
      while((emissivity>1)or(emissivity<0)) do
   begin
      writeln('The emissivity should be between 0 and 1');
       readln(emissivity);
    end;{while}
```

```
 writeln('What is the transmissivity of the atmosphere?');
 readln(transmissivity);
   while((transmissivity>1)or(transmissivity<0)) do
begin
    writeln('The atmospheric transmissivity should be between 0 and 1');
     readln(transmissivity);
 end;{while}
writeln('What are the background DN values for bands 4, 5, and 7?');
  readln(bkgr4,bkgr5,bkgr7);
writeln('What is the estimated temperature of the magmatic component?');
readln(temphot);
{The emissivity and transmissivity are both constants.}
{To make the program neater, I will combine the two here.}
   emissivity:=(emissivity*transmissivity);
{Now, get array size, DN values, and calculate radiance.}
 writeln('What are the array dimensions? x first, then y. Limit is 30.');
readln(xmax,ymax);
 while((xmax>30)or(xmax<1)) do
begin
   writeln('The number of columns should be between 1 and 30');
   readln(xmax);
 end;{while}
  while((ymax>30)or(ymax<1)) do
begin
   writeln('The number of rows should be between 1 and 30');
   readln(ymax);
 end;{while}
for k:=1 to 3 do begin
 i:=1;
 j:=1;
 if (k=1) then begin
   band:=4;
    bkgrtemp:=bkgr4
 end
   else if (k=2) then begin
     band:=5;
      bkgrtemp:=bkgr5
    end
      else if (k=3) then begin
        band:=7;
         bkgrtemp:=bkgr7
       end;{if identifying background and bandnumber}
  writeln('What are the array values for band',band);
 for j:=1 to ymax do
    for i:=1 to xmax do read (DNvalue[i,j,k]);
 for j:=1 to ymax do begin
  for i:=1 to xmax do
       write(DNvalue[i,j,k]:4);
  writeln
```

```
  end;
  {Subtract the background from the reported DN values}
  for j:=1 to ymax do
     for i:=1 to xmax do
              DNcorrect[i,j,k]:=(DNvalue[i,j,k]-bkgrtemp);
  {Calculate radiance}
  for j:=1 to ymax do
     for i:=1 to xmax do
              Radiance(DNcorrect[i,j,k],band,pixrad[i,j,k]);
    writeln('The radiance for this band',band,'is');
  for j:=1 to ymax do begin
     for i:=1 to xmax do
             write(pixrad[i,j,k]:11:1);
      writeln
 end;
 readln;
 readln
 end;{for k}
 for j:=1 to ymax do
    for i:=1 to xmax do
   Temparea(pixrad[i,j,1],pixrad[i,j,2],pixrad[i,j,3],emissivity,DNvalue[i,j,1],
              DNvalue[i,j,2],DNvalue[i,j,3],DNcorrect[i,j,1],DNcorrect[i,j,2],
             DNcorrect[i,j,3],temphot,tempcold[i,j],hotarea[i,j]);
  writeln('The answer to the dual-band problem for this area is');
  writeln;
  writeln('The hot temperature was set at',temphot);
  writeln;
   writeln('The crust temperatures in this area are:');
 for j:=1 to ymax do begin
      for i:=1 to xmax do
           write(tempcold[i,j]:4);
      writeln
 end;
  writeln;
 readln;
  writeln('The hot fractional areas are:');
 for j:=1 to ymax do begin
      for i:=1 to xmax do
            write(hotarea[i,j]:10:6);
      writeln
  end;
readln
end.{LandsatTM}
```